

The hydrogen atom in an electric field and in crossed electric and magnetic fields: Closed-orbit theory and semiclassical quantization

Von der Fakultät für Physik der Universität Stuttgart
zur Erlangung der Würde eines Doktors der
Naturwissenschaften (Dr. rer. nat.) genehmigte
Abhandlung

Vorgelegt von
Thomas Bartsch
aus Essen

Hauptberichter:	Prof. Dr. G. Wunner
Mitberichter:	Prof. Dr. M. Föhnle
Tag der mündlichen Prüfung:	26. Juli 2002

Institut für Theoretische Physik I
Universität Stuttgart

2002

Contents

1	Introduction	1
2	Closed-orbit theory	5
2.1	The classical Hamiltonian	5
2.2	The S -matrix formulation of closed-orbit theory	8
2.3	Closed-orbit theory for crossed-fields systems	13
2.4	Closed-orbit theory for symmetric systems	17
3	Harmonic inversion	23
3.1	Harmonic inversion in semiclassical physics	23
3.2	Harmonic inversion of δ function signals	27
3.2.1	Method 1: discrete filter diagonalization	28
3.2.2	Method 2: δ function filter diagonalization	30
3.2.3	Method 3: discrete decimated signal diagonalization	32
3.2.4	Method 4: δ function decimated signal diagonalization	32
3.3	Numerical examples and discussion	33
3.3.1	Harmonic oscillator	33
3.3.2	Zeros of Riemann's zeta function	35
3.3.3	Conclusion	40
3.4	Quantization of non-scaling systems	41
4	The Kustaanheimo-Stiefel transformation	45
4.1	The spinor equation of motion	46
4.2	Canonical formalism	49
4.2.1	Fictitious-time transformations	49
4.2.2	Lagrangian description	52
4.2.3	Hamiltonian description	54
4.3	The Kepler problem	55
4.4	The KS description of closed orbits	57
5	Closed orbits in crossed fields	63
5.1	General bifurcation theory	64
5.2	Codimension-one generic bifurcations	69
5.2.1	The tangent bifurcation	70
5.2.2	The pitchfork bifurcation	70

5.3	Closed orbits in the diamagnetic Kepler problem	73
5.4	Closed orbit bifurcation scenarios	73
5.4.1	Planar orbits	74
5.4.2	Non-planar orbits	81
5.5	The classification of closed orbits	91
6	Semiclassical crossed-fields spectra	97
6.1	The quantum spectrum	97
6.2	Low-resolution semiclassical spectra	98
6.3	High-resolution semiclassical spectra	102
6.4	Semiclassical recurrence spectra	107
6.5	Uniform approximations	113
6.5.1	The construction of uniform approximations	113
6.5.2	The fold catastrophe uniform approximation	117
6.5.3	The cusp catastrophe uniform approximation	118
6.5.4	Uniformized recurrence spectra	121
7	Stark effect	125
7.1	Separation of the equation of motion	126
7.2	Closed orbits	130
7.3	Bifurcations at low energies	137
7.4	Uniform approximations	140
7.4.1	Isolated bifurcations	140
7.4.2	Non-isolated bifurcations	144
7.5	Semiclassical spectra	151
8	Conclusion	167
A	Atomic units	169
B	The angular functions $\mathcal{Y}(\vartheta, \varphi)$	171
C	Introduction to geometric algebra	175
C.1	The geometric algebra of Euclidean 3-space	175
C.2	The exponential function	178
C.3	Rotations in the geometric algebra	179
C.4	The multivector derivative	180
	Bibliography	183
	Zusammenfassung	193

Chapter 1

Introduction

Ever since the early days of quantum mechanics, the correspondence between classical trajectories and atomic spectra has been a question of fundamental interest and importance. The “old” quantum theory suffered from the severe drawback that the Bohr-Sommerfeld quantization rules could only be applied to integrable systems. Although it had already been noted by Einstein [1] that integrable systems are exceptional, the question of how to quantize classically non-integrable systems remained unsolved. After the advent of the “exact” quantum mechanics, quantum mechanical calculations no longer relied on the underlying classical mechanics, so that the interest in the correspondence between classical and quantum mechanics declined. It was only after the development of periodic-orbit theory [2] and, as a variant for the photo-excitation spectra of atomic systems, closed-orbit theory [3, 4], that techniques were available to explore the intimate connections between quantum spectra and the underlying classical dynamics. These theories triggered an enormous upsurge of interest in the long-standing problem of developing what is now called a semiclassical quantization procedure for classically non-integrable systems, i.e. a quantization scheme based on the underlying classical dynamics.

The hydrogen atom in external electric and magnetic fields has become a prototype example for semiclassical studies. Whereas the hydrogen atom in an electric field is classically integrable, in a magnetic field it shows a transition from regular to completely chaotic behaviour, so that it is ideally suited to investigate the impact of classical regularity or chaos on quantum mechanical spectra. Closed-orbit theory provides a semiclassical approach to atomic photo-absorption spectra [3, 4]. It gives the oscillator-strength density as a sum of two terms, one a smoothly varying part (as a function of energy) and the other a superposition of sinusoidal oscillations. Each oscillation is associated with a “closed” classical orbit starting at and returning to the nucleus. It is therefore possible to analyse a given photo-absorption spectrum in terms of the closed orbits contributing to it. For the hydrogen atom in a magnetic field, a comprehensive classification of closed orbits exists, and in this framework the large-scale structures of the spectrum found a convincing semiclassical interpretation. Conversely, atomic energy levels and the corresponding transition strengths could be calculated from

classical orbits [5].

Because the hydrogen atom in a purely magnetic field possesses a rotational symmetry around the magnetic field axis, the angular momentum component along this axis is conserved. Therefore, the dynamics can be reduced, effectively, to two degrees of freedom. If, to the contrary, the atom is subjected to the combined influences of perpendicular magnetic and electric fields, all continuous symmetries are broken and three non-separable degrees of freedom have to be dealt with. In addition, the dynamics depends on two external parameters, viz. the field strengths, instead of only one. Hence, both the classical and quantum dynamics of the crossed-fields hydrogen atom is significantly more complex than in a magnetic field. Even after ten years of intense study, this complex behaviour is far from being completely understood.

Although a closed-orbit theory can be derived for the crossed-fields [6,7] as well as for the magnetized hydrogen atom, and the large-scale structures of crossed-fields photo-absorption spectra have been interpreted successfully in terms of individual closed orbits [7–11], only contributions of rather short orbits have been identified, and a general overview of the closed orbits in the crossed-fields system is not yet available. What is more, closed orbits are known to proliferate through bifurcations as the external field strengths are increased. As a crucial step towards a classification of closed orbits, therefore, one needs a bifurcation theory describing the generic types of bifurcations one should expect to find. A bifurcation theory for periodic orbits in Hamiltonian systems was developed long ago by Mayer [12]. Nevertheless, an analogue for closed orbits is still unavailable.

Much effort has been spent since the advent of the modern semiclassical theories on the construction of a general semiclassical quantization scheme (see, e.g., [13–19]). Although closed-orbit theory provides a means of calculating smoothed spectra, it does not readily lend itself to a calculation of individual energy levels because the sum over all closed orbits is divergent. Periodic-orbit theory, which gives a semiclassical approximation to the density of states of a quantum system, is formally analogous to closed-orbit theory and shares this fundamental difficulty. A number of different techniques have been proposed to overcome the convergence problems of the semiclassical theories. All of them are limited in their applicability because they make certain assumptions about the underlying classical dynamics. In particular, no method proposed to date can be used if bifurcations of classical orbits must be taken into account.

Most of the work on semiclassical quantization was restricted to systems having two degrees of freedom. It is of fundamental importance to assess the applicability of semiclassical schemes to systems with three or more degrees of freedom. Nevertheless, due to the additional complications brought about by the third degree of freedom, previous studies [20–25] have been restricted to billiard systems. A full semiclassical quantization has so far been achieved for the three-dimensional Sinai billiard [20] and the N -sphere scattering system [23] only. As it exhibits a transition from regular to chaotic dynamics, the hydrogen atom in crossed fields is considerably more complicated than billiard systems, and a semiclassical quantization has not even been attempted to date. To achieve a quantization, a number

of rather diverse problems must be solved. First, a thorough understanding of the closed orbits in the crossed-fields system is required. Second, bifurcations of closed orbits will turn out to play an important role in the crossed-fields hydrogen atom. They introduce divergences into the semiclassical spectrum, and suitable uniform approximations smoothing these divergences must be found. Third, a semiclassical quantization procedure capable of dealing with uniform approximations must be developed. All of these problems will be tackled in the course of this work.

In chapter 2, the basic properties of the crossed-fields hydrogen atom will be described and the fundamental formulae of closed-orbit theory will be derived. Recently, Granger and Greene [26] proposed a novel formulation of closed-orbit theory for atoms in magnetic fields based on semiclassical S -matrices. Their formulation appears to be more flexible than the conventional treatment when applied to non-hydrogenic atoms or molecules. I have extended it to the case of crossed external fields. For the case of a magnetic field, I discuss and clarify some misleading conclusions arrived at by Granger and Greene.

The semiclassical investigations presented here are largely based on the method of harmonic inversion, which was introduced [19, 27] as a general technique for both semiclassical quantization and the semiclassical analysis of quantum spectra. Several variants of the method have been proposed in the literature. I will summarize these in chapter 3 and apply them to two simple example systems to compare their numerical efficiencies. Finally, I will generalize the method to the semiclassical quantization of systems without a classical scaling property. This generalization is relevant beyond the realm of closed-orbit theory, because it can also be applied in connection with semiclassical trace formulae. It is the first truly universal semiclassical quantization scheme proposed in the literature, because it does not make any assumptions whatsoever about the underlying classical dynamics.

The numerical integration of the classical equations of motion for the crossed-fields hydrogen atom is plagued by the presence of the Coulomb singularity. As is well-known, this singularity can be regularized by means of a Kustaanheimo-Stiefel transformation [28]. A novel formulation of the transformation in the language of geometric algebra was introduced by Hestenes [29]. It offers the advantages of greater calculational simplicity and a clearer geometric interpretation than provided by a matrix-based approach. In this formalism, I will develop Lagrangian and Hamiltonian formulations of the Kustaanheimo-Stiefel transformation in chapter 4. I will then discuss the problems specific to the description of closed orbits and demonstrate that the geometric algebra allows a particularly clear exposition.

In chapter 5, the general framework for a local theory of closed-orbit bifurcations will be set up and the codimension-one generic bifurcations will be identified. It will be shown that the presence of reflection symmetries in the crossed-fields hydrogen atom has a significant impact on the possible types of bifurcations. Subsequently, I will describe the actual closed orbits and their bifurcations at low scaled energies. The simple elementary bifurcations will be seen to form a

surprisingly rich structure of complicated bifurcation scenarios. Finally, I will propose a classification scheme for closed orbits which is inspired by the case of a pure magnetic field, and I will demonstrate that it is applicable for electric field strengths at least up to half the strength of the magnetic field (in atomic units).

Chapter 6 discusses the semiclassics of the crossed-fields system. I will present both low-resolution and high-resolution semiclassical photo-absorption spectra. In the latter case, the strongest spectral lines are resolved. The observation that the high-resolution spectra cannot easily be improved so as to yield more spectral lines leads to a closer inspection of the semiclassical signal. Semiclassical recurrence spectra reveal that closed-orbit theory can be applied in principle for long as well as for short closed orbits, but the semiclassical spectrum is marred by missing orbits and, in particular, by the presence of bifurcations of closed orbits. Bifurcations lead to a divergence of the usual closed-orbit formula and must be treated by uniform semiclassical approximations. I will propose a heuristic, easy-to-apply technique for the construction of uniform approximations and derive these for the two types of codimension-one bifurcations. I will then show how uniform approximations can be included in the semiclassical quantization by harmonic inversion.

As the bifurcation scenarios occurring in crossed fields turn out to be too complex for a semiclassical quantization to be actually carried out, I will focus my discussion, in chapter 7, on the hydrogen atom in an electric field. This system is integrable, hence its classical mechanics is easy to understand. I will derive semi-analytical formulae describing the closed orbits which have not been given before in the literature. In spite of its apparent simplicity, the system still exhibits a multitude of closed-orbit bifurcations, that have so far precluded a semiclassical quantization based on closed-orbit theory. A uniform approximation describing a single bifurcation in the Stark system has been given before [30, 31]. Using the general method of chapter 6, I will re-derive it in a form which is much easier to apply in practice and supplement it with a uniform approximation for a more complicated bifurcation scenario. The latter is of fundamental interest because it is the first uniform approximation described in the literature which depends on a topologically non-trivial configuration space. The uniform approximations will then be used for a semiclassical quantization in a spectral region where the conventional closed-orbit formula would be completely useless due to an abundance of bifurcations. In this way, it is demonstrated that the quantization scheme introduced in chapters 3 and 6 indeed permits the inclusion of uniform approximations into a semiclassical quantization, which has so far been impossible.

Because of their high topicality, part of the results in this work have been published in advance [32].

Chapter 2

Closed-orbit theory

2.1 The classical Hamiltonian

To obtain a classical model describing the dynamics of the hydrogen atom in external fields, I assume the nucleus to have infinite mass and regard the electron as a structureless point charge. In atomic units (see appendix A) the Hamiltonian reads

$$H = \frac{1}{2} (\mathbf{p} + \mathbf{A}(\mathbf{x}))^2 - \frac{1}{r} - V(\mathbf{x}) \quad (2.1)$$

in terms of the electronic position and momentum vectors \mathbf{x} and \mathbf{p} , the radial distance $r = |\mathbf{x}|$ from the nucleus and the electromagnetic scalar and vector potentials $V(\mathbf{x})$ and $\mathbf{A}(\mathbf{x})$ describing the external fields. (Note that the electron charge is $e = -1$.) For a discussion of non-hydrogenic Rydberg atoms, a core potential modelling the influence of the inner electronic shells can be added to (2.1) (see, e.g., [33, 34]). In this work, the analysis will be restricted to the hydrogen atom. For homogeneous external magnetic and electric fields \mathbf{B} and \mathbf{F} , the potentials are $V(\mathbf{x}) = -\mathbf{F} \cdot \mathbf{x}$ and $\mathbf{A}(\mathbf{x}) = \frac{1}{2}\mathbf{B} \times \mathbf{x}$. With a magnetic field directed along the z -axis and an electric field directed along the x -axis, which is the field configuration to be assumed throughout most of this work, the Hamiltonian (2.1) reads

$$H = \frac{1}{2}\mathbf{p}^2 - \frac{1}{r} + \frac{1}{2}BL_z + \frac{1}{8}B^2\rho^2 + Fx, \quad (2.2)$$

where $\rho^2 = x^2 + y^2$ and L_z is the z -component of the angular momentum vector.

In the absence of an external electric field, the motion described by the Hamiltonian (2.1) is bounded in space for all energies $E < 0$ because the electron cannot escape from the Coulomb potential. If an electric field is present, it will tend to tear the electron away from the nucleus. The combination of the Coulomb and the external potentials exhibits a saddle point on the negative x -axis at the energy $E_S = -2\sqrt{F}$. For energies $E > E_S$, the electron can cross the Stark saddle point and escape to infinity, so that the motion is no longer bounded.

At first glance, the dynamics of the Hamiltonian (2.1) appears to depend on three external parameters, namely the field strengths B and F and the energy

	B	F	E	w
magnetic field strength B	1	$F^{-3/4}B$	$ E ^{-3/2}B$	w^3B
electric field strength \tilde{F}	$B^{-4/3}F$	1	$ E ^{-2}F$	w^4F
energy \tilde{E}	$B^{-2/3}E$	$F^{-1/2}E$	± 1	w^2E
position $\tilde{\mathbf{x}}$	$B^{2/3}\mathbf{x}$	$F^{1/2}\mathbf{x}$	$ E \mathbf{x}$	$w^{-2}\mathbf{x}$
momentum $\tilde{\mathbf{p}}$	$B^{-1/3}\mathbf{p}$	$F^{-1/4}\mathbf{p}$	$ E ^{-1/2}\mathbf{p}$	$w\mathbf{p}$
action \tilde{S}	$B^{1/3}S$	$F^{1/4}S$	$ E ^{1/2}S$	$w^{-1}S$
time \tilde{T}	BT	$F^{3/4}T$	$ E ^{3/2}T$	$w^{-3}T$
scaling parameter w	$B^{-1/3}$	$F^{-1/4}$	$ E ^{-1/2}$	

Table 2.1: Scaling prescriptions when scaling with the magnetic field strength B , the electric field strength F , the energy E , or the generic scaling parameter w .

E . The number of parameters can be reduced to two by exploiting the scaling properties of (2.1). They allow one to assign the fixed value 1 to any of the parameters. The dynamics will be left invariant if at the same time all classical quantities are multiplied by suitable powers of the scaling parameter. The details of this procedure are summarized in table 2.1. Notice, in particular, that when expressed in terms of the generic scaling parameter $w = B^{-1/3}$, $w = F^{-1/4}$ or $w = |E|^{-1/2}$, respectively, the scaling prescriptions in all three cases agree. The parameter w plays the role of an inverse effective Planck's constant $\hbar_{\text{eff}} = w^{-1}$ because, due to $S = w\tilde{S}$, the classical actions are large if w is. For configurations characterized by fixed scaled quantities, i.e. the same classical dynamics, the semiclassical limit thus corresponds to the limit $w \rightarrow \infty$.

The scaling prescription most frequently used in the literature is the scaling with the magnetic field strength B . I will adhere to this custom throughout, except when discussing the Stark effect in chapter 7, where the scaling with the electric field strength will be used. The scaling with respect to the energy E treats the two external field strengths on the same footing and thus best preserves their symmetry. It is not well suited, on the other hand, to discuss the transition from negative to positive energies, because the scaling can only be done with respect to the absolute value $|E|$, so that the scaled Hamiltonian changes its value discontinuously from -1 to $+1$ at $E = 0$.

The dynamics described by the Hamiltonian (2.1) depends crucially on the symmetries the field configuration possesses. For the semiclassical calculation of photo-absorption spectra, mainly classical trajectories starting at and returning to the nucleus are relevant. The discussion of symmetries will therefore focus on these trajectories, which will henceforth be called closed orbits. If only one external field is present and is assumed to be directed along the z -axis, there is a rotational symmetry around this axis. Consequently, the z -component of the angular momentum L_z is conserved and allows an effective reduction of the number of degrees of freedom from three to two. For trajectories passing through the nucleus, in particular, $L_z = 0$.

Due to the rotational symmetry, all closed orbits occur in one-parameter families obtained by rotating a single orbit around the field axis. The starting and

	x	y	z	p_x	p_y	p_z
Z	x	y	$-z$	p_x	p_y	$-p_z$
T	x	$-y$	z	$-p_x$	p_y	$-p_z$
C	x	$-y$	$-z$	$-p_x$	p_y	p_z

Table 2.2: The symmetry transformations of the crossed-fields system, expressed in Cartesian coordinates.

returning directions of the orbits in a given family can be characterized by giving the angle ϑ between the outgoing direction and the field axis. An exception is formed by orbits starting along the field axis, i.e. with $\vartheta = 0$ or $\vartheta = \pi$. These orbits are invariant under a rotation around the axis. Therefore they do not occur in families.

In the absence of a magnetic field, the dynamics is invariant under time-reversal. The presence of a magnetic field in general destroys this symmetry, but if there is no external electric field, time-reversal invariance holds in the subspace with $L_z = 0$. For a discussion of closed orbits, therefore, time-reversal invariance effectively holds whenever there is a single external field. In these cases, an electron returning to the nucleus will therefore rebound from the Coulomb centre into its direction of incidence and retrace its previous trajectory back to its starting direction. Therefore, any closed orbit, if it is not itself periodic, is half of a periodic orbit. In particular, closed orbits possess repetitions. In the special case when the starting and returning angles of the orbit are equal, the closed orbit is itself periodic.

In the presence of non-parallel electric and magnetic fields there is no continuous symmetry so that apart from the energy no constant of the motion exists. Thus, three non-separable degrees of freedom have to be dealt with. I will always assume the electric and magnetic fields to be perpendicular and choose coordinates so that the magnetic field is directed along the positive z -axis and the electric field along the positive x -axis. In the crossed-fields case, two angles are required to characterize the starting or returning direction of an orbit. I will use the polar angle ϑ between the trajectory and the magnetic field axis and the azimuthal angle φ between the projection of the trajectory into the x - y -plane and the electric field axis.

There are three discrete symmetry transformations of the crossed-fields system:

- the reflection Z at the x - y -plane,
- the combination T of time-reversal and a reflection at the x - z -plane,¹
- the combination C=ZT of the above.

Note that the crossed-fields system is not invariant under time-reversal, so that closed orbits do not in general possess repetitions. The effects of the transforma-

¹Note that the T operation is not time-reversal.

	Transformation				Symmetry conditions
	ϑ_i	φ_i	ϑ_f	φ_f	
Z	$\pi - \vartheta_i$	φ_i	$\pi - \vartheta_f$	φ_f	$\vartheta_i = \vartheta_f = \frac{\pi}{2}$
T	ϑ_f	$-\varphi_f$	ϑ_i	$-\varphi_i$	$\vartheta_i = \vartheta_f$ and $\varphi_i = -\varphi_f$
C	$\pi - \vartheta_f$	$-\varphi_f$	$\pi - \vartheta_i$	$-\varphi_i$	$\vartheta_i = \pi - \vartheta_f$ and $\varphi_i = -\varphi_f$

Table 2.3: The symmetry transformations of the crossed-fields system: Transformation of initial and final angles and symmetry conditions for doublets. Singlets satisfy $\vartheta_i = \vartheta_f = \frac{\pi}{2}$ and $\varphi_i = -\varphi_f$.

tions on the Cartesian coordinates as well as on the initial and final angles of a closed orbit are summarized in tables 2.2 and 2.3.

The application of these transformations to a given closed orbit yields a group of four closed orbits of equal length. Typically, these orbits will all be distinct, so that closed orbits in the crossed-fields system occur in quartets. In particular cases, a closed orbit can be invariant under one of the symmetry transformations. In this case, there are only two distinct orbits related by symmetry transformations. I will refer to them as a doublet, or more specifically as a Z-, T-, or C-doublet, giving the transformation under which the orbits are invariant. The transformations of the initial and final angles given in table 2.3 yield symmetry conditions that an orbit invariant under any of the transformations must satisfy. They are also given in table 2.3. In special cases, a closed orbit can be invariant under all three symmetry transformations of the crossed-fields system. It then occurs as a singlet, since no distinct orbits can be generated from it by a symmetry transformation.

Among the symmetry transformations, the reflection Z plays a special role in that it is a purely geometric transformation. There is, therefore, an invariant subspace of the phase space, viz. the x - y -plane perpendicular to the magnetic field. This plane is invariant under the dynamics and therefore forms a subsystem with two degrees of freedom. In addition, in quantum mechanics the Z-transformation gives rise to a conserved parity quantum number.

In connection with bifurcations of orbits it is essential to study ghost orbits, i.e. to allow coordinates and momenta to assume complex values. For ghost orbits, another reflection symmetry arises, viz. the symmetry with respect to complex conjugation. As the Hamiltonian (2.1) is real, it is obviously invariant under complex conjugation. Therefore, ghost orbits always occur in pairs of conjugate orbits.

2.2 The S -matrix formulation of closed-orbit theory

Closed-orbit theory was first introduced by Du and Delos [3] and Bogomolny [4] some twenty years ago to interpret the modulations observed in the photo-absorp-

tion spectra of hydrogenic Rydberg atoms in a magnetic field close to the ionization threshold. Since that time, it has proven a powerful and flexible tool for the semiclassical interpretation of a variety of spectra. It has been used to describe atoms in electric [35] as well as parallel [36, 37] or crossed [6–8, 38] electric and magnetic fields. In the case of non-hydrogenic atoms, the influence of the ionic core can be modelled either by means of an effective classical potential [33, 34] or in terms of quantum defects [39, 40]. Recently, closed-orbit theory has even been shown to be applicable to the spectra of simple molecules in external fields [41].

The basic observation fundamental to all of closed-orbit theory is a partition of space into physically distinct regions. In the core region close to the nucleus, the Rydberg electron interacts in a complicated manner with all electrons of the ionic core. This interaction is manifestly quantum mechanical in nature, it cannot be described in the framework of semiclassical theories. On the other hand, the interaction of the Rydberg electron with the external fields is much weaker in the core region than its interaction with the core, so that the fields can safely be neglected. Therefore, a description of the core obtained in the field-free case can be used. In particular, the initial state of the photo-absorption process is assumed to be localized in the core region and not to be influenced by the external fields.

In the long-range region far away from the nucleus, on the other hand, the external fields play a dominant role, whereas there is no interaction with the ionic core except for the Coulomb attraction of its residual charge. In this region, the dynamics of the Rydberg electron is well-suited for a semiclassical description. It is independent of the details of the ionic core.

In order to establish a link between the dynamics in the core and long-range regions, a matching region is assumed to exist at intermediate distances from the nucleus where both the external fields and the interaction with the core are negligible. Thus, in the matching region the simple physics of an electron subject to the residual Coulomb field of the core is observed.

Recently, Granger and Greene [26] proposed a novel formulation of the theory based on ideas borrowed from quantum-defect theory. Their formulation achieves a clear separation between properties of the external field configuration and the ionic core, which are encoded in separate *S*-matrices. Suitable approximations to the core and the long-range *S*-matrices can be derived independently. Therefore, the formalism can be expected to allow a generalization of closed-orbit theory to atoms with ionic cores exhibiting more complicated internal dynamics than have been treated so far.

The derivation given by Granger and Greene treated the case of an atom in a magnetic field only. It will now be extended in such a way that it holds for combined electric and magnetic fields with arbitrary field configurations. To this end, the ansatz and basic formulae of Granger and Greene’s theory will be summarized in this section. A more detailed treatment can be found in their paper [26]. In subsequent sections, I will then turn to a discussion of the long-range scattering matrices pertinent to different external field configurations.

To lay the foundation for a definition of the *S*-matrices, I pick a basis set Ψ_k^{core} and Ψ_k^{LR} of wave functions of the Rydberg electron valid in the core and

long-range regions, respectively, and expand in terms of spherical harmonics

$$\Psi_k^{\text{core(LR)}}(r, \vartheta, \varphi) = \frac{1}{r} \sum_{k'} Y_{k'}(\vartheta, \varphi) F_{k'k}^{\text{core(LR)}}(r) . \quad (2.3)$$

The channel index k is to be understood as a double index (l, m) characterizing the spherical harmonics. When studying a complicated atom with more than one relevant state of the core, additional information can be included in the channel functions Y_k .

In the matching region, the radial function matrices $\underline{F}^{\text{core}}$ and $\underline{F}^{\text{LR}}$ can both be expressed in terms of radial Coulomb functions. I use the functions $f_k^+(r)$ and $f_k^-(r)$ satisfying outgoing and incoming wave boundary conditions, respectively, given by [42] and choose the radial functions to be of the form²

$$F_{k'k}^{\text{core}}(r) = -i [f_{k'}^+(r) S_{k'k}^{\text{core}} - f_{k'}^-(r) \delta_{k'k}] , \quad (2.4)$$

$$F_{k'k}^{\text{LR}}(r) = -i [f_{k'}^+(r) \delta_{k'k} - f_{k'}^-(r) S_{k'k}^{\text{LR}}] . \quad (2.5)$$

Physically, these choices mean that the basis function Ψ_k^{core} is a superposition of a single incoming wave in channel k and the outgoing waves in different channels produced from it by scattering off the core. Similarly, Ψ_k^{LR} consists of an outgoing wave in channel k and the returning waves generated by scattering off the external fields. The scattering matrices $\underline{S}^{\text{core}}$ and $\underline{S}^{\text{LR}}$ thus summarize the physical properties of the core and the external fields, respectively. They are determined by the condition that the radial functions obey suitable boundary conditions, i.e. $\underline{F}^{\text{core}}$ is regular at the origin, whereas $\underline{F}^{\text{LR}}$ vanishes or satisfies outgoing-wave boundary conditions at infinity for bound and free states, respectively.

For hydrogen atoms, the expansion (2.4) in terms of Coulomb functions is valid arbitrarily close to the nucleus. To make the wave functions regular at the origin, $\underline{S}^{\text{core}}$ must be chosen equal to the identity matrix. The fact that it is a diagonal matrix reflects the conservation of angular momentum. For alkali metal atoms, the wave functions experience an additional phase shift upon scattering off the core. The core S -matrix can be expressed in terms of the quantum defects μ_k (which in fact depend on l only) as

$$S_{kk'}^{\text{core}} = \delta_{kk'} e^{2\pi i \mu_k} . \quad (2.6)$$

Similarly, the expansion (2.5) of the long-range radial functions is valid for arbitrarily large r if no external fields are present. The long-range S -matrix can then be determined from the asymptotic behaviour of the Coulomb functions. To a good approximation [43], it reads

$$S_{kk'}^{\text{LR}} = e^{2i\beta_k} \delta_{kk'} \quad (2.7)$$

²The regular and irregular Coulomb functions f and g used by Granger and Greene [26] differ from those used by Robicheaux [43] in that they are energy-normalized in Rydberg rather than in Hartree units. The radial function matrices given here agree in normalization with those adopted by Robicheaux, so that they are consistent with (2.13) below, which is adapted from [43]. The matrices used by Granger and Greene are inconsistent with their equation (12).

with

$$\beta_k = \begin{cases} \pi(\nu - l) & \text{if } E < 0, \\ i\infty & \text{if } E > 0, \end{cases} \quad (2.8)$$

and the effective quantum number $\nu = 1/\sqrt{-2E}$. In the presence of external fields, $\underline{S}^{\text{LR}}$ encodes the details of the field configuration. As it describes the dynamics at long distances from the nucleus, it lends itself to a semiclassical approximation.

A complete description of photo-absorption spectra requires the calculation of the energies E_n of the excited atomic states and the strengths of the spectral lines, which is characterized by the dipole matrix elements $\langle i|D|n\rangle$ between the initial state $|i\rangle$ and the Rydberg state $|n\rangle$, where D is the component of the dipole operator describing the polarization of the exciting laser field. Alternatively, the oscillator strengths $f_n = 2(E_n - E_i) |\langle i|D|n\rangle|^2$ or the scattering cross sections $\sigma_n = 4\pi^2\alpha(E_n - E_i) |\langle i|D|n\rangle|^2$ with the fine structure constant α can be specified. These quantities are neatly summarized in the response function

$$g(E) = -\frac{1}{\pi} \langle i|D G(E) D|i\rangle = -\frac{1}{\pi} \sum_n \frac{|\langle i|D|n\rangle|^2}{E - E_n + i\epsilon}, \quad (2.9)$$

where

$$G(E) = \sum_n \frac{|n\rangle\langle n|}{E - E_n + i\epsilon} \quad (2.10)$$

denotes the retarded Green's function. From $g(E)$, both the oscillator strength density

$$f(E) = \sum_n f_n \delta(E - E_n) = 2(E - E_i) \text{Im } g(E) \quad (2.11)$$

and the cross section density

$$\sigma(E) = \sum_n \sigma_n \delta(E - E_n) = 4\pi^2\alpha(E - E_i) \text{Im } g(E) \quad (2.12)$$

can easily be computed.

Following previous work by Robicheaux [43], Granger and Greene derive the following expression for the response function:

$$g = i \underline{d}^\dagger (\underline{1} - \underline{S}^{\text{core}} \underline{S}^{\text{LR}})^{-1} (\underline{1} + \underline{S}^{\text{core}} \underline{S}^{\text{LR}}) \underline{d}, \quad (2.13)$$

where the vector \underline{d} comprises the energy-dependent dipole matrix elements

$$d_k(E) = \langle \Psi_k^{\text{core}}(E) | D | i \rangle \quad (2.14)$$

between the initial state and the core-region channel wave functions. Usually, due to angular-momentum selection rules, only a few of the d_k are non-zero. Their calculation requires a detailed knowledge of the atomic core. For hydrogen the core wave functions are known analytically, so that the d_k can easily be computed (see appendix B).

An expression for the response function which is easier to interpret is gained by expanding the matrix inverse in equation (2.13) in a geometric series, which yields

$$g = i \underline{d}^\dagger \left(\underline{1} + 2 (\underline{S}^{\text{core}} \underline{S}^{\text{LR}}) + 2 (\underline{S}^{\text{core}} \underline{S}^{\text{LR}})^2 + 2 (\underline{S}^{\text{core}} \underline{S}^{\text{LR}})^3 + \dots \right) \underline{d}. \quad (2.15)$$

The terms in this series embody contributions from paths where the Rydberg electron takes zero, one, two \dots trips out into the long-range region and back to the core before interfering with the initial outgoing wave. In the semiclassical approximation, $\underline{S}^{\text{LR}}$ will be given in terms of closed orbits. A returning wave is associated with each returning classical orbit. By a general ionic core, it is scattered into all directions. The parts of the wave scattered into the outgoing direction of a closed orbit will then follow this orbit until they return to the core again. Thus, core scattering leads to a concatenation of different closed orbits [39, 40]. In hydrogen, the Coulomb centre scatters the incoming wave back into its direction of incidence, so that there is no coupling of closed orbits. Terms describing repeated scattering off the external fields are therefore absent from the sum, and the hydrogen response function can be decomposed into a smooth part

$$g_0 = i \underline{d}^\dagger \underline{d}, \quad (2.16)$$

which is the same as in the field-free case and contains “direct” contributions where the electron does not scatter off the external fields at all, and an oscillatory part

$$g^{\text{osc}} = 2i \underline{d}^\dagger \underline{S}^{\text{LR}} \underline{d} \quad (2.17)$$

generated by the electron going out into the long-range region and being scattered back to the nucleus. It is this part which describes the impact of the external fields. The semiclassical approximation will be of the form

$$g^{\text{osc}} = \sum_{\text{c.o.}} \mathcal{A}_{\text{c.o.}} e^{iS_{\text{c.o.}}}, \quad (2.18)$$

where the sum extends over all classical closed orbits starting from the nucleus and returning to it after being deflected by the external fields,

$$S_{\text{c.o.}} = \oint \mathbf{p} \cdot d\mathbf{x} \quad (2.19)$$

is the classical action of the closed orbit, and the amplitude $\mathcal{A}_{\text{c.o.}}$ describes its stability and its starting and returning directions. The precise form of $\mathcal{A}_{\text{c.o.}}$ depends on the geometry of the external fields and will be derived below for systems with and without a rotational symmetry. In any case, $\mathcal{A}_{\text{c.o.}}$ can be computed from purely classical quantities.

The basis for a semiclassical approximation is provided by the retarded Green’s function $G(\mathbf{x}, \mathbf{x}'; E)$ describing the propagation of the electron from \mathbf{x}' to \mathbf{x} at the energy E . It can be expanded in terms of the channel functions as

$$G(\mathbf{x}, \mathbf{x}'; E) = \frac{1}{rr'} \sum_{kk'} Y_k(\vartheta, \varphi) \tilde{G}_{kk'}(r, r'; E) Y_{k'}^*(\vartheta', \varphi') \quad (2.20)$$

with

$$\tilde{G}_{kk'}(r, r'; E) = rr' \langle k | G(\mathbf{x}, \mathbf{x}'; E) | k' \rangle . \quad (2.21)$$

The long-range scattering matrix is related to the Green's function matrix by [26]

$$\underline{S}^{\text{LR}} = \frac{1}{i\pi} [\underline{f}^-(r_0)]^{-1} \underline{G}(r_0, r_0) [\underline{f}^-(r_0)]^{-1} , \quad (2.22)$$

where r_0 is the matching radius, \underline{f}^- is the diagonal matrix

$$f_{kk'}^-(r) = f_k^-(r) \delta_{kk'} \quad (2.23)$$

comprising the radial wave functions, and $\underline{G}(r, r')$ denotes the part of $\tilde{G}(r, r')$ satisfying incoming-wave boundary conditions at the final radius r . The latter condition ensures that only electron paths approaching the matching radius from the long-range region contribute to $\underline{S}^{\text{LR}}$, whereas paths that traverse the core region are omitted.

2.3 Closed-orbit theory for crossed-fields systems

To obtain a semiclassical approximation to the long-range scattering matrix, I make use of the semiclassical Green's function derived by Gutzwiller [2]

$$G^{\text{scl}}(\mathbf{x}, \mathbf{x}'; E) = \frac{2\pi}{(2\pi i)^{(n+1)/2}} \sum_{\text{class. traj.}} \sqrt{|D|} \exp\left(iS - i\frac{\pi}{2}\sigma\right) , \quad (2.24)$$

where the sum extends over all classical trajectories leading from \mathbf{x}' to \mathbf{x} at the energy E , n is the number of degrees of freedom,

$$S = \int_{\mathbf{x}'}^{\mathbf{x}} \mathbf{p} \cdot d\mathbf{x} , \quad (2.25)$$

is the classical action along the trajectory, σ the number of caustics along the trajectory, and

$$D = \det \begin{pmatrix} \frac{\partial^2 S}{\partial \mathbf{x} \partial \mathbf{x}'} & \frac{\partial^2 S}{\partial \mathbf{x} \partial E} \\ \frac{\partial^2 S}{\partial E \partial \mathbf{x}'} & \frac{\partial^2 S}{\partial E^2} \end{pmatrix} \quad (2.26)$$

is the amplitude for the contribution of the trajectory. By (2.21), I obtain a semiclassical approximation to the Green's function matrix

$$\begin{aligned} G_{kk'}^{\text{scl}}(r_0, r_0; E) &= r_0^2 \int d\vartheta d\vartheta' d\varphi d\varphi' \sin \vartheta \sin \vartheta' Y_k^*(\vartheta, \varphi) Y_{k'}(\vartheta', \varphi') \\ &\times \frac{2\pi}{(2\pi i)^2} \sum_{\text{class. traj.}} \sqrt{|D|} \exp\left(iS(r_0, r_0) - i\frac{\pi}{2}\sigma\right) . \end{aligned} \quad (2.27)$$

As usual in semiclassics, the integrals will be evaluated in the stationary-phase approximation. It yields a sum over all classical trajectories leaving the matching sphere at a direction given by (ϑ_i, φ_i) and returning to it at (ϑ_f, φ_f) . The condition that $\underline{G}(r_0, r_0)$ obeys incoming-wave boundary conditions at the final radius translates into the condition that only orbits going out from the matching sphere into the long-range region and then returning to r_0 are to be included, whereas orbits passing through the core region are omitted. If all factors in the integrand except for the exponential are assumed to vary slowly, the stationary-phase approximation reads

$$G_{kk'}^{\text{scl}}(r_0, r_0; E) = 2\pi r_0^2 \sum_{i \rightarrow f} \sin \vartheta_i \sin \vartheta_f Y_k^*(\vartheta_f, \varphi_f) Y_{k'}(\vartheta_i, \varphi_i) \\ \times \frac{\sqrt{|D_{\text{s.p.}}|}}{\sqrt{\left| \det \frac{\partial^2 S}{\partial(\vartheta', \varphi', \vartheta, \varphi)^2} \right|}} \exp\left(iS(r_0, r_0) - i\frac{\pi}{2}(\sigma + \kappa)\right), \quad (2.28)$$

where κ is the number of negative eigenvalues of the Hessian matrix of S occurring in the prefactor.

Because the initial state is assumed to be well localized, it is clear that the outgoing waves generated by the photo-excitation originate in the immediate neighbourhood of the nucleus. Therefore, only trajectories leaving the matching sphere radially need to be included in (2.28). By the same token, the trajectories can be assumed to return to the matching radius radially. Thus, they are parts of closed orbits starting precisely at the nucleus and returning there.

By transforming (2.26) to spherical coordinates and making use of the relations

$$\frac{\partial S}{\partial \mathbf{x}} = \mathbf{p}, \quad \frac{\partial S}{\partial E} = t, \quad (2.29)$$

the amplitude factor D for radial trajectories can be simplified to

$$D = -\frac{1}{\dot{r} \dot{r}' r^2 r'^2 \sin \vartheta \sin \vartheta'} \det \frac{\partial(p'_\vartheta, p'_\varphi)}{\partial(\vartheta, \varphi)}. \quad (2.30)$$

The determinants occurring in (2.28) combine to

$$\det \frac{\partial(p'_\vartheta, p'_\varphi)}{\partial(\vartheta, \varphi)} \cdot \left(\det \frac{\partial^2 S}{\partial(\vartheta', \varphi', \vartheta, \varphi)^2} \right)^{-1} \\ = \det \frac{\partial(p'_\vartheta, p'_\varphi, p_\vartheta, p_\varphi)}{\partial(\vartheta, \varphi, p_\vartheta, p_\varphi)} \cdot \left(\det \frac{\partial(-p'_\vartheta, -p'_\varphi, p_\vartheta, p_\varphi)}{\partial(\vartheta', \varphi', \vartheta, \varphi)} \right)^{-1} \\ = \det \frac{\partial(\vartheta', \varphi')}{\partial(p_\vartheta, p_\varphi)}. \quad (2.31)$$

With these results, the Green's function matrix assumes the form

$$G_{kk'}^{\text{scl}}(r_0, r_0; E) = 2\pi \sum_{\text{c.o.}} \frac{\sqrt{\sin \vartheta_i \sin \vartheta_f}}{\sqrt{|\dot{r}\dot{r}'|}} \times \frac{Y_k^*(\vartheta_f, \varphi_f) Y_{k'}(\vartheta_i, \varphi_i)}{\sqrt{\left| \det \frac{\partial(p_{\vartheta_f}, p_{\varphi_f})}{\partial(\vartheta_i, \varphi_i)} \right|}} \exp \left(iS(r_0, r_0) - i\frac{\pi}{2}(\sigma + \kappa) \right). \quad (2.32)$$

The determinant in the denominator of (2.32) measures the dependence of the final angular momenta of the trajectory upon the starting angles. As it stands, it suffers from the singularities of the spherical coordinate chart: At the poles, neither the angle φ nor the angular momenta p_{ϑ} and p_{φ} are well defined, so that close to the poles, the calculation of the determinant becomes numerically unstable. In section 4.4, the determinant will be rewritten in the form

$$\det \frac{\partial(p_{\vartheta_f}, p_{\varphi_f})}{\partial(\vartheta_i, \varphi_i)} = \sin \vartheta_i \sin \vartheta_f M \quad (2.33)$$

with a 2×2 -determinant M devoid of any singularities. With this form of the stability determinant, the semiclassical Green's function matrix reads

$$G_{kk'} = 2\pi \sum_{\text{c.o.}} \frac{1}{\sqrt{|\dot{r}\dot{r}'|}} \frac{Y_k^*(\vartheta_f, \varphi_f) Y_{k'}(\vartheta_i, \varphi_i)}{\sqrt{|M|}} \exp \left(iS(r_0, r_0) - i\frac{\pi}{2}(\sigma + \kappa) \right), \quad (2.34)$$

which is free of any singularities introduced by the spherical coordinates.

By virtue of (2.22), the semiclassical long-range scattering matrix reads

$$S_{kk'}^{\text{LR}} = 2i \sum_{\text{c.o.}} \frac{1}{\sqrt{|\dot{r}\dot{r}'|}} \frac{1}{f_k^-(r_0)} \frac{1}{f_{k'}^-(r_0)} \frac{Y_k^*(\vartheta_f, \varphi_f) Y_{k'}(\vartheta_i, \varphi_i)}{\sqrt{|M|}} \times \exp \left(iS(r_0, r_0) - i\frac{\pi}{2}(\sigma + \kappa) \right). \quad (2.35)$$

This expression can be further simplified if, for excited states close to the ionization threshold, the radial wave functions

$$f_l^-(r) \approx -i\sqrt{r} H_{2l+1}^{(2)}(\sqrt{8r}) \quad (2.36)$$

are approximated by the zero-energy wave functions, and the Hankel functions are replaced with their asymptotic forms for large arguments [44]

$$H_\nu^{(2)}(x) \approx \sqrt{\frac{2}{\pi x}} \exp \left(-ix + i\frac{\pi}{2}\nu + i\frac{\pi}{4} \right). \quad (2.37)$$

This approximation has proven accurate in many cases of interest, but it was called into question by Granger and Greene [26]. It will be discussed further in

section 2.4, where I will show that there is no reason to doubt its reliability. It leads to

$$S_{lm,l'm'}^{\text{LR}} = -2\pi \sum_{\text{c.o.}} (-1)^{l+l'} \frac{Y_{lm}^*(\vartheta_f, \varphi_f) Y_{l'm'}(\vartheta_i, \varphi_i)}{\sqrt{|M|}} \times \exp \left(i \left(S(r_0, r_0) + 2\sqrt{8r_0} \right) - i\frac{\pi}{2}(\sigma + \kappa) \right), \quad (2.38)$$

because, due to the conservation of energy, $r^2/2 = 1/r$ if $E = 0$. In equation 2.38, the channel indices $k = (l, m)$ are finally written out explicitly.

For a radial trajectory in a hydrogen atom going out from the nucleus to $r = r_0$ at zero energy, the action is $\sqrt{8r_0}$, so that

$$S_{\text{c.o.}} = S(r_0, r_0) + 2\sqrt{8r_0} \quad (2.39)$$

is the action of a closed orbit, measured from its start at the nucleus to its return. The semiclassical long-range S -matrix finally reads

$$S_{lm,l'm'}^{\text{LR}} = -2\pi \sum_{\text{c.o.}} (-1)^{l+l'} \frac{Y_{lm}^*(\vartheta_f, \varphi_f) Y_{l'm'}(\vartheta_i, \varphi_i)}{\sqrt{|M|}} \exp \left(iS_{\text{c.o.}} - i\frac{\pi}{2}(\sigma + \kappa) \right), \quad (2.40)$$

Both the action $S_{\text{c.o.}}$ and the stability determinant M are evaluated at the nucleus rather than on the matching sphere. The response function is given by

$$g^{\text{osc}}(E) = 4\pi \sum_{\text{c.o.}} \frac{\mathcal{Y}^*(\vartheta_f, \varphi_f) \mathcal{Y}(\vartheta_i, \varphi_i)}{\sqrt{|M|}} \exp \left(iS_{\text{c.o.}} - i\frac{\pi}{2}\mu \right), \quad (2.41)$$

where the Maslov index $\mu = \sigma + \kappa + 1$ was increased by 1 to absorb an additional phase, and the angular function

$$\mathcal{Y}(\vartheta, \varphi) = \sum_{lm} (-1)^l d_{lm} Y_{lm}(\vartheta, \varphi), \quad (2.42)$$

with the core-region matrix elements d_{lm} given by (2.14), characterizes the initial state and the exciting photon. Through the d_{lm} , the function $\mathcal{Y}(\vartheta, \varphi)$ is energy-dependent. In accordance with the choice of zero-energy radial wave functions in the S -matrix elements, the angular function will be evaluated at zero energy (see appendix B. This approximation has proven accurate in all applications of closed-orbit theory considered in the literature so far. However, from the S -matrix theory derivation it is obvious that the energy-dependence of both the dipole matrix elements d_{lm} and the S -matrix elements can easily be included should the need arise. The semiclassical response function (2.41) has the anticipated form (2.18) with

$$\mathcal{A}_{\text{c.o.}} = 4\pi \frac{\mathcal{Y}^*(\vartheta_f, \varphi_f) \mathcal{Y}(\vartheta_i, \varphi_i)}{\sqrt{|M|}} e^{i(\pi/2)\mu}. \quad (2.43)$$

2.4 Closed-orbit theory for rotationally symmetric systems

In the case of an atom in a single external field, a semiclassical expression for the long-range scattering matrix can in principle be derived along the lines followed in the previous section. The derivation is complicated, however, by the rotational symmetry of the system, which makes closed classical orbits occur in families. Due to this symmetry, the integrations over φ and φ' in (2.27) cannot be evaluated in the stationary-phase approximation, but must be calculated exactly. A semiclassical theory dealing with these degeneracies can be developed for arbitrary symmetry groups [45,46]. The treatment can be simplified, however, if the symmetry reduction is performed at the level of the Schrödinger equation instead of the semiclassical Green's function.

The rotational symmetry gives rise to a conserved magnetic quantum number m , so that the angular momentum quantum number l remains the only relevant channel index. The semiclassical scattering matrix reads [26]

$$S_{ll'}^{\text{LR}} = 2^{3/2} \pi^{1/2} \sum_{i \rightarrow f} \frac{\sqrt{|A| \sin \vartheta_i \sin \vartheta_f}}{|\dot{r}| f_i^-(r_0) f_{l'}^-(r_0)} Y_{lm}^*(\vartheta_f, 0) Y_{l'm'}(\vartheta_i, 0) \times \exp \left(iS(r_0, r_0) - i\frac{\pi}{2} \tilde{\mu} - i\frac{3\pi}{4} \right), \quad (2.44)$$

where

$$A = \left. \frac{\partial \vartheta_i}{\partial p_{\vartheta_f}} \right|_{p_{\vartheta_i}}, \quad (2.45)$$

$\tilde{\mu}$ is the number of poles of A encountered along the trajectory, and the sum includes all classical trajectories with azimuthal angular momentum m joining the circles given by polar angles ϑ_i and ϑ_f on the matching sphere. If the radius of the matching sphere is much larger than the extent of the initial state, the trajectories can again be assumed to leave the sphere and return to it radially. Strictly speaking, this condition can only be met if $m = 0$, which I will assume in what follows. If $m \neq 0$, the initial angular velocity $\dot{\varphi}$ must be non-zero, but it will be small if the matching radius is large. In this case, the trajectory will not actually close at the nucleus, but swing by at a short distance.

Using, as above, the radial wave functions at zero energy, I obtain the semiclassical scattering matrix

$$S_{ll'}^{\text{LR}} = -(2\pi)^{3/2} (-1)^{l+l'} i \sum_{\text{c.o.}} \sqrt{|A| \sin \vartheta_i \sin \vartheta_f} Y_{lm}^*(\vartheta_f, 0) Y_{l'm'}(\vartheta_i, 0) \times \exp \left(iS_{\text{c.o.}} - i\frac{\pi}{2} \tilde{\mu} - i\frac{3\pi}{4} \right) \quad (2.46)$$

and the response function

$$g^{\text{osc}}(E) = 2(2\pi)^{3/2} \sum_{\text{c.o.}} \sqrt{|A| \sin \vartheta_i \sin \vartheta_f} \mathcal{Y}^*(\vartheta_f) \mathcal{Y}(\vartheta_i) \times \exp\left(iS_{\text{c.o.}} - i\frac{\pi}{2}\mu + i\frac{\pi}{4}\right) \quad (2.47)$$

with $\mu = \tilde{\mu} + 2$ and

$$\mathcal{Y}(\vartheta) = \sum_l (-1)^l d_l Y_{lm}(\vartheta, 0). \quad (2.48)$$

The angular function \mathcal{Y} thus defined is a special case of that defined in (2.42) with φ set to zero.

This result has the form (2.18) with

$$\mathcal{A}_{\text{c.o.}} = 2(2\pi)^{3/2} \sqrt{|A| \sin \vartheta_i \sin \vartheta_f} \mathcal{Y}^*(\vartheta_f) \mathcal{Y}(\vartheta_i) \exp\left(i\frac{\pi}{2}\mu + i\frac{\pi}{4}\right). \quad (2.49)$$

It differs from the result obtained previously by Du and Delos [3]; in that in their work the amplitude factor A of (2.45) is replaced with

$$A_1 = \sqrt{\frac{2}{r_0}} \left. \frac{\partial \vartheta_i}{\partial \vartheta_f} \right|_{p_{\vartheta_i}}. \quad (2.50)$$

This discrepancy was noted and numerically investigated by Granger and Greene [26]. They attribute it to the approximation of using zero-energy wave functions, which can easily be avoided in the S -matrix theory, but is an integral part of the derivation given by Du and Delos.

For the closed orbit perpendicular to the field in the diamagnetic Kepler problem and a scaled matching radius of $\tilde{r}_0 = 0.01$, the amplitudes (2.45) and (2.50) are plotted in figure 2.1. This figure is similar to figure 1 in [26], although for the latter the matching radius is not given. The agreement is excellent at scaled energies close to zero, but becomes poor if the energy decreases. However, contrary to their conclusions, the lack of agreement is not due to the zero-energy approximation, but rather to the dependence of the amplitudes on the matching radius.

This statement can be verified most conveniently if the motion is described in semiparabolic coordinates

$$\mu = \sqrt{r+z}, \quad \nu = \sqrt{r-z}. \quad (2.51)$$

If the trajectory is recorded as a function of a parameter τ related to the time t by

$$dt = 2r d\tau, \quad (2.52)$$

and a prime denotes differentiation with respect to τ , for trajectories with vanishing azimuthal angular momentum the equations of motion in the Coulomb region read

$$\begin{aligned} \mu' &= p_\mu, & \nu' &= p_\nu, \\ p'_\mu &= 2E\mu, & p'_\nu &= 2E\nu. \end{aligned} \quad (2.53)$$

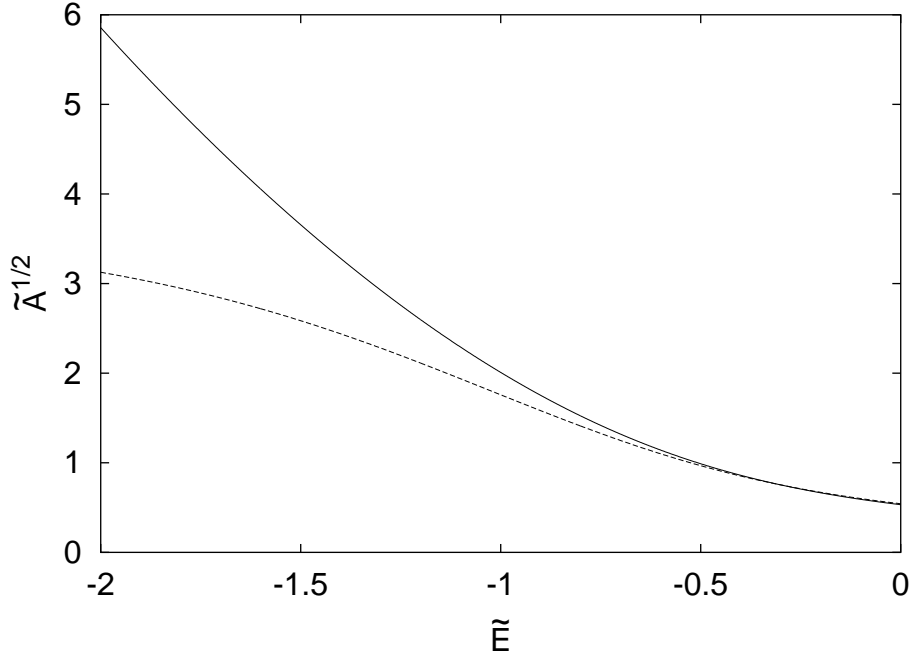


Figure 2.1: Scaled semiclassical amplitude factors after Granger and Greene (2.45, solid line) and after Du and Delos (2.50, dashed line) for the closed orbit perpendicular to the magnetic field as a function of the scaled energy. The scaled matching radius is $\tilde{r}_0 = 0.01$.

These equations are devoid of any singularities, so that they can conveniently be used to discuss the motion close to the nucleus. In fact, the transformation described here is a special case of the Kustaanheimo-Stiefel regularization discussed in chapter 4. The transformation inverse to (2.51) is given by

$$r = \frac{1}{2} (\mu^2 + \nu^2) , \quad \vartheta = \arccos \frac{\mu^2 - \nu^2}{\mu^2 + \nu^2} . \quad (2.54)$$

The momenta transform according to

$$p_r = \frac{\mu p_\mu + \nu p_\nu}{\mu^2 + \nu^2} , \quad p_\vartheta = \frac{\mu p_\nu - \nu p_\mu}{2 \operatorname{sign}(\mu\nu)} . \quad (2.55)$$

Note that the transformation from semiparabolic to Cartesian coordinates is not one-to-one, but that μ and ν are fixed up to the choice of sign only.

To evaluate (2.45) and (2.50), the derivatives $\partial p_{\vartheta_f} / \partial \vartheta_i$ and $\partial \vartheta_f / \partial \vartheta_i$, must be calculated and their dependence on the matching radius r must be determined. As the radial trajectory specified by a starting angle ϑ_i is independent of the radius where the angle is measured, the r -dependence of the derivatives is determined by the returning trajectories only. It can be evaluated as follows:

I arbitrarily fix the returning time of a closed orbit at $\tau = 0$, so that $\mu(0) = \nu(0) = 0$. The solution to (2.53) describing a trajectory returning at an angle ϑ_f

is given by

$$\begin{aligned}
\mu(\tau) &= 2 \frac{\cos(\vartheta_f/2)}{\sqrt{-2E}} \sin\left(\sqrt{-2E}\tau\right) = -\sqrt{2r} \cos\frac{\vartheta_f}{2}, \\
\nu(\tau) &= 2 \frac{\sin(\vartheta_f/2)}{\sqrt{-2E}} \sin\left(\sqrt{-2E}\tau\right) = -\sqrt{2r} \sin\frac{\vartheta_f}{2}, \\
p_\mu(\tau) &= 2 \cos\frac{\vartheta_f}{2} \cos\left(\sqrt{-2E}\tau\right) = 2\sqrt{1+Er} \cos\frac{\vartheta_f}{2}, \\
p_\nu(\tau) &= 2 \sin\frac{\vartheta_f}{2} \cos\left(\sqrt{-2E}\tau\right) = 2\sqrt{1+Er} \sin\frac{\vartheta_f}{2},
\end{aligned} \tag{2.56}$$

where the coefficients were chosen to satisfy the conservation of energy and to give the correct returning angle after a transformation to Cartesian coordinates. The second expression in each line follows from $\mu^2 + \nu^2 = 2r$, whence for $\tau < 0$

$$\sin\left(\sqrt{-2E}\tau\right) = -\sqrt{-Er}, \quad \cos\left(\sqrt{-2E}\tau\right) = \sqrt{1+Er}. \tag{2.57}$$

Equations of motion for the derivatives $\partial\mu/\partial\vartheta_i$ and $\partial\nu/\partial\vartheta_i$ are obtained by linearizing (2.53). Since (2.53) is already linear, the derivatives satisfy the same equations of motion as the coordinates themselves as long as the electron moves in the Coulomb region. There the solutions read

$$\frac{\partial\mu}{\partial\vartheta_i} = \frac{a_\mu}{\sqrt{-2E}} \sin\left(\sqrt{-2E}\tau\right) + b_\mu \cos\left(\sqrt{-2E}\tau\right) \tag{2.58}$$

and

$$\frac{\partial p_\mu}{\partial\vartheta_i} = \frac{d}{d\tau} \frac{\partial\mu}{\partial\vartheta_i} = a_\mu \cos\left(\sqrt{-2E}\tau\right) - \sqrt{-2E} b_\mu \sin\left(\sqrt{-2E}\tau\right). \tag{2.59}$$

Equation (2.57) yields

$$\begin{aligned}
\frac{\partial\mu}{\partial\vartheta_i} &= -a_\mu \sqrt{\frac{r}{2}} + b_\mu \sqrt{1+Er}, \\
\frac{\partial p_\mu}{\partial\vartheta_i} &= a_\mu \sqrt{1+Er} - \sqrt{2r} E b_\mu,
\end{aligned} \tag{2.60}$$

so that the coefficients

$$a_\mu = \frac{\partial p_{\mu_f}}{\partial\vartheta_i}, \quad b_\mu = \frac{\partial\mu_f}{\partial\vartheta_i} \tag{2.61}$$

can be identified with the values of the derivatives obtained at $r = 0$. Analogous expressions hold for $\partial\nu/\partial\vartheta_i$.

From (2.55), the amplitude (2.45)

$$\begin{aligned}
\frac{1}{A} &= \frac{\partial p_\vartheta}{\partial\vartheta_i} \\
&= \frac{1}{2 \operatorname{sign}(\mu\nu)} \left(\mu \frac{\partial p_\nu}{\partial\vartheta_i} + p_\nu \frac{\partial\mu}{\partial\vartheta_i} - \nu \frac{\partial p_\mu}{\partial\vartheta_i} - p_\mu \frac{\partial\nu}{\partial\vartheta_i} \right) \\
&= \frac{1}{2 \operatorname{sign}(\mu\nu)} \left(\frac{\partial\mu_f}{\partial\vartheta_i} p_{\nu_f} - \frac{\partial\nu_f}{\partial\vartheta_i} p_{\mu_f} \right)
\end{aligned} \tag{2.62}$$

can be evaluated. It is independent of r , as could have been anticipated from the fact that p_ϑ is a component of the total angular momentum and thus is conserved along the trajectory once the electron has entered the Coulomb region. The amplitude A^{-1} can also, up to an immaterial choice of sign, be identified with the monodromy matrix element

$$m_{12} = \frac{1}{2} \left(\frac{\partial \nu_f}{\partial \vartheta_i} p_{\mu_f} - \frac{\partial \mu_f}{\partial \vartheta_i} p_{\nu_f} \right) \quad (2.63)$$

introduced by Bogomolny [4] to describe the semiclassical amplitudes, so that the amplitudes derived by Granger and Greene from the S -matrix theory agree with Bogomolny's.

Similarly, the amplitude (2.50) used by Du and Delos reads, by (2.54),

$$\begin{aligned} \frac{1}{A_1} &= \sqrt{\frac{r}{2}} \frac{\partial \vartheta}{\partial \vartheta_i} \\ &= \frac{\text{sign}(\mu\nu)}{2} \left[p_{\mu_f} \left(\sqrt{\frac{r}{2}} \frac{\partial p_{\nu_f}}{\partial \vartheta_i} - \sqrt{1+Er} \frac{\partial \nu_f}{\partial \vartheta_i} \right) \right. \\ &\quad \left. - p_{\nu_f} \left(\sqrt{\frac{r}{2}} \frac{\partial p_{\mu_f}}{\partial \vartheta_i} - \sqrt{1+Er} \frac{\partial \mu_f}{\partial \vartheta_i} \right) \right] \\ &= \frac{1}{A} + \mathcal{O}(\sqrt{r}) . \end{aligned} \quad (2.64)$$

Thus, the amplitudes A and A_1 agree in the limit of vanishing matching radius, but the amplitude A_1 proposed by Du and Delos exhibits a strong dependence on r , whereas the amplitude A given by Granger and Greene does not. These findings can also be confirmed numerically. Figure 2.2 shows the two amplitudes for the closed orbit perpendicular to the magnetic field at a scaled energy of $\tilde{E} = -2$ as a function of the scaled matching radius \tilde{r}_0 . The dependence of A_1 on \tilde{r}_0 is considerable.

I have thus shown that, contrary to the claim by Granger and Greene, the discrepancy between their semiclassical amplitude and that obtained by Du and Delos is not due to the zero-energy approximation, but rather due to the choice of a finite matching radius. In addition, the amplitude derived by Granger and Greene is not specific to the S -matrix formulation, it agrees with the result derived earlier by Bogomolny in the context of a semiclassical wave function formalism. Nevertheless, as it eliminates the need to specify a finite matching radius and allows one to calculate all classical quantities at the nucleus, it seems more appropriate than the amplitude given by Du and Delos, which introduces a certain arbitrariness in the choice of a matching radius. I will henceforth use Bogomolny's notation and write the amplitude as

$$\mathcal{A}_{\text{c.o.}} = 2(2\pi)^{3/2} \frac{\sqrt{\sin \vartheta_i \sin \vartheta_f}}{\sqrt{|m_{12}|}} \mathcal{Y}^*(\vartheta_f) \mathcal{Y}(\vartheta_i) \exp\left(i\frac{\pi}{2}\mu + i\frac{\pi}{4}\right) . \quad (2.65)$$

A final remark is in order concerning closed orbits directed along the external field axis, i.e. $\vartheta_i = \vartheta_f = 0$ or π . Such orbits exist in both external magnetic and

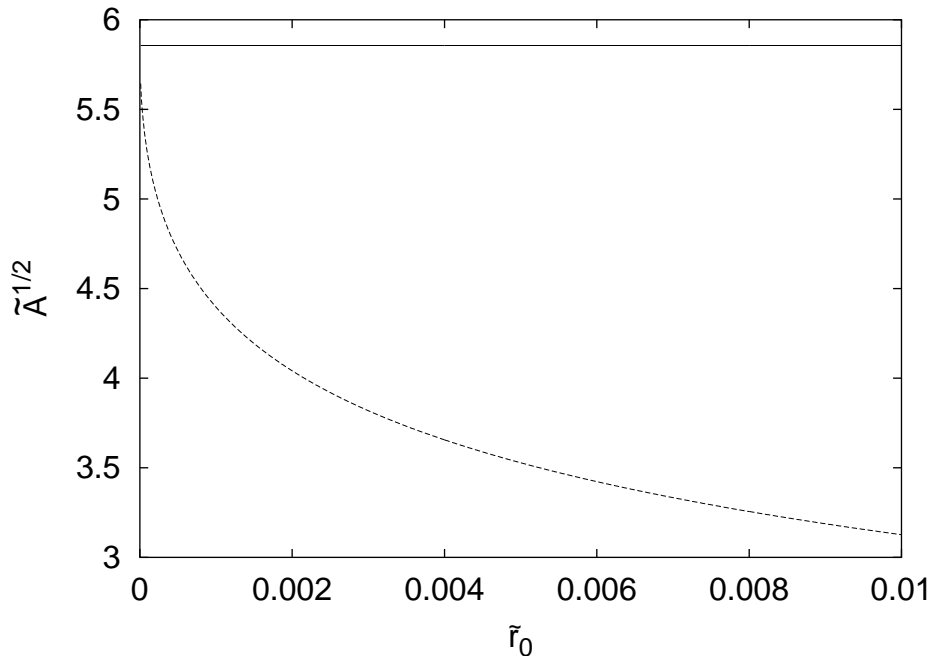


Figure 2.2: Scaled semiclassical amplitude factors after Granger and Greene (2.45, solid line) and after Du and Delos (2.50, dashed line) for the closed orbit perpendicular to the magnetic field as a function of the matching radius at $\tilde{E} = -2$.

electric fields. According to (2.65), their contribution to photo-absorption spectra is zero. However, as these orbits are invariant under rotations around the field axis, they occur as isolated orbits rather than in one-parameter families. Thus, the appropriate amplitude describing their contribution is given by the crossed-fields amplitude (2.43) rather than (2.65). As will be shown in section 4.4, for these orbits $M = m_{12}^2$. The amplitude for an axial orbit thus reads

$$\mathcal{A}_{\text{c.o.}} = 4\pi \frac{\mathcal{Y}^*(\vartheta_f, 0) \mathcal{Y}(\vartheta_i, 0)}{|m_{12}|} e^{i(\pi/2)\mu}. \quad (2.66)$$

In terms of the generic scaling parameter w of section 2.1, the monodromy matrix element scales as $m_{12} = w\tilde{m}_{12}$. Therefore, the semiclassical amplitudes scale according to $\mathcal{A}_{\text{c.o.}} = w^{-1}\tilde{\mathcal{A}}_{\text{c.o.}}$ for axial orbits and $\mathcal{A}_{\text{c.o.}} = w^{-1/2}\tilde{\mathcal{A}}_{\text{c.o.}}$ for non-axial orbits. Thus, in the semiclassical limit of large w , the contributions of the axial orbits are small compared to those of the non-axial orbits.

Chapter 3

Harmonic inversion

3.1 Harmonic inversion in semiclassical physics

The semiclassical closed-orbit theory developed in the previous chapter provides an expression for the quantum mechanical response function (2.9) in terms of classical orbits. Its general form is

$$g(E) = -\frac{1}{\pi} \sum_n \frac{m_n}{E - E_n + i\epsilon} = g_0(E) + \sum_{\text{c.o.}} \mathcal{A}_{\text{c.o.}}(E) e^{iS_{\text{c.o.}}(E)}, \quad (3.1)$$

where the coefficients $m_n = |\langle i|D|n\rangle|^2$ are the dipole matrix elements connecting the initial state to the excited states and $g_0(E)$ is the smooth part of the spectrum. Equation (3.1) offers a way, in principle, of calculating quantum mechanical eigenenergies E_n and their dipole matrix elements m_n from classical closed orbits or, vice versa, of determining the classical quantities $S_{\text{c.o.}}$ and $\mathcal{A}_{\text{c.o.}}$ from a quantum spectrum.

In recent years, methods of high-resolution spectral analysis have been shown to be a powerful tool for this conversion from the classical to the quantum regime and back [19, 27, 47, 48]. The present chapter will be concerned with describing these techniques. The first section is devoted to a discussion of the ansatz rendering the harmonic signal analysis a powerful tool for the conversion problems described above. Subsequent sections will introduce different algorithms for the harmonic inversion and compare their numerical efficiencies. Actual applications to closed-orbit theory will be presented in later chapters.

The scope of the algorithms discussed here is actually much wider than that of closed-orbit theory, because semiclassical trace formulae [2, 49] also lead to expansions of the form (3.1). Trace formulae can be applied to arbitrary quantum systems possessing a classical counterpart. In their case, m_n is the multiplicity of the energy eigenvalue E_n , and the semiclassical sum extends over all periodic (rather than closed) orbits of the pertinent classical system. The exact form of the semiclassical amplitudes \mathcal{A} depends on the details of the underlying classical dynamics. Although trace formulae for systems possessing arbitrary discrete [50] or continuous [45, 46] symmetry groups can be derived, the most well-known forms are Gutzwiller's original trace formula [51] for chaotic systems and the

Berry-Tabor trace formula [52,53] for integrable systems. For systems with mixed regular-chaotic classical phase space, both forms of the trace formula have to be combined. In these cases, periodic-orbit theory is more difficult to apply than closed-orbit theory, which yields the same semiclassical amplitudes throughout the transition from regular to chaotic dynamics.

An obstacle to the extraction of the classical actions and amplitudes from a quantum spectrum via (3.1) arises from the fact that these parameters are energy dependent and thus vary across the spectrum. This difficulty can be overcome with the help of the scaling properties discussed in section 2.1. If, e.g., scaling with respect to the magnetic field strength is used, a quantum state can be characterized by the scaled energy \tilde{E} , the scaled electric field strength \tilde{F} and the scaling parameter $w = B^{-1/3}$ instead of the energy E and the field strengths B and F . If the spectrum of scaling parameters w_n corresponding to states with fixed \tilde{E} and \tilde{F} is recorded, (3.1) can be rewritten as

$$g(w) = -\frac{1}{\pi} \sum_n \frac{m_n}{w - w_n + i\epsilon} = g_0(w) + w^\gamma \sum_{\text{c.o.}} \tilde{\mathcal{A}}_{\text{c.o.}} e^{iw\tilde{S}_{\text{c.o.}}} . \quad (3.2)$$

The exponent γ is determined by the scaling properties of the semiclassical amplitudes.¹ In this form of the semiclassical expansion, the scaled classical parameters $\tilde{S}_{\text{c.o.}}$ and $\tilde{\mathcal{A}}_{\text{c.o.}}$ are constant throughout the spectrum. This technique, which is known as scaled-energy spectroscopy, has become customary in both experimental and theoretical studies [54,55].

A quantum calculation yields the bound state spectrum

$$\rho(w) = \sum_n m_n \delta(w - w_n) = \text{Im } g(w) . \quad (3.3)$$

By (3.2),

$$w^{-\gamma} \rho(w) = w^{-\gamma} \text{Im } g_0(w) - \frac{i}{2} \sum_{\text{c.o.}} \left\{ \tilde{\mathcal{A}}_{\text{c.o.}} e^{iw\tilde{S}_{\text{c.o.}}} - \tilde{\mathcal{A}}_{\text{c.o.}}^* e^{iw\tilde{S}_{\text{c.o.}}^*} \right\} \quad (3.4)$$

is obtained as a sum of sinusoidal oscillations with frequencies equal to the scaled actions of classical closed orbits and amplitudes equal to their semiclassical recurrence amplitudes. The most obvious method of extracting the classical information from the quantum spectrum is, therefore, to take a Fourier transform of the spectrum. It will exhibit a series of peaks associated with the closed orbits. The smooth part $g_0(w)$ of the semiclassical spectrum will contribute to the Fourier transform at very low frequencies only. In general it will not interfere with the closed orbit recurrence peaks.

In practice, the quantum spectrum is known in a finite range $0 \leq w \leq w_{\text{max}}$ only. Therefore, the Fourier transform yields peaks having a finite width $2\pi/w_{\text{max}}$

¹In the case of rotationally-symmetric systems, the scaling properties of the amplitudes of axial and non-axial closed orbits differ. However, as discussed at the end of section 2.4, in the semiclassical limit the amplitudes of the axial orbits are small enough to be neglected.

instead of the ideal δ function peaks. The analysis of the signal by means of a Fourier transform is thus limited by the “uncertainty principle,” which states that in a signal of finite length w_{\max} , two frequencies can only be resolved if their difference is larger than $2\pi/w_{\max}$. This limitation can be overcome by noting that one is not actually interested in the smooth spectrum the Fourier transform produces, but rather in a set of discrete actions $\tilde{S}_{c.o.}$ and the corresponding amplitudes $\mathcal{A}_{c.o.}$. In abstract terms, the problem is to extract the frequencies ω_k and the amplitudes d_k from a given signal $C(t)$ of the form

$$C(t) = \sum_k d_k e^{-i\omega_k t} . \quad (3.5)$$

In the present case, the signal

$$C(w) = w^{-\gamma} \rho(w) = \sum_n w_n^{-\gamma} m_n \delta(w - w_n) \quad (3.6)$$

is given as a sum of δ functions.

The application of a high-resolution method of spectral analysis instead of a conventional Fourier transform circumvents the uncertainty principle. However, an uncertainty remains in the weaker form of the “informational uncertainty principle” [56], which states that the signal length T_{\max} required to resolve the frequencies is given by

$$T_{\max} \gtrsim 4\pi \bar{\rho}(\omega) \quad (3.7)$$

in terms of the local average density of frequencies $\bar{\rho}(\omega)$. Since this relation involves the average instead of the minimum spacing between frequencies, the signals can usually be significantly shorter than required by the Fourier transform.

The inverse problem, i.e. the extraction of the quantum mechanical eigenenergies E_n and their matrix elements m_n from the classical closed orbits, appears straightforward at first sight: summation of the closed orbit sum in (3.1) immediately gives a semiclassical approximation to the quantum response function. In practice, however, apart from the obvious difficulty that only finitely many closed orbits can be calculated, the closed orbit sum turns out to diverge due to the large number of classical closed orbits. This is in fact to be expected since the quantum response function has poles at the eigenenergies, whereas the closed orbit sum, if it converged, would give a smooth function of the energy. One must therefore search for a method to overcome the fundamental convergence problems of the semiclassical closed orbit sum and extract the eigenenergies from a finite set of closed orbits. This turns out to be even more challenging a problem than the semiclassical analysis of quantum spectra.

An obvious method of dealing with the convergence problems is to simply cut off the closed orbit sum at a finite maximum orbital period T_{\max} . This corresponds to averaging the response function over an energy range $\Delta E \approx \hbar/T_{\max}$. Therefore, it produces spectral peaks of finite width instead of δ peaks. In this sense, it is analogous to the spectral analysis by means of the Fourier transform, which also gives a smooth recurrence spectrum instead of identifying individual orbits. High-resolution methods are clearly desirable.

In the context of semiclassical trace formulae, several techniques have been proposed for the calculation of individual energy levels. Although many of them have proven very efficient for specific classes of systems, most of them suffer from the disadvantage of non-universality. The cycle expansion technique [13, 14], for example, requires a completely hyperbolic dynamics and the existence of a symbolic code. By contrast, the Riemann-Siegel look-alike formula and pseudo-orbit expansion of Berry and Keating [15, 16] can only be applied to bound systems.

As a general method of semiclassical quantization, Main *et al.* [19, 47] introduced high-resolution harmonic inversion. This method only assumes the general form (3.1) of the semiclassical expansion. So far, it has only been applied to systems possessing a scaling property. I will stick to this restriction for the moment. In section 3.4, an extension to non-scaling systems will be presented.

In the case of a scaling system, I start from equation (3.2). Multiplying (3.2) by $w^{-\gamma}$, taking the Fourier transform and neglecting the smooth part of the spectrum, I obtain

$$\frac{i}{\pi} \sum_n w_n^{-\gamma} m_n e^{-i w_n s} = C(s) \quad (3.8)$$

with

$$C(s) = \frac{1}{2\pi} \int_{-\infty}^{+\infty} dw \sum_{\text{c.o.}} \tilde{\mathcal{A}}_{\text{c.o.}} e^{i w \tilde{S}_{\text{c.o.}}} e^{-i w s} = \sum_{\text{c.o.}} \tilde{\mathcal{A}}_{\text{c.o.}} \delta(s - \tilde{S}_{\text{c.o.}}) . \quad (3.9)$$

The problem of semiclassical quantization has thus been recast as a harmonic inversion problem (3.5), where the signal is again given as a sum of δ functions. The method thus inherits the advantages of the high-resolution methods found valuable in the context of spectral analysis.

For a semiclassical quantization orbits up to a certain maximum length are required. Usually, the maximum length is measured in units of the Heisenberg time

$$T_{\text{H}} = \frac{2\pi\hbar}{\Delta E} \quad (3.10)$$

with the mean level spacing ΔE . In connection with semiclassical trace formulae, quantization schemes that require orbits up to a maximum period of the order of the Heisenberg time have been devised [18, 20]. In completely chaotic bound systems, a functional equation can be used to reduce the maximum period to half the Heisenberg time [16].

In scaling systems, the analogue of the Heisenberg time the Heisenberg action

$$\tilde{S}_{\text{H}} = 2\pi/\Delta w . \quad (3.11)$$

Due to the informational uncertainty principle (3.7), the harmonic inversion method requires orbits with scaled actions up to

$$S_{\text{max}} \gtrsim 4\pi\bar{\rho}(w) = \frac{4\pi}{\Delta w} = 2\tilde{S}_{\text{H}} , \quad (3.12)$$

which is twice as long as required by other methods. Taking into account the exponential proliferation of periodic orbits in typical chaotic systems, this requirement is severe. On the other hand, the harmonic inversion does not only extract the eigenvalues w_n , but also the matrix elements m_n . It thus yields the double amount of information, so that it should not come as a surprise that twice as much input data is needed. In the context of closed-orbit theory, the m_n contain useful information other methods cannot extract from a semiclassical spectrum. If semiclassical trace formulae are used, m_n is the multiplicity of the level w_n , so that it must be equal to 1 in non-degenerate systems² and does not convey any useful information. A method of implementing this *a priori* knowledge into the quantization procedure has recently been devised by J. Main [57]. In this case, the required signal length can be reduced to the Heisenberg time. For a bound system, all eigenvalues must be real. This knowledge leads to an analogue of the functional equation which reduces the signal length further to half the Heisenberg time.

3.2 Harmonic inversion of δ function signals

As described in the previous section, a reliable method of extracting the frequencies ω_k and amplitudes d_k from a given time signal of the form (3.5)

$$C(t) = \sum_k d_k e^{-i\omega_k t} ,$$

especially in the case where $C(t)$ is given as a sum of δ functions, provides the key to both semiclassical quantization and the semiclassical analysis of quantum spectra. In contrast to the Fast Fourier Transform, which represents a signal in the form (3.5) with fixed, evenly spaced frequencies ω_k and is therefore a stable linear operation, the general harmonic inversion problem with unknown ω_k is highly non-linear. Therefore, although a variety of algorithms for the harmonic inversion have been known for a long time [58, 59], they are all numerically unstable if the number of frequencies contained in the signal is large. None of them is thus fit for an application to semiclassics.

This situation was first remedied when Wall and Neuhauser [60] developed filter diagonalization (FD) as a method of extracting the frequencies contained in a given interval rather than the complete list of frequencies contained in the signal. Due to this local ansatz, FD is limited by the local average density rather than the total number of frequencies. This limitation is expressed by the informational uncertainty principle (3.7).

The spectral resolution of FD as well as of any other spectral analyser improves with increasing signal length, which is often fixed or at least hard to increase, e.g., for periodic-orbit quantization of classically chaotic systems where the number of periodic orbits proliferates exponentially with the signal length. To obtain the

²In degenerate systems, the multiplicity of an energy level is a small integer. If it is artificially set equal to 1 for all levels, degenerate levels appear several times in the list of frequencies.

optimum results from the harmonic inversion procedure, it is essential to choose an algorithm that allows one to extract the most precise estimates for the spectral parameters $\{\omega_k, d_k\}$ from a signal of a given length.

Since the advent of FD, various computational procedures have been proposed for the harmonic inversion of time signals, some of which are specially adapted to δ function signals. However, a systematic study of the relative merits and demerits of the different methods and a quantitative study of their efficiencies is still lacking. To remedy this situation, I summarize and discuss different techniques of harmonic inversion and compare their accuracies in the application to two simple albeit typical example systems for which exact trace formulae are known. The aim is to pin down the numerically most efficient method for harmonic inversion.

The present section introduces four different methods for the harmonic inversion of δ function signals, section 3.3 contains numerical results comparing their efficiencies.

3.2.1 Method 1: discrete filter diagonalization

The crucial idea of the filter diagonalization method by Wall and Neuhauser [60] is to associate the signal $C(t)$ with the auto-correlation function of a suitable dynamical system,

$$C(t) = \left(\Phi_0 \left| e^{-it\hat{\Omega}} \right| \Phi_0 \right), \quad (3.13)$$

where $(\cdot|\cdot)$ is a complex symmetric inner product on an abstract vector space, Φ_0 is an arbitrary vector and $\hat{\Omega}$ a complex symmetric Hamiltonian operator. If ω_k are the eigenvalues of $\hat{\Omega}$ with eigenvectors Υ_k , assumed orthonormal, and $d_k = (\Phi_0|\Upsilon_k)^2$, the auto-correlation function $C(t)$ is of the form (3.5). As the scalar product was chosen complex symmetric rather than Hermitian, ω_k and d_k can be arbitrary complex numbers. The harmonic inversion of the time signal is the equivalent to the diagonalization of $\hat{\Omega}$. It was shown by Wall and Neuhauser that a diagonalization procedure relying solely on the knowledge of the time signal $C(t)$ can be devised.

Mandelstam and Taylor [56] developed a variant of the original FD method adapted to signals given on a discrete equidistant time grid $c_n = C(n\tau)$ with a constant step width τ . They introduced the one-step time-evolution operator

$$\hat{U} = e^{-i\hat{\Omega}\tau} = \sum_k u_k |\Upsilon_k\rangle \langle \Upsilon_k| \quad (3.14)$$

with $u_k = e^{-i\omega_k\tau}$. In an arbitrary non-orthonormal basis set Ψ_j , the eigenvalue problem for \hat{U} can be written as

$$\underline{U} \underline{B}_k = u_k \underline{S} \underline{B}_k \quad (3.15)$$

with the matrices

$$U_{jj'} = \left(\Psi_j \left| \hat{U} \right| \Psi_{j'} \right), \quad S_{jj'} = (\Psi_j | \Psi_{j'}) \quad (3.16)$$

and

$$\Upsilon_k = \sum_j B_{jk} \Psi_j . \quad (3.17)$$

The most obvious choice for the Ψ_j is the Krylov basis,

$$\Phi_n = \hat{U}^n \Phi_0 , \quad n = 0, 1, \dots, M , \quad (3.18)$$

which gives

$$U_{nn'} = c_{n+n'+1} , \quad S_{nn'} = c_{n+n'} . \quad (3.19)$$

These matrix elements can be evaluated if $2M$ is less than the number of signal points. The harmonic inversion problem has thus been reduced to a generalized eigenvalue problem that can be solved by standard methods. However, the number of basis vectors must be chosen as large as the total number of frequencies contained in the signal, which results in huge and generally ill-conditioned eigenvalue problems if the number of frequencies is large.

To extract frequencies in a given window $[\omega_{\min}, \omega_{\max}]$, Mandelshtam and Taylor [56], changing the original Gaussian filter by Wall and Neuhauser into a rectangular filter, proposed to introduce a set of trial values $\omega_{\min}\tau \leq \varphi_j \leq \omega_{\max}\tau$, $j = 1, 2, \dots, J$, and $z_j = e^{-i\varphi_j}$ and define a Fourier-type basis

$$\Psi_j = \Psi(z_j) = \sum_{n=0}^M e^{in\varphi_j} \Phi_n = \sum_{n=0}^M (\hat{U}/z_j)^n \Phi_0 . \quad (3.20)$$

The basis vector Ψ_j is dominated by eigenvectors corresponding to eigenvalues close to φ_j , so that in the Fourier basis the matrices \underline{U} and \underline{S} have significant elements close to the diagonal only. Frequencies not too close to the edges of the window can thus accurately be calculated from the eigenvalue problem (3.15) even if an incomplete basis set is used. Only the local completeness condition that the density of φ_j/τ be larger than the local density of frequencies must be met. Therefore, the number of basis vectors can usually be chosen considerably smaller than the total number of frequencies.

The matrix elements

$$U^{(p)}(z, z') = (\Psi(z) | \hat{U}^p | \Psi(z')) \quad (3.21)$$

in the Fourier basis are given by

$$U^{(p)}(z, z') = \frac{1}{z - z'} \left(z \sum_{l=0}^M c_{l+p} z'^{-l} - z' \sum_{l=0}^M c_{l+p} z^{-l} \right. \\ \left. - z^{-M} \sum_{l=M+1}^{2M} c_{l+p} z'^{M-l+1} \right. \\ \left. + z'^{-M} \sum_{l=M+1}^{2M} c_{l+p} z^{M-l+1} \right) \quad \text{if } z \neq z' , \quad (3.22)$$

$$U^{(p)}(z, z) = \sum_{l=0}^{2M} (M - |M - l| + 1) c_{l+p} z^{-l} ,$$

and the eigenvalue problem (3.15) reads

$$\underline{U}^{(1)} \underline{B}_k = u_k \underline{U}^{(0)} \underline{B}_k . \quad (3.23)$$

After the diagonalization, the amplitudes can be calculated from the eigenvectors by

$$d_k = \left(\frac{1}{M+1} \sum_{j=1}^J B_{jk} U^{(0)}(z_j, u_k) \right)^2 . \quad (3.24)$$

To obtain well-converged frequencies, the number of basis vectors must generally be chosen 10-30% larger than implied by the local completeness condition, so that the diagonalization yields too many frequencies. To distinguish between true and spurious frequencies, the eigenvalue equation (3.15) can be generalized to

$$\underline{U}^{(p)} \underline{B}_k = u_k \underline{U}^{(p-1)} \underline{B}_k \quad (3.25)$$

and solved for different values of p . If an incomplete basis set is used, spurious eigenvalues will depend on p whereas true eigenvalues will not. The method by Mandelshtam and Taylor thus has a built-in error estimator.

As it stands, the method is not well adapted to the analysis of δ function signals because they cannot be evaluated on an equidistant grid unless the δ functions are given an artificial width σ which spans several grid points, e.g., by convoluting the signal with a narrow Gaussian function. In this form the FD method was applied in [19, 48] as a tool for semiclassical periodic-orbit quantization.

The convolution of the signal $C(t)$ results in a damping of the amplitudes $d_k \rightarrow d_k^{(\sigma)} = d_k \exp(-w_k^2 \sigma^2 / 2)$. The width σ of the Gaussian function should be chosen sufficiently small to avoid an overly strong damping, e.g., by setting $\sigma \lesssim |w_{\max}|^{-1}$ where w_{\max} is the largest frequency of interest. To properly sample each Gaussian a dense grid with sufficiently small step size ($\tau \approx \sigma/3$) is required. Therefore, the convoluted signal to be processed by FD usually consists of a large number of data points, in particular when high frequency regions of the signal are to be analysed. The numerical treatment of such large data sets may suffer from rounding errors and loss of accuracy.

3.2.2 Method 2: δ function filter diagonalization

An approach to the harmonic inversion of δ function signals circumventing the artificial smoothing of the signal was suggested by Grémaud and Delande [61]. They revert to a continuous-time formulation of the FD algorithm close to the original ansatz in [60], but keep the rectangular filter introduced by Mandelshtam and Taylor [56].

In the continuous-time formulation, the time evolution generated by the Hamiltonian $\hat{\Omega}$ is given by a one-parameter family of time evolution operators

$$\hat{U}(t) = e^{-i\hat{\Omega}t} . \quad (3.26)$$

The Fourier basis used by Grémaud and Delande for a signal of total length T reads

$$\Psi(\varphi_j) = \int_0^{T/2} dt e^{i\varphi_j t} U(t) \Phi_0. \quad (3.27)$$

Notice the close analogy with (3.20). The trial frequencies φ_j are now to be chosen in the frequency interval $\omega_{\min} \leq \varphi_j \leq \omega_{\max}$ of interest.

The harmonic inversion problem is recast as a generalized eigenvalue problem for $-i\hat{\Omega}$, viz.

$$\underline{\Omega} \underline{B}_k = -i\omega_k \underline{S} \underline{B}_k \quad (3.28)$$

with

$$\Omega(\varphi_j, \varphi_{j'}) = \left(\Psi(\varphi_j) \left| -i\hat{\Omega} \right| \Psi(\varphi_{j'}) \right), \quad S(\varphi_j, \varphi_{j'}) = (\Psi(\varphi_j) | \Psi(\varphi_{j'})) . \quad (3.29)$$

In terms of the given signal, the matrix elements read

$$\begin{aligned} \Omega(\varphi, \varphi') = \frac{1}{\varphi - \varphi'} \left(\varphi' \int_0^{T/2} dt C(t) e^{i\varphi' t} - \varphi \int_0^{T/2} dt C(t) e^{i\varphi t} \right. \\ \left. - \varphi' e^{i(\varphi - \varphi')T/2} \int_{T/2}^T dt C(t) e^{i\varphi' t} \right. \\ \left. + \varphi e^{i(\varphi' - \varphi)T/2} \int_{T/2}^T dt C(t) e^{i\varphi t} \right) \quad \text{if } \varphi \neq \varphi', \quad (3.30) \end{aligned}$$

$$\begin{aligned} \Omega(\varphi, \varphi) = \int_0^T dt C(t) \text{sign} \left(t - \frac{T}{2} \right) e^{i\varphi t} \\ + i\varphi \int_0^T dt C(t) t \text{sign} \left(t - \frac{T}{2} \right) e^{i\varphi t} - i\varphi T \int_{T/2}^T dt C(t) e^{i\varphi t} \end{aligned}$$

and

$$\begin{aligned} S(\varphi, \varphi') = \frac{i}{\varphi - \varphi'} \left(\int_0^{T/2} dt C(t) e^{i\varphi' t} - \int_0^{T/2} dt C(t) e^{i\varphi t} \right. \\ \left. - e^{i(\varphi - \varphi')T/2} \int_{T/2}^T dt C(t) e^{i\varphi' t} \right. \\ \left. + e^{i(\varphi' - \varphi)T/2} \int_{T/2}^T dt C(t) e^{i\varphi t} \right) \quad \text{if } \varphi \neq \varphi', \quad (3.31) \end{aligned}$$

$$S(\varphi, \varphi) = \int_0^T dt C(t) \left(\frac{T}{2} - \left| \frac{T}{2} - t \right| \right) e^{i\varphi t} .$$

Once the eigenvalue problem (3.28) is solved, the amplitudes are obtained from

$$d_k = \left(\frac{2}{T} \sum_{j=1}^J B_{jk} S(\varphi_j, \omega_k) \right)^2 . \quad (3.32)$$

The matrix elements (3.30) were derived under the assumption that $C(0) = C(T/2) = C(T) = 0$. This condition renders them useless for general signals, but it is satisfied for δ function signals. In this case, the integrals occurring in the matrix elements reduce to simple sums. They can therefore easily be evaluated without any prior smoothing of the signal.

3.2.3 Method 3: discrete decimated signal diagonalization

An alternative method to FD for high-resolution signal processing is decimated signal diagonalization (DSD), which was introduced by Belkić *et al.* [62] in a formulation suitable for signals given on an equidistant time grid. DSD is a two-step process for harmonic inversion. In the first step a low-resolution frequency filter is applied to the signal. The resulting band-limited signal contains only a small number of frequencies and is given on a small number of grid points. It can, therefore, be processed, in the second step, by conventional high-resolution methods without incurring numerical instabilities. For the processing stage, Belkić *et al.* [62] discuss linear prediction, Padé approximants or the FD method using the primitive Krylov basis, which does no filtering of the signal.

The filtering required in the first step is achieved by first subjecting the signal to a conventional discrete Fourier transform. The resulting spectrum has low resolution, but still contains all the information contained in the signal. All spectral information outside the frequency window of interest is then discarded, i.e. the Fourier transform is set to zero there. The window is shifted such as to be centred at zero frequency, and an inverse discrete Fourier transform is applied to obtain the band-limited signal. The number of band-limited signal points is equal to the number of spectral data points in the frequency window and usually much smaller than the original number of data points, so that the step width of the time grid is increased. However, as the maximum frequency contained in the band-limited signal is smaller than half the window width, in the course of this reduction all spectral information in the window of interest is kept.

The DSD method of reference [62] is easy to implement as it basically resorts to standard algorithms for discrete Fourier transform and matrix diagonalization. However, the application of the low-resolution Fourier filter in the first step of the method implicitly assumes periodicity of the signal with period equal to the signal length. In this case, the DSD filter is exact. In general, of course, this condition is not met, so that only approximate filtering can be achieved. Therefore, DSD must be expected to be less accurate than FD (method 1) for frequencies close to the borders of the window, or when very short frequency windows are chosen.

Because it is designed for signals given on an equidistant grid, the DSD technique, in the same way as method 1, can only be applied to δ function signals after an artificial smoothing of the signal.

3.2.4 Method 4: δ function decimated signal diagonalization

The DSD technique of method 3 can be modified for a more direct application to a δ function signal without the necessity of smoothing the signal. Because the signal $C(t)$ is given as a sum of δ functions, the ‘filtering’ step can be performed analytically if the discrete Fourier transform is replaced with the continuous form of the Fourier transform. This technique was proposed by Main *et al.* [63]. The application of the analytical filter for a rectangular frequency window $[\omega_0 - \Delta\omega, \omega_0 + \Delta\omega]$

results in replacing the signal

$$C(t) = \sum_j \mathcal{A}_j \delta(t - t_j) \quad (3.33)$$

with a band-limited (bl) signal [63]

$$C_{\text{bl}}(t) = \sum_j \mathcal{A}_j \frac{\sin [(t - t_j)\Delta\omega]}{\pi(t - t_j)} e^{i\omega_0 t_j}, \quad (3.34)$$

where the δ functions are basically replaced with sinc functions [$\text{sinc } x = (\sin x)/x$]. The band-limited signal (3.34) contains the same shift of the frequency window as applied in method 3, so that it can be discretized with a small number of points and further processed, in the second step, by conventional harmonic inversion methods as described above.

In practice, the band-limited signal can only be evaluated approximately because the signal is only known up to a finite length. Since the sinc functions decay slowly at infinity, peaks well beyond the end of the known signal may have an influence on the band-limited signal points. Omitting contributions from the unknown peaks beyond the limit of the given signal amounts to the assumption that the signal is zero outside the given range. Thus, the low-resolution filter of method 4 is different from the filter of method 3 where the signal is implicitly assumed to be periodic.

In summary, the four methods can be classified according to whether they are discrete-time algorithms (methods 1 and 3), which require a regularization of δ function signals, or continuous-time algorithms adapted to δ function signals (methods 2 and 4). Alternatively, they can be classified into filter diagonalization (FD) methods (methods 1 and 2) and decimated signal diagonalization (DSD) methods (methods 3 and 4) where the low-resolution ‘filtering’ and high-resolution signal processing is performed in two separate steps.

3.3 Numerical examples and discussion

To quantitatively assess the relative performances of the different algorithms, I present a comparison of the numerical accuracy achieved by all of these methods for two simple but archetypal examples, viz. firstly, the high-resolution analysis of the spectrum of the harmonic oscillator and, secondly, the search for the zeros of Riemann’s zeta function as a mathematical model for periodic-orbit quantization in chaotic systems. These systems possess exact trace formulae, so that the harmonic ansatz (3.5) for the semiclassical signal is known to be exact.

3.3.1 Harmonic oscillator

The one-dimensional harmonic oscillator (with $\hbar\omega = 1$) has energy eigenvalues $E_n = n + \frac{1}{2}$, $n = 0, 1, 2, \dots$. Its density of states can be written as an exact trace

formula [49]:

$$\rho(E) = \text{Im } g(E) = \sum_{n=0}^{\infty} \delta(E - E_n) = \sum_{k=-\infty}^{\infty} (-1)^k e^{2\pi i k E}. \quad (3.35)$$

The right-hand side of (3.35) can be interpreted as a periodic-orbit sum in analogy with (3.1), where $S_k = 2\pi k E$ is the action of the (k times traversed) periodic orbit and $d_k = (-1)^k$ is the periodic orbit amplitude. (The interpretation of the $k = 0$ Thomas-Fermi term is special, see [49] for more details.) The high-resolution analysis of the quantum spectrum $\rho(E) = \sum_{n=0}^{\infty} \delta(E - E_n)$ should yield equally spaced real frequencies $\omega_k = 2\pi k$ and amplitudes $d_k = (-1)^k$ of equal magnitude. Thus, this simple application of harmonic inversion to the extraction of classical periodic orbit parameters from a quantum spectrum [47, 48, 61] is ideally suited to compare the efficiencies of the different methods for the harmonic inversion of δ function signals.

Since the signal is periodic with period $\Delta E = 1$, an integer signal length would render the low-resolution Fourier filter of method 3 exact. To avoid this atypical situation I choose a rational multiple of π as signal length. According to the informational uncertainty principle (3.7) a signal length of $E_{\text{max}} \gtrsim 2$ should suffice to resolve the frequencies. Typically, (3.7) slightly underestimates the required signal length. I therefore present results calculated with a signal of length $E_{\text{max}} = \pi$, which means that only three energy levels contribute to the signal. To assess the accuracy of the results, I use the absolute values of the imaginary parts of the calculated frequencies and amplitudes as error indicators. If the analysis of the signal were exact, all imaginary parts should vanish. Therefore, by an inspection of the sizes of the imaginary parts the accuracy of the calculation can be checked. This sort of accuracy test can be applied to all bound systems. If the exact frequencies are known, as is the case in our example systems, the real parts can also be compared. The errors of the real and imaginary parts typically are of the same order of magnitude and exhibit, at least qualitatively, the same behaviour.

Results for the harmonic inversion of the quantum spectrum $\rho(E)$ obtained with the four methods introduced in section 3.2 are presented in figures 3.1 and 3.2 for the imaginary parts of the frequencies ω_k and amplitudes d_k , respectively. For frequencies which appear to be missing, imaginary parts of zero have been obtained by the pertinent method. From figure 3.1 parts (a) to (f), the width $\Delta\omega$ of the frequency filter is increased. For the application of methods 1 and 3 the signal has been discretized with step width $\tau = 0.002$ after convolution of the signal with a Gaussian function with width $\sigma = 0.006$. In all cases it can be seen that the precision achieved decreases to the boundaries of the frequency window. The reason is that none of the filtering methods is exact and can neither completely remove the influence of frequencies outside the window under consideration nor exactly preserve the contributions of frequencies inside the window. For narrow windows, the FD methods 1 and 2 outperform the DSD algorithms 3 and 4, for wide windows the situation is reversed. The frequencies obtained by methods 1

and 2 are equally precise for small windows, whereas for wide windows method 2 gains superiority and even competes with the DSD methods. In general, the distance from the window boundaries where a method acquires its full precision is smaller for the FD than for the DSD methods. Calculations were carried out with double precision. For the widest window shown, frequencies have practically been obtained to machine precision.

For all methods, the precision of the amplitudes in figure 3.2 is somewhat lower than that of the frequencies in figure 3.1 because the amplitudes are calculated from the eigenvectors of a generalized eigenvalue problem, which in general are obtained less accurately than the eigenvalues. In particular, the difference in precision between the frequencies and amplitudes is considerably larger for method 1 than for any other method, so that even for small windows the amplitudes obtained by this technique are the least accurate (see the \times symbols in figure 3.2).

3.3.2 Zeros of Riemann's zeta function

It is a peculiar feature of the harmonic oscillator signal that the density of frequencies is constant, i.e. the precision of frequencies obtained from a signal of a given length is the same throughout the whole frequency domain. However, in typical systems the density of states grows rapidly with the frequency, which means that a longer signal is required to extract higher frequencies. As an example of a system exhibiting this typical behaviour, I discuss the Riemann zeta function, which has served as a mathematical model for the periodic-orbit quantization of chaotic systems [19, 64]. If the zeros of $\zeta(z)$ on the critical line $\text{Re } z = \frac{1}{2}$ are written as $z = \frac{1}{2} - iw$, the density of zeros on the critical line can be expressed as [64]

$$\rho^{\text{osc}}(w) = \text{Im } g^{\text{osc}}(w) = -\frac{1}{\pi} \sum_p \sum_{m=1}^{\infty} \frac{\ln p}{p^{m/2}} \cos(wm \ln p), \quad (3.36)$$

where p runs over all prime numbers. Equation (3.36) is formally identical to a semiclassical trace formula with $S_{pm} = wm \ln p$ corresponding to the classical actions and $\mathcal{A}_{pm} = -(i \ln p)/(\pi p^{m/2})$ corresponding to the amplitudes. With this interpretation, the Riemann zeta function can be used as a mathematical model for chaotic dynamical systems, and the Riemann zeros are obtained by harmonic inversion of the δ function signal [19]

$$C(s) = -\frac{i}{\pi} \sum_p \sum_{m=1}^{\infty} \frac{\ln p}{p^{m/2}} \delta(s - m \ln p). \quad (3.37)$$

Unlike typical semiclassical trace formulae, equation (3.36) is exact. As the zeta function has only simple zeros, the amplitudes d_k obtained from the harmonic inversion of the signal (3.37) must all be equal to 1.

In figure 3.3 I present numerical results obtained by the application of methods 1 to 4 to extract the (numerically complex valued) Riemann zeros with $\text{Re } w_k <$

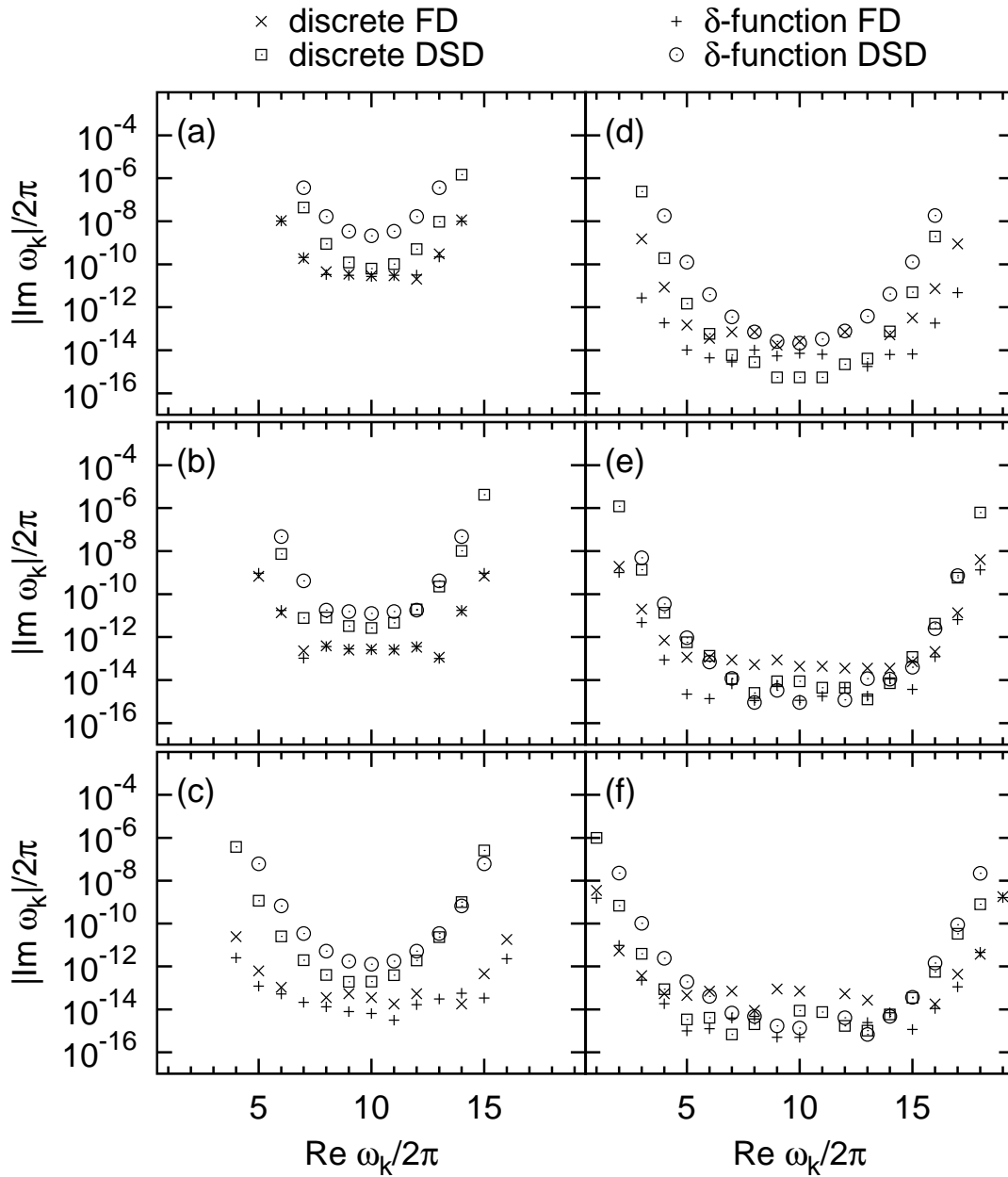
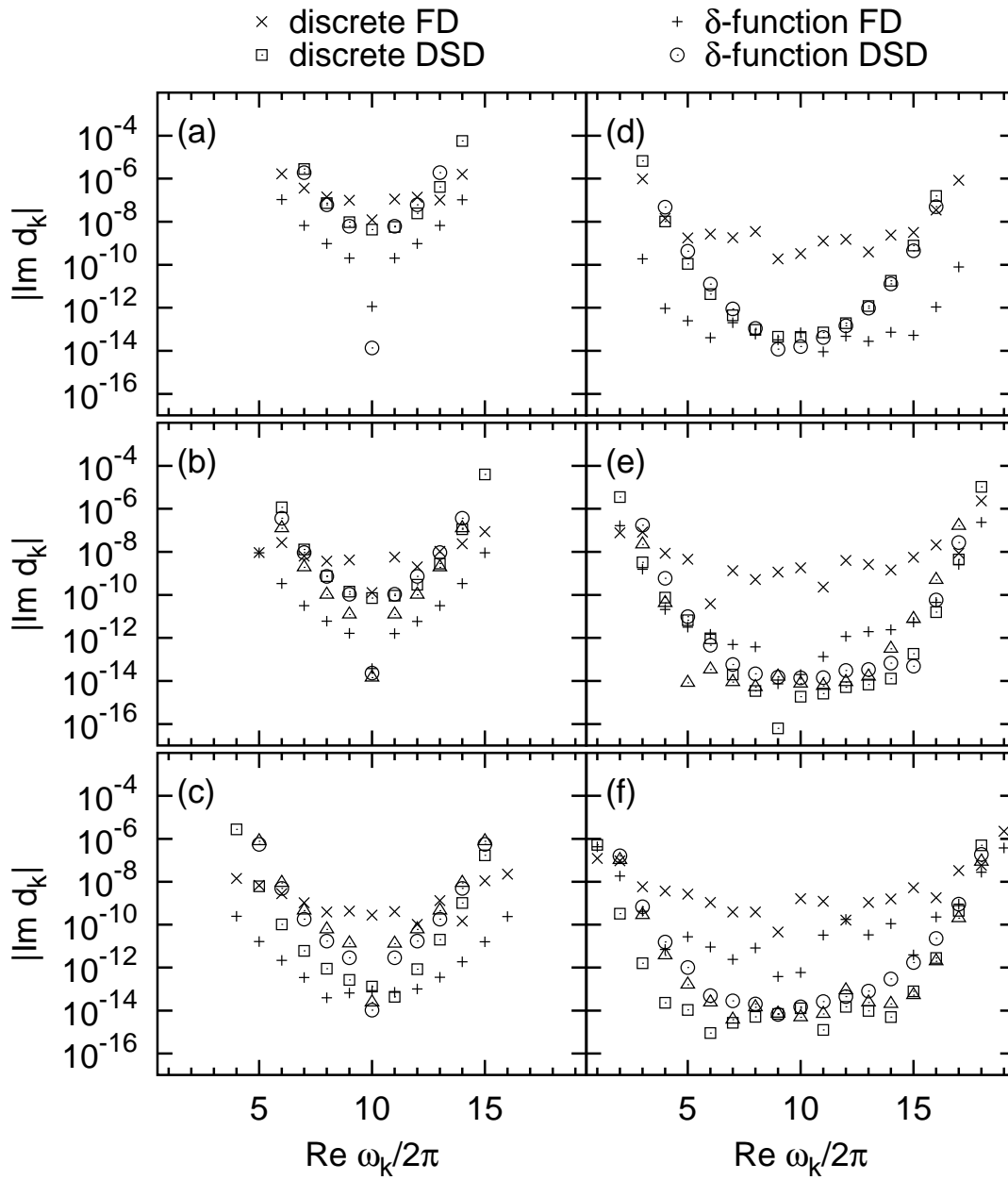


Figure 3.1: Imaginary parts (absolute values) of the frequencies ω_k extracted from a harmonic oscillator signal of length $E_{\max} = \pi$. Symbols \times , $+$, \square , and \odot denote methods 1 to 4, respectively. Windows are $[10 - \Delta\omega, 10 + \Delta\omega]$ with $\Delta\omega =$ (a) 4.5, (b) 5.5, (c) 6.5, (d) 7.5, (e) 8.5, (f) 9.5.

Figure 3.2: Same as figure 3.1, but for the imaginary parts of the amplitudes d_k .

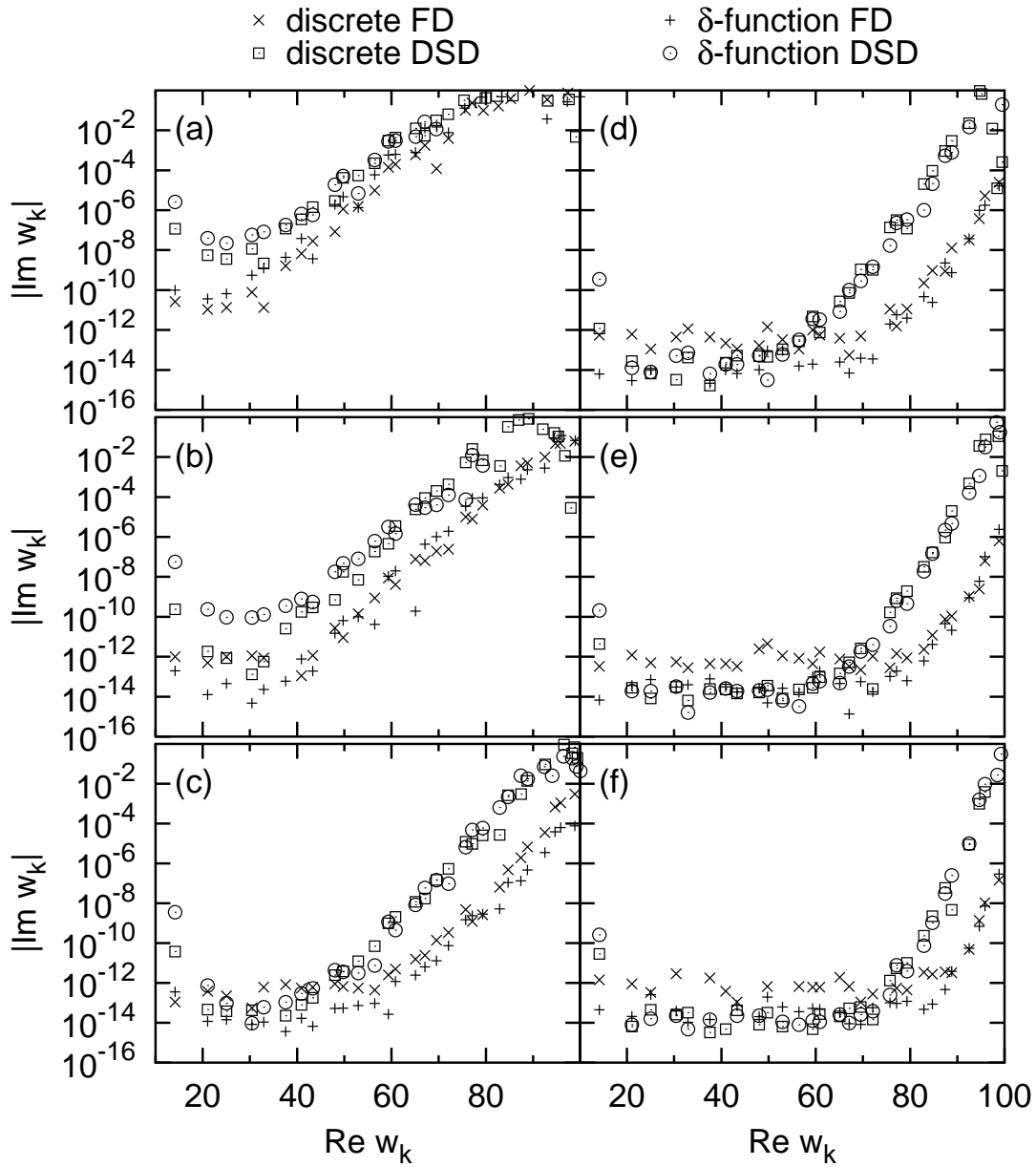


Figure 3.3: Imaginary parts (absolute values) of locations w_k of zeros of the Riemann zeta function in the frequency window $[10, 100]$. Symbols \times , $+$, \square , and \odot denote to Methods 1 to 4, respectively. Signal lengths are $S_{\max} =$ (a) 4.5, (b) 5.0, (c) 5.5, (d) 6.0, (e) 6.5, (f) 7.0.

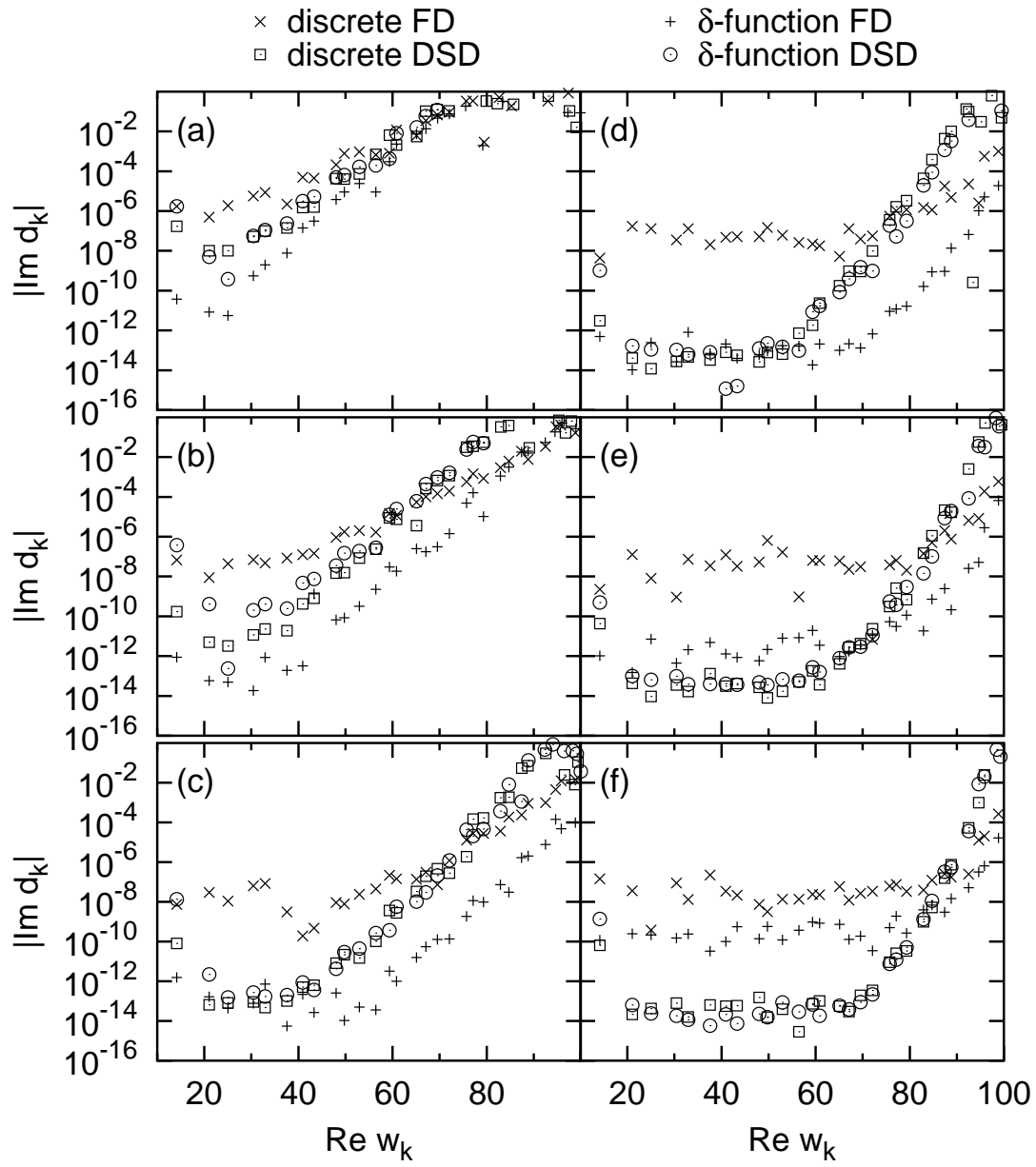


Figure 3.4: Same as Figure 3.3, but for the imaginary parts of the multiplicities d_k .

100. Ideally, all values w_k should be real. Therefore, the absolute values of the imaginary parts of the w_k can again serve as a measure for the accuracy of the harmonic inversion process. For the application of methods 1 and 3 the signal has been discretized with step width $\tau = 0.002$ after a convolution of the signal with a Gaussian function with width $\sigma = 0.006$.

It is no problem to construct the signal (3.37) for the Riemann zeros up to quite large maximum values S_{\max} because the prime numbers used as input are easy to compute. However, the periodic-orbit quantization of physical systems usually requires a numerical periodic orbit search which becomes more and more expensive for longer orbits, especially in chaotic systems, where the number of orbits proliferates exponentially with increasing signal length. Therefore, in practical applications of periodic-orbit quantization the given signal length is often rather short. In figure 3.3 I present the results for the accuracy of the methods for various signal lengths, increasing from $S_{\max} = 4.5$ in figure 3.3(a) to $S_{\max} = 7.0$ in figure 3.3(f). The frequency window $w \in [10, 100]$ is kept fixed.

For a fixed signal length, the zeros up to a certain critical value can be obtained to a constant precision. Above the critical frequency, the precision decreases rapidly due to the higher density of states. As was to be expected, for all methods the critical frequency increases with growing signal length, which means that frequencies in regions of higher spectral density can be resolved. Roughly, the critical frequency is determined by the informational uncertainty principle (3.7). In fact, it is slightly higher for the FD methods 1 and 2 than for the DSD methods 3 and 4. As before, the maximum accuracy below the critical frequency is obtained by the DSD methods. However, above the critical frequency the precision yielded by the FD methods is higher.

The lowest zero of the zeta function is located at $w = 14.1347$, not far above the lower boundary of the frequency window at $w = 10$. For the first zeros a decrease in accuracy due to the proximity of the boundary can be seen. Evidently, the influence of the boundary diminishes with increasing signal length. Again, it is considerably more pronounced for the DSD than for the FD methods. For the latter, it can only be seen in the shortest signals. With any of the four methods, the boundary effects on the lowest zeros can be removed if the lower boundary of the frequency window is decreased to $w = 0$.

Figure 3.4 presents results similar to those shown in figure 3.3, but for the imaginary parts of the multiplicities d_k . The accuracy of the results achieved with the different methods resemble those obtained for the imaginary parts of the frequencies w_k , with the exception of method 1 (see the \times symbols) which provides amplitudes with significantly lower precision.

3.3.3 Conclusion

In this section I have quantitatively determined the accuracies of four different algorithms for the high-resolution harmonic inversion of δ function signals, by applying all algorithms to two, physically motivated, example signals. For sufficiently long signals and broad frequency windows all four methods provide

excellent results of very high accuracy, in the case of the examples selected even close to the machine precision. However, when either the width of the frequency filter or the signal length is considerably reduced, the accuracy of the results obtained by the four methods can vary by several orders of magnitude.

The calculations show that no general clear-cut answer to the question “Which method is the best in all physical situations?” is possible. In practice, the window width can be regarded as a free parameter, i.e. it can usually be chosen sufficiently large to achieve good results before increasing computational effort or numerical instabilities become a restriction. The signal length, on the contrary, is often fixed or at least hard to increase. In such a case the proper choice of the algorithm for harmonic inversion of the signal will be essential to achieve optimum results. When the signal length is quite at the limit for convergence of the frequencies and amplitudes, the filter diagonalization (FD) methods 1 and 2 provide superior accuracy compared to the decimated signal diagonalization (DSD) methods 3 and 4. For signals given as the sum of δ functions method 2 will often prove to be the method of choice.

Finally, note that harmonic inversion techniques can be generalized so as to cope with the analysis of multidimensional signals, with important applications in other areas of physics [65–67]. The knowledge gained from the comparison of methods for one-dimensional harmonic inversion should also serve as a useful guide in future developments and applications of accurate and efficient algorithms for multidimensional high-resolution signal processing.

3.4 Quantization of non-scaling systems

So far, applications of harmonic inversion techniques to semiclassics have been restricted to systems possessing a scaling property. Although this restriction is fairly weak in that it encompasses, among others, billiard systems, systems with homogeneous potentials and atoms in external fields, in many cases scaled spectra do not provide the most natural approach to a problem. For atoms in external fields, for example, the most obvious question to ask is for spectra at fixed external field strengths rather than for scaled spectra. Although scaled-energy spectroscopy [54, 55] has become a well-established tool, a semiclassical approach to this more general problem is still desirable. Furthermore, there is the need to quantize systems without a scaling property as, e.g., simple molecules.

As to the semiclassical analysis of quantum spectra, for non-scaling systems the classical actions and amplitudes occurring in (3.1) are functions of the energy, and there is obviously no hope of determining these continuous functions from a given discrete set of energy eigenvalues by any means. On the other hand, the energy eigenvalues E_n and matrix elements m_n determining the quantum response function are well-defined constants for non-scaling as well as for scaling systems, so that the problem of generalizing the semiclassical quantization procedure can be expected to be a technical rather than a fundamental issue.

To generalize the approach to semiclassical quantization given in section 3.1,

I first take the Fourier transform of (3.1). I obtain

$$-i \sum_n m_n e^{-iE_n t} = C(t) \quad (3.38)$$

with

$$C(t) = \frac{1}{2\pi} \int_{-\infty}^{+\infty} dE \sum_{\text{c.o.}} \mathcal{A}_{\text{c.o.}}(E) e^{iS_{\text{c.o.}}(E)} e^{-iEt} . \quad (3.39)$$

The left-hand (“quantum”) side of (3.38) has precisely the form needed for the application of the harmonic inversion. However, whereas the integral (3.39) giving the semiclassical signal could easily be evaluated analytically in the case of scaling systems, there appears to be no way of computing it in general. Apart from the fact that the classical quantities can always be calculated in a finite energy range only, the integral (3.39) can, in general, not even be expected to converge. Thus, no analytical nor numerical approach to (3.39) will give a useful semiclassical signal.

A solution to these problems can be found by noting that (3.38) contains the spectral information describing the system at all energies. No computational procedure should be expected to handle a signal containing unlimited spectral information. It is now crucial to note that a band-limited signal can be obtained by taking the Fourier transform of (3.1) over a fixed energy interval $[E_0 - \Delta E, E_0 + \Delta E]$ only. This procedure yields

$$-i \sum_{|E_n - E_0| < \Delta E} m_n e^{-i(E_n - E_0)t} = C_{\text{bl}}(t) \quad (3.40)$$

with

$$\begin{aligned} C_{\text{bl}}(t) &= \frac{1}{2\pi} \int_{E_0 - \Delta E}^{E_0 + \Delta E} dE \sum_{\text{c.o.}} \mathcal{A}_{\text{c.o.}}(E) e^{iS_{\text{c.o.}}(E)} e^{-i(E - E_0)t} \\ &= \frac{1}{2\pi} \int_{E_0 - \Delta E}^{E_0 + \Delta E} dE g^{\text{osc}}(E) e^{-i(E - E_0)t} . \end{aligned} \quad (3.41)$$

The integral in (3.41) can be evaluated numerically once the classical data is known in the energy range considered. Again, as in methods 3 and 4 in section 3.2, the frequency window was shifted such as to be centred at zero. This shift makes the integral easier to evaluate because the integrand is less oscillatory, and it allows the step width for the discretization of the band-limited signal to be larger, so that fewer signal points need to be computed.

The procedure described above achieves the goal of making the semiclassical quantization by harmonic inversion applicable to non-scaling as well as scaling systems, so that it can now be regarded as a truly universal semiclassical technique. It does not impose any conditions on the classical dynamics of the system under study. As is obvious from the second line in (3.41), the method does not even depend on the general form (3.1) of the semiclassical approximation to the recurrence function. It is therefore possible to include uniform approximations or

other non-standard contributions in the semiclassical spectrum. Thus, the generalization of the harmonic inversion procedure developed here is not only the first semiclassical quantization scheme which is applicable to arbitrary systems, it also constitutes a major step towards a semiclassical quantization of the crossed-fields hydrogen atom, where bifurcating orbits will be shown to play an important role.

Numerical results for the hydrogen atom in an electric field confirming the reliability of the technique in the presence of bifurcating orbits will be presented in chapter 7.

Chapter 4

The Kustaanheimo-Stiefel transformation

The classical description of the electron dynamics for the hydrogen atom in external fields is that of a perturbed Kepler problem. The motion of the electron close to the nucleus is dominated by the Coulomb potential, which introduces a singularity into the equations of motion. For numerical studies of the dynamics it is mandatory to find a representation of the equations of motion which avoids this singularity.

For the one-dimensional Kepler motion, it was already found by Euler [68] that the introduction of a square-root coordinate $u = \sqrt{x}$ and a fictitious time τ defined by $dt = x d\tau$ reduces the Kepler equation of motion

$$\frac{d^2x}{dt^2} = -\frac{1}{x^2} \quad (4.1)$$

to the regular equation of motion of a one-dimensional harmonic oscillator

$$\frac{d^2u}{ds^2} + 2Eu = 0, \quad (4.2)$$

where E is the energy of the Kepler motion.

Generalizing this approach, Levi-Civita [69] regularized the two-dimensional Kepler problem by combining the two spatial coordinates into a complex number $x = x_1 + ix_2$ and introducing a complex square-root coordinate $u = \sqrt{x}$, which together with the fictitious-time transformation $dt = |x| d\tau$ reduces the Kepler problem to a two-dimensional harmonic oscillator.

Attempts to extend this regularization scheme to the three-dimensional Kepler problem failed, until in 1964 Kustaanheimo and Stiefel [70, 71] proposed the introduction of four regularizing coordinates instead of three and thereby achieved the reduction of the three-dimensional Kepler problem to a four-dimensional harmonic oscillator. This transformation, which is known as the Kustaanheimo-Stiefel (KS) transformation, is discussed in detail in the monograph by Stiefel and Scheifele [28].

In this chapter, a formulation of the KS-transformation in terms of the geometric algebra of Euclidean three-space is presented. In this formalism, the four

KS coordinates are interpreted as the components of a position spinor. Thus, the KS coordinates are given a clear geometric interpretation. In addition, the formalism offers computational advantages over the conventional matrix-based approach because it unites the four coordinates into a single spinor.

In section 4.1, the regularized spinor equation of motion for motion under the combined influences of the Coulomb potential and arbitrary additional forces will be derived. This equation of motion was first obtained in the context of geometric algebra by Hestenes [29]. Subsequent sections will then go on to show that the geometric algebra formulation readily lends itself to an incorporation into the Lagrangian and Hamiltonian formulations of dynamics. A short introduction into the properties of geometric algebra needed here is given in Appendix C, where the notation used in what follows is also explained.

4.1 The spinor equation of motion

The KS-transformation in three dimensions can be found by representing an arbitrary position in space not by its position vector \boldsymbol{x} , but by a position spinor, i.e. the rotation-dilatation operator transforming a fixed reference vector into the position vector \boldsymbol{x} . According to appendix C, a rotation-dilatation of the reference vector $\boldsymbol{\sigma}_3$ is represented in the geometric algebra by an even multivector U according to

$$\boldsymbol{x} = \frac{1}{2}U\boldsymbol{\sigma}_3U^\dagger. \quad (4.3)$$

The factor $1/2$ was introduced here to stay in touch with earlier applications of the KS-transformation to atomic dynamics [6,7], although the present formulation of the theory would suggest dropping it. It implies the normalization

$$U^\dagger U = UU^\dagger = 2r = 2|\boldsymbol{x}|. \quad (4.4)$$

Up to normalization, the ansatz (4.3) reproduces the square-root coordinates introduced by Euler and Levi-Civita, respectively, if it is applied to spaces of one or two dimensions.

Given a position vector \boldsymbol{x} , the choice of the spinor U is not unique. More precisely, the gauge transformation

$$U \mapsto Ue^{-I_3\alpha/2} \quad (4.5)$$

with arbitrary real α does not alter \boldsymbol{x} , because the additional exponential factor describes a rotation of the reference vector $\boldsymbol{\sigma}_3$ around itself. This consideration immediately clarifies why a position spinor representation in three dimensions must introduce a fourth degree of freedom. In lower dimensions, a rotation does not leave any vector invariant, so that the spinor transformation does not possess a gauge degree of freedom. It is also clear from (4.5) that all fibres of the KS transformation except $U = 0$ are circles in spinor space.

The inverse KS transformation can be found from equation (C.23) by adapting the normalization to (4.4). The position spinors corresponding to a vector \mathbf{x} are given by

$$U = \frac{r + \mathbf{x}\sigma_3}{\sqrt{r+z}} e^{-I_3\alpha/2} \quad (4.6)$$

with arbitrary real α .

In components, the spinor U can be represented as $U = u_0 + I\mathbf{u}$ with $\mathbf{u} = \sum_{k=1}^3 u_k \sigma_k$. The transformation (4.3) then decomposes into

$$\begin{aligned} x &= u_1 u_3 - u_0 u_2, \\ y &= u_1 u_0 + u_2 u_3, \\ z &= \frac{1}{2}(u_0^2 - u_1^2 - u_2^2 + u_3^2). \end{aligned} \quad (4.7)$$

Up to renumbering the components, this agrees with the conventions of [6, 7].

To obtain an equation of motion for U , time derivatives of U must be calculated. Differentiating (4.3) leads to

$$\dot{\mathbf{x}} = \frac{1}{2}\dot{U}\sigma_3U^\dagger + \frac{1}{2}U\sigma_3\dot{U}^\dagger = \left\langle \dot{U}\sigma_3U^\dagger \right\rangle_1. \quad (4.8)$$

Equation (4.8) obviously cannot be solved for \dot{U} because the time derivative of the gauge parameter α in (4.5) cannot be determined from the dynamics of the position vector. To arrive at an equation of motion for U , I must therefore impose a constraint on α . This can be done in a convenient and geometrically appealing fashion by requiring

$$\left\langle \dot{U}\sigma_3U^\dagger \right\rangle_3 = 0, \quad (4.9)$$

This condition means that \dot{U} is chosen such as not to contain a component of rotation around the instantaneous position vector \mathbf{x} . Under this constraint, (4.8) yields

$$\dot{\mathbf{x}} = \dot{U}\sigma_3U^\dagger \quad (4.10)$$

and

$$\dot{U} = \dot{\mathbf{x}}U^{\dagger-1}\sigma_3 = \dot{\mathbf{x}}\frac{U}{2r}\sigma_3. \quad (4.11)$$

As in the one- and two-dimensional cases, the regularization of the three-dimensional Kepler motion requires the introduction of a fictitious-time parameter τ . It is defined by

$$dt = 2r d\tau \quad (4.12)$$

Derivatives with respect to τ will be denoted with a prime. Equation (4.11) then yields

$$U' = 2r\dot{U} = \dot{\mathbf{x}}U\sigma_3. \quad (4.13)$$

For the second derivative of U , I obtain

$$\begin{aligned}
U'' &= \left(\frac{d}{d\tau} \dot{\mathbf{x}} \right) U \boldsymbol{\sigma}_3 + \dot{\mathbf{x}} U' \boldsymbol{\sigma}_3 \\
&= 2r \ddot{\mathbf{x}} U \boldsymbol{\sigma}_3 \frac{U^\dagger}{2r} U + \dot{\mathbf{x}}^2 U \\
&= 2 \left(\ddot{\mathbf{x}} \mathbf{x} + \frac{1}{2} \dot{\mathbf{x}}^2 \right) U .
\end{aligned} \tag{4.14}$$

Together with Newton's equation of motion

$$\ddot{\mathbf{x}} = -\frac{\mathbf{x}}{r^3} + \mathbf{f} \tag{4.15}$$

with an arbitrary non-Coulombic force \mathbf{f} , equation (4.14) yields the spinor equation of motion

$$U'' = 2(E_K + \mathbf{f} \mathbf{x}) U , \tag{4.16}$$

where the Kepler energy

$$E_K = \frac{1}{2} \dot{\mathbf{x}}^2 - \frac{1}{r} \tag{4.17}$$

denotes the sum of the kinetic and Coulombic potential energies.

In the special case of pure Kepler motion, i.e. $\mathbf{f} = 0$, the Kepler energy E_K is equal to the total energy E and is conserved. In this case, (4.16) reduces to the linear equation of motion

$$U'' = 2E U . \tag{4.18}$$

If $E < 0$, this is the equation of motion of a four-dimensional isotropic harmonic oscillator with frequency $\omega = \sqrt{-2E}$ with respect to τ .

If additional forces \mathbf{f} are present, the Kepler energy is not conserved in general, so that the work done by the external forces must be taken into account [71]. This can easily be achieved if the external forces are generated by static electromagnetic fields, because the work done by a magnetic field \mathbf{B} is zero, whereas an electric field $\mathbf{F} = -\nabla V$ can be derived from a potential $V(\mathbf{x})$. In this case, the total energy $E = E_K - V$ is conserved¹, so that the equation of motion reads

$$U'' = 2(E + V(\mathbf{x}) + \mathbf{f} \mathbf{x}) U \tag{4.19}$$

with $\mathbf{f} = -\mathbf{F} - \dot{\mathbf{x}} \times \mathbf{B}$.

It finally remains to verify that the equation of motion (4.16) is consistent with the constraint (4.9). To prove this, I first note that

$$\xi = \langle U' \boldsymbol{\sigma}_3 U^\dagger \rangle_3 \tag{4.20}$$

¹Note that the electron charge is negative.

is a constant of motion for any external forces \mathbf{f} [71], because by (4.16)

$$\begin{aligned}
 \frac{d\xi}{d\tau} &= \langle U'' \boldsymbol{\sigma}_3 U^\dagger \rangle_3 + \underbrace{\langle U' \boldsymbol{\sigma}_3 U'^\dagger \rangle_3}_{=0 \text{ by (C.22)}} \\
 &= \langle (E_K + \mathbf{f} \mathbf{x}) \mathbf{x} \rangle_3 \\
 &= \langle E_K \mathbf{x} + r^2 \mathbf{f} \rangle_3 \\
 &= 0.
 \end{aligned} \tag{4.21}$$

Therefore, if the initial conditions are chosen so that $\xi = 0$ at $\tau = 0$, equation (4.21) guarantees $\langle \dot{U} \boldsymbol{\sigma}_3 U^\dagger \rangle_3 = 2r \xi = 0$ at all times.

4.2 Canonical formalism

In classical investigations of atoms in external fields, the Hamiltonian nature of the dynamics plays a central role. It is therefore essential to show how the spinor equation of motion found in the previous section can be derived in the context of a Lagrangian or Hamiltonian formalism. In the matrix theory of the KS transformation, a Hamiltonian formulation is well known and widely applied in the literature [6, 7]. Due to the introduction of an additional degree of freedom and a fictitious-time parameter, it cannot be found by a straightforward change of variables. In this section it will be shown that the application of geometric algebra allows an easy and general derivation of the Hamiltonian. At the same time, the Hamiltonian formalism will be generalized to arbitrary inhomogeneous static external fields.

4.2.1 Fictitious-time transformations

Elementary expositions of Lagrangian and Hamiltonian dynamics usually treat the time t as the externally prescribed independent variable fundamentally different from the spatial coordinates, velocities, and momenta. The formalisms are then shown to be invariant under point transformations or canonical transformations, respectively, which may be time-dependent, but may not transform the time variable. However, both the Lagrangian and the Hamiltonian formalisms can be reformulated in such a way that it is possible to introduce an arbitrary orbital parameter τ and to treat the physical time t as an additional coordinate on the same footing as the spatial coordinates. This formalism is discussed in its full generality by Dirac [72, 73]. For the special case of autonomous Lagrangian dynamics and the simple form of the fictitious-time transformation used above, the full flexibility of Dirac's homogeneous formalism is not needed. Instead, the modifications needed to achieve the fictitious-time transformation can be derived in a straightforward manner from Hamilton's variational principle.

The Lagrangian equations of motion can be derived from the action functional

$$S = \int_{t_1}^{t_2} dt L(q(t), \dot{q}(t)) \tag{4.22}$$

by requiring that for the classical paths the variation of S with respect to the path $q(t)$ vanishes if the variation is performed with the initial and final times t_1 and t_2 and the coordinates $q(t_1)$ and $q(t_2)$ kept fixed. If a fictitious-time parameter τ is introduced by the prescription

$$dt = f(q, \dot{q}) d\tau \quad (4.23)$$

with an arbitrary function f , it is tempting to rewrite the action functional as

$$S = \int_{\tau_1}^{\tau_2} d\tau f(q, \dot{q}) L(q, \dot{q}) \quad (4.24)$$

and regard

$$\tilde{L} = f(q, \dot{q}) L(q, \dot{q}) = \frac{dt}{d\tau} L \quad (4.25)$$

as the Lagrangian describing the dynamics with respect to τ . However, this simple procedure is incorrect in general, because to derive the Lagrangian equations with respect to \tilde{L} from (4.24), the variation of S has to be performed with the initial and final fictitious times τ_1 and τ_2 kept fixed, and due to (4.23) a variation of the path will alter the relation between t and τ , so that the initial and final physical times t_1 and t_2 will vary.

To establish the true relation between (4.22) and (4.24), I calculate the variation of (4.24) taking the variation of t into account, i.e. q and t are varied according to

$$\begin{aligned} q(\tau) &\mapsto q(\tau) + \delta q(\tau) , \\ t(\tau) &\mapsto t(\tau) + \delta t(\tau) , \end{aligned} \quad (4.26)$$

subject to the boundary conditions

$$\delta q(\tau_1) = \delta q(\tau_2) = 0 \quad (4.27)$$

and with τ_1 and τ_2 kept fixed. Under this variation,

$$\begin{aligned} \frac{d\tau}{dt} &\mapsto \frac{d\tau}{d(t + \delta t)} = \frac{1}{\frac{dt}{d\tau} + \frac{d\delta t}{d\tau}} \\ &= \frac{d\tau}{dt} \left(1 - \frac{d\tau}{dt} \frac{d\delta t}{d\tau} \right) , \end{aligned} \quad (4.28)$$

so that

$$\delta \frac{d\tau}{dt} = - \left(\frac{d\tau}{dt} \right)^2 \frac{d\delta t}{d\tau} \quad (4.29)$$

and hence

$$\begin{aligned} \delta \dot{q} &= \delta \left(\frac{dq}{d\tau} \frac{d\tau}{dt} \right) \\ &= \delta \left(\frac{dq}{d\tau} \right) \cdot \frac{d\tau}{dt} + \frac{dq}{d\tau} \cdot \delta \left(\frac{d\tau}{dt} \right) \\ &= \frac{d\delta q}{dt} - \dot{q} \frac{d\tau}{dt} \frac{d\delta t}{d\tau} . \end{aligned} \quad (4.30)$$

The variation of (4.24) then reads

$$\begin{aligned}
\delta S &= \int d\tau \left[\delta \left(\frac{dt}{d\tau} \right) L + \frac{dt}{d\tau} \left(\frac{\partial L}{\partial q} \delta q + \frac{\partial L}{\partial \dot{q}} \delta \dot{q} \right) \right] \\
&= \int d\tau \frac{d\delta t}{d\tau} \left(L - \dot{q} \frac{\partial L}{\partial \dot{q}} \right) + \int dt \left(\frac{\partial L}{\partial q} \delta q + \frac{\partial L}{\partial \dot{q}} \frac{d\delta q}{dt} \right) \\
&= - \int d\tau \frac{d\delta t}{d\tau} H + \int dt \left(\frac{\partial L}{\partial q} - \frac{d}{dt} \frac{\partial L}{\partial \dot{q}} \right) \delta q,
\end{aligned} \tag{4.31}$$

where the customary partial integration was performed, the boundary conditions (4.27) were used and the Hamiltonian

$$H = \dot{q} \frac{\partial L}{\partial \dot{q}} - L \tag{4.32}$$

was introduced.

If only the second integral in the last line of (4.31) was present, it would yield the correct equations of motion. Thus, the action functionals (4.22) and (4.24) are equivalent if the Hamiltonian H vanishes. For autonomous systems, H is a constant of motion equal to the energy E . If the Lagrangian L is replaced with $L + E$, with E regarded as a constant, the equations of motion derived from L are unchanged, but the Hamiltonian (4.32) changes to $H - E = 0$. Thus, the dynamics of trajectories with energy E with respect to the fictitious-time parameter τ is described by the Lagrangian

$$\mathcal{L} = \frac{dt}{d\tau} (L + E) = f(q, \dot{q}) (L + E). \tag{4.33}$$

This Lagrangian has to be written as a function of the coordinates q and the fictitious-time velocities q' . If the function f is independent of the velocities, the canonical momenta are invariant under the fictitious-time transformation, because $q' = f(q) \dot{q}$ and

$$\frac{\partial \mathcal{L}}{\partial q'} = f(q) \frac{d\dot{q}}{dq'} \frac{\partial L}{\partial \dot{q}} = \frac{\partial L}{\partial \dot{q}}. \tag{4.34}$$

From the time-transformed Lagrangian (4.33), the transformed Hamiltonian

$$\mathcal{H} = q' \frac{\partial \mathcal{L}}{\partial q'} - \mathcal{L} = f(q, \dot{q}) (H - E) \tag{4.35}$$

is obtained by the usual Legendre transformation. It must be written as a function of the coordinates and momenta. In some cases the passage from the Lagrangian to the Hamiltonian description of the dynamics is impossible because the relation $p = \partial \mathcal{L}(q, q') / \partial q'$ cannot be solved for q' . In these cases, the Hamiltonian (4.35) can be shown to describe the fictitious-time dynamics by a discussion of the modified Hamilton's principle analogous to the derivation of the Lagrangian \mathcal{L} above.

4.2.2 Lagrangian description

The dynamics of an atomic electron under the combined influences of the nuclear Coulomb potential, an additional scalar potential $V(\mathbf{x})$ and a magnetic field represented by a vector potential $\mathbf{A}(\mathbf{x})$ is described by the Lagrangian

$$L = \frac{\dot{\mathbf{x}}^2}{2} + \frac{1}{r} + V(\mathbf{x}) - \mathbf{A} \cdot \dot{\mathbf{x}} . \quad (4.36)$$

This Lagrangian must be transformed to a Lagrangian \mathcal{L} describing the fictitious-time dynamics of the position spinor U . With $f(q) = 2r = U^\dagger U$ by (4.12), the fictitious-time Lagrangian (4.33) reads

$$\mathcal{L} = \frac{1}{4} U'^\dagger U' + \frac{1}{8r} \left\langle (U' \boldsymbol{\sigma}_3 U^\dagger)^2 \right\rangle + E U^\dagger U + U^\dagger U V(\mathbf{x}) - \langle \mathbf{A}(\mathbf{x}) U' \boldsymbol{\sigma}_3 U^\dagger \rangle + 2 \quad (4.37)$$

with $\mathbf{x} = \frac{1}{2} U \boldsymbol{\sigma}_3 U^\dagger$. If the constraint (4.9) is used, \mathcal{L} simplifies to

$$\mathcal{L} = \frac{1}{2} U'^\dagger U' + E U^\dagger U + U^\dagger U V(\mathbf{x}) - \langle \mathbf{A}(\mathbf{x}) U' \boldsymbol{\sigma}_3 U^\dagger \rangle + 2 \quad (4.38)$$

Both forms of the Lagrangian yield the same ‘‘on-shell’’ dynamics for trajectories satisfying (4.9). Note that only the kinetic term is influenced by the constraint, whereas potential and vector potential terms are not.

The momentum conjugate to U is given by

$$P = \partial_{U'} \mathcal{L} = \frac{1}{2r} \boldsymbol{\sigma}_3 U^\dagger \langle U' \boldsymbol{\sigma}_3 U^\dagger \rangle_1 - \boldsymbol{\sigma}_3 U^\dagger \mathbf{A} , \quad (4.39)$$

which simplifies to

$$P = U'^\dagger - \boldsymbol{\sigma}_3 U^\dagger \mathbf{A} \quad (4.40)$$

if (4.9) is applied.

As the spinor equation of motion (4.16) is valid under the constraint (4.9) only, the Lagrangian \mathcal{L} provides a suitable description of the dynamics if it reproduces (4.16) for trajectories satisfying (4.9). The simplified Lagrangian (4.38) can therefore be used. When equations of motion are derived from (4.38), the constraint (4.9) must be taken into account by a Lagrangian multiplier. I will now show, however, that the unconstrained equation of motion [74]

$$\frac{d}{d\tau} \partial_{U'} \mathcal{L} - \partial_U \mathcal{L} = 0 \quad (4.41)$$

derived from (4.38) reproduces (4.16) without the constraint being explicitly dealt with, i.e. the Lagrangian multiplier to be introduced turns out to vanish identically. I therefore ignore it from the outset.

For the case of vanishing external potentials, (4.41) can easily be seen to yield

$$U''^\dagger - 2EU^\dagger = 0 , \quad (4.42)$$

which is the reversion of (4.18). For the terms containing the potentials, the calculation of (4.41) is still straightforward, but requires a more intimate familiarity with the properties of the multivector derivative. I will therefore present the calculation in detail.

The contribution of the scalar potential term

$$\mathcal{V} = U^\dagger U V(\mathbf{x}(U)) \quad (4.43)$$

with $\mathbf{x}(U) = \frac{1}{2}U\boldsymbol{\sigma}_3U^\dagger$ reads, by (C.28) and (C.33),

$$\partial_U \mathcal{V} = 2U^\dagger V(\mathbf{x}) + U^\dagger U \partial_U V(\mathbf{x}(U)) . \quad (4.44)$$

The chain rule (C.30) then yields for any even multivector M

$$M * \partial_U V(\mathbf{x}(U)) = (M * \partial_U \mathbf{x}(U)) * \partial_{\mathbf{x}} V \quad (4.45)$$

with

$$\begin{aligned} M * \partial_U \mathbf{x}(U) &= (M * \partial_U) \frac{1}{2} U \boldsymbol{\sigma}_3 U^\dagger \\ &= \frac{1}{2} M \boldsymbol{\sigma}_3 U^\dagger + \frac{1}{2} U \boldsymbol{\sigma}_3 M^\dagger \\ &= \langle M \boldsymbol{\sigma}_3 U^\dagger \rangle_1 . \end{aligned} \quad (4.46)$$

In the absence of a magnetic field the external force is $\mathbf{f} = \partial_{\mathbf{x}} V$, so that

$$M * \partial_U V(\mathbf{x}(U)) = \langle \langle M \boldsymbol{\sigma}_3 U^\dagger \rangle_1 \mathbf{f} \rangle = \langle M \boldsymbol{\sigma}_3 U^\dagger \mathbf{f} \rangle . \quad (4.47)$$

Thus,

$$\partial_U V = \partial_M (M * \partial_U V) = \boldsymbol{\sigma}_3 U^\dagger \mathbf{f} , \quad (4.48)$$

and finally

$$\partial_U \mathcal{V} = 2U^\dagger V(\mathbf{x}) + 2U^\dagger \mathbf{x} \mathbf{f} . \quad (4.49)$$

This is the reversion of the scalar-potential terms in (4.16). Therefore, (4.49) together with (4.42) indeed yields the correct equation of motion.

To evaluate the contribution of the vector potential term

$$\mathcal{A} = \langle \mathbf{A}(\mathbf{x}) U' \boldsymbol{\sigma}_3 U^\dagger \rangle \quad (4.50)$$

to (4.41), first note that

$$\begin{aligned} \frac{d}{d\tau} \partial_{U'} \mathcal{A} &= \frac{d}{d\tau} (\boldsymbol{\sigma}_3 U^\dagger \mathbf{A}(\mathbf{x})) \\ &= \boldsymbol{\sigma}_3 U'^\dagger \mathbf{A}(\mathbf{x}) + \boldsymbol{\sigma}_3 U^\dagger (\mathbf{x}' \cdot \partial_{\mathbf{x}}) \mathbf{A}(\mathbf{x}) . \end{aligned} \quad (4.51)$$

By Leibniz' rule and (4.8),

$$\begin{aligned} \partial_U \mathcal{A} &= \overset{*}{\partial}_U \left\langle \mathbf{A} U' \boldsymbol{\sigma}_3 U^\dagger \right\rangle + \overset{*}{\partial}_U \left\langle \overset{*}{\mathbf{A}} U' \boldsymbol{\sigma}_3 U^\dagger \right\rangle \\ &= \boldsymbol{\sigma}_3 U'^\dagger \mathbf{A} + \partial_U \langle \mathbf{A}(\mathbf{x}(U)) \mathbf{x}' \rangle . \end{aligned} \quad (4.52)$$

The second term on the right-hand side can be evaluated by first calculating directional derivatives. For an arbitrary even M , (4.46) and the chain rule (C.30) yield

$$\begin{aligned}
(M * \partial_U) \langle \mathbf{A}(\mathbf{x}(U)) \mathbf{x}' \rangle &= (M * \partial_U \mathbf{A}) * \partial_{\mathbf{A}} \langle \mathbf{A} \mathbf{x}' \rangle \\
&= \langle (M * \partial_U \mathbf{A}(\mathbf{x}(U))) \mathbf{x}' \rangle \\
&= \langle (M * \partial_U \mathbf{x}) * \partial_{\mathbf{x}} \mathbf{A} \mathbf{x}' \rangle \\
&= \langle \langle \langle M \sigma_3 U^\dagger \rangle_1 \partial_{\mathbf{x}} \rangle \mathbf{A} \mathbf{x}' \rangle \\
&= \langle M \sigma_3 U^\dagger \partial_{\mathbf{x}} \rangle \langle \mathbf{A} \mathbf{x}' \rangle ,
\end{aligned} \tag{4.53}$$

so that

$$\begin{aligned}
\partial_U \langle \mathbf{A}(\mathbf{x}(U)) \mathbf{x}' \rangle &= \partial_M (M * \partial_U) \langle \mathbf{A}(\mathbf{x}(U)) \mathbf{x}' \rangle \\
&= \sigma_3 U^\dagger \partial_{\mathbf{x}} (\mathbf{A} \cdot \mathbf{x}') .
\end{aligned} \tag{4.54}$$

Equations (4.51), (4.52) and (4.54) combine to

$$\begin{aligned}
\frac{d}{d\tau} \partial_{U'} \mathcal{A} - \partial_U \mathcal{A} &= \sigma_3 U^\dagger ((\mathbf{x}' \cdot \partial_{\mathbf{x}}) \mathbf{A} - \partial_{\mathbf{x}} (\mathbf{A} \cdot \mathbf{x}')) \\
&= -\sigma_3 U^\dagger (\mathbf{x}' \times (\partial_{\mathbf{x}} \times \mathbf{A})) \\
&= -2 U^\dagger \mathbf{x} (\dot{\mathbf{x}} \times \mathbf{B}) ,
\end{aligned} \tag{4.55}$$

which is the reversion of the magnetic-field contribution to (4.16).

Note that the derivation given here is valid for arbitrary external potentials V and \mathbf{A} , whereas conventional treatments restrict themselves to the special case of homogeneous external fields. Also note that the geometric algebra formalism allows one to do the calculations in a straightforward manner without having to resort to component decompositions of any of the vectorial or spinorial quantities involved.

4.2.3 Hamiltonian description

The transition from a Lagrangian to a Hamiltonian description of the dynamics leads from the Lagrangian (4.37) or (4.38), depending on whether or not the constraint (4.9) is applied, to the Hamiltonian

$$\mathcal{H} = (U' * \partial_{U'}) \mathcal{L} - \mathcal{L} , \tag{4.56}$$

in which the velocity U' has to be expressed in terms of the momentum P . The transformation requires that the relation (4.39) or (4.40) between velocity and momentum can be solved for the velocity, which is impossible in the case of (4.39). Thus, the constraint (4.9) is not only needed to obtain an unambiguous equation of motion for U , but also serves as a condition for a Hamiltonian description of the spinor dynamics to exist. If it is imposed and an inessential constant of 2 is added, the Hamiltonian reads

$$\mathcal{H} = \frac{1}{2} (P^\dagger + \mathbf{A} U \sigma_3) (P + \sigma_3 U^\dagger \mathbf{A}) - EU^\dagger U - U^\dagger U V(\mathbf{x}) = 2 \tag{4.57}$$

Because it is time-independent, the Hamiltonian (4.57) is a constant of motion. To describe the physical dynamics, its value must be chosen to be 2, whereas the physical energy E appears as a parameter in \mathcal{H} .

The equations of motion derived from (4.57) read

$$\begin{aligned} U' &= \partial_P \mathcal{H} = P^\dagger + \mathbf{A} U \boldsymbol{\sigma}_3, \\ P' &= -\partial_U \mathcal{H} \\ &= -2E U^\dagger - 2U^\dagger V(\mathbf{x}) - 2U^\dagger \mathbf{x} \partial_{\mathbf{x}} V \\ &\quad - \boldsymbol{\sigma}_3 (P + \boldsymbol{\sigma}_3 U^\dagger \mathbf{A}) \mathbf{A} - \boldsymbol{\sigma}_3 U^\dagger \overset{*}{\partial}_{\mathbf{x}} \left\langle \overset{*}{\mathbf{A}} \mathbf{x}' \right\rangle, \end{aligned} \quad (4.58)$$

where

$$\mathbf{x}' = U \boldsymbol{\sigma}_3 U'^\dagger = U \boldsymbol{\sigma}_3 P + U^\dagger U \mathbf{A} \quad (4.59)$$

was used. In terms of coordinates and momenta, the constraint (4.9) reads

$$\langle U \boldsymbol{\sigma}_3 P \rangle_3 = 0. \quad (4.60)$$

Equation (4.60) is equivalent to (4.9) both in the presence and in the absence of a magnetic field. Taken together, (4.58) and (4.59) lead back to the equation of motion (4.16).

Finally, let me mention an important subtlety regarding the component decomposition of the spinor equation. If, according to (4.7), U is represented as $U = u_0 + I \mathbf{u}$ with $\mathbf{u} = \sum_{k=1}^3 u_k \boldsymbol{\sigma}_k$ and p_k denotes the momentum component conjugate to u_k , the spinor momentum is $P = p_0 - I \mathbf{p}$ with $\mathbf{p} = \sum_{k=1}^3 p_k \boldsymbol{\sigma}_k$. The negative sign is necessary because in the spinor formulation the bivector $I_k p_k$ is conjugate to $I_k u_k$. Dropping the bivector factors I_k leads to the stated result.

4.3 The Kepler problem

The unperturbed Kepler motion is described by the Hamiltonian

$$\mathcal{H} = \frac{1}{2} P^\dagger P - E U^\dagger U = 2 \quad (4.61)$$

or the equation of motion (4.18)

$$U'' = 2EU.$$

If $E < 0$, this is the equation of motion of an isotropic four-dimensional harmonic oscillator, whose general solution reads

$$U = A \cos(\sqrt{-2E} \tau) + B \sin(\sqrt{-2E} \tau) \quad (4.62)$$

with two constant even multivectors A and B bound, by (4.9) and (4.61), to satisfy

$$\langle A \boldsymbol{\sigma}_3 B^\dagger \rangle_3 = 0 \quad (4.63)$$

and

$$A^\dagger A + B^\dagger B = -\frac{2}{E}. \quad (4.64)$$

In the case of the pure Kepler motion, the angular momentum vector \mathbf{L} and the Lenz vector $\boldsymbol{\varepsilon}$ are conserved. Together, they uniquely specify an orbit [29]. I will now derive the KS-transformed expressions for these constants of motion. Throughout, the validity of the constraint (4.9) will be assumed.

The angular momentum vector is given by

$$\mathbf{L} = \mathbf{x} \times \dot{\mathbf{x}} = -I \langle \mathbf{x} \dot{\mathbf{x}} \rangle_2. \quad (4.65)$$

Within the geometric algebra, it is more convenient to introduce the angular momentum bivector

$$l = I\mathbf{L} = \langle \mathbf{x} \dot{\mathbf{x}} \rangle_2, \quad (4.66)$$

which specifies the orbital plane instead of the direction perpendicular to it. By (4.3), (4.8) and (4.9),

$$\begin{aligned} l &= \left\langle \frac{1}{2} U \boldsymbol{\sigma}_3 U^\dagger U \boldsymbol{\sigma}_3 \dot{U}^\dagger \right\rangle_2 \\ &= \frac{1}{2} \langle U U^\dagger \rangle_2 \\ &= \frac{1}{2} \langle U P \rangle_2. \end{aligned} \quad (4.67)$$

That l is conserved, can be verified by a straightforward differentiation. Alternatively, it can be checked that the Poisson bracket vanishes,

$$\begin{aligned} \{l, \mathcal{H}\} &= (\partial_P \mathcal{H}) * \partial_U l - (\partial_U \mathcal{H}) * \partial_P l \\ &= P^\dagger * \partial_U l + 2E U^\dagger * \partial_P l \\ &= \frac{1}{2} \langle P^\dagger P \rangle_2 + E \langle U^\dagger U \rangle_2 \\ &= 0. \end{aligned} \quad (4.68)$$

Note how the Poisson bracket formalism extends not only to multivector coordinates U and P , but also to non-scalar arguments.

The Lenz vector is given by

$$\begin{aligned} \boldsymbol{\varepsilon} &= l \dot{\mathbf{x}} - \frac{\mathbf{x}}{r} \\ &= l P^\dagger \boldsymbol{\sigma}_3 U^{-1} - U \boldsymbol{\sigma}_3 U^{-1}. \end{aligned} \quad (4.69)$$

To calculate the Poisson bracket $\{\boldsymbol{\varepsilon}, \mathcal{H}\}$, use $\{l, \mathcal{H}\} = 0$ and

$$P^\dagger * \partial_U U^{-1} = -U^{-1} P^\dagger U^{-1} \quad (4.70)$$

to find

$$\begin{aligned}
\{\boldsymbol{\varepsilon}, \mathcal{H}\} &= l \{P^\dagger \boldsymbol{\sigma}_3 U^{-1}, \mathcal{H}\} - \{U \boldsymbol{\sigma}_3 U^{-1}, \mathcal{H}\} \\
&= l (P^\dagger * \partial_U (P^\dagger \boldsymbol{\sigma}_3 U^{-1}) + 2E U^\dagger * \partial_P (P^\dagger \boldsymbol{\sigma}_3 U^{-1})) \\
&\quad - P^\dagger * \partial_U (U \boldsymbol{\sigma}_3 U^{-1}) \\
&= l (-P^\dagger \boldsymbol{\sigma}_3 U^{-1} P^\dagger U^{-1} + 2E U \boldsymbol{\sigma}_3 U^{-1}) \\
&\quad - P^\dagger \boldsymbol{\sigma}_3 U^{-1} + U \boldsymbol{\sigma}_3 U^{-1} P^\dagger U^{-1} \\
&= [l(-P^\dagger \boldsymbol{\sigma}_3 U^{-1} P^\dagger \boldsymbol{\sigma}_3 U^\dagger + 2E U U^\dagger) \\
&\quad - P^\dagger U^\dagger + U \boldsymbol{\sigma}_3 U^{-1} P^\dagger \boldsymbol{\sigma}_3 U^\dagger] U^{\dagger^{-1}} \boldsymbol{\sigma}_3 U^{-1}
\end{aligned} \tag{4.71}$$

Due to the constraint (4.60),

$$P^\dagger \boldsymbol{\sigma}_3 U^\dagger = U \boldsymbol{\sigma}_3 P, \tag{4.72}$$

so that equation (4.71) simplifies to

$$\begin{aligned}
\{\boldsymbol{\varepsilon}, \mathcal{H}\} &= [l(-P^\dagger P + 2E U^\dagger U) - P^\dagger U^\dagger + UP] U^{\dagger^{-1}} \boldsymbol{\sigma}_3 U^{-1} \\
&= [-2l\mathcal{H} + 2\langle UP \rangle_2] U^{\dagger^{-1}} \boldsymbol{\sigma}_3 U^{-1} \\
&= 0.
\end{aligned} \tag{4.73}$$

Thus, the Lenz vector $\boldsymbol{\varepsilon}$ is actually conserved.

4.4 The Kustaanheimo-Stiefel description of closed orbits

If the initial conditions $\boldsymbol{x}(0)$ and $\dot{\boldsymbol{x}}(0)$ for a trajectory are given, the pertinent initial conditions for the spinors U and U' can usually be obtained, up to a choice of gauge, from (4.6) and (4.13). This prescription fails for trajectories starting at the origin, where the KS transformation is singular. To overcome this difficulty, note that in the vicinity of the nucleus the Coulomb interaction is so strong that it dominates all external forces. The dynamics close to the nucleus is therefore described by the Kepler equation of motion (4.18) and its solution (4.62). With the appropriate initial conditions implemented, (4.62) reads

$$U(\tau) = \frac{U'_0}{\sqrt{-2E}} \sin(\sqrt{-2E} \tau). \tag{4.74}$$

U'_0 is the initial velocity in KS-coordinates. It must be normalized to

$$U_0'^\dagger U'_0 = 4. \tag{4.75}$$

The choice of gauge for U'_0 is arbitrary.

The position vector corresponding to (4.74) is

$$\boldsymbol{x}(\tau) = \frac{1}{2} U'_0 \boldsymbol{\sigma}_3 U_0'^\dagger \frac{\sin^2(\sqrt{-2E} \tau)}{-2E}. \tag{4.76}$$

Thus, (4.74) describes an electron moving out from the nucleus in the direction of the unit vector

$$\mathbf{s} = \frac{1}{4}U'_0\boldsymbol{\sigma}_3U_0^\dagger . \quad (4.77)$$

U'_0 is therefore a spinor rotating the vector $\boldsymbol{\sigma}_3$ to the starting direction \mathbf{s} and normalized according to (4.75). In terms of the starting angles ϑ and φ it is given by

$$U'_0 = 2e^{-I_3\varphi/2}e^{-I_2\vartheta/2}e^{-I_3\alpha/2} \quad (4.78)$$

with an arbitrary gauge parameter α . The exponentials in (4.78) describe a sequence of three rotations taking the reference vector $\boldsymbol{\sigma}_3$ to the starting direction \mathbf{s} . The initial momentum reads

$$P_0 = U_0^\dagger = 2e^{I_3\alpha/2}e^{I_2\vartheta/2}e^{I_3\varphi/2} . \quad (4.79)$$

Its component decomposition is

$$\begin{aligned} p_0 &= 2 \cos \frac{\vartheta}{2} \cos \frac{\varphi + \alpha}{2} , \\ p_1 &= 2 \sin \frac{\vartheta}{2} \sin \frac{\varphi - \alpha}{2} , \\ p_2 &= -2 \sin \frac{\vartheta}{2} \cos \frac{\varphi - \alpha}{2} , \\ p_3 &= -2 \cos \frac{\vartheta}{2} \sin \frac{\varphi + \alpha}{2} . \end{aligned} \quad (4.80)$$

To describe the stability of a classical trajectory, a coordinate system with one coordinate along the trajectory and two coordinates perpendicular to it is customarily introduced in the neighbourhood of the trajectory. A linear stability analysis then requires calculating the derivatives of positions and momenta with respect to the transverse initial conditions. Most conveniently, derivatives with respect to two orthonormal directions can be used. If these derivatives are to be calculated within the framework of the KS theory, for a given starting direction \mathbf{s} and a direction $\mathbf{s}_\omega \perp \mathbf{s}$, a KS spinor P_ω must be found such that a variation of the initial KS momentum P_0 in the direction of P_ω corresponds to a variation of \mathbf{s} in the direction of \mathbf{s}_ω .

As the initial momentum is given in terms of the starting angles in (4.79), the derivatives $\partial P_0/\partial\vartheta$ and $\partial P_0/\partial\varphi$ can be expected to describe variations of the starting direction in the directions of increasing ϑ and φ , respectively. To check this and to find the correct normalization of the spinors, I will now construct, for a fixed direction \mathbf{s} , a basis of the spinor space such that one of the basis spinors describes a variation of initial momentum along the orbit, two give variations in the directions of two perpendicular unit vectors, and the fourth basis spinor describes the gauge degree of freedom introduced by the KS regularization.

To this end, I consider a family of trajectories parameterized by an arbitrary parameter ω . All trajectories start at the nucleus, the starting direction is given by a family of vectors $\mathbf{s}(\omega)$. By (4.77), the initial KS momenta $P_0(\omega)$ then satisfy

$$\mathbf{s}(\omega) = \frac{1}{4}P_0^\dagger(\omega)\boldsymbol{\sigma}_3P_0(\omega) , \quad (4.81)$$

so that in complete analogy with (4.8) and (4.11)

$$\frac{\partial \mathbf{s}}{\partial \omega} = \frac{1}{2} \left\langle P_0^\dagger \boldsymbol{\sigma}_3 \frac{\partial P_0}{\partial \omega} \right\rangle_1 \quad (4.82)$$

and

$$\frac{\partial P_0}{\partial \omega} = \frac{1}{2} \boldsymbol{\sigma}_3 P_0 \frac{\partial \mathbf{s}}{\partial \omega} = \frac{1}{2} P_0 \mathbf{s} \frac{\partial \mathbf{s}}{\partial \omega} \quad (4.83)$$

if the gauge condition

$$\left\langle P_0^\dagger \boldsymbol{\sigma}_3 \frac{\partial P_0}{\partial \omega} \right\rangle_3 = 0 \quad (4.84)$$

is imposed. Equation (4.83) gives the variation in the initial KS momentum pertinent to a given variation in the starting direction. If two different variations are given, the scalar product of the momentum variations is

$$\left(\frac{\partial P_0}{\partial \omega_1} \right)^\dagger * \frac{\partial P_0}{\partial \omega_2} = \frac{\partial \mathbf{s}}{\partial \omega_1} * \frac{\partial \mathbf{s}}{\partial \omega_2}, \quad (4.85)$$

so that the variations of KS momentum calculated from (4.83) are orthonormal if the prescribed variations of the starting direction are.

For a fixed starting direction

$$\mathbf{s} = e^{-I_3 \varphi / 2} e^{-I_2 \vartheta} \boldsymbol{\sigma}_3 e^{I_3 \varphi / 2} \quad (4.86)$$

given by the starting angles ϑ and φ , I now introduce the orthogonal vectors

$$\begin{aligned} \mathbf{s}_\vartheta &= e^{-I_3 \varphi / 2} e^{-I_2 \vartheta} \boldsymbol{\sigma}_1 e^{I_3 \varphi / 2}, \\ \mathbf{s}_\varphi &= e^{-I_3 \varphi / 2} \boldsymbol{\sigma}_2 e^{I_3 \varphi / 2}. \end{aligned} \quad (4.87)$$

These are the unit vectors in the directions of $\partial \mathbf{s} / \partial \vartheta$ and $\partial \mathbf{s} / \partial \varphi$, respectively. The orthonormal basis \mathbf{s} , \mathbf{s}_ϑ and \mathbf{s}_φ of the position space gives rise to the three orthonormal KS spinors

$$\begin{aligned} P_s &= \frac{1}{2} \boldsymbol{\sigma}_3 P_0 \mathbf{s} = \frac{1}{2} P_0, \\ P_\vartheta &= \frac{1}{2} \boldsymbol{\sigma}_3 P_0 \mathbf{s}_\vartheta = \frac{I_2}{2} e^{-I_3 \alpha} P_0, \\ P_\varphi &= \frac{1}{2} \boldsymbol{\sigma}_3 P_0 \mathbf{s}_\varphi = -\frac{I_1}{2} e^{-I_3 \alpha} P_0. \end{aligned} \quad (4.88)$$

This set is complemented by a fourth orthonormal spinor

$$P_\alpha = \frac{\partial P_0}{\partial \alpha} = \frac{1}{2} \boldsymbol{\sigma}_3 P_0 I. \quad (4.89)$$

(Note the analogy with (4.83).) The spinor P_α maximally violates the gauge condition (4.84) in the sense that

$$P_0^\dagger \boldsymbol{\sigma}_3 P_\alpha = \left\langle P_0^\dagger \boldsymbol{\sigma}_3 P_\alpha \right\rangle_3. \quad (4.90)$$

It therefore gives the direction in spinor space corresponding to a gauge transformation, whereas P_s describes a change of momentum along the orbit (i.e. a change of the energy) and P_ϑ and P_φ give directions perpendicular to the trajectory. The desired separation of the physically distinct degrees of freedom has thus been achieved. Note that $P_\vartheta = \partial P_0 / \partial \vartheta$ as anticipated, whereas $\partial P_0 / \partial \varphi = P_0 I_3 / 2$ does not satisfy (4.84). Instead,

$$\frac{\partial P_0}{\partial \varphi} = P_\alpha \cos \vartheta + P_\varphi \sin \vartheta . \quad (4.91)$$

In components, the four basis spinors read

$$\begin{aligned} P_s &= \cos \frac{\vartheta}{2} \cos \frac{\varphi+\alpha}{2} - I_1 \sin \frac{\vartheta}{2} \sin \frac{\varphi-\alpha}{2} + I_2 \sin \frac{\vartheta}{2} \cos \frac{\varphi-\alpha}{2} + I_3 \cos \frac{\vartheta}{2} \sin \frac{\varphi+\alpha}{2} , \\ P_\vartheta &= -\sin \frac{\vartheta}{2} \cos \frac{\varphi+\alpha}{2} - I_1 \cos \frac{\vartheta}{2} \sin \frac{\varphi-\alpha}{2} + I_2 \cos \frac{\vartheta}{2} \cos \frac{\varphi-\alpha}{2} - I_3 \sin \frac{\vartheta}{2} \sin \frac{\varphi+\alpha}{2} , \\ P_\varphi &= -\sin \frac{\vartheta}{2} \sin \frac{\varphi+\alpha}{2} - I_1 \cos \frac{\vartheta}{2} \cos \frac{\varphi-\alpha}{2} - I_2 \cos \frac{\vartheta}{2} \sin \frac{\varphi-\alpha}{2} + I_3 \sin \frac{\vartheta}{2} \cos \frac{\varphi+\alpha}{2} , \\ P_\alpha &= -\cos \frac{\vartheta}{2} \sin \frac{\varphi+\alpha}{2} + I_1 \sin \frac{\vartheta}{2} \cos \frac{\varphi-\alpha}{2} + I_2 \sin \frac{\vartheta}{2} \sin \frac{\varphi-\alpha}{2} + I_3 \cos \frac{\vartheta}{2} \cos \frac{\varphi+\alpha}{2} . \end{aligned} \quad (4.92)$$

These formulae prescribe a basis of the spinor space uniquely up to the choice of α if $\vartheta \neq 0, \pi$. At the poles, the angle φ is undefined. Because in this case (4.87) gives a pair of orthonormal tangent vectors for any choice of φ , (4.92) can be used with arbitrary φ .

The basis $P_s, P_\vartheta, P_\varphi, P_\alpha$ of KS momentum space can be supplemented by position spinors $U_j = P_j^\dagger$ to obtain the basis of a canonical coordinate system in spinor space. By construction, this basis set is appropriate for orbits starting at the nucleus. However, as it is derived from the description (4.74) of a radial Coulomb orbit, the same basis set is obtained if the construction is carried out at a finite matching radius r_0 in the Coulomb region.

The spinor basis thus obtained can now be used to calculate the stability determinant

$$M' = \det \frac{\partial(p_{\vartheta_f}, p_{\varphi_f})}{\partial(\vartheta_i, \varphi_i)} \quad (4.93)$$

occurring in the crossed-fields semiclassical Green's function (2.32). For a trajectory returning to the nucleus at time $\tau = 0$ with a final KS momentum P_f , the solution (4.74) of the Kepler equation of motion takes the form

$$\begin{aligned} U(\tau) &= \frac{P_f^\dagger}{\sqrt{-2E}} \sin(\sqrt{-2E} \tau) = -\sqrt{\frac{r}{2}} P_f^\dagger , \\ P(\tau) &= P_f \cos(\sqrt{-2E} \tau) = \sqrt{1 + Er} P_f , \end{aligned} \quad (4.94)$$

which is valid within the Coulomb region. The derivative of U and P with respect to an arbitrary parameter ω_1 reads, in complete analogy with (2.60),

$$\begin{aligned} \frac{\partial U}{\partial \omega_1} &= -\sqrt{\frac{r}{2}} \left(\frac{\partial P_f}{\partial \omega_1} \right)^\dagger + \sqrt{1 + Er} \frac{\partial U_f}{\partial \omega_1} , \\ \frac{\partial P}{\partial \omega_1} &= \sqrt{1 + Er} \frac{\partial P_f}{\partial \omega_1} - \sqrt{2rE} \left(\frac{\partial U_f}{\partial \omega_1} \right)^\dagger . \end{aligned} \quad (4.95)$$

The constants $\partial U_f/\partial\omega_1$ and $\partial P_f/\partial\omega_1$ are the values of the derivatives obtained at $r = 0$.

According to (4.67), the angular momentum component in a plane specified by a bivector B is

$$L_B = L * B = \frac{1}{2} \langle BUP \rangle . \quad (4.96)$$

The derivative of L_B with respect to a parameter ω_1 can then be calculated with the help of (4.95). It is given by

$$\frac{\partial L_B}{\partial\omega_1} = \frac{1}{2} \left\langle P_f B \frac{\partial U_f}{\partial\omega_1} \right\rangle . \quad (4.97)$$

As anticipated, it does not depend on r due to angular-momentum conservation.

For the angular momentum component p_{ω_2} conjugate to an angular coordinate ω_2 , the relevant bivector is

$$B = \mathbf{s} \frac{\partial \mathbf{s}}{\partial\omega_2} , \quad (4.98)$$

so that

$$\frac{\partial p_{\omega_2}}{\partial\omega_1} = \frac{1}{2} \left\langle P_f \mathbf{s} \frac{\partial \mathbf{s}}{\partial\omega_2} \frac{\partial U_f}{\partial\omega_1} \right\rangle = \left\langle P_{\omega_2} \frac{\partial U_f}{\partial\omega_1} \right\rangle , \quad (4.99)$$

where P_{ω_2} denotes the basis spinor corresponding to ω_2 by (4.83) with the final momentum P_f used in place of P_0 .

I introduce coordinates ϑ and $\bar{\varphi}$, such that $\partial \mathbf{s}/\partial\vartheta = \mathbf{s}_\vartheta$ and $\partial \mathbf{s}/\partial\bar{\varphi} = \mathbf{s}_\varphi$ are unit vectors given by (4.87). The stability determinant M' can then be rewritten as

$$\det \frac{\partial(p_{\vartheta_f}, p_{\varphi_f})}{\partial(\vartheta_i, \varphi_i)} = \det \begin{pmatrix} \frac{\partial p_{\bar{\varphi}_f}}{\partial\vartheta_i} & \sin\vartheta_i \frac{\partial p_{\bar{\varphi}_f}}{\partial\bar{\varphi}_i} \\ \sin\vartheta_f \frac{\partial p_{\bar{\varphi}_f}}{\partial\bar{\vartheta}_i} & \sin\vartheta_i \sin\vartheta_f \frac{\partial p_{\bar{\varphi}_f}}{\partial\bar{\varphi}_i} \end{pmatrix} = \sin\vartheta_i \sin\vartheta_f M \quad (4.100)$$

with a 2×2 -determinant

$$M = \det \begin{pmatrix} \left\langle P_\vartheta \frac{\partial U_f}{\partial\bar{\vartheta}_i} \right\rangle & \left\langle P_\vartheta \frac{\partial U_f}{\partial\bar{\varphi}_i} \right\rangle \\ \left\langle P_\varphi \frac{\partial U_f}{\partial\bar{\vartheta}_i} \right\rangle & \left\langle P_\varphi \frac{\partial U_f}{\partial\bar{\varphi}_i} \right\rangle \end{pmatrix} \quad (4.101)$$

free of any coordinate-induced singularities. In this form, the stability determinant was incorporated into (2.34).

A special case arises in rotationally symmetric systems. Due to the conservation of angular momentum, a trajectory in these systems is confined to a two-dimensional surface in space which contains the symmetry axis. The returning direction of a closed orbit must therefore be contained in the plane spanned by the initial direction and the symmetry axis. The stability of such an orbit is characterized by a single monodromy matrix element $m_{12} = \left\langle P_\vartheta \frac{\partial U_f}{\partial\bar{\vartheta}_i} \right\rangle$, which describes a variation of the initial direction in the plane. The orbit is neutrally stable with respect to variations perpendicular to the plane.

If the orbit is directed along the symmetry axis, any two directions perpendicular to it are equivalent. As a consequence, the matrix in (4.101) is diagonal, and the diagonal elements are equal. Thus, $M = m_{12}^2$. This relation has already been used in (2.66).

The derivatives $\partial U_f / \partial \omega$ needed in (4.101) are evaluated at the position of the nucleus, so that, as desired, they do not depend on the matching radius. They can be calculated numerically by integrating the linearized equations of motion

$$\begin{aligned} \frac{d}{d\tau} \frac{\partial U}{\partial \omega} &= \left(\frac{\partial U}{\partial \omega} * \partial_U \right) \partial_P \mathcal{H} + \left(\frac{\partial P}{\partial \omega} * \partial_P \right) \partial_P \mathcal{H}, \\ \frac{d}{d\tau} \frac{\partial P}{\partial \omega} &= - \left(\frac{\partial U}{\partial \omega} * \partial_U \right) \partial_U \mathcal{H} - \left(\frac{\partial P}{\partial \omega} * \partial_P \right) \partial_U \mathcal{H} \end{aligned} \quad (4.102)$$

along the closed orbit with initial conditions

$$\frac{\partial U}{\partial \omega}(0) = 0, \quad \frac{\partial P}{\partial \omega}(0) = P_\omega. \quad (4.103)$$

Chapter 5

Closed orbits in crossed fields

The crucial pre-requisite for any semiclassical quantization is a sufficiently detailed understanding of the underlying classical dynamics. In particular, a quantization based on closed-orbit theory requires the knowledge of all closed orbits up to a certain maximum length. As all atomic systems in external fields, with the sole exception of the hydrogen atom in an electric field, are classically non-integrable, closed orbits must in general be computed numerically. Nevertheless, it is desirable to obtain a qualitative overview over the set of orbits, because on the one hand the classification itself plays an important role in the interpretation of structures observed in quantum spectra and, on the other, it provides a means to verify the completeness of a numerically computed list of orbits.

For the hydrogen atom in a magnetic field, the systematics of closed orbits and their bifurcations is known [7, 75–79]. For the hydrogen atom in crossed electric and magnetic fields, the classical mechanics is much more complicated because three non-separable degrees of freedom have to be dealt with. Although a number of closed orbits have been identified in experimental or theoretical quantum spectra [7–11], a systematic study of these orbits and their bifurcations is still lacking.

Considerable effort has been spent during the past decade on the study of the classical mechanics of the crossed-fields hydrogen atom in the limit of weak external fields [80–87]. This work relies on the observation that for weak external fields the principal quantum number n or its classical analogue $n = 1/\sqrt{-2E}$ is conserved to a higher degree of precision than the angular-momentum and Lenz vectors \mathbf{L} and \mathbf{A} . The latter are conserved in the pure Kepler problem, but acquire a slow time-dependence in weak fields, so that the electron can be visualized as moving on a slowly precessing Kepler ellipse.

The most important result in the present context is the observation first described in [81] that there are four Kepler ellipses that are unperturbed by the external fields to first order in the field strength, i.e. among the continuous infinity of periodic orbits of the unperturbed Kepler problem, there are four orbits that remain periodic in the presence of external fields. These fundamental periodic orbits can be regarded as the roots of “family trees” of periodic orbits. More complicated orbits are created out of the fundamental orbits by bifurcations as

the field strengths increase.

However, none of the fundamental periodic orbits is closed at the nucleus. Their knowledge therefore does not aid in the classification of closed orbits. A study of closed orbits in the crossed-fields system and their bifurcations was performed by Wang and Delos [88]. These authors present orderly sequences of bifurcations of planar closed orbits (i.e. orbits in the plane perpendicular to the magnetic field), which they interpret in terms of an integrable model Hamiltonian.

In the present chapter I undertake a systematic study of closed orbits in the crossed-fields system. As the key to a classification of closed orbits is an understanding of their bifurcations, section 5.1 will present the general framework of a local bifurcation theory of closed orbits, and section 5.2 will describe the generic codimension-one bifurcations. The following sections will then describe the bifurcation scenarios actually observed in the crossed-fields system, taking the well-known closed orbits of the hydrogen atom in a magnetic field as a starting point. Although the present analysis cannot yet claim to have achieved a complete classification of closed orbits, it does give a detailed impression of how orbits bifurcate as the electric field strength increases. It thus introduces a high degree of order into the complex set of closed orbits.

5.1 General bifurcation theory

As described in section 2.1, the dynamics of the hydrogen atom in a single external field possesses a time-reversal invariance that makes the electron retrace its own path after an encounter with the nucleus. Therefore, any closed orbit is either itself periodic or it is one half of a periodic orbit. This symmetry has a profound influence on the bifurcation theory of closed orbits. As closed orbits possess repetitions in pure fields, arbitrary m -tupling bifurcations are possible. Due to the close link between closed orbits and periodic orbits, closed-orbit bifurcations can be described in the framework of periodic-orbit bifurcation theory developed by Mayer [12, 79].

In the presence of non-parallel electric and magnetic fields, the time-reversal invariance is broken, and no general connection between closed orbits and periodic orbits remains. As a consequence, the techniques of periodic-orbit bifurcation theory are no longer applicable, and a novel approach to the classification of closed-orbit bifurcations must be found. In this section, a general framework for the discussion of closed-orbit bifurcations will be introduced.

The crucial step in the development of the bifurcation theory of periodic orbits is the introduction of a Poincaré surface of section map in the neighbourhood of the orbit. The Poincaré map describes the dynamics of the degrees of freedom transverse to the orbit, and the orbit bifurcates when the transverse dynamics becomes resonant with the motion along the orbit.

For periodic orbits, a Poincaré map is specified by fixing a surface of section in phase space which is transverse to the orbit. For a point P on the surface of section, the trajectory starting at P is followed until it intersects the surface of

type	transformation	non-singular matrix
$F_1(q_i, q_f)$	$p_i = +\partial F_1/\partial q_i$ $p_f = -\partial F_1/\partial q_f$	B
$F_2(q_i, p_f)$	$p_i = +\partial F_2/\partial q_i$ $q_f = +\partial F_2/\partial p_f$	D
$F_3(p_i, q_f)$	$q_i = -\partial F_3/\partial p_i$ $p_f = -\partial F_3/\partial q_f$	A
$F_4(p_i, p_f)$	$q_i = -\partial F_4/\partial p_i$ $q_f = +\partial F_4/\partial p_f$	C

Table 5.1: Overview of generating functions of different types (cf. [89]).

section again. This intersection point is defined to be the image of P under the Poincaré map. The periodic orbit itself returns to its starting point, so that it appears as a fixed point of the Poincaré map.

This prescription is not directly applicable to closed orbits because they do not return to their starting point in phase space. Therefore, a trajectory starting on the surface of section will not in general intersect the surface again. To arrive at a meaningful definition of a Poincaré map, one must use two surfaces of section: the first transverse to the initial direction of the orbit, the second transverse to its final direction. A trajectory starting in the neighbourhood of the closed orbit on the initial surface of section Σ_i will then have an intersection with the final section Σ_f , so that a Poincaré map is well defined. As in the case of a periodic orbit, the Poincaré map is symplectic.

Unlike with periodic orbits, the notion of a closed orbit is not invariant under canonical transformations. The distinction between position space and momentum space must therefore be kept. Let (q_i, p_i) and (q_f, p_f) be canonical coordinates on the surfaces Σ_i and Σ_f chosen so that q_i and q_f are position space coordinates in the directions perpendicular to the initial or final directions of the orbit. The origins of the coordinate systems are fixed so that the position of the nucleus is $q_i = 0$ or $q_f = 0$, respectively. Closed orbits are then characterized by $q_i = q_f = 0$. In crossed fields three spatial dimensions must be dealt with, so that each of q_i, p_i, q_f, p_f is a two-dimensional vector.

A closed orbit can start in Σ_i with arbitrary initial momentum p_i , but it must start in the plane $q_i = 0$. The Poincaré map maps this plane into a Lagrangian manifold in Σ_f . Closed orbits are given by the intersections of this manifold with the plane $q_f = 0$. In a less geometrical way of speaking, closed orbits can be described as solutions of the equation $q_f(p_i, q_i = 0) = 0$. A particular solution of this equation, corresponding to the orbit the construction started with, is given by $q_f(p_i = 0) = 0$. If the matrix $B = \partial q_f/\partial p_i$ is non-singular at $p_i = 0$, this solution is locally unique by the implicit function theorem. Thus, the closed orbit cannot undergo a bifurcation unless $\det B = 0$. This result was to be expected in view of the semiclassical amplitude (2.43), because if the coordinates q_i are chosen orthonormal, $M = \det B$ is the stability determinant (4.101), and a bifurcation of closed orbits is known to lead to a divergence of the pertinent semiclassical amplitudes. It has now been obtained within classical mechanics, as is appropriate for a purely classical result, which should be independent of any semiclassical theory.

An overview of the bifurcation scenarios to be expected when $\det B = 0$ can

be obtained from a description of the possible modes of behaviour of the Poincaré map. This can most conveniently be achieved if the Poincaré map is represented by a generating function [89,90]. The generating function can be chosen to depend on any combination of initial and final positions and momenta, as long as they form a complete set of independent coordinates. I will adopt the well-known conventions of Goldstein [89] for denoting different types of generating functions, which are summarized in table 5.1.

For a generic symplectic map, all possible sets of coordinates and momenta are independent, so that generating functions of any type exist. At a closed-orbit bifurcation, however, a degeneracy indicated by the condition that $B = \partial q_f / \partial p_i$ be singular arises, so that care must be taken in choosing a generating function. Loosely speaking, if B is singular, p_i cannot be determined from q_i and q_f , so that it may be conjectured that no generating function of type F_1 exists. To confirm this conjecture, I study a linear symplectic map

$$q_f = Aq_i + Bp_i, \quad p_f = Cq_i + Dp_i \quad (5.1)$$

with four matrices A, B, C, D satisfying the symplecticity conditions [90]

$$\begin{aligned} A^\top C &= C^\top A, & B^\top D &= D^\top B, & A^\top D - C^\top B &= 1, \\ AB^\top &= BA^\top, & CD^\top &= DC^\top, & AD^\top - BC^\top &= 1, \end{aligned} \quad (5.2)$$

where $^\top$ denotes the transpose. A generating function for the linear map (5.1) must be quadratic in its variables. From the ansatz

$$F_1(q_i, q_f) = \frac{1}{2}q_f^\top Rq_f + q_f^\top Sq_i + \frac{1}{2}q_i^\top Tq_i \quad (5.3)$$

with matrices R, S, T , the map (5.1) is obtained if

$$R = -DB^{-1}, \quad S = B^{-1\top} = DB^{-1}A - C, \quad T = -B^{-1\top}A. \quad (5.4)$$

The two expressions given for S are equal by virtue of (5.2). As expected, a generating function of type F_1 does not exist if B is singular. A similar calculation can be made for the other types of generating functions. For each type, one of the matrices A, B, C, D must be non-singular. These results are given in table 5.1. Locally, they can be extended to non-linear maps by means of the implicit function theorem.

I have thus shown that at a bifurcation of closed orbits the Poincaré map possesses generating functions of all types except F_1 . The most convenient choice is a function of type $F_4(p_i, p_f)$. The transformation equations associated with this type of generating function read

$$q_i = -\frac{\partial F_4}{\partial p_i}, \quad q_f = +\frac{\partial F_4}{\partial p_f}. \quad (5.5)$$

Closed orbits are characterized by $q_i = q_f = 0$. They agree with the stationary points of the F_4 function. The classification problem of closed-orbit bifurcation

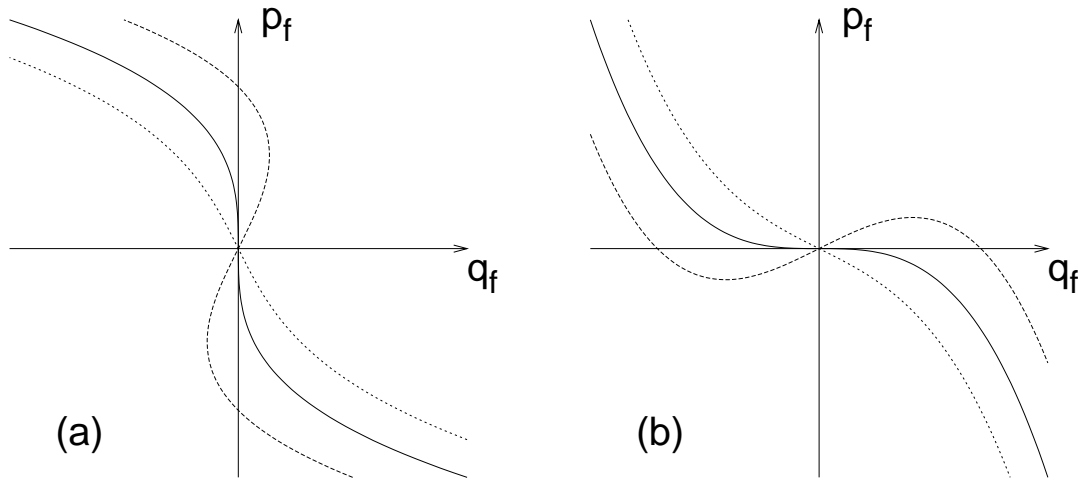


Figure 5.1: Schematic plot of the Lagrangian manifold $q_i = 0$ in Σ_f for the case (a) $B = \partial q_f / \partial p_i = 0$ and (b) $D = \partial p_f / \partial p_i = 0$. The dashed lines indicate the position of the manifold at slightly varied parameter values. Only in case (a) additional intersections with the plane $q_f = 0$ can arise.

theory can thus be rephrased as the problem to determine how stationary points of a real function change upon the variation of parameters. This question is the subject of catastrophe theory [91–93].

Catastrophe theory studies smooth real-valued functions $f(\mathbf{x})$ and $\tilde{f}(\mathbf{x})$ defined in a neighbourhood of the origin in an n -dimensional configuration space. They are said to be equivalent if there is a diffeomorphism $\psi(\mathbf{x})$ of the configuration space so that

$$\tilde{f}(\mathbf{x}) = f(\psi(\mathbf{x})). \quad (5.6)$$

The coordinate transformation ψ maps the stationary points of \tilde{f} to those of f . In this sense, the distributions of stationary points of f and \tilde{f} agree qualitatively. Without loss of generality it can be assumed that f and \tilde{f} have stationary points at the origin, because any stationary point can be moved there by a coordinate transformation. After adding a constant, one has $f(0) = 0$.

f is said to be structurally stable if any small perturbation \tilde{f} of f (i.e. $\tilde{f}(\mathbf{x}) = f(\mathbf{x}) + \epsilon g(\mathbf{x})$ with a smooth function $g(\mathbf{x})$ and sufficiently small ϵ) is equivalent to f . Notice that catastrophe theory is a purely local theory. It is concerned with the structural stability or instability of a single stationary point and the pattern of stationary points that can be generated from a structurally unstable stationary point by a small perturbation.

In the present context, non-bifurcating closed orbits correspond to structurally stable stationary points of F_4 , because a small variation of parameters will bring about a variation of F_4 which is small in the above sense and preserves the stationary point. The most elementary result of catastrophe theory states that a stationary point of a function f is structurally stable if its Hessian matrix, i.e.

the matrix of second derivatives of f , is non-singular. For the linear symplectic transformation (5.1), the F_4 generating function is

$$F_4 = \frac{1}{2}p_f^\top AC^{-1}p_f - p_f^\top C^{-1\top}p_i + \frac{1}{2}p_i^\top C^{-1}Dp_i, \quad (5.7)$$

so that its Hessian determinant at $p_i = p_f = 0$ can be found to be

$$\det \text{Hess } F_4 = \frac{\det B \det D}{\det C}. \quad (5.8)$$

The Hessian matrix of F_4 is thus singular if either $B = \partial q_f / \partial p_i$ or $D = \partial p_f / \partial p_i$ is. It has been shown above that bifurcations of closed orbits can only occur if $\det B = 0$, i.e. a bifurcating orbit corresponds to a degenerate stationary point of F_4 . The case $\det D = 0$ also leads to a degeneracy of F_4 , but it cannot be associated with a closed-orbit bifurcation. This can also be understood geometrically: As illustrated in figure 5.1, if $\det B = 0$, the Lagrangian manifold given by $q_i = 0$ is tangent to the plane $q_f = 0$, so that it can develop further intersections with that plane upon a small variation of parameters. If $\det D = 0$, the manifold is tangent to the plane $p_f = 0$, whence, upon a variation of parameters, it can acquire additional intersections with that plane, but not with the plane $q_f = 0$, so that no bifurcation of closed orbits can arise.

The discussion of stationary points with degenerate Hessian matrices, also called ‘‘catastrophes’’, is simplified considerably by the splitting lemma of catastrophe theory [93]. It states that if the dimension of the configuration space is n and a function f on the configuration space has a stationary point at the origin whose Hessian matrix has rank $n - m$, a coordinate system x_1, \dots, x_n can be introduced in a neighbourhood of the stationary point so that

$$f(x_1, \dots, x_n) = g(x_1, \dots, x_m) + q(x_{m+1}, \dots, x_n), \quad (5.9)$$

where q is a non-degenerate quadratic form of $n - m$ variables and the function g has a stationary point with zero Hessian matrix at the origin. As the non-degenerate stationary point of q is structurally stable, the behaviour of the stationary points of f under a small perturbation is determined by g only. The number of relevant variables is thus only m , which is called the corank of the catastrophe. It will be assumed henceforth that a splitting according to (5.9) has been carried out and the non-degenerate part q is ignored, so that the Hessian matrix of f vanishes at the origin.

Under a small perturbation of the function f , a degenerate stationary point will in general split into several distinct stationary points. This process will be used to model bifurcations of closed orbits. The degenerate stationary points relevant to bifurcation theory are those of finite codimension, i.e. those for which there are smooth functions $g_1(\mathbf{x}), \dots, g_k(\mathbf{x})$ so that any small perturbation of f is equivalent to

$$F(\mathbf{x}) = f(\mathbf{x}) + \alpha_1 g_1(\mathbf{x}) + \dots + \alpha_k g_k(\mathbf{x}) \quad (5.10)$$

with suitably chosen constants α_i . The function $F(\mathbf{x})$ is called an unfolding of $f(\mathbf{x})$, because the degenerate stationary point of f can be regarded as a set of

several stationary points that accidentally coincide and are “unfolded” by the parameters α_i . The smallest value of k that can be chosen in (5.10) is called the codimension of f . An unfolding of f with k equal to the codimension of f is referred to as universal.

In the bifurcation problem, the generating function F_4 depends on external control parameters ρ_1, \dots, ρ_l such as, e.g., the energy E or the external field strengths. If, for a critical value of the parameters, F_4 has a degenerate stationary point equivalent to that of f , in a neighbourhood of the critical value F_4 is equivalent to the unfolding (5.10), where the unfolding parameters α_i are smooth functions of the control parameters ρ_j . The critical parameter values themselves are characterized by the condition that all unfolding parameters vanish, i.e. by the set of equations

$$\begin{aligned} \alpha_1(\rho_1, \dots, \rho_l) &= 0, \\ &\dots \\ \alpha_k(\rho_1, \dots, \rho_l) &= 0. \end{aligned} \tag{5.11}$$

These are k equations in l unknowns. They can “generically” only be expected to possess a solution if $k \leq l$, that is, the codimension of the degenerate stationary point must not be larger than the number of external parameters. This construction introduces a notion of codimension for bifurcations of closed orbits which is entirely analogous to the codimension of bifurcations of periodic orbits: Bifurcations of a codimension higher than the number of external parameters cannot be expected to exist because they are structurally unstable. Under a small perturbation of the system they would split into a sequence of “generic” bifurcations of lower codimensions.

5.2 Codimension-one generic bifurcations

The considerations of the preceding section reduce the bifurcation theory for closed orbits to the problem of determining all catastrophes having a codimension smaller than the number of external parameters. In particular, it explains why only catastrophes of finite codimension are relevant. In the crossed-fields system, the number of parameters is two, if the scaling properties are taken into account. However, I will only describe bifurcations of codimension one in the following. They suffice to describe the bifurcations encountered if a single parameter is varied while the second is kept fixed. They also give a good impression of the codimension-two scenarios because a bifurcation of codimension two must split into a sequence of codimension-one bifurcations as soon as any of the parameters is changed.

For generic functions without special symmetries, a list of catastrophes of codimensions up to six with their universal unfoldings is readily available in the literature [91–93]. The classification of closed-orbit bifurcations presented here relies on these results.

5.2.1 The tangent bifurcation

There is a single catastrophe of codimension one, which has corank one and is known as the fold catastrophe. Its universal unfolding is given by

$$\Phi_a(t) = \frac{1}{3}t^3 - at, \quad (5.12)$$

with a denoting the unfolding parameter. The fold has two stationary points at

$$t = \pm\sqrt{a}, \quad (5.13)$$

where it assumes the stationary values

$$\Phi_a(\pm\sqrt{a}) = \mp\frac{2}{3}a^{3/2}. \quad (5.14)$$

The second derivative in the stationary points is

$$\Phi_a''(\pm\sqrt{a}) = \pm 2\sqrt{a}. \quad (5.15)$$

The stationary points are real if $a > 0$. If $a < 0$, there are no stationary points on the real axis, because the solutions (5.13) are imaginary. These complex stationary points correspond to closed “ghost” orbits in the complexified phase space. Ghost orbits can be thought of as preceding real orbits generated in a bifurcation. Semiclassically, they play a crucial role both in periodic-orbit and closed-orbit theories [94–96]. As a is varied, a tangent bifurcation occurs at $a = 0$, where two complex conjugate ghost orbits turn into two real orbits or vice versa.

All qualitative features of the bifurcation are described by the normal form (5.12). The stationary points, i.e. the closed orbits, initially move apart as \sqrt{a} . As will become clear in the discussion of uniform approximations in section 6.5, the difference between the stationary values gives the action difference between the closed orbits, whereas the second derivatives – or, more generally, the Hessian determinants – at the stationary points are proportional to the stability determinant M . All these quantities are shown in figure 5.2. When they are compared to the corresponding quantities calculated for an actual bifurcation in section 5.4, the qualitative agreement will become clear.

The fold catastrophe (5.12) describes the generation of two closed orbits in a tangent bifurcation. As this is the only generic catastrophe of codimension one, it follows that the tangent bifurcation is the only possible type of closed-orbit bifurcations. In particular, once it has been generated a closed orbit cannot split into several orbits, as periodic orbits typically do. However, this statement needs some modification due to the presence of reflection symmetries in the crossed-fields system.

5.2.2 The pitchfork bifurcation

If the orbit under study is symmetric under one of the reflections, i.e. it is a singlet or a doublet orbit, the generating function F_4 in the neighbourhood of this orbit

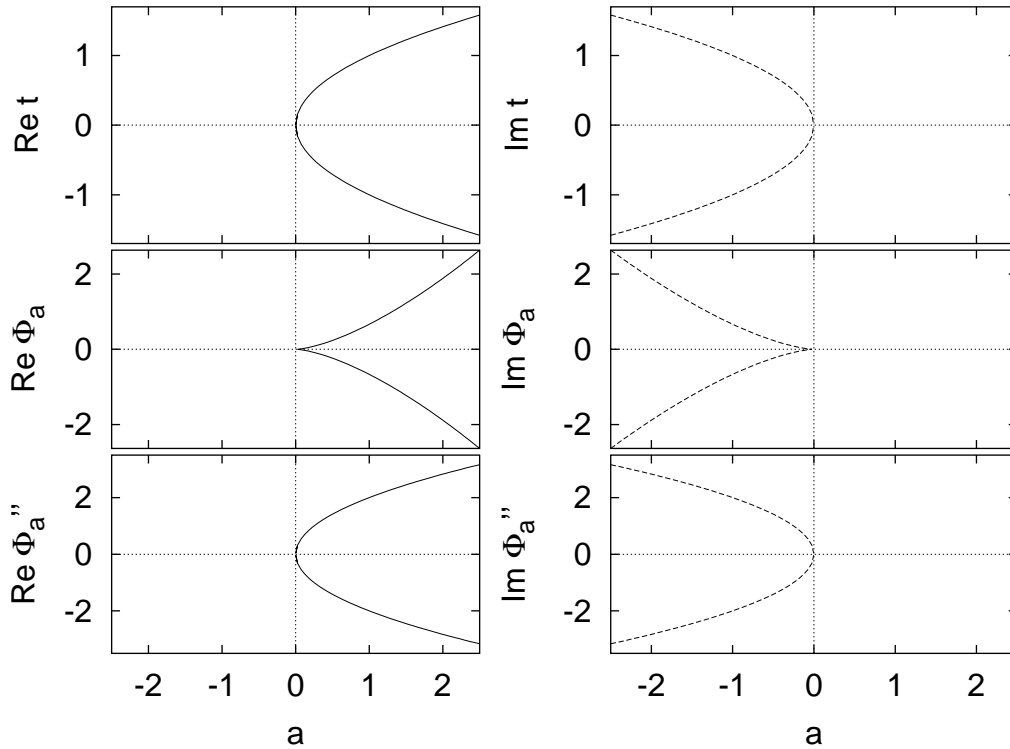


Figure 5.2: The positions of stationary points, stationary values and second derivatives in the fold catastrophe. Solid lines indicate real stationary points, dashed lines complex stationary points. Dotted lines are coordinate axes.

must also possess this reflection symmetry. By this constraint, several of the elementary catastrophes are excluded altogether. For others, the codimension is reduced because the unfolding can only contain symmetric terms.

One additional catastrophe of codimension one arises, viz. the symmetrized version of the cusp catastrophe

$$\Phi_a(t) = \frac{1}{4}t^4 - \frac{1}{2}at^2. \quad (5.16)$$

This normal form possesses the reflection symmetry $t \mapsto -t$, so that the origin is mapped onto itself under the symmetry transformation. There is a stationary point at the origin for all values of the parameter a , corresponding to a closed orbit which is invariant under the reflection. Additional stationary points are located at

$$t = \pm\sqrt{a}. \quad (5.17)$$

They are real if $a > 0$ and are mapped onto each other under a reflection. Thus, the symmetric cusp (5.16) describes a pitchfork bifurcation at $a = 0$, where two asymmetric orbits bifurcate off a symmetric orbit, generating a quartet from a doublet or a doublet from a singlet.

The stationary values at the asymmetric stationary points are given by

$$\Phi_a(\pm\sqrt{a}) = -\frac{1}{4}a^2, \quad (5.18)$$

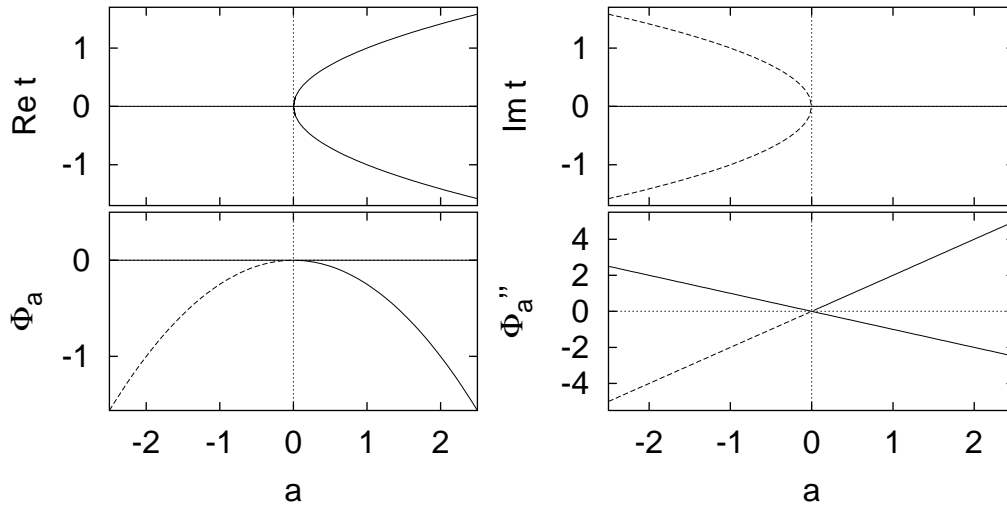


Figure 5.3: The positions of stationary points, stationary values and second derivatives in the cusp catastrophe. Solid lines indicate real stationary points, dashed lines complex stationary points. Dotted lines are coordinate axes. Note that stationary values and second derivatives are real even for complex stationary points.

the second derivative is

$$\Phi_a''(\pm\sqrt{a}) = 2a . \quad (5.19)$$

Both the stationary values and the values of the second derivative are real even for $a < 0$, when the stationary points themselves are complex. Therefore, these stationary points correspond to ghost orbits having real actions and stability determinants. The existence of this remarkable type of ghost orbits is again a consequence of the reflection symmetry: As the stationary points (5.17) are imaginary, the reflection $t \mapsto -t$ changes a stationary point and its stationary value into their complex conjugates. On the other hand, the stationary values are invariant under the reflection, so they must be real. A ghost orbit having this symmetry property will be referred to as a symmetric ghost orbit.

The characteristic quantities of the symmetric cusp catastrophe are shown in figure 5.3 as a function of a . Again, they describe the qualitative behaviour of the bifurcating orbits close to the bifurcation. It should be noted that the stationary values (5.18) are negative for all values of a , so that for a bifurcation described by (5.16), the actions of the asymmetric orbits must be smaller than those of the symmetric orbit. An alternative bifurcation scenario is described by the dual cusp, viz. the negative of (5.16). The dual cusp is inequivalent to the regular cusp, but the scenario it describes agrees with the above except that the stationary values and the second derivatives change their signs, so that the actions of the asymmetric orbits are now larger than that of the symmetric orbit.

5.3 Closed orbits in the diamagnetic Kepler problem

As a basis for the description of closed orbits in the crossed-fields hydrogen atom, I will choose the closed orbits in the diamagnetic Kepler problem (DKP), i.e. in the hydrogen atom in a pure magnetic field. For these orbits a complete classification is available [7, 75–79]. It will now be recapitulated briefly. As usual, the classical quantities will be scaled with respect to the magnetic field strength B , and the classical dynamics will be described as a function of the scaled energy $\tilde{E} = EB^{-2/3}$.

For low scaled energies $\tilde{E} \rightarrow -\infty$, there are two fundamental closed orbits: In one case, the electron leaves the nucleus parallel to the magnetic field until the Coulomb attraction forces it back. This orbit is purely Coulombic because the electron does not feel a Lorentz force when moving parallel to the magnetic field. The second closed orbit lies in the plane perpendicular to the magnetic field. Its shape is determined by the combined influences of the Coulomb and magnetic fields.

Due to time-reversal invariance, both elementary orbits possess arbitrary repetitions. As the scaled energy increases, each repetition of an elementary orbit undergoes a sequence of bifurcations labelled by an integer $\nu = 1, 2, 3, \dots$ in order of increasing bifurcation energy. The orbits born in these bifurcations can be characterized by the repetition number μ of the bifurcating orbit and the bifurcation number ν . They are referred to [7] as vibrators V_μ^ν if they bifurcate out of the orbit parallel to the magnetic field and as rotators R_μ^ν if they bifurcate out of the orbit perpendicular to \mathbf{B} .

Further bifurcations create additional orbits from the V_μ^ν and R_μ^ν or “exotic” orbits not related to one of the two fundamental orbits. These orbits are of importance at scaled energies higher than those considered in this work, so that they will not be discussed further. For the scaled energy $\tilde{E} = -1.4$, the scaled actions and starting angles of the closed orbits are presented in figure 5.4. It can be seen that only orbits fitting into the classification scheme described above are present. Furthermore, orbits having a common bifurcation number ν lie on a smooth curve in the plot. For this reason, I will refer to orbits characterized by a fixed ν as a series of rotators or vibrators, respectively, and call ν the series number.

5.4 Closed orbit bifurcation scenarios

In the presence of a magnetic field only, the atomic system possesses a rotational symmetry around the field axis. As a consequence, all closed orbits except for the orbit parallel to the magnetic field occur in continuous one-parameter families. When a perpendicular electric field is added, the rotational symmetry is destroyed. Out of each family, only two orbits survive [97], or, in other words, each family of orbits splits into two independent orbits.

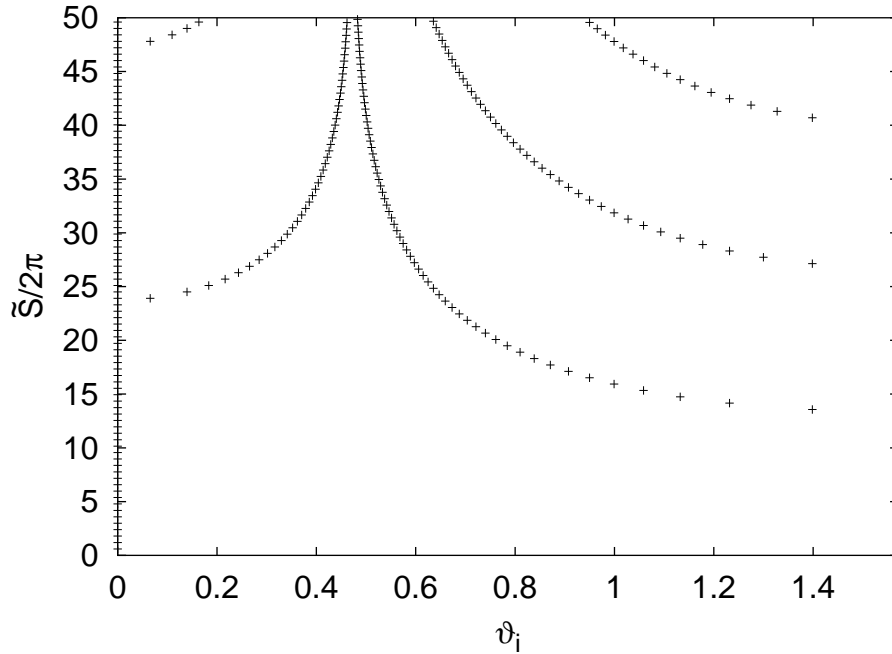


Figure 5.4: Actions \tilde{S} as functions of the starting angles ϑ_i of closed orbits in the DKP for $\tilde{E} = -1.4$.

In a pure magnetic field the starting direction of a family of orbits can be specified by giving the starting angle ϑ_i with respect to the field direction. In crossed fields, two angles are required. In addition to ϑ_i , measured to the magnetic field direction, the azimuthal angle φ_i between the electric field and the projection of the starting direction into the plane perpendicular to \mathbf{B} will be used.

5.4.1 Planar orbits

The splitting of a family of orbits upon the introduction of an electric field can most clearly be seen for planar orbits, i.e. for orbits lying in the plane perpendicular to the magnetic field. Due to the Z -symmetry, this plane is invariant under the dynamics. Thus, the initial direction of an orbit can be specified by means of the azimuthal angle φ_i only.

Figure 5.5 shows the actions and initial directions of the planar orbits for a scaled energy of $\tilde{E} = -1.4$ and scaled electric field strengths $\tilde{F} = 0.03$ and $\tilde{F} = 0.05$. At $\tilde{F} = 0$, the orbits bifurcate off a certain repetition of the planar closed orbit of the diamagnetic Kepler problem. For low \tilde{F} they can therefore be assigned a repetition number. It can clearly be discerned in figure 5.5 from the actions of the orbits.

As expected from the theory of the rotational symmetry breaking [97], there are two orbits for each repetition number, and they start in opposite directions from the nucleus. Moreover, the starting angle varies linearly with the repetition number. These findings are illustrated in figure 5.6, where for a few low repetition

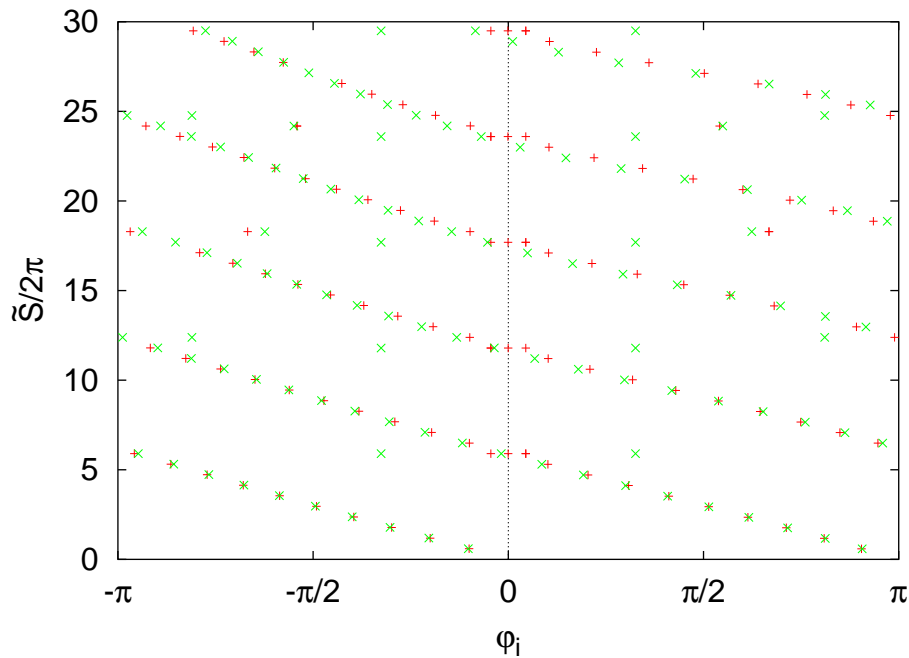


Figure 5.5: Actions \tilde{S} and azimuthal starting angles φ_i for planar orbits at $\tilde{E} = -1.4$ and $\tilde{F} = 0.03$ (+ symbols) and $\tilde{F} = 0.05$ (× symbols).

numbers one of the two orbits is shown. It can be seen that the orbits consist of more and more “loops” and that the starting angle increases regularly. The shapes are symmetric with respect to the x -axis, because the orbits are invariant under the Γ -transformation. In the terminology of section 2.1 these orbits are singlets.

A few orbits in figure 5.5 do not fit into this simple scheme. A closer inspection reveals that these orbits are not singlets, but Z -doublets, and indeed they obviously occur in pairs. They are generated by symmetry-breaking pitchfork bifurcations from singlet orbits. Figure 5.7 presents the orbital parameters for closed orbits involved in a bifurcation of this kind. The plots should be compared to figure 5.3, which displays the scenario described by the symmetric cusp catastrophe. The qualitative agreement between the catastrophe theory predictions and the numerical findings is evident.

The asymmetric orbits have the surprising property of having equal initial and final azimuthal angles $\varphi_i = \varphi_f$. According to table 2.3, this property does not correspond to any of the reflections symmetries of the Hamiltonian, so that it should not be expected to be generic. Numerically, however, it is found that the equality holds for all parameter values. The reason for this seemingly non-generic behaviour is that a closed orbit with equal initial and final directions is actually periodic. Upon a variation of the parameters a periodic closed orbit must not only persist as a closed orbit according to the results of section 5.1, it must also remain periodic unless it is destroyed in a periodic-orbit bifurcation. Together, these two requirements guarantee that the property of having equal initial and

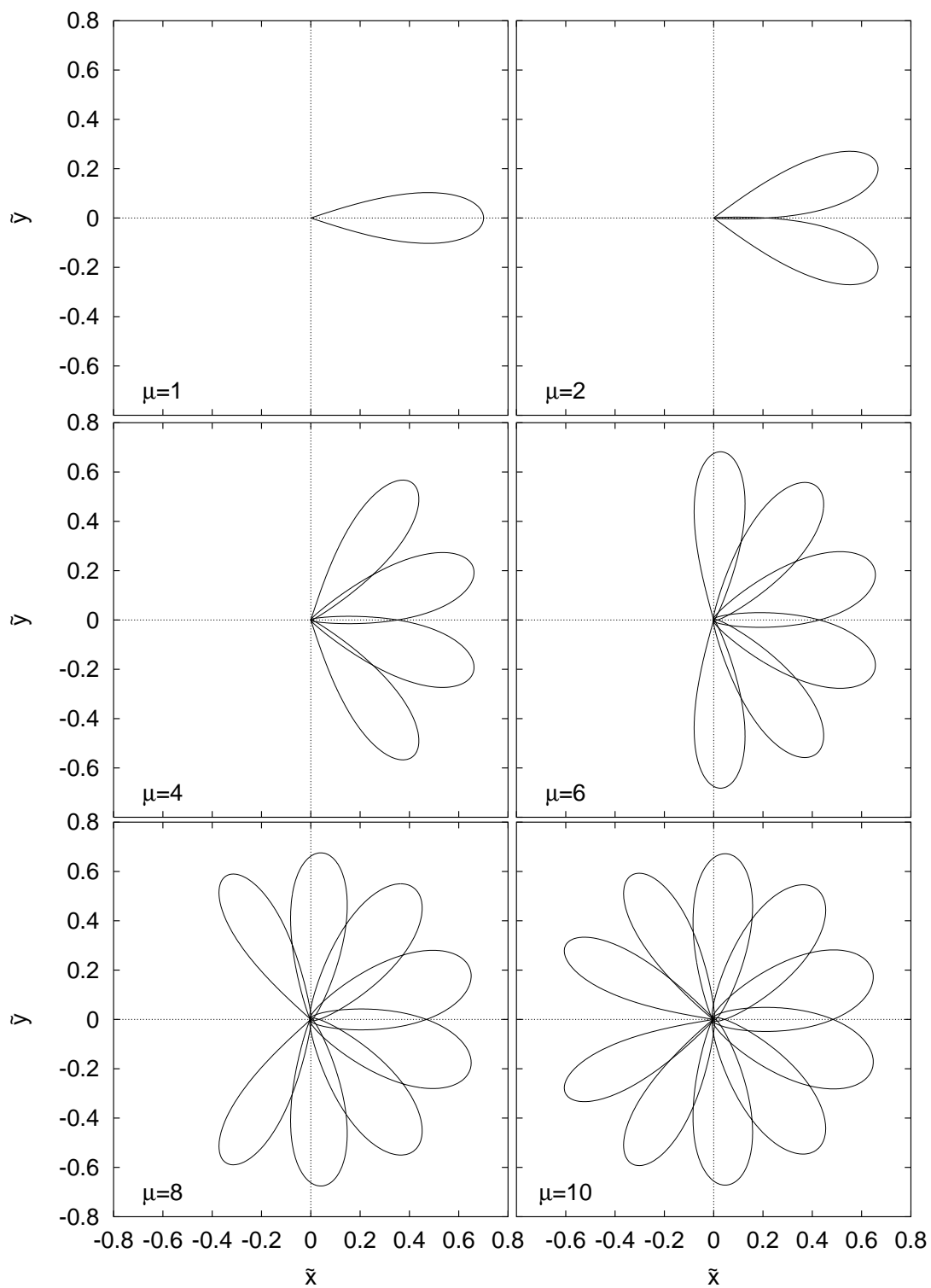


Figure 5.6: Elementary planar closed orbits at $\tilde{E} = -1.4$ and $\tilde{F} = 0.05$. μ is the repetition number. The orbits are symmetric with respect to the x -axis, in particular, $\varphi_i = -\varphi_f$.

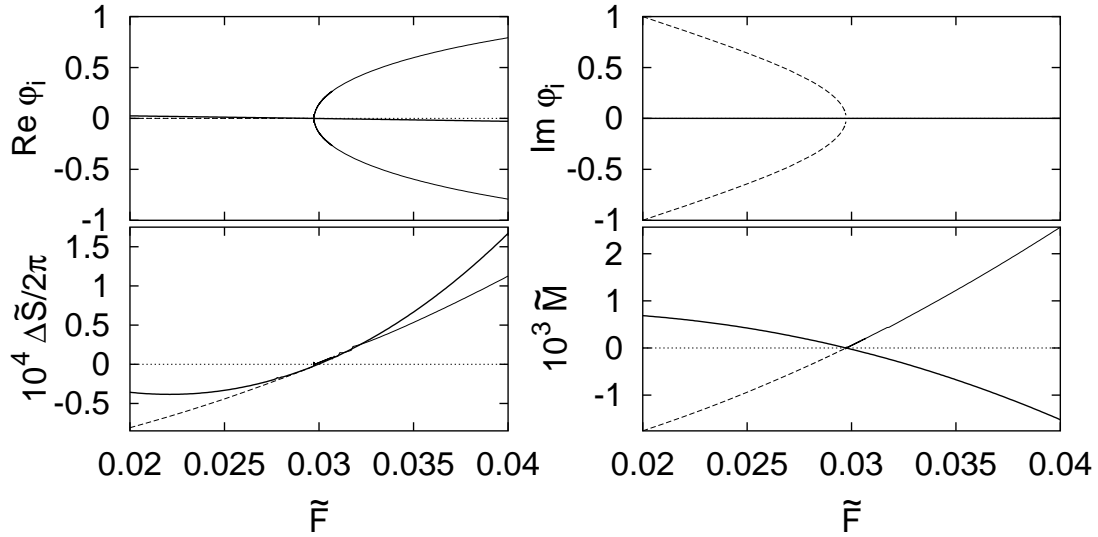


Figure 5.7: Orbital parameters close to a pitchfork bifurcation creating a Z-doublet of closed orbits from a singlet at $\tilde{E} = -1.4$, repetition number $\mu = 10$. φ_i is the azimuthal starting angle, \tilde{S} the scaled action and \tilde{M} the scaled stability determinant, $\Delta\tilde{S} = \tilde{S} - 2\pi \times 5.898159$ was introduced for graphical purposes. Thick solid lines: singlet orbit, thin solid lines: doublet orbits, dashed line: ghost orbits symmetric with respect to complex conjugation. Dotted lines indicate coordinate axes.

final directions is a stable property of a closed orbit.

The initial and final angles of the asymmetric orbits satisfy $\varphi_i^{(1)} = -\varphi_f^{(2)}$ because they are symmetry partners and $\varphi_i^{(2)} = \varphi_f^{(2)}$ because they are periodic. Thus, they must fulfil $\varphi_i^{(1)} = -\varphi_i^{(2)}$. At the bifurcation, the initial angles of the two orbits must coincide, so that a bifurcation can only take place when $\varphi_i = 0$ or $\varphi_i = \pi$, and it actually does take place every time one of these conditions is fulfilled. This process can be seen in figure 5.5, e.g., at $S/2\pi \approx 25$: At $\tilde{F} = 0.03$, the symmetric orbit has not yet crossed the line $\varphi_i = \pi$, so that no bifurcation has occurred. At $\tilde{F} = 0.05$, this line has been crossed and two asymmetric orbits have been created.

As the electric field strength is increased, the dependence of the starting angle on the repetition number ceases to be linear. Instead, the curves interpolating the functions $S(\varphi_i)$ start to develop humps, so that at certain values of S , i.e. at certain repetition numbers, more than two possible values of φ_i exist. This development is illustrated in figure 5.8. The humps indicate the occurrence of tangent bifurcations generating additional pairs of singlet orbits. This is the type of bifurcation described by the fold catastrophe (5.12). Orbital parameters for orbits involved in a bifurcation of this kind are shown in figure 5.9. As for the pitchfork bifurcation, a comparison of that figure to the catastrophe theory predictions in figure 5.2 reveals that the bifurcation is well described qualitatively by the fold catastrophe.

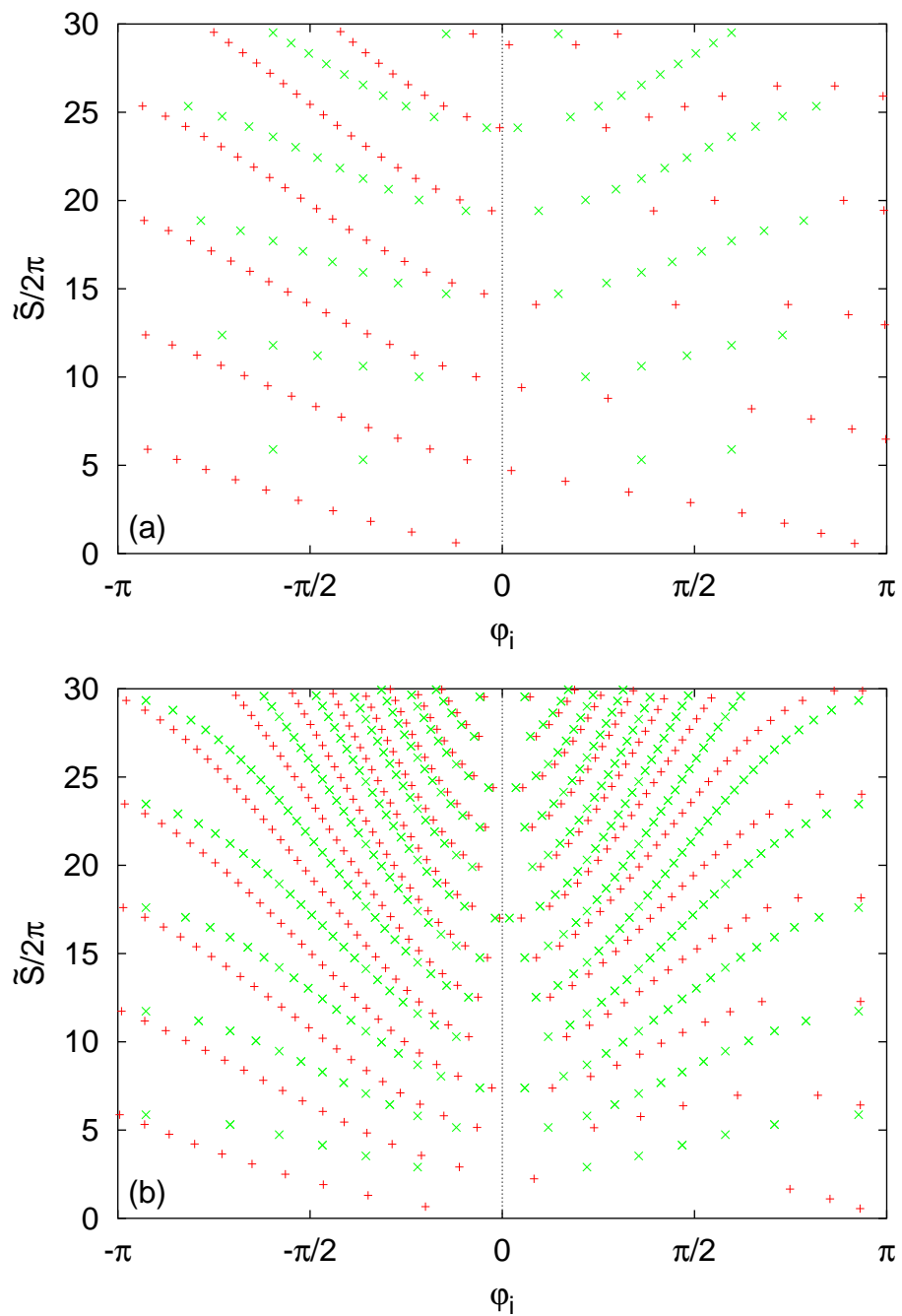


Figure 5.8: Actions and azimuthal starting angles for planar orbits at $\tilde{E} = -1.4$ and (a) $\tilde{F} = 0.2$, (b) $\tilde{F} = 0.5$. Singlets are indicated by + symbols, Z-doublets by \times symbols.

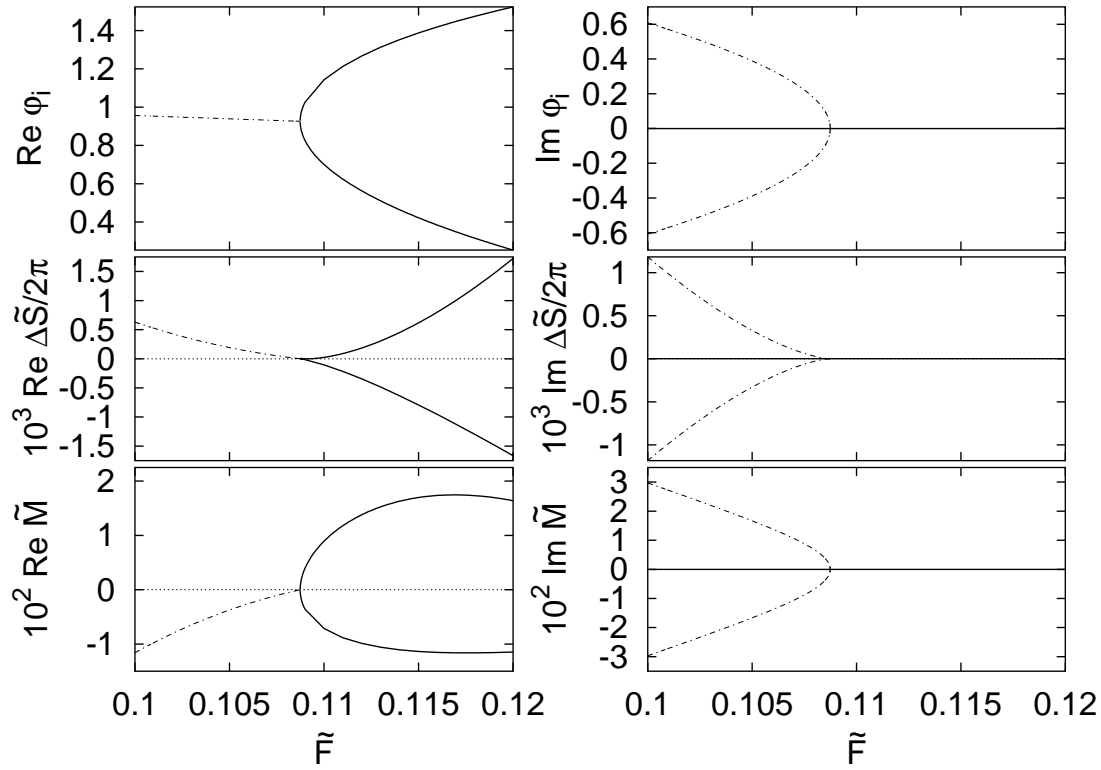


Figure 5.9: Orbital parameters close to a tangent bifurcation of planar orbits at a $\tilde{E} = -1.4$ and a winding number of $\mu = 45$. ($\Delta \tilde{S} = \tilde{S} - 2\pi \times 26.512735$.) Solid lines: real orbits, dashed-dotted lines: ghost orbits.

Once additional singlet orbits have been generated in a tangent bifurcation, doublet orbits can be generated by pitchfork bifurcations in the same way as from the original singlet orbits, i.e. a bifurcation will occur whenever a singlet orbit crosses one of the lines $\varphi_i = 0$ or $\varphi_i = \pi$. This is illustrated in figure 5.10, which presents the tangent bifurcation already shown in figure 5.9 at $\tilde{F} \approx 0.11$. At $\tilde{F} = 0.135$, one of the orbits thus generated crosses the line $\varphi_i = 0$, and two doublet orbits are created from it. Together, the two bifurcations form what Wang and Delos [88] call the “normal sequence” of bifurcations, whereas a pitchfork bifurcation of a singlet orbit generated at $\tilde{F} = 0$, which is not preceded by a tangent bifurcation, is called a “truncated series”. These authors introduce an integrable model Hamiltonian to explain why this kind of sequences can often be observed for planar orbits. The bifurcation theory of sections 5.1 and 5.2 sheds new light on this question, suggesting that normal sequences can actually be expected to occur even more generally than surmised by Wang and Delos. In particular, although the crossed-fields system is close to integrable at the field strengths considered here, integrability is not needed to make pitchfork bifurcations a generic phenomenon. Instead, the presence of a reflection symmetry suffices to reduce its codimension from two to one. The sequence of a tangent and a pitchfork bifurcation, represented as a sequence of a fold and a symmetric cusp catastrophe, can be regarded as an unfolding of the symmetrized version of

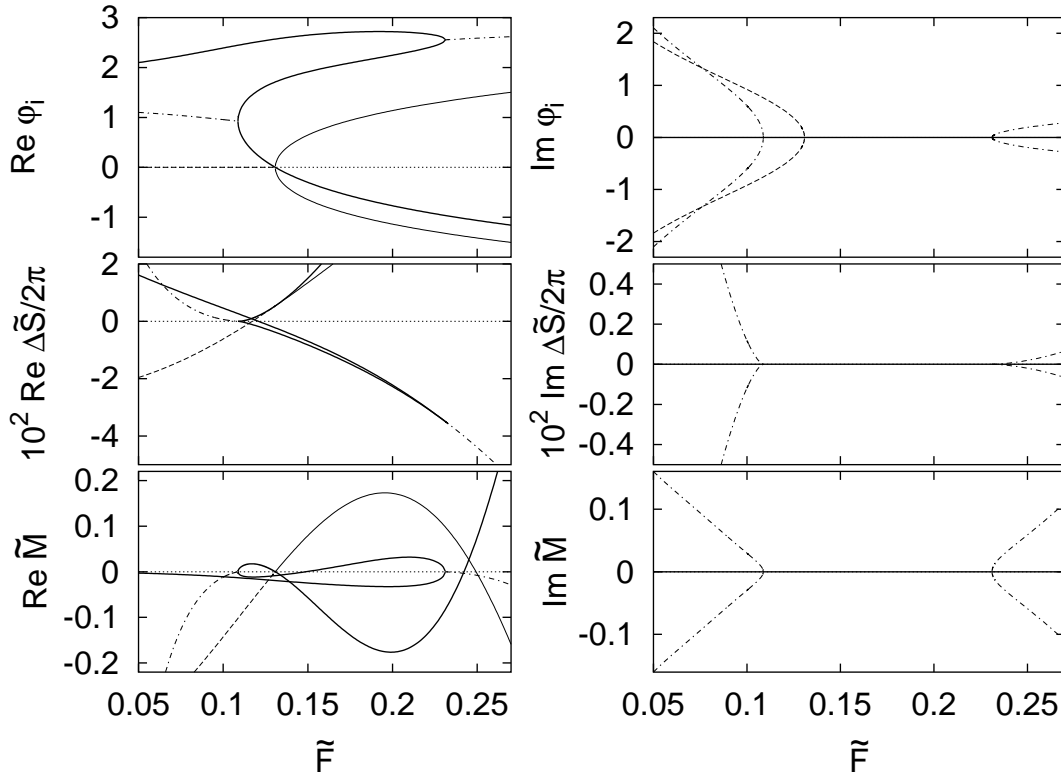


Figure 5.10: The bifurcation scenario taking place in the neighbourhood of the tangent bifurcation shown in figure 5.9. ($\Delta\tilde{S} = \tilde{S} - 2\pi \times 26.2735$). Thick solid lines: real singlet orbits, thin solid lines: real Z-doublet orbits, dashed lines: symmetric ghost orbits, dashed-dotted lines: asymmetric ghost orbits. Dotted lines are coordinate axes.

the butterfly catastrophe [92, 96]

$$\Phi_{a,b}(t) = \frac{1}{6}t^6 - \frac{1}{4}at^4 - \frac{1}{2}bt^2, \quad (5.20)$$

which is of codimension two, so that its unfolding can be expected to occur frequently in codimension one.

A third bifurcation can be discerned in figure 5.10: At $\tilde{F} \approx 0.225$, a singlet orbit generated at $\tilde{F} = 0$ and a singlet orbit generated in the tangent bifurcation discussed above collide and are destroyed. This is an instant of an inverse tangent bifurcation, which can be described by the fold catastrophe in the same way as the “regular” tangent bifurcation. It forms the third building block for the bifurcation scenario changing the pattern of planar orbits as the electric field strength is increased.

Besides the three bifurcations described above, in figure 5.10 three further zeros of the stability determinant \tilde{M} occur for certain real orbits, indicating the presence of even more bifurcations. These bifurcations involve non-planar orbits, i.e. they are pitchfork bifurcations breaking the Z-symmetry all planar orbits possess. They will be discussed further in subsequent sections. At the moment

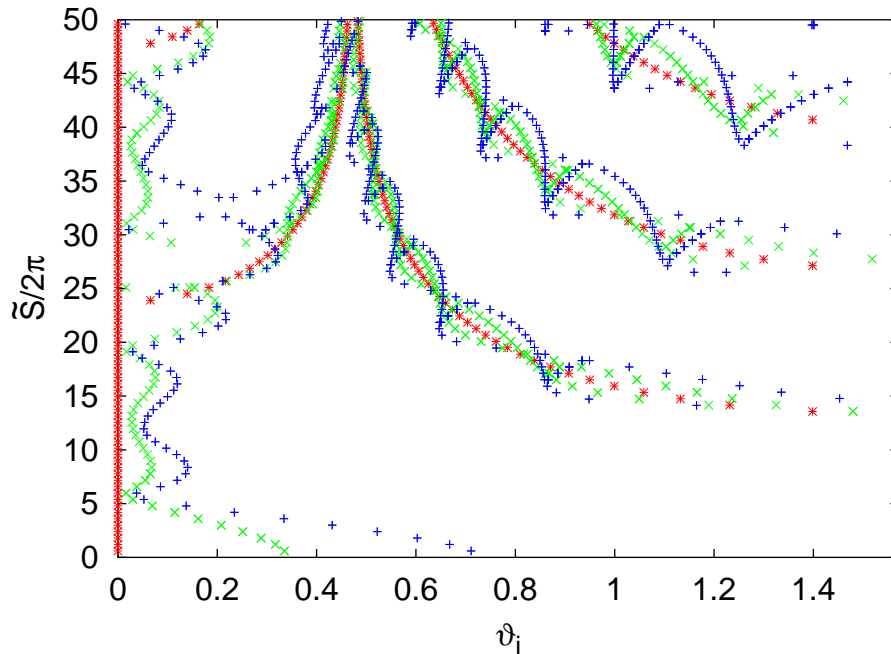


Figure 5.11: Scaled actions and polar starting angles of closed orbits at $\tilde{E} = -1.4$ and $\tilde{F} = 0$ (pure magnetic field, + symbols), $\tilde{F} = 0.05$ (\times symbols) and $\tilde{F} = 0.1$ ($*$ symbols). Due to the Z-symmetry, the figure should be extended to be symmetric with respect to the line $\vartheta_i = \pi/2$.

it suffices to note that in this scenario six individual bifurcations take place in a comparatively small interval of the electric field strength. This is the first example of a phenomenon to be encountered repeatedly: In the crossed-fields hydrogen atom bifurcations of closed orbits abound, exacerbating both the classical and the semiclassical treatment of the dynamics.

5.4.2 Non-planar orbits

The transition from the rotationally-symmetric case of a pure magnetic field to crossed fields occurs for non-planar orbits in much the same way as for planar orbits. As soon as a small perpendicular electric field is present, a one-parameter family of DKP orbits is destroyed and splits into two isolated closed orbits. These orbits start in opposite directions with respect to the electric field, so that their azimuthal starting angles φ_i differ by π , in complete analogy with what was shown in figure 5.5. An additional complication arises because the polar starting angle ϑ_i is no longer bound to the fixed value $\pi/2$, so that the two orbits will in general have different ϑ_i . Figure 5.11 presents the polar starting angles and the scaled actions of the closed orbits for the scaled energy $\tilde{E} = -1.4$ in a pure magnetic field and for two different perpendicular electric field strengths. It is obvious from the figure how a family of orbits splits in two isolated orbits and the two orbits move apart as the electric field strength is increased. This process takes place in

the same way for both rotator and vibrator orbits.

An exceptional role is played by the DKP orbit parallel to the magnetic field. This orbit is isolated even in a pure magnetic field. In the presence of a perpendicular electric field it is distorted and torn away from the magnetic field axis, but it remains isolated. It does not split into two orbits. This process is also apparent from figure 5.11. Notice again that closed orbits in crossed fields do not possess repetitions. Any repetition of the parallel DKP orbit gives rise to a closed orbit in crossed fields (for sufficiently small \tilde{F}), but these orbits are not repetitions of each other. They have, in particular, different starting angles.

The symmetries of the closed orbits are worth noting. All non-planar orbits described so far are doublets. More precisely, the vibrator orbits are T-doublets, i.e. they are invariant under the T operation. Their initial and final polar angles are small, as the orbits are mainly directed along the magnetic field axis.

For the rotator orbits the situation is more complex. Their main component is the motion in the plane perpendicular to the magnetic field, whereas the z -component is comparatively small. They have, therefore, initial and final polar angles close to $\pi/2$, so that it is conceivable that they can start at an angle $\vartheta_i < \pi/2$ “above” the x - y -plane and return at $\vartheta_f > \pi/2$ “below” that plane. This is in fact the case for the rotators of the first series. They turn out to be C-doublets.

The second series of rotators contains orbits which, in the case of a pure magnetic field, are composed of a first-series orbit and its Z-reflected counterpart. The orbits of the second series therefore have $\vartheta_i = \vartheta_f$ and are T-doublets. By the same token, orbits of the third series return “below” the x - y -plane again and are C-doublets, and higher series of rotators alternately contain T-doublets and C-doublets.

The distribution of symmetries is illustrated in figure 5.12(a). It extends the data given in figure 5.11 to longer orbits and classifies the orbits according to their symmetries. Notice that the set of orbits shown is obviously incomplete at starting angles around $\vartheta_i \approx 0.45$, where rotator and vibrator orbits coexist. This incompleteness will be discussed further in section 6.4.

So far, only orbits present at arbitrarily low electric field strengths have been described. As the electric field strength increases, further bifurcations occur. Their general pattern can be identified in figures 5.11 and 5.12(a). The most obvious consequence of the bifurcations is the appearance of quartet orbits in each series of both rotator and vibrator orbits. They are generated by pitchfork bifurcations from the adjacent doublet orbits. As figure 5.13 reveals if it is compared to figure 5.7, this bifurcation is very similar to a pitchfork bifurcation of planar orbits. A difference arises because, due to the absence of Z-symmetry, the angle ϑ_i is not restricted to a fixed value. As the C-symmetry to be broken concerns the azimuth angles, it still is predominantly the angle φ_i that shows a square root behaviour at the bifurcation and obtains an imaginary part when ghost orbits exist. Nevertheless the polar angle ϑ_i also acquires a small imaginary part. The real part of ϑ_i apparently behaves linear close to the bifurcation, although for electric field strengths above the critical value a square root behaviour must be

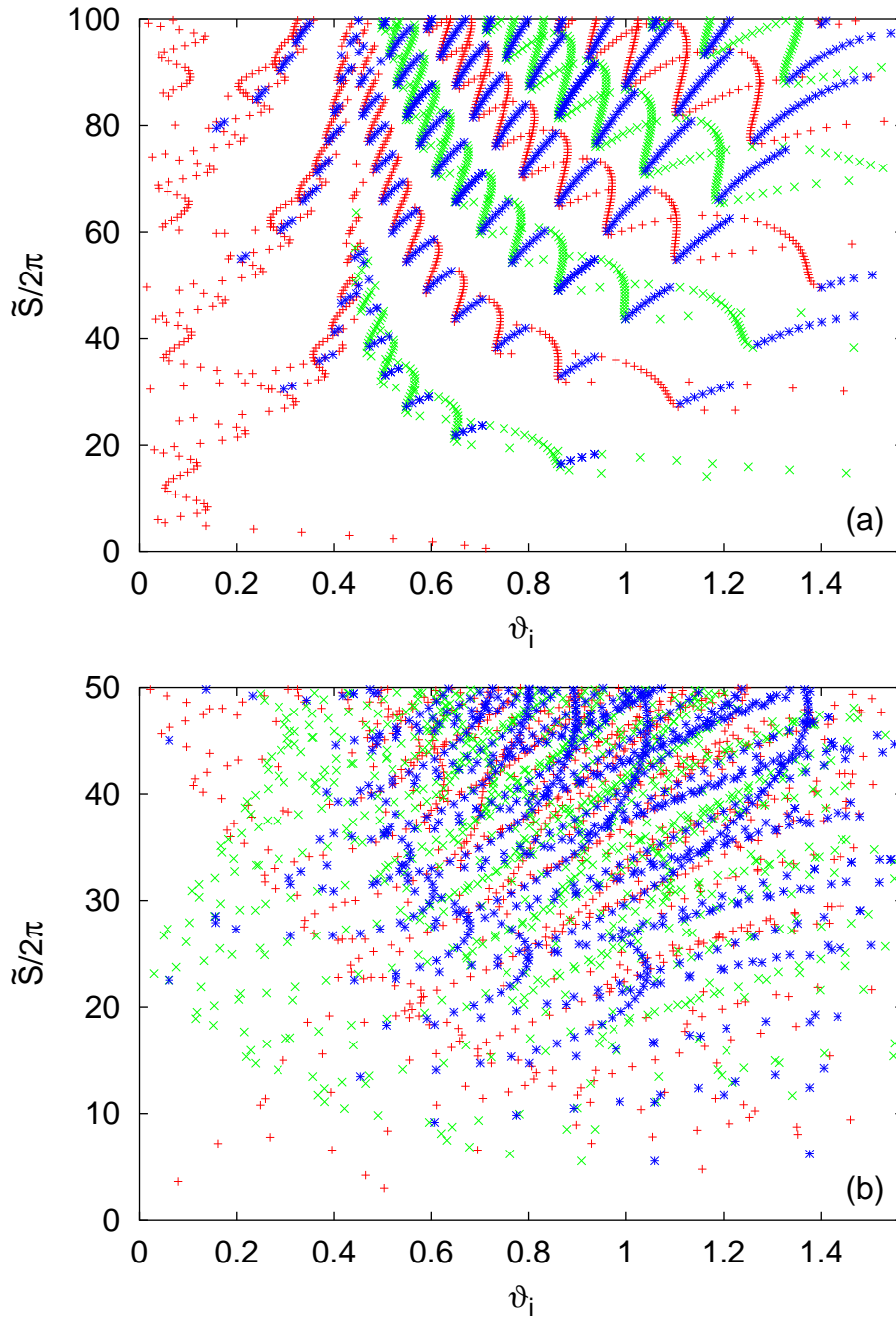


Figure 5.12: Scaled actions and polar starting angles of closed orbits at $\tilde{E} = -1.4$ and (a) $\tilde{F} = 0.1$, (b) $\tilde{F} = 0.6$. Orbits are classified according to their symmetries: T-doublers are indicated by + symbols, C-doublers by \times symbols, quartets by * symbols. Planar orbits (Z-doublers and singlets) are omitted. Notice that the range of actions shown is smaller in (b).

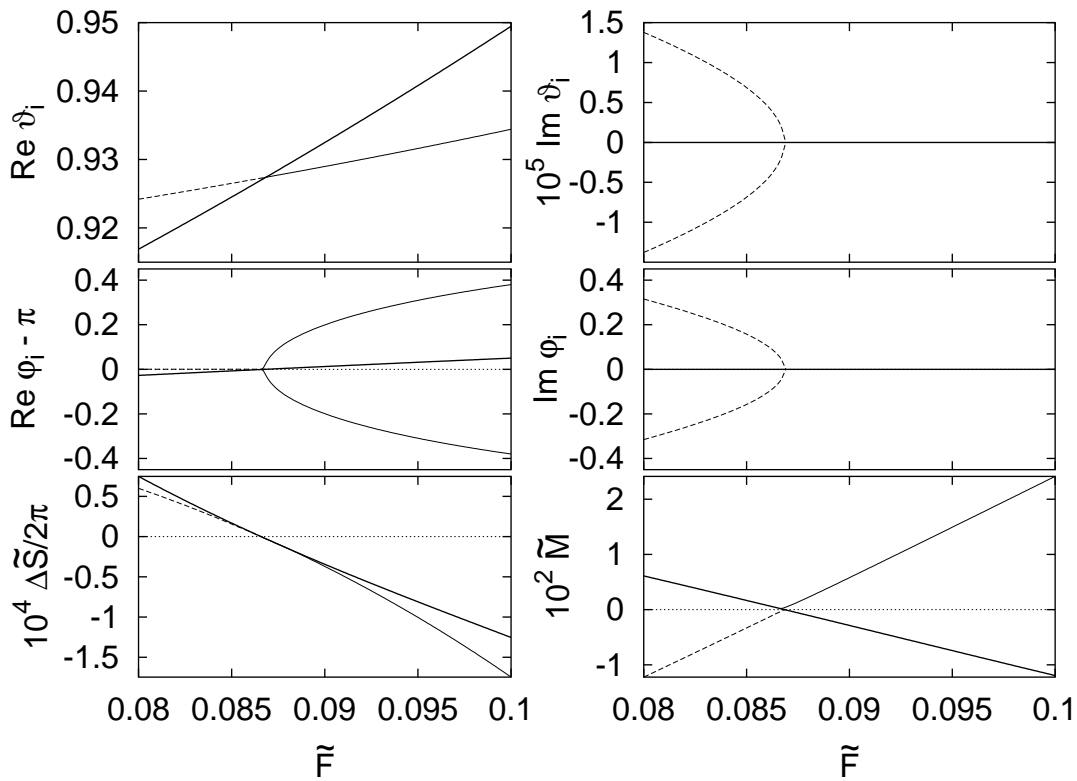


Figure 5.13: Orbital parameters close to a pitchfork bifurcation of a first-series rotator and a repetition number of $\mu = 38$. The bifurcation creates a quartet of orbits from a C-doublet. ($\Delta \tilde{S} = \tilde{S} - 2\pi \times 18.297822$.)

present. It is too small to be seen in the figure. Even though in quantitative terms the ϑ -direction is only marginally involved in the bifurcation, its presence has the important consequence that the quartet orbits are no longer constrained to be periodic. As the distance from the bifurcation is increased, the periodicity condition $\varphi_i = \varphi_f$ is increasingly, albeit slowly, violated. The same features can be found for the bifurcations introducing the quartet orbits into the vibrator series.

The second important type of bifurcations is a tangent bifurcation introducing new doublet orbits into the series. The occurrence of this phenomenon can be noticed in figure 5.11, if the numbers of orbits of a given repetition number are compared for different electric field strengths. An example of this bifurcation is given in figure 5.14. The tangent bifurcation involves both angles to roughly equal extent. The two doublet orbits thus generated are implanted into the regular pattern of their series, so that one of them subsequently undergoes a pitchfork bifurcation which creates a quartet. This phenomenon is entirely analogous to the “normal sequence” of bifurcations that was found for planar orbits, except that the quartet orbits thus generated are not periodic.

As the electric field strength increases, the rotator orbits of a given series are torn apart and span an ever wider interval of ϑ_i . Those moving towards higher

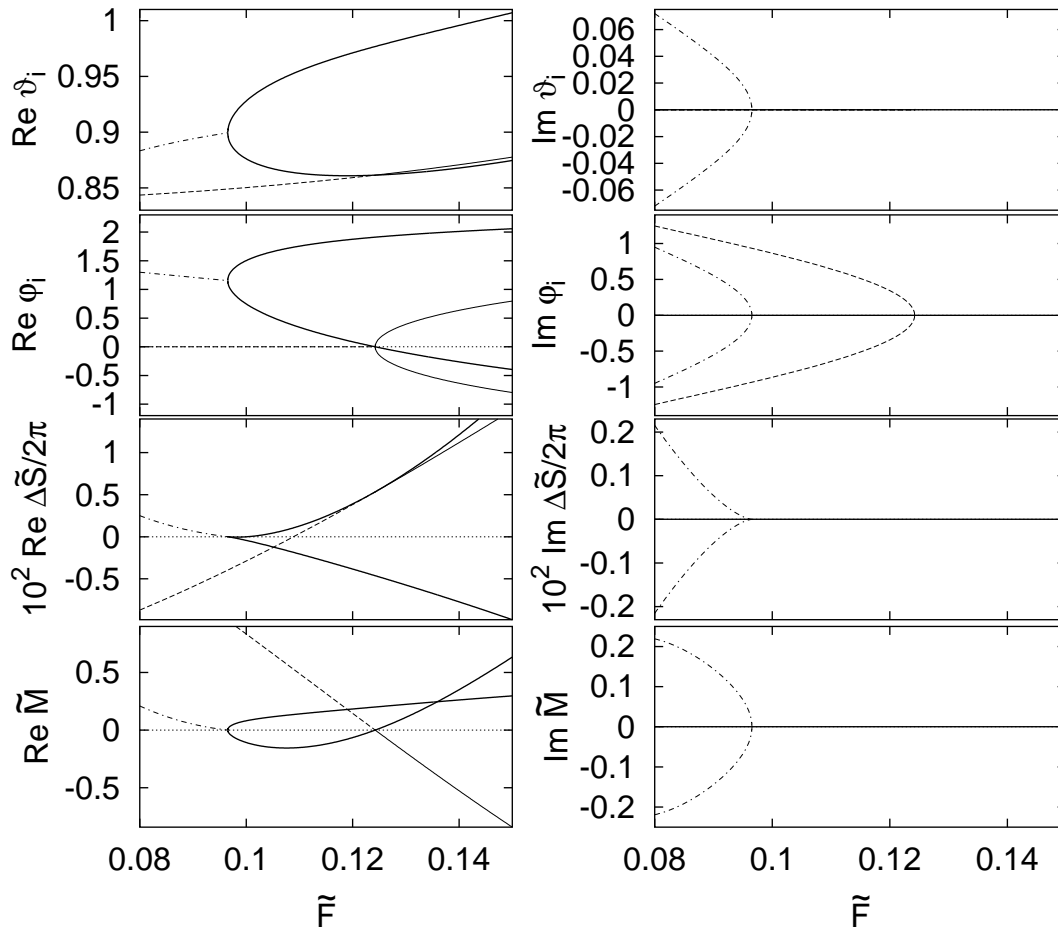


Figure 5.14: “Normal sequence” of bifurcations for non-planar rotator orbits of the second series and a repetition number of $\mu = 54$. ($\Delta\tilde{S} = \tilde{S} - 2\pi \times 31.84035$.)

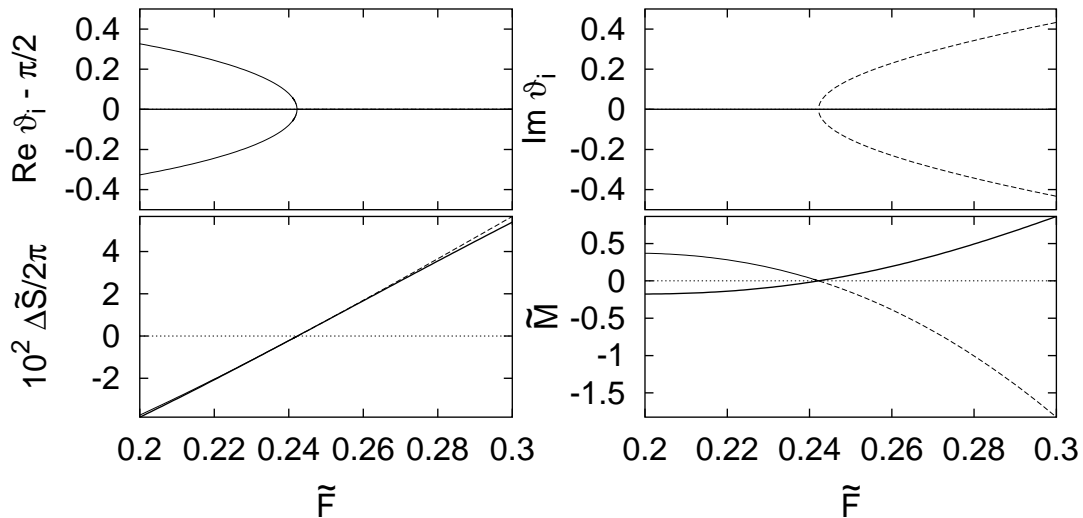


Figure 5.15: Destruction of T-doublet orbits in a collision with a singlet orbit. ($\Delta\tilde{S} = \tilde{S} - 2\pi \times 27.60324$.)

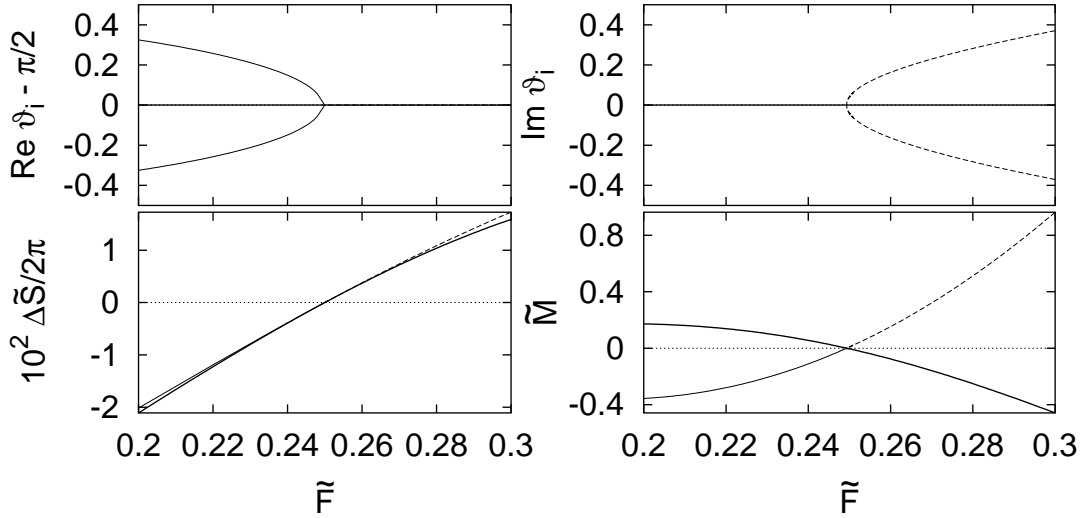


Figure 5.16: Destruction of quartet orbits in a collision with Z-doublet orbits. ($\Delta \tilde{S} = \tilde{S} - 2\pi \times 26.569655$.)

values of ϑ_i eventually hit the plane $\vartheta_i = \pi/2$, where they collide with their Z-reflected partner and are destroyed. It turns out that there is always a planar orbit involved in the collision, so that it is a pitchfork rather than a tangent bifurcation that destroys the non-planar orbits. Depending on whether the non-planar orbits colliding with the plane are doublets or quartets, the planar orbit must be a singlet or a Z-doublet, respectively. If the destruction scenario is regarded in the direction of decreasing field strengths, it appears as the creation of orbits with broken Z-symmetry from an orbit possessing this symmetry. It is therefore the Z-breaking analogue of the T- and C-symmetry breaking bifurcations described above. As this type of bifurcation involves a planar orbit, it must give rise to a zero in the stability determinant \tilde{M} of the planar orbit. In fact, the examples given in figures 5.15 and 5.16 for both the destruction of a doublet and a quartet are two of the three bifurcations whose presence was inferred from figure 5.10 the discussion of the planar orbits.

The scenario just described is not restricted to rotator orbits. As can be seen in figure 5.11, the short vibrator orbits can, even at low electric field strengths, reach rather high values of ϑ_i . At $\tilde{F} = 0.15550$, the first of them collides, at $\vartheta_i = \pi/2$, with its Z-reflected counterpart and is annihilated. This is a pitchfork bifurcation in which one of the planar orbits with repetition number $\mu = 1$ takes part. Similarly, longer vibrators are destroyed in collisions with planar rotators of the appropriate repetition numbers. This example demonstrates, that the distinction between vibrators and rotators, which was borrowed from the case of vanishing electric field, does not apply, strictly speaking, if an electric field is present. Although it is generally useful for rather high electric field strengths, it can fail in some instances. This is clearly the case when a bifurcation involves both vibrator and rotator orbits.

A collision with the plane perpendicular to the magnetic field occurs only for

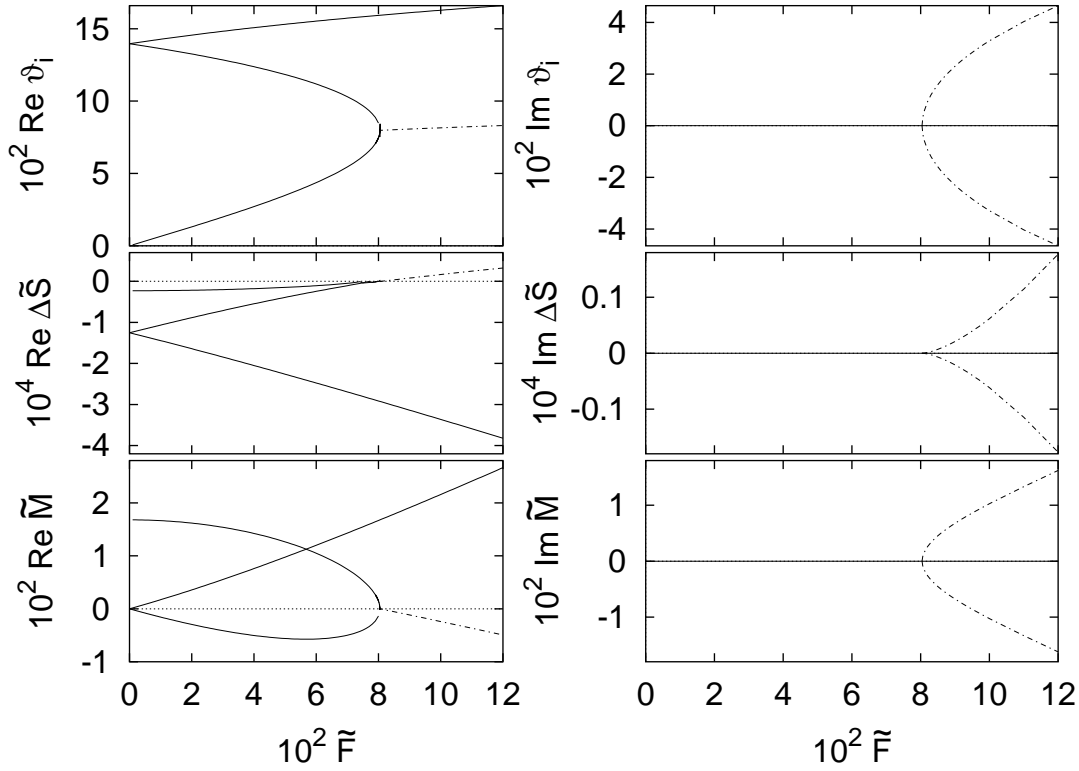


Figure 5.17: Simple bifurcation scenario for vibrator orbits of repetition number $\mu = 41$. ($\Delta\tilde{S} = \tilde{S} - 2\pi \times 24.50221$.)

vibrators of low repetition numbers, and only for vibrators that descend from the orbit parallel to the magnetic field. For longer orbits, the usual scenario is different. At low electric field strength there is, for sufficiently high repetition numbers, one orbit stemming from the orbit parallel to the magnetic field and one or several pairs of orbits created from non-parallel vibrators. It can be seen in figure 5.11, however, that for certain repetition numbers two of these orbits can be missing. This happens when the descendant of the parallel orbit and one of the other vibrators annihilate in a tangent bifurcation. A simple example of how this can come about is provided by the orbits with the repetition number $\mu = 41$. Their bifurcations are illustrated in figure 5.17. Two of the orbits obviously bifurcate from a common family at $\tilde{F} = 0$, whereas the orbit proceeding from the parallel orbit is isolated there and starts at $\vartheta_i = 0$. It then merges with one of the other orbits in a tangent bifurcation to form a pair of ghost orbits.

This bifurcation is as simple as one could expect. For the neighbouring vibration number $\mu = 42$ the scenario is more complicated. It is illustrated in figure 5.18. In this case, one of the orbits generated in the rotational symmetry breaking at $\tilde{F} = 0$, which is a T-doublet, undergoes a pitchfork bifurcation and gives birth to a quartet of orbits before it annihilates with the descendant of the parallel orbit. The quartet then collides with the third, leftover T-doublet and is destroyed in a second pitchfork bifurcation.

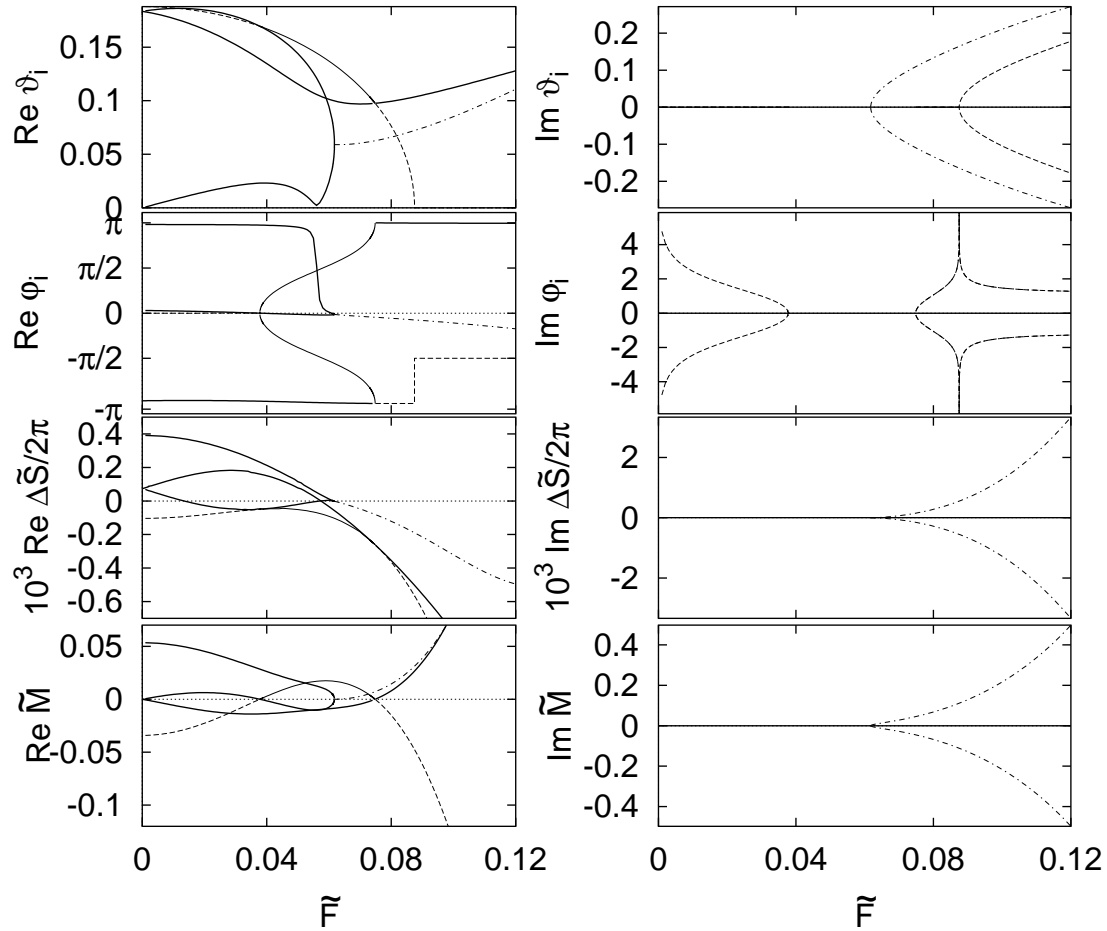


Figure 5.18: Complicated bifurcation scenario for vibrator orbits of repetition number $\mu = 42$. ($\Delta\tilde{S} = \tilde{S} - 2\pi \times 25.09941$.)

Corresponding to the three elementary bifurcations, there are three ghost orbits involved in the scenario. For one of them, the starting angles ϑ_i and φ_i show a peculiar behaviour at the electric field strength $\tilde{F}_0 = 0.08750$: Whereas ϑ_i exhibits a square root behaviour, changing from nearly real to nearly imaginary, the real part of φ_i changes discontinuously by $\pi/2$, and the imaginary part of φ_i seems to diverge. Neither the action nor the stability determinant of the orbit, on the contrary, show any kind of special behaviour. In particular, \tilde{M} is non-zero, so that there cannot be a bifurcation of the ghost orbit.

The Cartesian components of the unit vector \mathbf{s} in the starting direction are given in figure 5.19. For all of them either the real or the imaginary parts are small, so that their numerical calculation is hard. Nevertheless, to within the numerical accuracy all components are smooth at \tilde{F}_0 , although the angles ϑ_i and φ_i used to calculate them are not. Thus, the singularity must be due to the transformation from Cartesian to angular coordinates. In the real case it is obvious that the (ϑ, φ) coordinate chart is singular at $\vartheta = 0$. To elucidate the details in the case of ghost orbits, I assume a model situation where $s_z = \cos \vartheta_i$

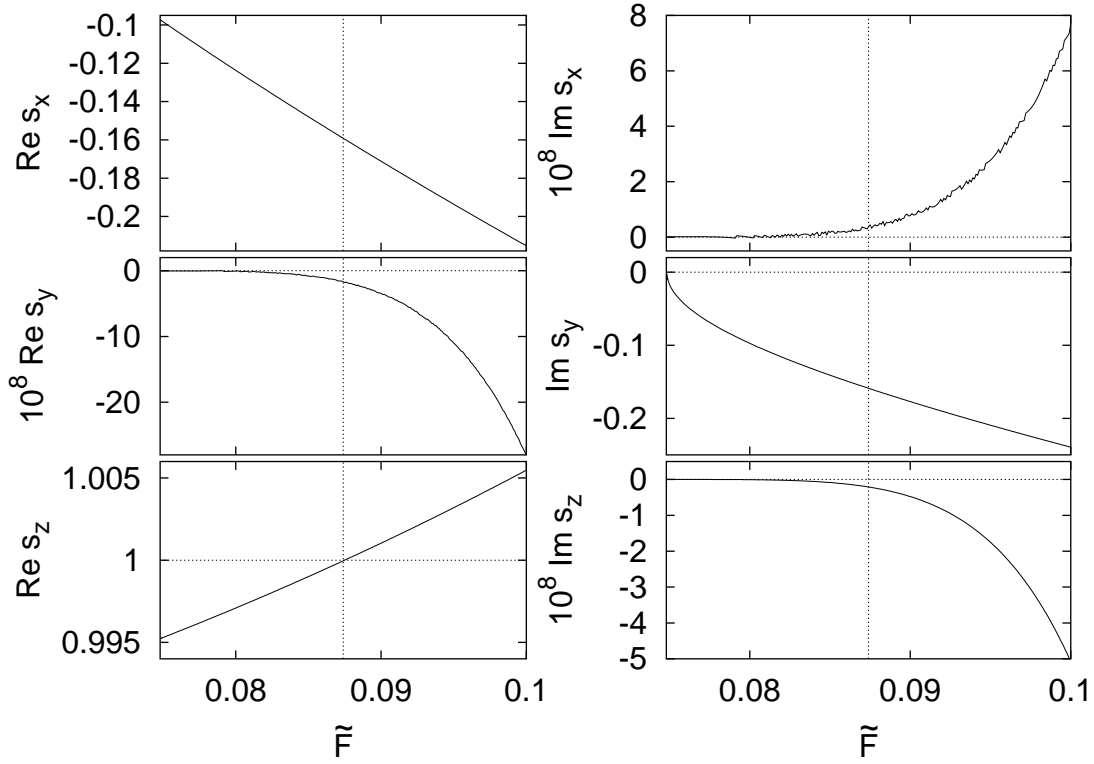


Figure 5.19: Cartesian components of the unit vector \mathbf{s} specifying the starting direction of the ghost orbit ($s_x = \sin \vartheta_i \cos \varphi_i$, $s_y = \sin \vartheta_i \sin \varphi_i$, $s_z = \cos \vartheta_i$). Vertical dotted lines mark the field strength $\tilde{F}_0 = 0.08750$ where the singularity of $\text{Im } \varphi_i$ is encountered.

is exactly real and $s_z = 1$ at $\tilde{F} = \tilde{F}_0$. For ghost orbits, s_z is not bound to be smaller than 1, so that generically, to first order in $\varepsilon = \tilde{F} - \tilde{F}_0$, $\cos \vartheta_i - 1 \propto \varepsilon$. Therefore, $\vartheta_i \propto \sqrt{\varepsilon}$ shows a square root behaviour and changes from purely real to purely imaginary values. At the same time, $\sin \vartheta_i \propto \sqrt{\varepsilon}$ has a zero, so that for $s_x = \sin \vartheta_i \cos \varphi_i$ and $s_y = \sin \vartheta_i \sin \varphi_i$ to assume finite values, $\sin \varphi_i$ and $\cos \varphi_i$ must diverge as $\varepsilon^{-1/2}$. This is only possible if the imaginary part of φ_i is large. More precisely, if $\text{Im } \varphi_i > 0$ is assumed to be large, $\sin \varphi_i$ and $\cos \varphi_i$ are proportional to $e^{-i\varphi_i}$, whence

$$\varphi_i = \frac{1}{2i} \ln \varepsilon + \mathcal{O}(\varepsilon^0) \quad (5.21)$$

achieves the desired divergence of $\sin \varphi_i$ and $\cos \varphi_i$. Now $\text{Re} \ln \varepsilon = \ln |\varepsilon|$ diverges at $\varepsilon = 0$, whereas $\text{Im} \ln \varepsilon$ changes discontinuously from 0 to $\pm\pi$, depending on what branch of the logarithm is chosen. This behaviour results in the observed divergence of $\text{Im } \varphi_i$ and a discontinuous jump in $\text{Re } \varphi_i$ of size $\pi/2$.

Whereas the starting vector \mathbf{s} is a smooth function of \tilde{F} in the neighbourhood of the singularity, the starting values (4.80) in KS coordinates are not, because they depend on the half angles $\vartheta_i/2$ and $\varphi_i/2$. With the above value for φ_i , the angular functions $\sin \varphi_i/2$ and $\cos \varphi_i/2$ diverge as $\varepsilon^{-1/4}$. Therefore, the KS

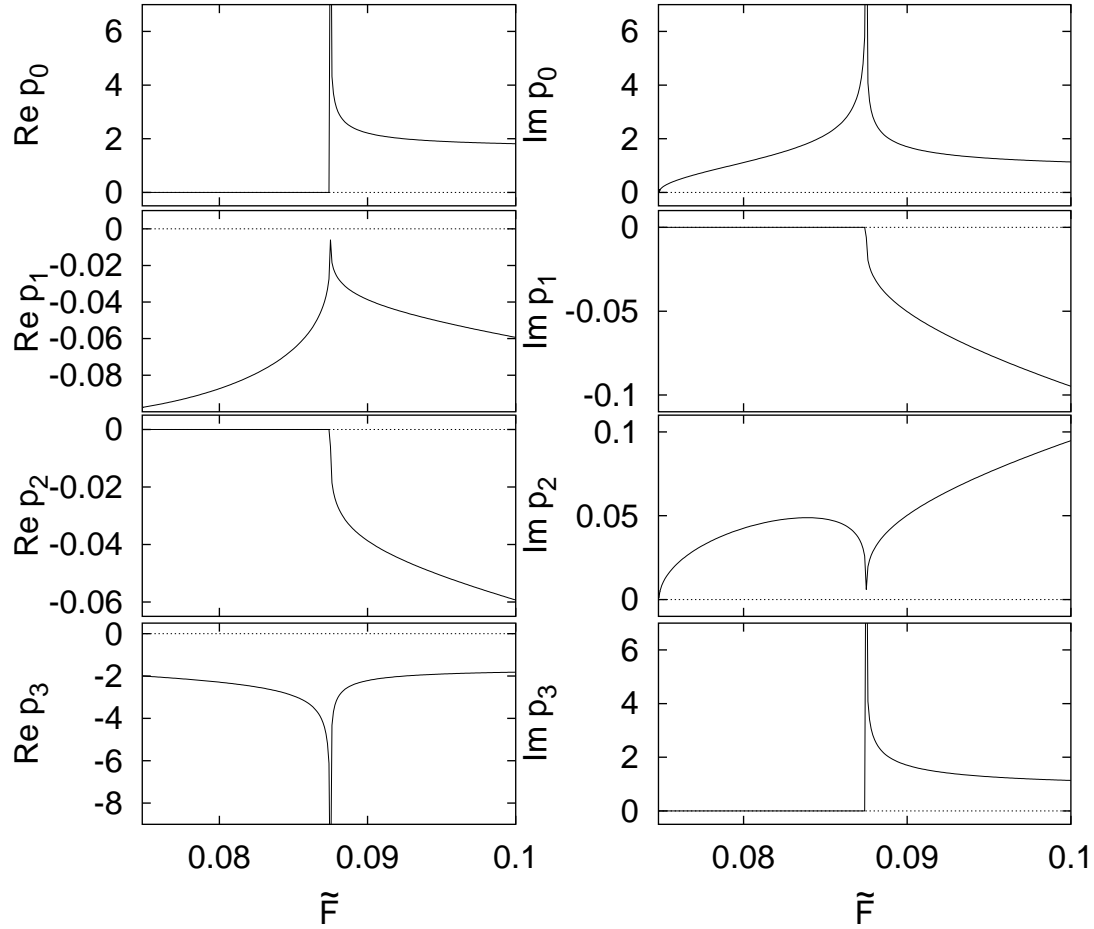


Figure 5.20: Starting values of the ghost orbit in KS coordinates as given by (4.80) with $\alpha = 0$.

coordinates proportional to $\cos \vartheta_i/2$ must diverge as $\varepsilon^{-1/4}$, whereas those proportional to $\sin \vartheta_i/2$ vanish in a non-smooth manner as $\varepsilon^{1/4}$. It is somewhat ironic that in this case it is the KS transformation, which was thought of as regularizing the equations of motion, that introduces singularities. This type of singularity can occur for ghost orbits only. It is due to the circumstance that, contrary to Cartesian coordinates, KS coordinates rely for their definition on a specified reference vector σ_3 . A more detailed study of the geometry of the complex KS transformation than that presented here should help to clarify the precise nature of the singularity and determine if it is actually inevitable or can be eliminated by a generalized gauge transformation.

In the actual scenario s_z will not be exactly equal to 1 at \tilde{F}_0 because this is a situation of real codimension two. However, if $\text{Im } s_z$ is small, the singular behaviour described above will be closely approximated. Indeed, a closer look at ϑ_i (see figure 5.21) reveals that it is actually smooth, but close to $\tilde{F} = \tilde{F}_0$ it changes extremely rapidly from almost real to predominantly imaginary values. Similarly, the real part of φ_i is smooth, although it changes over an even smaller

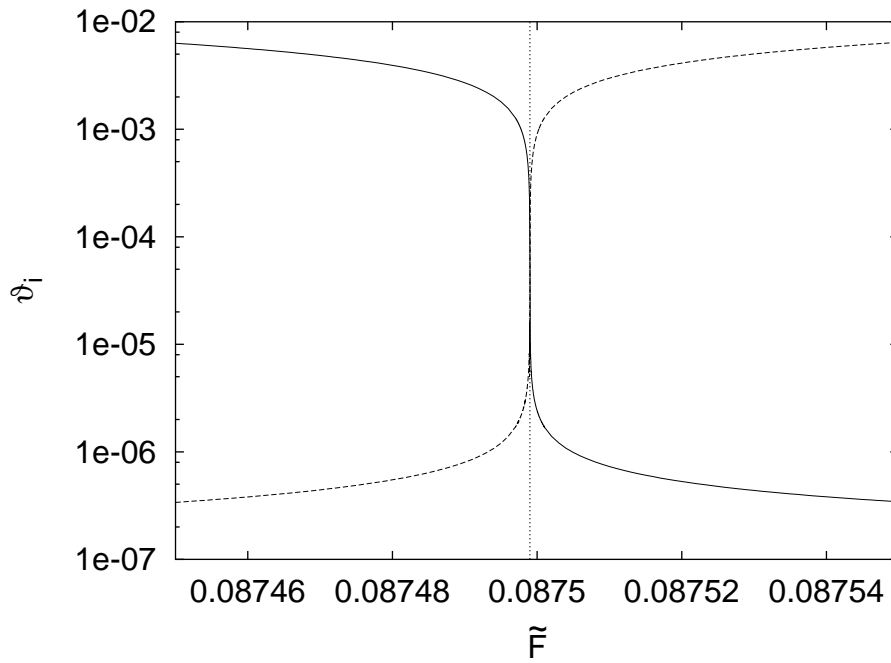


Figure 5.21: The starting angle ϑ_i of the ghost orbit close to the coordinate singularity. Solid line: real part, dashed line: imaginary part. Note the logarithmic scale.

range of \tilde{F} . From the numerical data it cannot be determined if $\text{Im } \varphi_i$ is also smooth or actually diverges. From the above discussion it is clear that it must be smooth, because the coordinate singularity at $\vartheta_i = 0$ is not actually encountered.

It should be noted that the singularity described here can occur for ghost orbits only. In the real case, as the pole $\vartheta_i = 0$ on the real unit sphere (which still has codimension two) is approached, both s_x and s_y must vanish instead of assuming finite values, so that no divergences of any kind are required.

With the discussion of this somewhat unexpected singularity occurring in the “regularizing” KS coordinates, I finish the description of the bifurcation scenarios in crossed fields. I have demonstrated that, even though only two types of elementary bifurcations exist, they form a rich variety of bifurcation scenarios that re-shape the distribution of closed orbits as the electric field strength is increased. It remains to find a classification scheme for closed orbits in the crossed-fields regime.

5.5 The classification of closed orbits

The fundamental classification scheme used in the above description of closed orbit bifurcations is the distinction between rotators and vibrators. This distinction was adopted from the case of vanishing electric field strength, so it can be expected to be applicable if the electric field is not too strong. In fact, from figure 5.12(a) it is obvious that for $\tilde{E} = -1.4$ and $\tilde{F} = 0.1$ orbits can uniquely

be classified as rotators or vibrators and can be assigned both a series number and a repetition number. However, for long orbits neighbouring series of rotators already start to overlap in the plot, and if the electric field strength is increased to $\tilde{F} = 0.6$, all orbits get completely mixed up, producing the somewhat messy picture shown in figure 5.12(b). Although the pattern of orbits is still dominated by the magnetic field¹, figure 5.12(b) suggests that there is no way to achieve a classification.

A more suitable starting point for a classification is provided by the complete trajectories. Of course, since the classification must gradually break down for sufficiently strong electric fields, it can only be based on heuristic criteria. The criteria I am going to propose are largely based on the behaviour of the z -coordinate of the motion as a function of time. To illustrate them, this function is plotted for rotators of roughly equal length from different series in figure 5.22. Figure 5.23 shows the analogous data for vibrators.

First of all, vibrators are connected to an orbit along the z -axis in the pure magnetic field case. In this limit, the motion takes place either “above” the x - y -plane, i.e. in the half-space $z > 0$, or “below” the plane. Rotators, on the contrary, stem from the elementary orbit in the plane. Their motion takes place both above or below the plane. Rotators can therefore be distinguished from vibrators if the maximum and minimum values of the coordinate z are compared: For a rotator, they must have roughly equal absolute values, whereas for a vibrator “above” the plane, the minimum value is much smaller in magnitude than the maximum value.

For the vibrators of a given length shown in figure 5.23, this criterion gets better the higher the series of the vibrator is chosen. For the vibrator of the first series, which is closest to the domain of rotators, the excursion into the lower half space is of the same order of magnitude as that into the upper half space. As the electric field strength increases further, the vibrator orbit will eventually become indistinguishable, by the present criteria, from a rotator of the second series.

It has already been noted in the discussion of orbital symmetries that a rotator of the first series that starts from the nucleus into the upper half space returns to it from the lower half space, whereas a rotator of the second series returns from the upper half space. This alternation between motion in the upper and lower half spaces is obvious from figure 5.22. It can be used to determine the series of a rotator. If the value of $z(\tau)$ in a maximum is compared to its value in the subsequent minimum, the transitions between motion in the upper and lower half spaces can easily be monitored.

Assigning a series number to a vibrator is considerably more difficult. It relies on the beat structure present in $z(\tau)$ for a vibrator. Subsequent maxima of this function have varying heights. I consider the maxima that have minimal height

¹A convenient way of comparing the relative strengths of the electric and magnetic fields is provided by the scaling with the energy described in section 2.1. If the energy is scaled to $\tilde{E} = -1$, for the present parameter values the scaled field strengths are $\tilde{B} = 0.60$ and $\tilde{F} = 0.30$, so that the magnetic field is still stronger than the electric field, although the latter is no longer negligibly small.

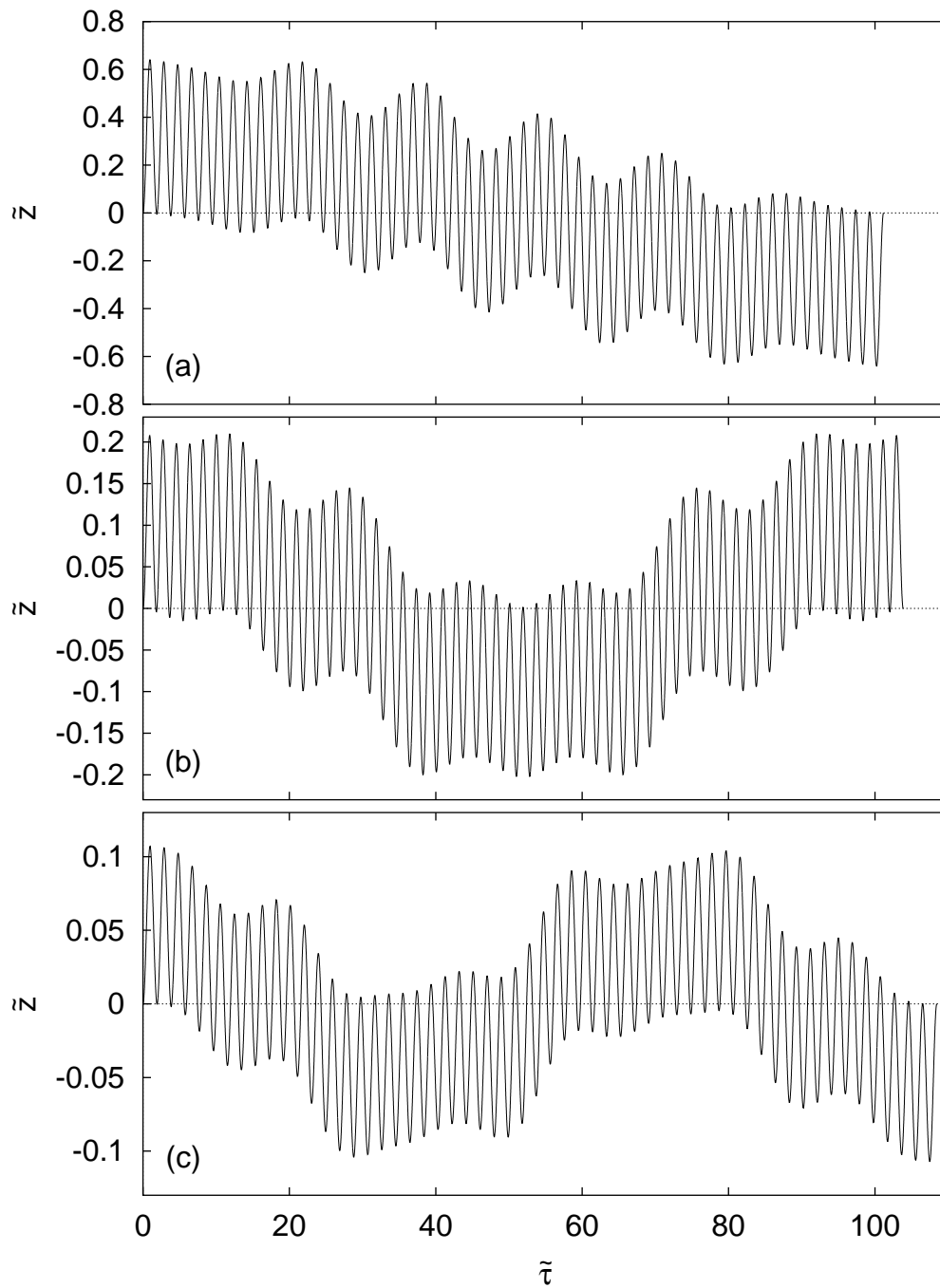


Figure 5.22: Rotor orbits of the (a) first, (b) second and (c) third series: scaled coordinate \tilde{z} as a function of the scaled pseudotime $\tilde{\tau}$ for $\tilde{E} = -1.4$ and $\tilde{F} = 0.2$.

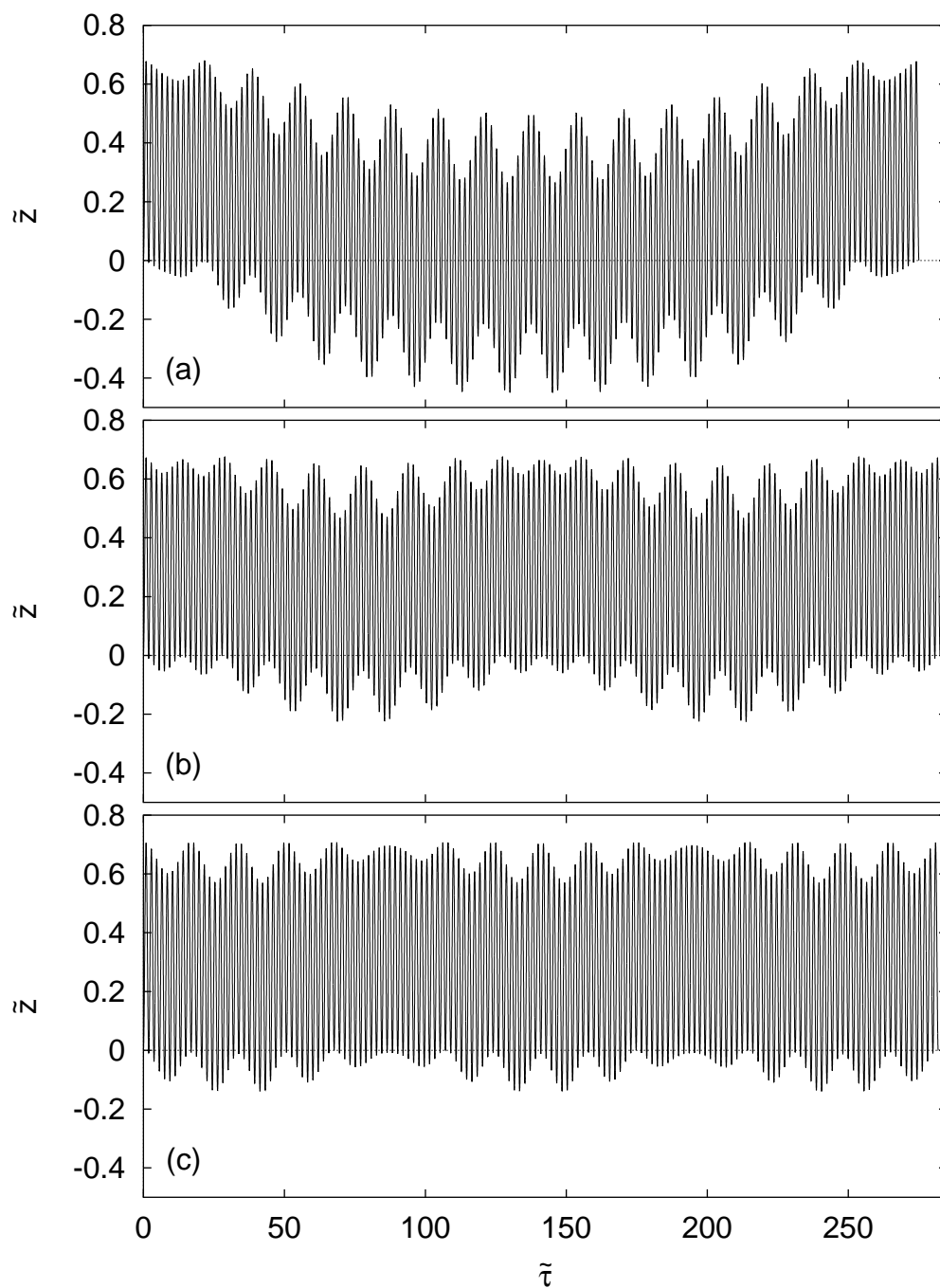


Figure 5.23: Vibrator orbits of the (a) first, (b) second and (c) third series: scaled coordinate \tilde{z} as a function of the scaled pseudotime $\tilde{\tau}$ for $\tilde{E} = -1.4$ and $\tilde{F} = 0.2$.

compared to neighbouring maxima, i.e. the minima of the beats apparent in figure 5.23. The height of these beat minima slowly oscillates, and the number of their oscillations turns out to give the series number of the vibrator. It can be found by counting the number of minima in the oscillation. Notice that the method uses extrema of the third order: the minima in the minima in the height of maxima. It therefore requires vibrators of sufficiently high repetition numbers, so that many maxima of $z(\tau)$ exist. The method will fail when applied to vibrators of very small repetition numbers. However, these vibrators exist for fairly high scaled energies only, where even in the absence of an electric field the dynamics is mixed or chaotic. In these regions, the classification suggested here might not be meaningful at all.

Finally, orbits can be assigned a repetition number. For vibrators, this can be done by simply counting the number of maxima in $z(\tau)$. For rotators, maxima in $\rho(\tau)$ must be counted, where $\rho = (x^2 + y^2)^{1/2}$ is the distance from the magnetic field axis. In this case, an additional difficulty arises because ρ cannot assume negative values, so that between two maxima corresponding to repetitions of the elementary orbits, additional maxima arise from the “swing-by” around the nucleus. These maxima tend to be extremely small and narrow close to the beginning and the end of an orbit, so that they are hard to detect, but they can reach considerable heights in the middle of an orbit. The present form of the classification algorithm, which is certainly open to improvements, counts a maximum in $\rho(\tau)$ if its height exceeds a certain fraction of the height of the previous maximum. In this form, the assignment of rotator repetition numbers turns out to be the least robust part of the classification procedure.

The criteria described above readily lend themselves to a numerical implementation, so that the classification of orbits can be achieved automatically. As an example, the rotators of the first series are shown in figure 5.24 for three different electric field strengths. Although the neat “wiggly-line” structure characterizing the series in figure 5.11 quickly breaks down for larger electric field strengths, the distinction between different series persists. Figure 5.24(c) should be compared to figure 5.12(b). It might appear surprising that the messy-looking set of orbits still allows for a classification, but with the help of the criteria just described an ordered pattern of closed orbits can still be discerned. In this sense, the classification scheme derived from the DKP turns out to be remarkably robust.

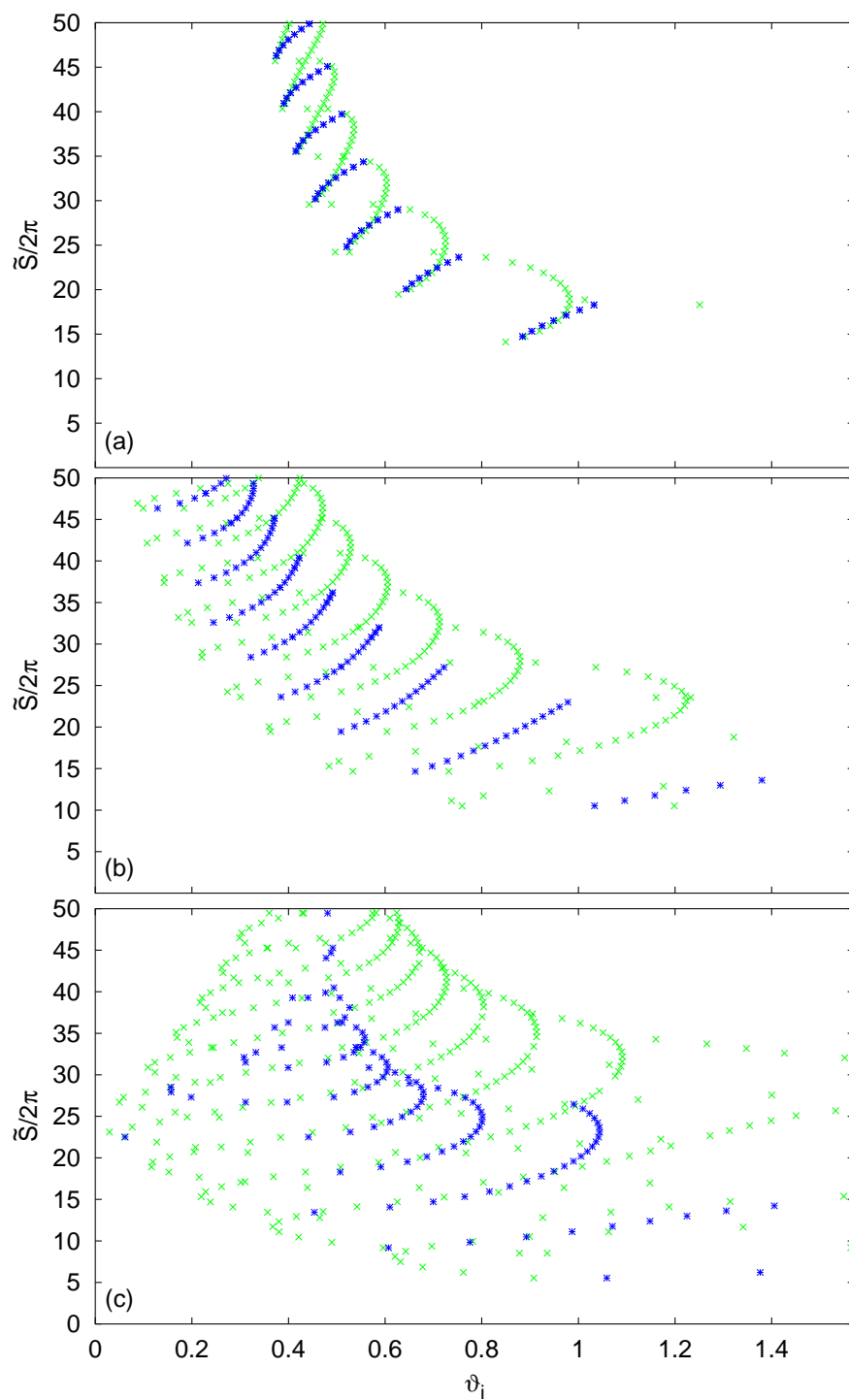


Figure 5.24: Rotators of the first series for $\tilde{E} = -1.4$ and (a) $\tilde{F} = 0.2$, (b) $\tilde{F} = 0.4$, and (c) $\tilde{F} = 0.6$. C-doublets are indicated by \times symbols, quartets by $*$ symbols.

Chapter 6

Semiclassical crossed-fields spectra

After the description of the closed orbits in the crossed-fields hydrogen atom, I now turn to the discussion of their impact on quantum mechanical photo-absorption spectra. I will present the results of both a low- and a high-resolution semiclassical quantization of the crossed-fields system based on closed-orbit theory. In the latter case, only the strongest spectral lines will be resolved. The reason why a more detailed semiclassical quantization cannot be achieved will be identified by means of a detailed semiclassical analysis of a quantum spectrum. It will be shown that the semiclassical spectrum is distorted by a multitude of closed-orbit bifurcations. I will then describe uniform approximations that smooth the divergences caused by bifurcations and devise a method to include uniform approximations in a semiclassical quantization. Due to the diversity of closed-orbit bifurcation scenarios in the crossed-fields hydrogen atom, however, a systematic inclusion of all relevant uniform approximations poses great technical difficulties. For this reason, the hydrogen atom in an electric field will be analysed along these lines in chapter 7: In that system, a single type of bifurcations occurs, so that the semiclassical quantization in the presence of bifurcations can be carried out in detail.

As mentioned in chapter 3, the way of recording a quantum spectrum which is most suitable to semiclassical investigations is provided by scaled-energy spectroscopy. A spectrum then consists of a list of the scaling parameters w_n characterizing the quantum states for a given scaled energy \tilde{E} and scaled electric field strength \tilde{F} , if the usual scaling with the magnetic field strength is used, i.e. $\tilde{B} = 1$.

6.1 The quantum spectrum

If Schrödinger's equation for the crossed-fields hydrogen atom is rewritten in terms of the scaled energy and the scaled electric field strength, a quadratic eigenvalue problem for the scaling parameter w is obtained. An exact numerical

method of solution for the quadratic eigenvalue problem has become available only recently [10]. I resort to the method introduced by Main [48], which relies on an approximate linearization of the eigenvalue problem to compute eigenvalues in a small spectral interval. The accuracy of the linearization can be verified by comparing results calculated using different overlapping intervals. The eigenvalues are obtained to a relative accuracy of at least 10^{-7} , which is far beyond the typical accuracy of semiclassical approximations, so that the algorithm is well suited to this study.

In the following I will discuss quantum and semiclassical photo-absorption spectra obtained for the scaled energy $\tilde{E} = -1.4$ and the scaled electric field strength $\tilde{F} = 0.1$ with the initial state $|2p0\rangle$ and light linearly polarized along the magnetic field axis. A quantum spectrum for these parameter values is shown in figure 6.1. As for a semiclassical analysis (see section 6.4) it is essential to have as many eigenvalues available as possible, the calculation was extended up to $w = 100$. This value is close to the limit of what can be reached with the computer power available, as regards both computing time and memory requirements. The spectrum shown in figure 6.1 contains nearly 30,000 lines, many of which are too weak to be discernible in the plot.

The eigenenergies of the field-free hydrogen atom satisfy

$$E = w^{-2}\tilde{E} = -\frac{1}{2n^2}, \quad (6.1)$$

so that in the scaled spectrum the unperturbed n -manifolds appear equidistantly spaced at

$$w = \sqrt{-2\tilde{E}} n. \quad (6.2)$$

These spacings can clearly be recognized in figure 6.1. At low values of w , neighbouring n -manifolds are isolated. Furthermore, in this region the magnetic quantum number m is nearly conserved. This is apparent from the fact that each n -manifold contains a central group of strong levels corresponding to $m = 0$, which can be excited even at $\tilde{F} = 0$, and adjacent groups of considerably weaker levels with $m = \pm 1$. Levels with higher magnetic quantum numbers are too weak in this region to be seen in the figure. At higher values of w , the conservation of m is violated, and individual n -manifolds acquire strong side bands. At even higher w , different n -manifolds strongly overlap. Throughout the spectral range shown, groups of strong lines indicating the centres of different n -manifolds are clearly discernible.

6.2 Low-resolution semiclassical spectra

To obtain a semiclassical approximation to a scaled photo-absorption spectrum, the closed-orbit theory formulae of chapter 2 must be rewritten in terms of scaled quantities. Since the angular coordinates ϑ and φ obviously do not scale, the scaling properties of the semiclassical amplitude (2.43) are determined by those of the stability determinant M . By virtue of (4.101) the scaling prescription

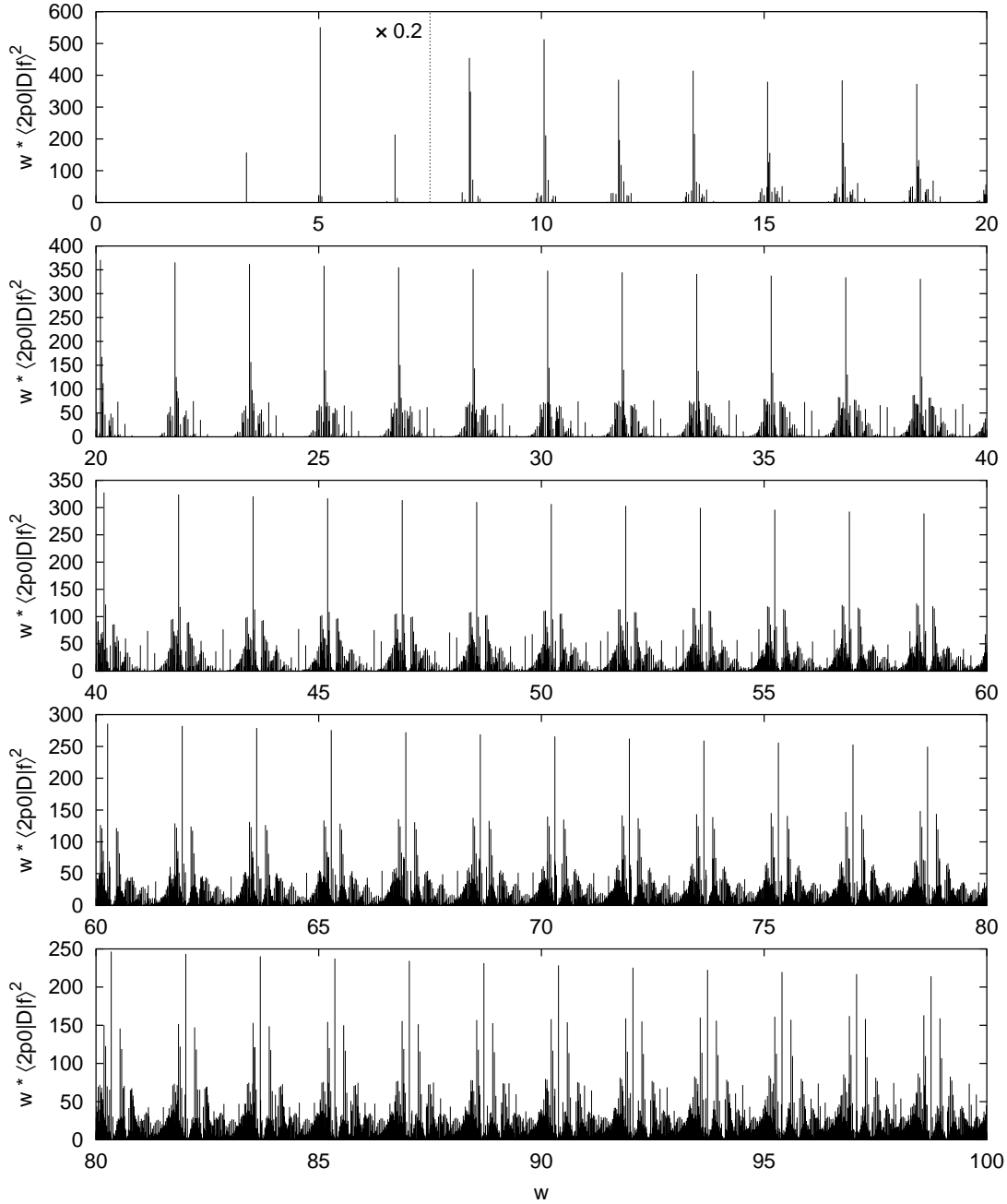


Figure 6.1: Quantum photo-absorption spectrum at the scaled energy $\tilde{E} = -1.4$ and the scaled electric field strength $\tilde{F} = 0.1$. The initial state is $|2p0\rangle$, the light is polarized along the magnetic field axis. The plot shows the squared dipole matrix elements, which for graphical reasons are multiplied by w . The strengths of the extraordinarily strong lines of the lowest n -manifolds at $w < 7.5$ are scaled down by a factor of 0.2.

is $M = w^2 \tilde{M}$, so that the oscillatory part (2.41) of the semiclassical response function reads

$$g^{\text{osc}}(w) = \frac{1}{w} \sum_{\text{c.o.}} \tilde{\mathcal{A}}_{\text{c.o.}} \exp\left(iw \tilde{S}_{\text{c.o.}}\right) \quad (6.3)$$

with

$$\tilde{\mathcal{A}}_{\text{c.o.}} = 4\pi \frac{\mathcal{Y}^*(\vartheta_f, \varphi_f) \mathcal{Y}(\vartheta_i, \varphi_i)}{\sqrt{|\tilde{M}|}} e^{i(\pi/2)\mu}, \quad (6.4)$$

which is of the form anticipated in (3.2), with $\gamma = -1$.

When low-resolution photo-absorption spectra are to be calculated from (6.3), a method of cut-off must be adopted to deal with the divergence of the semiclassical closed-orbit sum. For this section, I choose a Gaussian cut-off, i.e. (6.3) is replaced with

$$g_{\sigma}^{\text{osc}}(w) = \frac{1}{w} \sum_{\text{c.o.}} \tilde{\mathcal{A}}_{\text{c.o.}} \exp\left(iw \tilde{S}_{\text{c.o.}} - \frac{\tilde{S}_{\text{c.o.}}^2}{2\sigma^2}\right), \quad (6.5)$$

so that orbits with scaled actions larger than the cut-off action σ are smoothly suppressed. This smoothing corresponds to a convolution of the quantum signal with the Gaussian

$$f_{\sigma}(w) = \frac{\sigma}{\sqrt{2\pi}} \exp(-w^2 \sigma^2 / 2), \quad (6.6)$$

whereby individual spectral lines are replaced with Gaussians of width $1/\sigma$. The function f_{σ} is normalized according to

$$\int_{-\infty}^{\infty} f_{\sigma}(w) dw = 1, \quad (6.7)$$

so that the smoothing does not change the average spectral density taken over an interval larger than $1/\sigma$.

To facilitate the comparison of (6.5) with the convoluted quantum spectrum, I added the smooth part of the spectrum to g_{σ}^{osc} , which was calculated by convoluting the quantum spectrum with $f_{\sigma=1}$. This function is broad enough to wipe out the distinction between neighbouring principal quantum numbers. Results obtained for $\sigma = 20$ and $\sigma = 50$ are shown in figure 6.2. In both cases it is apparent that the large-scale structure of equidistant principal quantum numbers is well reproduced by the semiclassical approximation. In the quantum spectra, the substructure of the individual n -shells can be discerned to a certain degree, given by the smoothing width $1/\sigma$. In the case of $\sigma = 20$, much of this fine structure is also present in the semiclassical spectrum, but often the agreement is not good quantitatively. In particular, the peaks corresponding to the lowest n -manifolds are considerably wider in the semiclassical than in the quantum spectrum.

If the cut-off action is increased to $\sigma = 50$, finer details are resolved in the quantum spectrum. At the same time, the semiclassical closed-orbit sum becomes more oscillatory to reproduce this fine structure. It appears, however, to be somewhat over-oscillatory, developing structures absent from the quantum spectrum. This type of behaviour is typical of closed-orbit sums in non-integrable systems.

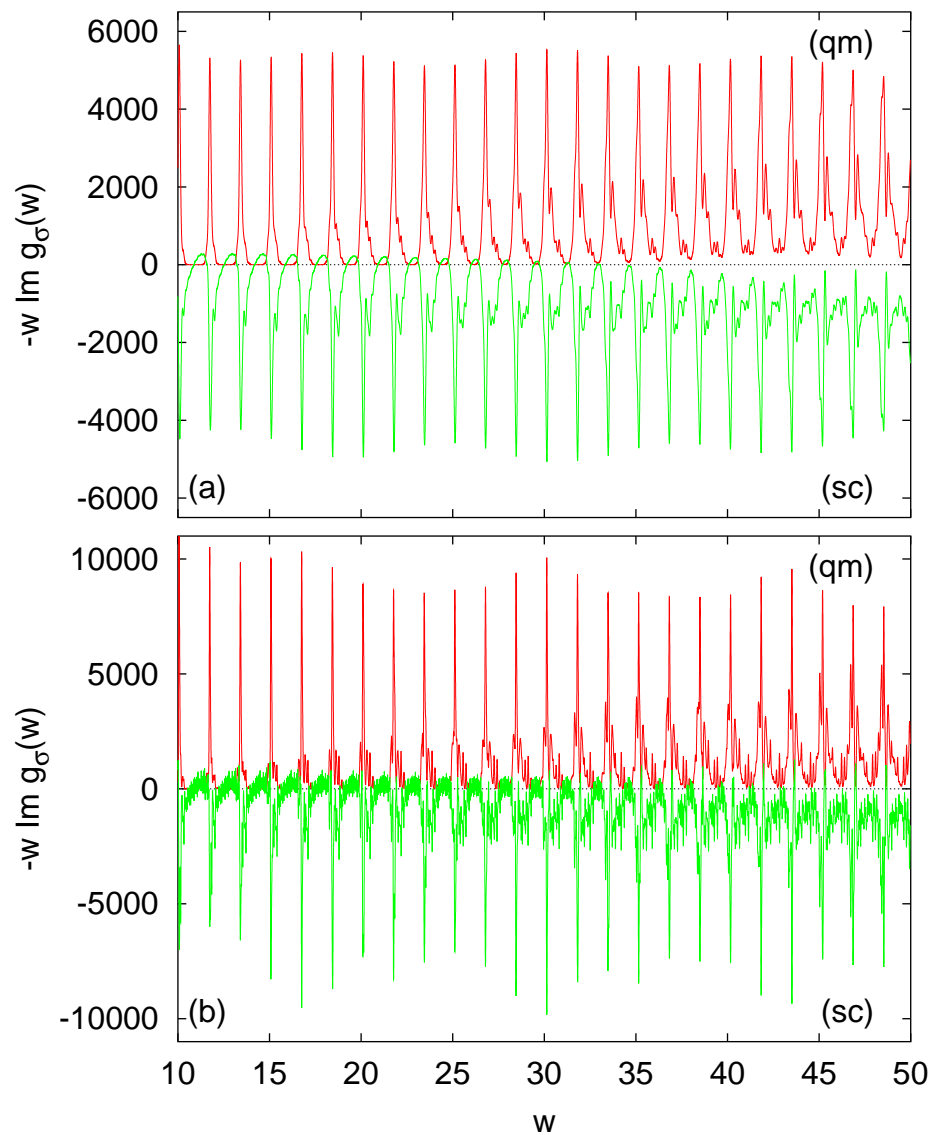


Figure 6.2: Smoothed quantum (upper halves) and semiclassical (lower halves, inverted) photo-absorption spectra with cut-off action (a) $\sigma = 20$ and (b) $\sigma = 50$.

Thus, it can be questioned if the low-resolution closed-orbit sum can meaningfully be extended to even longer orbits. A high-resolution quantization based on the present semiclassical approximation will be presented in the following section.

6.3 High-resolution semiclassical spectra

For the calculation of a scaled semiclassical spectrum, the method of semiclassical quantization by harmonic inversion of δ function signals described in section 3.1 can be applied. This technique requires the inclusion of closed orbits up to a maximum scaled action, i.e. it replaces the Gaussian cut-off used for the low-resolution semiclassical spectra presented in the previous section with a rectangular cut-off. A rough estimate for the required cut-off action can be obtained by using first-order perturbation theory. This approach cannot be expected to yield precise results, but if the field strengths are small, a reasonable estimate is obtained for low n -manifolds.

To first order in the external field strengths, the atomic energy levels are given by [98]

$$E_{nq} = -\frac{1}{2n^2} + \omega q, \quad (6.8)$$

where

$$\omega = \frac{1}{2}\sqrt{B^2 + 9n^2F^2} \quad (6.9)$$

and $q = -(n-1), -(n-1)+1, \dots, n-1$. If (6.8) is rewritten in terms of eigenvalues of w for a scaled spectrum, one obtains

$$w_{nq} = \sqrt{-2\tilde{E}}n + \sqrt{-2\tilde{E}}\tilde{\omega}q \approx \sqrt{-2\tilde{E}}n + \frac{q}{-4\tilde{E}} \quad (6.10)$$

with

$$\tilde{\omega} = n^3\omega = \frac{1}{8\tilde{E}^2}\sqrt{9\tilde{F}^2 - 2\tilde{E}} \approx \frac{1}{2}(-2\tilde{E})^{-3/2}. \quad (6.11)$$

The last approximation could be made because in the region of low field strengths \tilde{F} is small, whereas \tilde{E} is large. Therefore, to first order each n -manifold splits into $2n-1$ lines. To higher order in the field strengths, the degeneracy is lifted completely, and the lines split into groups characterized by n and q and containing $n-q-1$ levels. For low electric field strength and the initial state $|2p0\rangle$, it is mainly the states with $q=0$ that contribute to the spectrum. The group $q=0$ contains $n-1$ individual levels, but in a photo-absorption spectrum every second level is absent due to parity selection rules, so that the group effectively consists of approximately $n/2$ lines.

The splitting of lines in a q group, and thus the effective spectral density, is a second-order effect. To estimate it, therefore, second-order perturbation theory is required. To circumvent this necessity, I assume the spectral lines in a group to be evenly scattered across an interval whose width is the distance of groups obtained from first-order perturbation theory. In view of the spectrum in figure 6.1, this approximation appears reasonable. I can therefore estimate the spectral density

by regarding the $q = 0$ group as containing $n/2$ lines in an interval whose width is the distance between groups, viz. $1/(-4\tilde{E})$. The spectral density is therefore $\bar{\rho} = -2\tilde{E}n$, and the required signal length is

$$\tilde{S}_{\max} = 4\pi\bar{\rho} = -8\pi\tilde{E}n. \quad (6.12)$$

As the number of levels in a group with $q \neq 0$ is smaller than for $q = 0$, this signal length should suffice for all groups whose levels are strong enough to be semiclassically detected in the spectrum. For the case $\tilde{E} = -1.4$ and $n = 9$, i.e. $w = 15.06$, this estimate yields $\tilde{S}_{\max}/2\pi = 50$.

In the present case, the quantum spectrum is known. From the spectrum, a test signal composed of the given spectral lines can be constructed. If a sufficiently long part of this signal is subjected to a high-resolution harmonic analysis, the known frequencies must be regained. The signal length required for the harmonic inversion to succeed can thus be determined. This approach confirms that the perturbative result (6.12) yields good results if n is odd. For even n , (6.12) should be used with n replaced with $n - 1$, because the $q = 0$ groups in the manifold n and $n - 1$ actually contain the same number of spectral lines. In practice, because the semiclassical signal contains some noise, the required signal length must be expected to be slightly larger than for the ideal test signal.

According to (6.12), to compute levels at high quantum numbers n a long semiclassical signal is needed, which can be hard or even impossible to obtain. I calculated closed orbits up to $\tilde{S}_{\max} = 200$, so that the orbital data is available for nearly 18,000 closed-orbit multiplets. However, for reasons to be described below a useful semiclassical signal can be constructed up to $\tilde{S}_{\max}/2\pi \approx 60 - 70$ only, so that, from the above estimate, the semiclassical calculation cannot reach manifolds much higher than $n = 10$. On the other hand, the semiclassical approximation must be expected to yield more accurate results for higher quantum numbers. Thus, when a high-resolution semiclassical spectrum is to be calculated, a compromise must be made between the contradictory requirements of describing a spectral region at sufficiently high quantum numbers and with a sufficiently low spectral density.

Results obtained for $\tilde{E} = -1.4$ and $\tilde{F} = 0.1$ with a signal length of $\tilde{S}_{\max}/2\pi = 60$ and the method of δ function decimated signal diagonalization (method 4 of section 3.2.4) are compiled in table 6.1. The table contains the quantum eigenvalues of w and their dipole matrix elements for levels satisfying $\langle 2p0|D|f \rangle^2 > 0.7$. It is obvious at a glance that out of the multitude of spectral lines with intensities varying over many orders of magnitude (most of which are not contained in the table) only the strongest lines were detected in the semiclassical spectrum. The semiclassical eigenvalues given are characterized by having small imaginary parts, small error parameters (see chapter 3) and large amplitudes as well as being stable with respect to a variation of numerical parameters. The calculation operates at the edge of convergence, and in a few cases one can be in doubt whether a level should be included according to these fairly “soft” criteria, but in general a clear decision can be made. Semiclassical values for the transition strengths are not given because they are not reasonably well converged and depend strongly on the numerical parameters.

n	w_f (scl.)	w_f (qm.)	$\langle 2p0 D f\rangle^2$	n	w_f (scl.)	w_f (qm.)	$\langle 2p0 D f\rangle^2$
6		9.88321	1.3617	9	15.12905	15.12748	10.3140
		9.91431	3.1145		15.17892	15.17491	2.2476
		9.97747	1.7474		15.23623	15.23830	3.1064
	10.05366	10.05912	51.0512		15.26111	15.27005	1.7749
	10.09551	10.09621	20.9313			15.30024	2.3710
	10.15461	10.15378	7.0060			15.34449	1.0296
		10.24076	0.9608			15.40389	3.3462
		10.26612	2.0777			16.57908	0.7173
7		10.31803	1.9385		16.58435	1.7007	
		11.56497	2.5663		16.60357	1.7437	
	11.60898	11.60820	2.5875	16.64355	16.63843	2.9662	
	11.66889	11.67341	2.3104	16.69069	16.69180	0.9974	
	11.72048	11.73128	32.8808	16.74965	16.75258	22.9143	
		11.75121	16.7278		16.76016	3.4901	
		11.78850	10.0092	10	16.78346	16.78269	11.1809
		11.84856	5.6249		16.81329	16.81827	6.6898
		11.92188	1.9229			16.86870	0.9825
		11.95821	1.7923		16.93431	16.93323	2.0584
8		12.01338	2.4821			16.94303	1.4143
		13.23441	1.3668			16.96000	1.4406
		13.25629	2.5141			16.99085	2.3893
		13.30255	1.9971			17.09909	3.5870
	13.36921	13.36913	2.8189			17.25847	0.7647
	13.40177	13.40568	30.8875			18.25950	2.1201
	13.44313	13.43744	16.0829			18.27572	0.9781
	13.48737	13.48146	4.8263			18.29004	2.6665
		13.54340	4.3111			18.33096	2.7709
		13.59258	1.0747		18.42131	18.42600	20.2420
		13.61133	1.9475			18.45136	6.1451
		13.65111	1.4081			18.45555	3.5970
9		13.70866	2.9676	11	18.47472	18.47149	7.2231
		14.91192	2.1880			18.50996	4.0510
		14.94654	2.9922			18.61835	1.7975
		14.99711	1.4563			18.62818	1.2089
	15.06960	15.06470	3.2226			18.64563	2.2348
		15.07888	25.1866			18.68226	2.2558
		15.10074	8.4317			18.79427	3.6707
						18.93585	1.0263
						18.95442	

Table 6.1: Semiclassical and quantum eigenvalues w_f of the scaling parameter for $\tilde{E} = -1.4$ and $\tilde{F} = 0.1$. See text for a detailed description. The dipole matrix elements $\langle 2p0|D|f\rangle^2$ were obtained from a quantum spectrum.

One might expect that in each n -manifold it is the strongest lines that are detected semiclassically, and in general this expectation is confirmed by the numerical data. This can clearly be seen, e.g., in the manifold $n = 6$, which contains the most stably converged lines in the spectrum. There are, however, a few conspicuous exceptions, e.g. at $n = 7$, where strong lines are missing whereas comparatively weak lines are found. For $n = 5$, no lines at all can be computed from the given semiclassical signal. If the signal length is decreased to $\tilde{S}_{\max}/2\pi = 50$, the three strongest lines appear in the spectrum in this manifold.

At higher n , the number of strong lines in the quantum spectrum increases. So does the number of lines in the semiclassical spectrum until $n = 11$, where only three semiclassical lines are found. They appear rather arbitrarily scattered across the quantum spectrum, and their convergence is notably worse than in lower manifolds. It is clear that in this n -shell the semiclassical quantization with the given signal is about to break down. At $n = 12$, no lines can be detected semiclassically. As, from the above discussion, this failure was to be expected because the required signal length becomes too large, the obvious way to improve convergence seems to be to use a longer signal. However, if the signal length is increased to $\tilde{S}_{\max}/2\pi = 70$, no reasonably converged semiclassical lines can be found in any n -manifold. Neither are results improved if the technique of harmonic inversion of cross-correlated closed-orbit sums [5, 99] is applied. This method has proven powerful in reducing the signal length required in a semiclassical quantization. In the present case, however, because the cross-correlation increases the total number of frequencies obtained from the harmonic inversion, the true eigenvalues are hidden among a multitude of spurious frequencies, and no useful results can be obtained.

For the time being, therefore, the results given in table 6.1 represent what can be achieved in the semiclassical quantization of the crossed-fields hydrogen atom. They confirm the applicability of the closed-orbit theory approach in principle, but they also reveal a fundamental problem in its present formulation. From the analysis of the ideal test signal it is clear that the signal length available is sufficient for a stable signal analysis. Thus, if the semiclassical results are not good, the semiclassical signal itself, rather than the signal analysis, must be to blame. This conclusion is confirmed by the observation that an increased signal length destroys the results rather than improves them. I therefore start searching for a flaw in the construction of the semiclassical photo-absorption spectrum.

The most conspicuous problem has already been mentioned in the description of figure 5.12: The set of closed orbits available is incomplete. In no series of rotators or vibrators can arbitrarily long orbits be calculated. In the case of vanishing electric field (see figure 5.4) there is a critical angle ϑ_c which the starting angles of both rotators and vibrators approach as the orbits get longer. This convergence indicates that the orbits approach a separatrix between two families of tori in phase space. If sufficiently long orbits are studied, there are many closed orbits with very similar initial conditions, so that they are hard to find numerically. For the closed-orbit search I use a shooting algorithm where a trajectory is launched from the nucleus in a given initial direction and followed

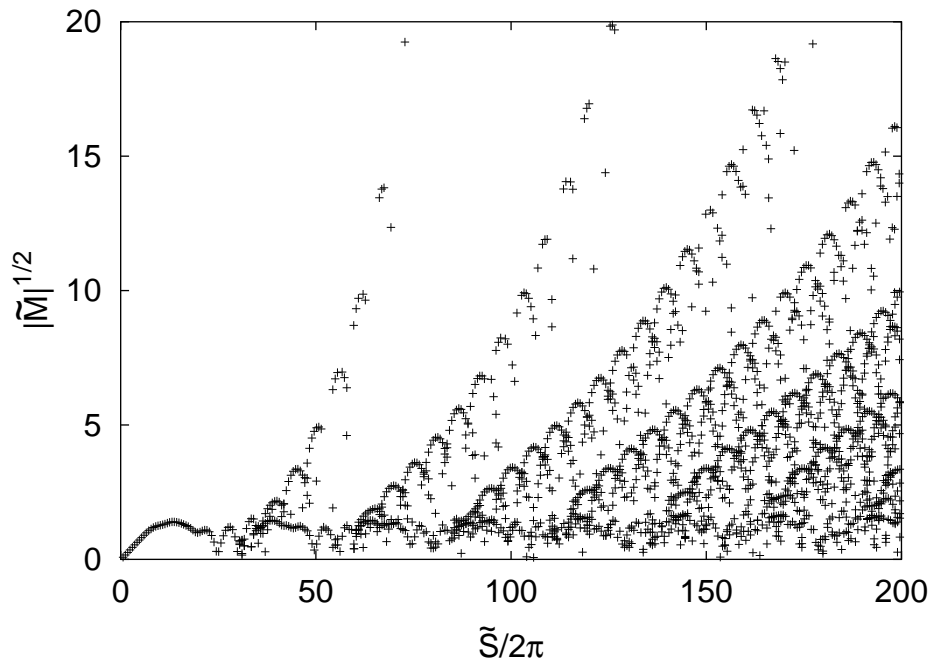


Figure 6.3: Stability determinants of vibrators as a function of the action for $\tilde{E} = -1.4$, $\tilde{F} = 0.1$.

for a given time. Newton's method is then used to adjust the initial conditions and the fictitious-time orbital period in such a way that the trajectory returns to the nucleus. This procedure must be repeated for different initial directions forming a sufficiently fine mesh if a complete set of closed orbits is required. To find closed orbits close to the separatrix, the initial conditions must be specified to an ever higher degree of accuracy. The situation is exacerbated in crossed fields, because each DKP orbit is split into two or more individual orbits, and because two initial angles ϑ_i and φ_i are to be varied in the shooting method, so that choosing an ever finer mesh size quickly exhausts the computer power available.

Because close to the separatrix Newton's method tends to converge to orbits whose initial conditions are quite far apart from where the root search originally started, I implemented a globally convergent root search using the backtracking algorithm described in [59, chapter 9.7]. In practice, this algorithm did not help to find any additional orbits close to the separatrix. As it drastically increases the computer time, it was abandoned again.

A weakness of the closed-orbit search might be the simple Adams-Bashforth integration scheme used to solve the equations of motion. Possibly, a symplectic integrator might have proven more stable in the critical region. However, as the equations of motion are not separable into a purely kinetic and a purely potential part, an implicit integrator is required. Its implementation would have required rather large an effort. As the incompleteness of the semiclassical signal did not seem to be the crucial problem in the quantization, I did not pursue this point further.

The region of phase space where the unknown orbits are located is lying close to a separatrix, so that it is highly unstable. The orbits can therefore be expected not to contribute much to the semiclassical signal. The magnitude of an orbit's contribution to the closed-orbit sum (2.41) is determined mainly by its stability determinant M . Figure 6.3 shows the stability determinants of the vibrator orbits for $\tilde{E} = -1.4$, $\tilde{F} = 0.1$ as a function of the scaled action. Different series of vibrators can clearly be discerned in the plot. It is indeed unstable orbits with large \tilde{M} that are missing in the data set, but on the other hand the stability determinants of the missing orbits are not large enough to regard the corresponding semiclassical amplitudes as negligibly small. Because a vast majority of orbits has small \tilde{M} and was found, one can still hope that useful results can be obtained from the semiclassical signal, at least for quantum states not located in the separatrix region in phase space, but it is clear that the quality of the semiclassical signal is reduced by its incompleteness.

To assess in detail the detrimental effect of the missing orbits and of any other sources of error that may exist, I carry out a semiclassical analysis of the quantum spectrum.

6.4 Semiclassical recurrence spectra

As described in section 3.1, in a scaled photo-absorption spectrum every closed orbit contributes a purely sinusoidal modulation which can be extracted from the spectrum either by a conventional Fourier transform or by means of a high-resolution method. The spectral analysis yields information about classical orbits returning to the nucleus. For this reason, the transformed spectrum is referred to as a recurrence spectrum. High-resolution methods extract the scaled actions and scaled semiclassical amplitudes of individual orbits and thus yield more complete information about the semiclassical spectrum than the Fourier transform, but they fail if the average density of closed orbits per unit of scaled action is too large. By contrast, due to its linearity the Fourier transform can be applied to any part of the recurrence spectrum with equal ease and numerical stability, irrespective of the spectral density. In dense regions, it will not be able to identify individual closed orbits, but it will nevertheless yield a recurrence spectrum that can be compared to the classical data. In this section I will present results obtained by both the Fourier transform and a high-resolution method. The semiclassical recurrence spectra will be compared to classical results in order to identify the reason why the semiclassical signal is only partially suitable to a semiclassical quantization.

Using either method, it is essential to note that the semiclassical closed-orbit formula cannot be expected to yield accurate results for the lowest levels. Thus, the low n -manifolds must be excluded from the semiclassical analysis, i.e. the analysis is based on the quantum spectrum given in an interval $[w_{\min}, w_{\max}]$ instead of $[0, w_{\max}]$. This shift introduces an additional phase factor $e^{iw_{\min}\tilde{S}_{c.o.}}$ into each closed-orbit contribution, which can easily be corrected for if the action $\tilde{S}_{c.o.}$ is determined by a high-resolution method. For the Fourier transform, this kind

of correction is impossible, so that a fast oscillation $e^{iw_{\min}\tilde{S}}$ arises in the Fourier recurrence spectrum. To circumvent this difficulty, only the absolute value of the Fourier spectrum will be discussed in the following.

Furthermore, to minimize the impact of boundary effects due to the finite length of the semiclassical spectrum, a smooth Gaussian cut-off with width κ centred at $w_0 = (w_{\min} + w_{\max})/2$ is introduced. In analogy with (6.6), the smoothing replaces the peaks of the semiclassical recurrence spectrum by Gaussians of width $1/\kappa$. The recurrence spectra presented here were calculated from the quantum spectrum shown in figure 6.1, for $\tilde{E} = -1.4$ and $\tilde{F} = 0.1$, with $w_{\min} = 20$, $w_{\max} = 100$, and $\kappa = 10$. For the high-resolution recurrence spectra, the method of δ function decimated signal diagonalization was used.

For low scaled actions, where only few closed orbits exist, the high-resolution analysis can be applied. Results are shown in figure 6.4, which compares both the scaled actions and the real and imaginary parts of the semiclassical amplitudes extracted from the quantum spectrum to the classical results. For most closed orbits, the agreement is excellent. Exceptions occur for the shortest orbits, where the actions of rotator and vibrator orbits are too similar to be resolved by the harmonic inversion. At somewhat larger actions, the three orbits in each group fall apart into two rotator orbits with similar actions and a vibrator orbit with a slightly larger action. Note that it is the vibrator orbit which has the largest amplitude. In this parameter regime, the spectrum is far from being dominated by planar orbits, as has often been observed in the literature [8, 84].

These observations can be made even more clearly if the absolute values of the amplitudes are considered. They are shown in figure 6.5, where the results of the high-resolution analysis are also compared to those of the Fourier transform. Notice that for the Fourier transform the semiclassical amplitude is given by the area under a peak rather than the peak height, so that an immediate comparison to the high-resolution results is difficult. In figure 6.5, the Fourier transform was arbitrarily scaled so that the peak heights roughly match the values of the high-resolution amplitudes. For isolated orbits identified both in the Fourier transform and the high-resolution spectrum, the agreement between the two methods is excellent. Where several peaks overlap in the semiclassical spectrum, no direct comparison is possible because the peak phases cannot be determined from the figure.

Figure 6.5 also extends the results shown in figure 6.4 to higher actions. In this region the density of closed orbits starts to increase because, on the one hand, rotators of the first series exist and, on the other, bifurcations of closed orbits generate additional orbits. Apart from the fact that many orbits cannot be identified individually even by the high-resolution method, the most conspicuous feature of figure 6.5 is that for many orbits the semiclassical amplitudes calculated from the classical data are considerably larger than those extracted from the quantum spectrum. In some cases, this is obvious at a glance, but a closer inspection of the figure reveals that this phenomenon is rather common. Some specific cases will be described in detail in section 6.5.

The occurrence of exceedingly large semiclassical amplitudes is a well-known

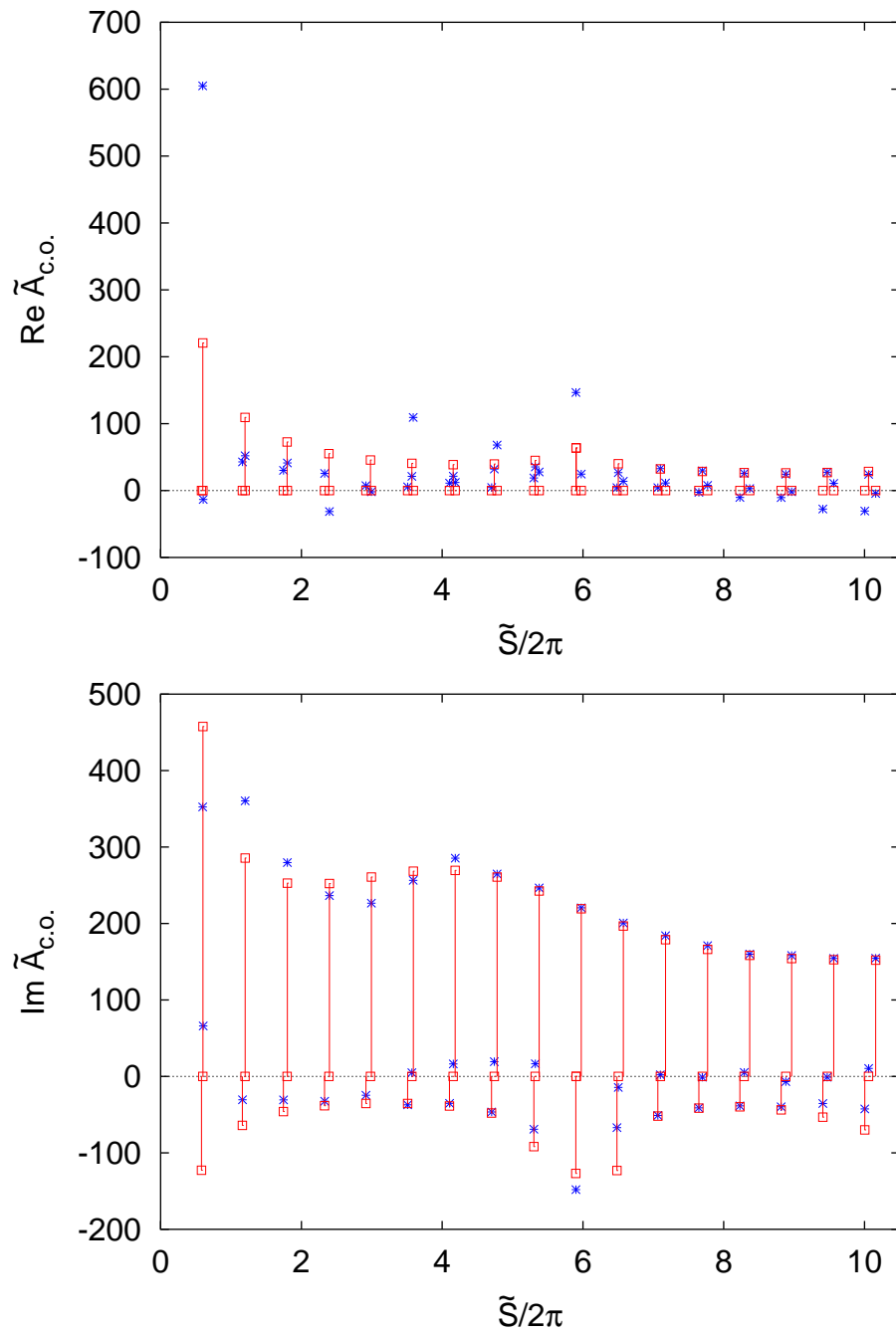


Figure 6.4: High-resolution recurrence spectrum for $\tilde{E} = -1.4$ and $\tilde{F} = 0.1$. Sticks and squares: semiclassical closed-orbit amplitudes, stars: harmonic inversion of the quantum spectrum.

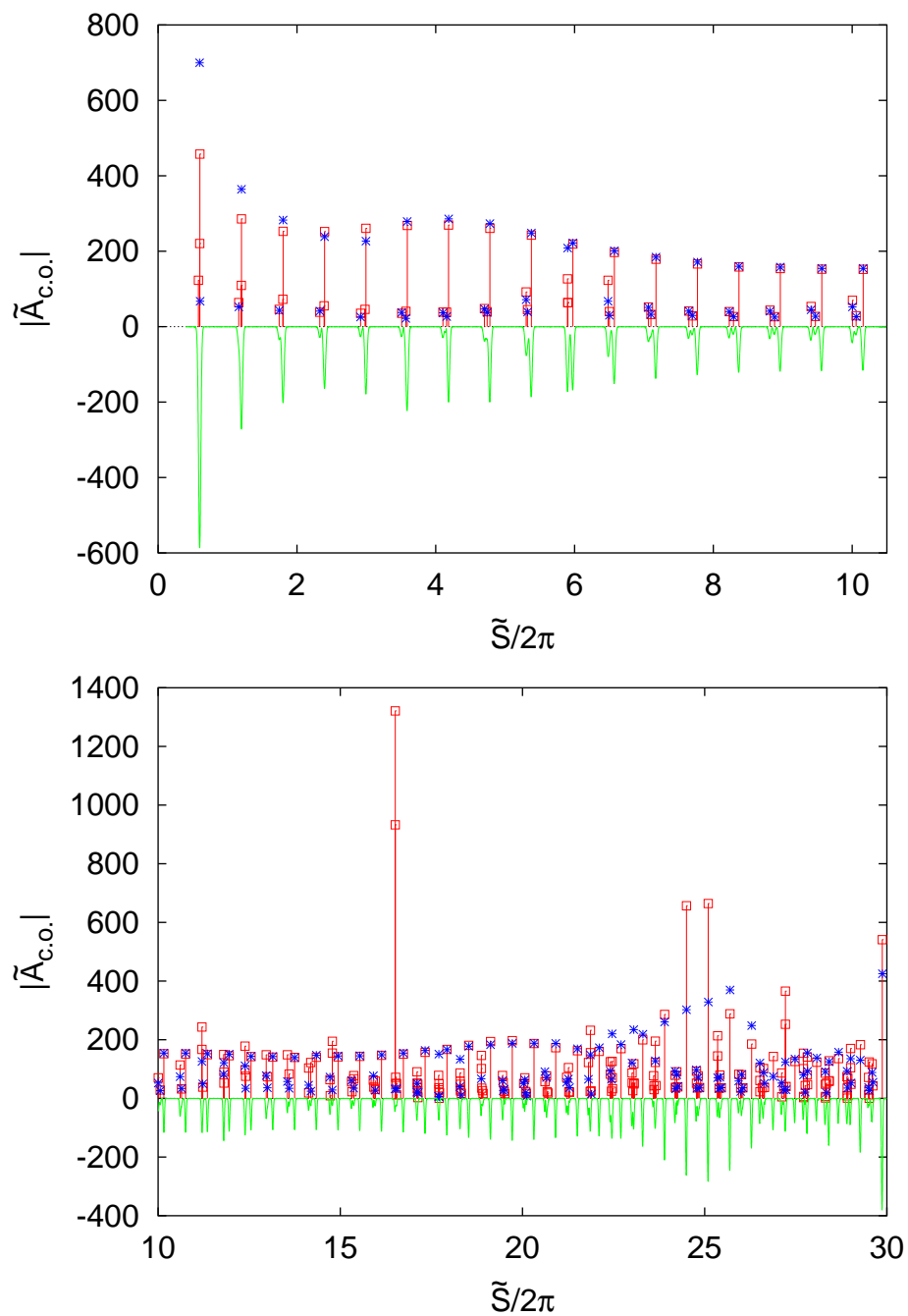


Figure 6.5: Absolute value of the recurrence spectrum. Sticks and squares: semi-classical closed-orbit amplitudes, stars: harmonic inversion of the quantum spectrum. Solid curve, inverted: Fourier transform (arbitrary units).

problem of both closed-orbit and periodic-orbit theory. It is associated with bifurcations of classical orbits, where, in the case of closed orbits, the stability determinant M vanishes and the closed-orbit amplitude (2.43) diverges. Close to the bifurcation, M is small. The semiclassical amplitude of the bifurcating orbit is therefore large and exceeds the value determined from the quantum spectrum. In a classical context, it has been shown in section 5.1 that vanishing M is both a necessary and sufficient condition for a bifurcation of closed orbits. In the context of semiclassical closed-orbit theory, it is necessary to overcome the divergence of the closed-orbit formula occurring close to a bifurcation. This problem will be addressed in section 6.5, after the impact of the bifurcations on the semiclassical signal at hand has been investigated further.

Whereas, in figure 6.5, the vibrator orbits are sufficiently isolated to be resolved by both the harmonic inversion and the Fourier transform across the entire range of actions, the rotators occur in groups of several orbits having nearly identical actions. They are not resolved properly by either method. Instead, the Fourier transform produces peaks describing the collective contribution of the orbits in a group. The harmonic inversion fits this contribution with fewer actions and amplitudes than the actual number of orbits. Although the results can be expected to reproduce the quantum spectrum fairly well, the principal virtue of the high-resolution analysis – that it is capable of giving individual rather than collective contributions – is lost. It is therefore pointless to extend the high-resolution analysis to higher actions unless a significantly longer quantum spectrum can be obtained, and only the Fourier transform will be used henceforth.

Figure 6.6 displays the Fourier recurrence spectrum with smoothing $\kappa = 10$ for scaled actions up to $\tilde{S}/2\pi = 100$ and compares it to the semiclassical spectrum. These results extend the semiclassical analysis of quantum spectra to significantly longer orbits than investigated in previous studies. They allow a verification of closed-orbit theory all the way up to the long orbits. It is immediately apparent from the figure that the quantum recurrence spectrum retains its pronounced peak structure. This is to be expected from closed-orbit theory, and indeed the peak locations are given by the actions of closed orbits for long as well as for short orbits. The basic idea of closed-orbit theory that recurrence peaks are related to classical closed orbits is therefore confirmed in principle even for very long orbits.

Even for the largest actions considered, the quantum and semiclassical recurrence spectra agree quantitatively for some peaks. For most peaks, however, the peak heights in the quantum and semiclassical spectra disagree. There are quantum peaks that are smaller in the semiclassical spectrum or even completely absent. They can be attributed to missing orbits. On the other hand, in many cases the semiclassical peaks are significantly higher than the quantum peaks, sometimes by several orders of magnitude. Exceedingly high peaks can be traced back to bifurcations of closed orbits if the possibility is ignored that a quantum peak can be small because orbits missing in the semiclassical spectrum interfere destructively with the orbits present. This latter mechanism becomes the more implausible the larger the semiclassical peak is in comparison to the quantum peak.

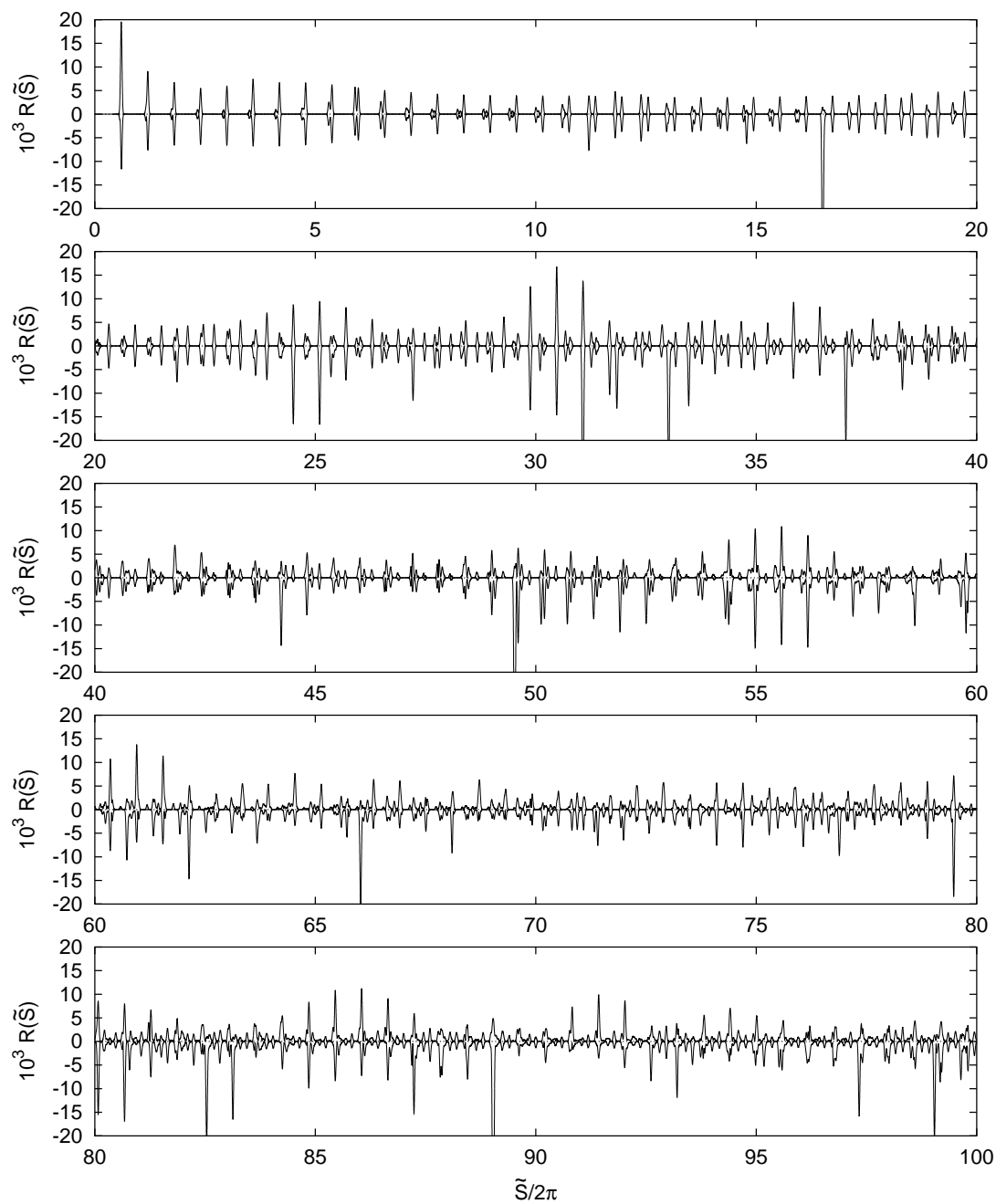


Figure 6.6: Absolute value $R(\tilde{S})$ of the recurrence spectrum with $\kappa = 10$ (see text). Upper part: Fourier transform of the quantum spectrum, lower part (inverted): smoothed semiclassical recurrence spectrum.

Taken together, the effects of missing orbits and of bifurcating orbits distort the semiclassical recurrence spectrum to the point where it can no longer be expected to provide a suitable basis for a quantization. A close inspection of the recurrence spectrum suggests that the problem posed by bifurcating orbits is more severe. Exceedingly high peaks do not only occur frequently, but in addition the very fact that they are high increases their detrimental effect on the semiclassical photo-absorption spectrum. Unless a suitable scheme for dealing with bifurcating orbits can be devised, no improvement of the semiclassical signal can be expected. I therefore turn to a description of the semiclassical treatment of bifurcating orbits by means of uniform approximations.

6.5 Uniform approximations

6.5.1 The construction of uniform approximations

The crucial step in the derivation of the semiclassical closed-orbit formula is the stationary-phase evaluation of the integrals in (2.27), where the semiclassical Green's function is projected onto the channel functions. This approximation leads to the sum (2.28) over individual closed orbits, and it assumes that the closed orbits are sufficiently isolated to yield independent stationary-phase contributions to the integral. This assumption fails close to a bifurcation of closed orbits, because orbits involved in a bifurcation approach each other arbitrarily closely before they eventually collide. It is this close approach of orbits that causes the divergence of the individual closed-orbit amplitudes.

This diagnosis of the problem already implies its cure: If close to a bifurcation several closed orbits cannot be regarded as isolated, a collective contribution of the bifurcating orbits must be found. This solution was first suggested by Ozorio de Almeida and Hannay [100] in the context of periodic-orbit theory. Their original approach was extended by different authors, so that today uniform approximations are a well-established tool of semiclassical physics. In the context of semiclassical trace formulae, uniform approximations for all generic types of periodic-orbit bifurcations were derived by Sieber and Schomerus [101–103]. Analogous work was done in the context of closed-orbit theory by Main and Wunner [96], although in this case a systematic classification of the generic bifurcations was missing. Of particular importance is the observation that bifurcations of codimension higher than one are relevant to semiclassics, although on a classical level they are not generically encountered. They appear as sequences of generic bifurcations, which, if the individual bifurcations are sufficiently close, must be described collectively by a single uniform approximation. Several examples of uniform approximations for these complicated bifurcation scenarios have been described in the literature [96, 104–107].

The principal requirement a uniform approximation must satisfy is to asymptotically reproduce the known isolated-orbits approximation when the distance from the bifurcation grows large, because in this limit the stationary-phase approximation can be expected to be accurate. In the following, I will advocate a

somewhat heuristic technique for the construction of a uniform approximation, which is easy to handle and yields a smooth interpolation between the asymptotic isolated-orbits approximations on either side of the bifurcation. It will first be described in general terms. In subsequent sections, uniform approximations describing the generic types of codimension-one bifurcations of closed orbits will be derived. I will then come to a discussion of how these uniform approximations can be used to improve the semiclassical recurrence spectra presented in the preceding section, and some complicated bifurcation scenarios presenting open problems will be described. Further applications of this method will be given in section 7.4.

In the present section, uniform approximations for semiclassical spectra recorded at fixed field strengths, rather than scaled spectra, will be described. In these spectra, the divergence of the isolated-orbits approximation is actually encountered as the energy is varied across the bifurcation energy. The modifications required for scaled spectra are straightforward. They will be described in section 6.5.4.

It was shown in section 5.1 that a bifurcation scenario can be described by a normal form $\Phi_a(t)$ depending on $n \geq 1$ variables t and $m \geq 1$ parameters a . For the generic codimension-one bifurcations, $\Phi_a(t)$ is either the fold catastrophe (5.12) or the symmetrized cusp catastrophe (5.16). Let, for a given bifurcation scenario, $\Phi_a(t)$ be a suitable normal form, i.e. for any fixed value of the parameters a there are stationary points of $\Phi_a(t)$ corresponding to the closed orbits involved in the bifurcation. The parameters a must then depend on the energy E to reproduce the bifurcations of the closed orbits.

For the uniform approximation I make the ansatz

$$\Psi(E) = I(a) e^{iS_0(E)} \quad (6.13)$$

with

$$I(a) = \int_{\mathbb{R}^n} d^n t p(t) e^{i\Phi_a(t)}. \quad (6.14)$$

Here, the functions $S_0(E)$ and $p(t)$ as well as the parameter values $a(E)$ have to be determined. All of them must be smooth functions of E .

To find the asymptotic behaviour of the uniform approximation (6.13) far from the bifurcations, (6.14) is evaluated in the stationary-phase approximation, which yields

$$\Psi(E) \approx \sum_{t_i} \frac{(2\pi i)^{n/2} p(t_i)}{\sqrt{|\text{Hess } \Phi_a(t_i)|}} e^{i(S_0(E) + \Phi_a(t_i))} e^{-i\pi\nu_i/2}, \quad (6.15)$$

where the sum extends over all stationary points t_i of $\Phi_a(t)$ that are real at the given a , $\text{Hess } \Phi_a$ is the Hessian determinant of Φ_a , and ν_i is the number of negative eigenvalues of $\text{Hess } \Phi_a(t_i)$. This expression is supposed to reproduce the isolated-orbits approximation

$$\Psi(E) \approx \sum_{\text{c.o. } i} \mathcal{A}_i(E) e^{iS_i(E)}. \quad (6.16)$$

In this case, the sum extends over all closed orbits involved in the bifurcation that are real at the given energy E . If the normal form $\Phi_a(t)$ has been chosen suitably, there is a one-to-one correspondence between these orbits and the stationary points t_i . A comparison of (6.15) to (6.16) yields the conditions

$$S_i(E) = S_0(E) + \Phi_a(t_i) \quad (6.17)$$

and

$$\mathcal{A}_i(E) = \frac{(2\pi i)^{n/2} p(t_i)}{\sqrt{|\text{Hess } \Phi_a(t_i)|}} e^{-i\pi\nu_i/2}. \quad (6.18)$$

These equations must be valid for real orbits. In most bifurcation scenarios, all orbits are real at least at certain energies. In these cases, it appears natural to postulate (6.18) also to hold for ghost orbits. The parameter values one obtains are then smooth functions of the energy even at the bifurcations where the orbits become ghosts. In some instances, bifurcations involving only ghost orbits occur [107, 108]. In these cases, the condition (6.18) still produces smoothly varying parameters and enforces the desired asymptotics.

The numbers ν_i of negative eigenvalues change discontinuously at a bifurcation. For orbits which are real on either side of the bifurcation, so do the Maslov indices contained in the semiclassical amplitudes \mathcal{A}_i . These changes must compensate each other if the values $p(t_i)$ are to be continuous across the bifurcation. For these orbits, therefore, the change of Maslov index occurring in a bifurcation must be equal to the change in ν_i and can be determined from the normal form. For ghost orbits, Maslov indices are not well defined classically. They must be chosen such as to make $p(t_i)$ continuous.

In some cases, in particular when many ghost orbits are involved, it can be easier to use semiclassical amplitudes not involving the Maslov indices, i.e. to decompose them as

$$\mathcal{A}_i = A_i e^{-i\mu_i\pi/2}, \quad (6.19)$$

where μ_i are the Maslov indices. In terms of the A_i , (6.18) reads

$$A_i(E) = \frac{(2\pi i)^{n/2} p(t_i)}{\sqrt{|\text{Hess } \Phi_a(t_i)|}}. \quad (6.20)$$

In the uniform approximation

$$\Psi(E) = I(a) e^{iS_0(E) - i\mu_0\pi/2} \quad (6.21)$$

a Maslov factor must be added to obtain the correct overall phase, i.e. $\mu_0 = \mu_i - \nu_i$ for an arbitrary real orbit i . In (6.20), the apparent discontinuity has disappeared, real orbits are given the correct Maslov phases in the asymptotic stationary phase approximation by the indices ν_i , and there is no need to ascribe a Maslov index to a ghost orbit.

The normal form parameters a and the action $S_0(E)$ can be determined from (6.17). They usually turn out to be unique. The amplitude function $p(t)$,

on the contrary, is unknown. Once the parameters a have been found, (6.18) specifies its values $p(t_i)$ at the stationary points of $\Phi_a(t)$. These values, of course, do not suffice to identify $p(t)$ uniquely, so that there is considerable freedom in the choice of $p(t)$. Usually, if there are k orbits participating in the bifurcation scenario, I will approximate $p(t)$ by a polynomial of degree $k - 1$. This choice is justified by the observation that the uniform approximation is needed only close to a bifurcation, where all orbits are close to $t = 0$. Thus, in the spirit of the stationary-phase approximation, the dominant contributions to the integral (6.14) stem from the neighbourhood of $t = 0$, whereas the regions of large t do not contribute. A suitable approximation to $p(t)$ must therefore be precise close to the origin. This is achieved by a Taylor series expansion, which leads to the polynomial ansatz.

Simple as it might appear, however, this choice can bring about a mathematical difficulty: A polynomial $p(t)$ diverges as $t \rightarrow \infty$, so that there is no guarantee that the integral (6.14) will converge. If it does not, its divergence is an artefact of the choice of $p(t)$, because by construction the regions of large t should not significantly influence the value of the integral. In this case, a suitable regularization scheme must be applied. It can be justified by verifying that the regularized integral possesses the correct asymptotics.

A slightly simpler form of the uniform approximation is obtained if the function $p(t)$ is assumed to be a constant. This approximation does not exactly reproduce the desired asymptotics, but as the transition across the bifurcation mainly results in a change of the stationary points of $\Phi_a(t)$ rather than essential changes in $p(t)$, it can be expected to capture the principal features. In particular, in the immediate vicinity of the bifurcations all orbits are extremely closely spaced, so that the $p(t_i)$ must be nearly equal. The amplitude equations (6.18), with $p(t_i)$ set equal to a constant p_0 , can then be read as a set of consistency conditions the semiclassical amplitudes \mathcal{A}_i must satisfy close to the bifurcation. Thus, the normal form allows one to derive the ratios of the semiclassical amplitudes of the bifurcating orbits. It turns out in practice that these consistency conditions guarantee that the higher-order polynomial coefficients determined from (6.18) remain finite at the bifurcation energies. Notice, however, that they are in general non-zero, so that the two forms of the uniform approximation are slightly different even at the bifurcation energies.

It is clear from the above description that there is a certain arbitrariness in the procedure. This arbitrariness can be reduced to the choice of a suitable amplitude function $p(t)$, because by the splitting lemma and the classification theorems of catastrophe theory the uniform approximation can always be brought into the form (6.13) by a suitable coordinate transformation, provided a normal form $\Phi_a(t)$ equivalent to the actual action function is given. For the case of the hydrogen atom in an electric field, Shaw and Robicheaux [31] calculated a uniform approximation by numerically computing the Lagrangian manifold in the final surface of section (see section 5.1) and then fitting it with a polynomial. This method is much more tedious than the one presented here because it requires more input data than only the actions and recurrence amplitudes of the closed

orbits. By the fit, the information is then reduced to a parametric ansatz, so that the advantage over the method described here is lost. However, the method by Shaw and Robicheaux does provide a means of actually calculating the coordinate transformation leading to (6.13) and thus to determine the amplitude function $p(t)$, should the simple Taylor series approximation turn out not to be sufficiently accurate.

In the following sections, uniform approximations for the two generic codimension-one bifurcations described in section 5.2 will be derived along the lines given here. They serve the double purpose of illustrating the abstract description given above and to extend the results of reference [5] to a complete uniform approximation possessing the correct asymptotics. The uniform approximations to be derived are analogous to those for isochronous and period-doubling bifurcations of periodic orbits given by Schomerus and Sieber [102].

6.5.2 The fold catastrophe uniform approximation

The simplest closed-orbit bifurcation is the creation of two orbits in a tangent bifurcation. It is described by the fold catastrophe (5.12)

$$\Phi_a(t) = \frac{1}{3}t^3 - at .$$

This normal form has stationary points at $t = \pm\sqrt{a}$, which are real if $a > 0$. Its stationary values are (5.14)

$$\Phi(\pm\sqrt{a}) = \mp \frac{2}{3} a^{3/2} .$$

By (6.17), the actions S_1 and S_2 of the bifurcating orbits must satisfy

$$\begin{aligned} S_1 &= S_0(E) - \frac{2}{3} a^{3/2} , \\ S_2 &= S_0(E) + \frac{2}{3} a^{3/2} . \end{aligned} \tag{6.22}$$

For these equations to hold, one must assume $S_1 < S_2$ if the orbits are real and $\text{Im } S_1 > 0, \text{Im } S_2 < 0$ if they are ghosts. These conditions determine how the orbits are to be associated with the stationary points of $\Phi_a(t)$. Equation (6.22) can be solved for

$$S_0(E) = \frac{S_1 + S_2}{2} \tag{6.23}$$

and

$$|a| = \left(\frac{3}{4} |S_2 - S_1|\right)^{2/3} . \tag{6.24}$$

The observation that the bifurcating orbits are real if $a > 0$ and ghosts if $a < 0$ fixes the sign of a . Both $S_0(E)$ and a have thus been determined.

For the semiclassical amplitudes, (6.18) yields

$$\begin{aligned} \mathcal{A}_1 &= \frac{\sqrt{\pi}}{|a|^{1/4}} p(+\sqrt{a}) e^{+i\pi/4} , \\ \mathcal{A}_2 &= \frac{\sqrt{\pi}}{|a|^{1/4}} p(-\sqrt{a}) e^{-i\pi/4} . \end{aligned} \tag{6.25}$$

With the ansatz

$$p(t) = \frac{p_0}{2\pi} + \frac{p_1}{2\pi} t \quad (6.26)$$

for the amplitude function $p(t)$, I can solve for the parameters p_0 and p_1 to obtain

$$\begin{aligned} p_0 &= \sqrt{\pi} |a|^{1/4} e^{-i\pi/4} (\mathcal{A}_1 + i\mathcal{A}_2) , \\ p_1 &= \sqrt{\pi} \frac{|a|^{1/4}}{\sqrt{a}} e^{-i\pi/4} (\mathcal{A}_1 - i\mathcal{A}_2) . \end{aligned} \quad (6.27)$$

The simpler form of the uniform approximation with $p(t) = p_0$ is obtained if $p(t) = p_0/2\pi$. In this case $p_1 = 0$ and thus $\mathcal{A}_1 = i\mathcal{A}_2$. Unless the semiclassical amplitudes satisfy this condition, p_1 diverges as the bifurcation is approached, and the complete uniform approximation is no longer finite. It takes the form

$$\Psi(E) = (p_0 I_0 + p_1 I_1) e^{iS_0(E)} \quad (6.28)$$

with

$$I_k = \frac{1}{2\pi} \int dt t^k e^{i\Phi_a(t)} . \quad (6.29)$$

The integral I_0 can be evaluated in terms of the Airy function [44] as

$$I_0 = \text{Ai}(-a) , \quad (6.30)$$

whereas I_1 is given by its derivative

$$I_1 = i \frac{d}{da} I_0 = -i \text{Ai}'(-a) . \quad (6.31)$$

With these results, the uniform approximation (6.28) can be computed once the classical quantities S_1, S_2 and $\mathcal{A}_1, \mathcal{A}_2$ are known. After some rearrangements, (6.28) can be found to agree with the uniform approximation derived by Schemerus and Sieber [102] for isochronous bifurcations of periodic orbits, although its present form is much simpler.

6.5.3 The cusp catastrophe uniform approximation

The normal form for the symmetrized cusp catastrophe is given by (5.16)

$$\Phi_a(t) = \frac{1}{4} t^4 - \frac{1}{2} a t^2 .$$

It has stationary points at $t = 0$ and $t = \pm\sqrt{a}$ and describes a pitchfork bifurcation, where two asymmetric orbits bifurcate off an orbit invariant under a reflection. I denote their actions and amplitudes by $S_{\text{sym}}, S_{\text{asym}}$ and $\mathcal{A}_{\text{sym}}, \mathcal{A}_{\text{asym}}$, respectively, where $\mathcal{A}_{\text{asym}}$ is understood to be the cumulative amplitude of both asymmetric orbits.

As $\Phi_a(t = 0) = 0$, the reference action $S_0(E)$ must be chosen equal to the action of the symmetric orbit. The action difference is given by the stationary value of $\Phi_a(t)$, so that

$$\Delta S = S_{\text{sym}} - S_{\text{asym}} = \frac{1}{4} a^2 , \quad (6.32)$$

and

$$a = \pm 2\sqrt{\Delta S} . \quad (6.33)$$

The parameter a has to be chosen positive if the asymmetric orbits are real, and negative otherwise. As has already been mentioned in section 5.2.2, the normal form Φ_a given by (5.16) is only applicable if $S_{\text{asym}} < S_{\text{sym}}$. In the opposite case, it must be replaced with $-\Phi_a$.

Due to the reflection symmetry, the amplitude function must be an even function of t . I make the ansatz

$$p(t) = p_0 + p_2 t^2 . \quad (6.34)$$

and solve (6.18) for the coefficients

$$\begin{aligned} p_0 &= \sqrt{\frac{a}{2\pi}} \mathcal{A}_{\text{sym}} e^{i\pi/4} , \\ p_2 &= \frac{e^{-i\pi/4}}{2\sqrt{\pi a}} \left(\mathcal{A}_{\text{asym}} - \sqrt{2} i \mathcal{A}_{\text{sym}} \right) . \end{aligned} \quad (6.35)$$

The simple uniform approximation with $p(t) = p_0$ corresponds to $p_2 = 0$ or

$$\mathcal{A}_{\text{asym}} = \sqrt{2} i \mathcal{A}_{\text{sym}} . \quad (6.36)$$

Only under this condition does p_2 remain finite as $a \rightarrow 0$.

The complete uniform approximation reads

$$\Psi(E) = \int dt p(t) e^{i\Phi_a(t)} = p_0 I_0 + p_2 I_2 \quad (6.37)$$

with

$$I_k = \int dt t^k e^{i\Phi_a(t)} . \quad (6.38)$$

The integral I_0 can be evaluated analytically in terms of Bessel functions [109]:

$$I_0 = \frac{\pi}{2} \sqrt{|a|} e^{-ia^2/8} \left[e^{i\pi/8} J_{-1/4} \left(\frac{a^2}{8} \right) + \text{sign } a e^{-i\pi/8} J_{1/4} \left(\frac{a^2}{8} \right) \right] . \quad (6.39)$$

Although it is not apparent at first sight, I_0 is a smooth function of a . This can be verified if the series expansion [44]

$$J_\nu(x) = \left(\frac{x}{2} \right)^\nu r_\nu(x) \quad (6.40)$$

with $r_\nu(x)$ a power series in x^2 is used. In terms of $r_\nu(x)$,

$$I_0 = \frac{\pi}{2} e^{-ia^2/8} \left[2e^{i\pi/8} r_{-1/4} \left(\frac{a^2}{8} \right) + \frac{a}{2} e^{-i\pi/8} r_{1/4} \left(\frac{a^2}{8} \right) \right] , \quad (6.41)$$

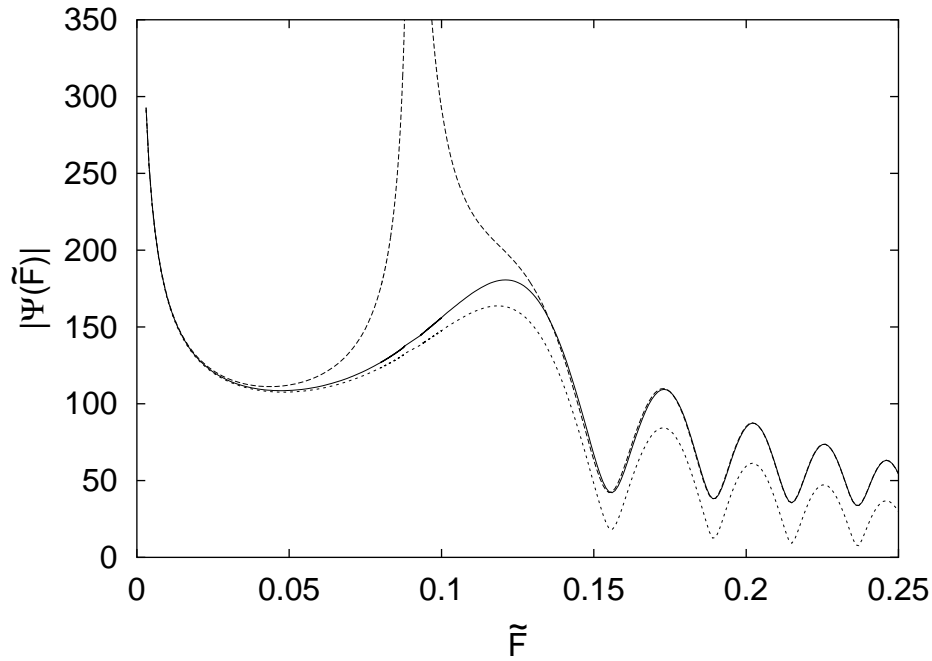


Figure 6.7: Uniform approximation (6.37) for a tangent bifurcation. Solid line: uniform approximation, long-dashed line: isolated-orbits approximation, short-dashed line: simple uniform approximation.

which is indeed smooth. The second integral I_2 can be evaluated from

$$\begin{aligned}
 I_2 &= \int dt \, 2i \frac{d}{da} e^{i\Phi_a(t)} \\
 &= 2i \frac{dI_0}{da} \\
 &= i\pi \sqrt{|a|} e^{-ia^2/8} \left\{ \left(\frac{1}{2a} - i\frac{a}{4} \right) \left[e^{i\pi/8} J_{-1/4} \left(\frac{a^2}{8} \right) + \text{sign } a e^{-i\pi/8} J_{1/4} \left(\frac{a^2}{8} \right) \right] \right. \\
 &\quad \left. + \frac{a}{8} e^{i\pi/8} \left[J_{-5/4} \left(\frac{a^2}{8} \right) - J_{3/4} \left(\frac{a^2}{8} \right) \right] \right. \\
 &\quad \left. + \text{sign } a \frac{a}{8} e^{-i\pi/8} \left[J_{-3/4} \left(\frac{a^2}{8} \right) - J_{5/4} \left(\frac{a^2}{8} \right) \right] \right\}. \tag{6.42}
 \end{aligned}$$

This derivation contains an interchange of differentiation and integration which achieves a regularization of the divergent integral I_2 . It can be justified by verifying that the asymptotic behaviour of (6.42) for $a \rightarrow \pm\infty$ agrees with the stationary phase approximation to (6.38).

The calculation of the uniform approximation (6.37) is thus complete. It is illustrated in figure 6.7 for the case of a pitchfork bifurcation generating a quartet of orbits from a C-doublet in the first series of rotators at the repetition number $\mu = 57$. For graphical purposes, only the absolute value of $\Psi(\tilde{F})$ is shown. The uniform approximation is plotted at a fixed scaled energy $\tilde{E} = -1.4$ for varying

scaled electric field strength \tilde{F} , so that \tilde{F} takes over the role of the energy \tilde{E} in the above discussion. The bifurcation takes place at $\tilde{F}_c = 0.0901$. It is obvious that the isolated-orbits approximation diverges there, whereas both forms of the uniform approximation remain finite. For $\tilde{F} > \tilde{F}_c$, if the distance from the bifurcation is large enough, the complete uniform approximation agrees with the isolated-orbits formula and reproduces the beats caused by the interference of the different real orbits. Because the pattern of beats is primarily determined by the phases of the interfering oscillations, i.e. the actions, it is also given by the simple uniform approximation. However, the simple approximation does not describe the amplitudes of the interfering contributions correctly, so that the heights of the beats differ from their correct values. At $\tilde{F} < \tilde{F}_c$, both the complete and the simple uniform approximation asymptotically agree with the isolated-orbits formula, and all three diverge as $\tilde{F} \rightarrow 0$. This divergence is caused by the rotational symmetry-breaking at $\tilde{F} = 0$, which is a bifurcation not taken into account by the normal form (5.16).

6.5.4 Uniformized recurrence spectra

The formulae derived in the preceding sections give the uniform approximations directly in terms of the semiclassical actions and amplitudes. This circumstance makes them easy to apply to scaled spectra: I simply put $S = w\tilde{S}$ and $\mathcal{A}_{c.o.} = w^\gamma \tilde{\mathcal{A}}_{c.o.}$. As w is varied, the bifurcation is not encountered because the classical mechanics does not change, so that the isolated-orbits approximation does not actually diverge. However, if w is small, the action differences between the bifurcating orbits are also small, so that the presence of the bifurcation is felt and the isolated-orbits formula produces exceedingly large contributions. For large w , the action differences also grow large, so that the isolated-orbits approximation should be recovered in the limit of large w .

These findings are illustrated in figure 6.8 for the same bifurcation as in figure 6.7 for fixed scaled energy $\tilde{E} = -1.4$ and scaled electric field strength¹ $\tilde{F} = 0.2$ and varying w . As anticipated, in the limit of $w \rightarrow \infty$ the complete uniform approximation agrees with the isolated-orbits formula, whereas the simple approximation correctly reproduces the beats, but has a smaller amplitude. Problems with the uniform approximation arise in the region of small w . To achieve a finite value of the contribution to the unscaled semiclassical spectrum $\Psi(w) = w^{-1} \tilde{\Psi}(w)$, the contribution to the scaled spectrum should vanish linearly in w . Whereas the simple approximation actually seems to vanish, albeit slowly, as $w \rightarrow 0$, the complete uniform approximation assumes a finite value. This failure is due to the fact that the neighbourhood of the stationary points that contributes to the integral (6.14) becomes arbitrarily large in this limit. Thus, the Taylor series approximation (6.34) to the amplitude function cannot be expected to be accurate throughout the region where it is needed. What is more, as the

¹If $\tilde{F} = 0.1$ is chosen as above, the scaled action difference is too small for the uniform approximation to reach its asymptotic behaviour for reasonably small w .

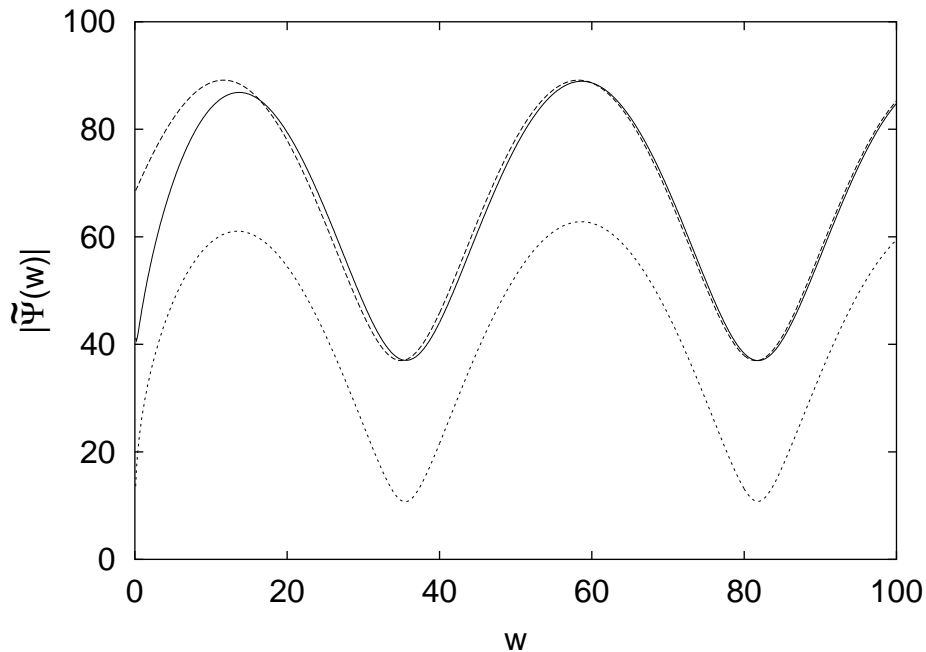


Figure 6.8: Uniform approximation as in figure 6.7 for the scaled spectrum at $\tilde{E} = -1.4$ and $\tilde{F} = 0.2$.

neighbourhood of the bifurcating orbits increases indefinitely, further closed orbits not participating in the bifurcation and not taken into account by the normal form (5.16) are eventually encountered. Therefore, the uniform approximations cannot be used in the limit $w \rightarrow 0$. In any case, however, this limit is beyond the validity of the semiclassical approximation, so that there is no need to study it further.

The scaled uniform approximation can be used to improve the semiclassical recurrence spectrum, but this requires some effort: Whereas the isolated-orbits approximation yields δ function peaks in the recurrence spectrum, which are replaced with Gaussians due to the smoothing of the recurrence spectrum (see section 6.4), the uniform approximation is a complicated function of w . It must be subjected to a numerical Fourier transform in the same way as the quantum spectrum is if its contribution to the recurrence spectrum is to be evaluated. Because a bifurcation involves orbits with roughly equal actions, the uniform approximation will produce a recurrence peak at the appropriate action. An example is shown in figure 6.9. It was calculated for the bifurcation already described in figures 6.7 and 6.8. The Gaussian smoothing used in section 6.4 was replaced with a rectangular window, so that a number of side peaks appear. In this case, the Fourier transform of both the uniform approximation and the isolated-orbits approximation was taken over the rectangular window $w \in [40, 60]$. The bifurcating orbits have the scaled action $\tilde{S}/2\pi \approx 21.86$, which is where the Fourier peaks are centred in both approximations. The peak produced by the uniform approximation is considerably smaller.

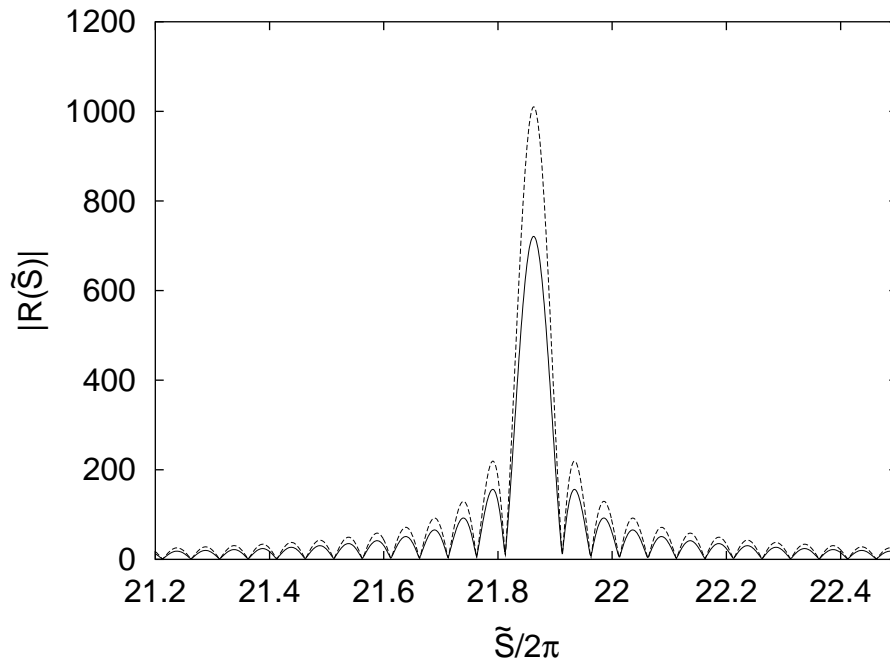


Figure 6.9: Contribution to the recurrence peak calculated from the uniform approximation (solid line) and the isolated-orbits approximation (dashed line) for the same bifurcation as in figure 6.7, $\tilde{E} = -1.4$ and $\tilde{F} = 0.1$.

If this uniformization procedure is carried out for all excessively high bifurcation peaks, it should be possible to bring the semiclassical recurrence spectrum in figure 6.6 into agreement with its quantum counterpart. In practice, however, several obstacles stand in the way. First of all, in many cases ghost orbits must be included in the uniform approximation. They must be found and identified as pertinent to a given bifurcation before the uniformization can be performed. Furthermore, even if all relevant orbits are real, those orbits connected with each other in a bifurcation must be recognized in the data set. This is by no means an easy task. For example, if in a given series of rotators and for a given winding number a quartet of orbits appears, there are two different doublet orbits out of which they may have bifurcated, and it is not clear in general which of them must be taken for the uniform approximation. In a single case, this can be found out fairly comfortably by hand. If many orbits are to be classified, however, it is essential to do the grouping automatically. I have not been able to devise a practical algorithm for this task, so that a automatized uniformization of all bifurcation peaks is presently impossible.

Apart from these rather technical difficulties, there are also some obstacles of more fundamental importance. Consider, e.g., the two high semiclassical peaks at $\tilde{S}/2\pi \approx 25$ in figure 6.5. They are notably too high, and they are well-isolated from neighbouring recurrence peaks, so that they may appear to be the ideal testing ground for the uniformization procedure. These peaks are generated by vibrators with repetition numbers $\mu = 41$ and $\mu = 42$, respectively. The pertinent

bifurcation scenarios were described in detail in section 5.4.2. The “simple” scenario taking place at $\mu = 41$ (see figure 5.17) consists of two orbits being generated in the rotational symmetry-breaking at $\tilde{F} = 0$, followed by a tangent bifurcation destroying one of them and a third orbit. To smooth this bifurcation peak, a uniform approximation describing the complete scenario must be found, which requires the construction of a suitable normal form. Although a uniform approximation for the symmetry-breaking is available [110–112], the derivation of the pertinent normal form relies on principles different from the catastrophe theory classification used here, and it is not clear how these two can be united into a single normal form. Thus, the construction of a uniform approximation for this bifurcation scenario, and even more so for the more complicated scenario at $\mu = 42$ (see figure 5.18), remains an open problem to be solved in the future. It can be solved within the framework of uniformization presented in section 6.5.1, but will require a novel way of constructing normal forms.

The approach to high-resolution semiclassical quantization described in section 3.1 and applied to the crossed-fields system in section 6.3 relies on the harmonic inversion of a Fourier transformed semiclassical spectrum, i.e. of a recurrence spectrum. The above method of uniformizing the bifurcation-induced excessively high recurrence peaks in a semiclassical spectrum would therefore, if it could be implemented systematically, also pave the way to the inclusion of uniform approximations into a high-resolution semiclassical quantization, which has not been possible so far. As the classical dynamics of the crossed-fields system is obviously too complicated to permit a systematic uniformization of all relevant bifurcation peaks, I resort to a system with simpler classical behaviour, namely the hydrogen atom in an electric field. This system is classically integrable, so that an overview over all closed orbits can easily be obtained. Nevertheless, bifurcations of closed orbits abound, rendering the system an ideal testing ground for the methods developed here. It will be described in detail in the following chapter.

Chapter 7

Stark effect

The classical dynamics of the hydrogen atom in a homogeneous electric field is well known to be integrable because the Hamilton-Jacobi equation is separable in parabolic coordinates [113]. It can therefore be regarded as the simplest atomic system apart from the field-free hydrogen atom, and consequently its semiclassical treatment is of fundamental importance. Due to the integrability, of course, the EBK torus quantization rules apply, and a semiclassical calculation of photo-absorption spectra based on the existence of quantized classical tori was indeed carried out by Kondratovich and Delos [114, 115].

Closed-orbit theory is intended to be applicable to atomic systems exhibiting either regular, chaotic or mixed classical behaviour, so that it is of vital interest to see how it can be applied to this apparently simple example. It turns out that, although the closed orbits of the Stark system are easy to describe and classify, a multitude of bifurcations exist. Thus, in a closed-orbit theory treatment this system presents all difficulties to be expected in a generic mixed regular-chaotic system. On the other hand, the sequence of bifurcations can easily be understood, so that the technical difficulties encountered in the crossed-fields hydrogen atom are absent. One can therefore hope that the semiclassical quantization based on uniform approximations can be applied successfully in this case.

In section 7.1 the classical dynamics of the Stark system will be described. It will be shown that the KS description of the dynamics immediately paves the way to a separation of the equation of motion, without having to resort to Hamilton-Jacobi theory. Again, the geometric algebra formulation streamlines the calculation. In sections 7.2 and 7.3, the closed orbits and their bifurcations are discussed. Semi-analytic formulae for all relevant orbital parameters will be derived which have not been given in the literature so far. In section 7.4, two pertinent uniform approximations are derived. The first of these is not new, but it is derived in a much simpler way as was done previously and it is brought into a form that is considerably easier to apply. The second uniform approximation is new in this thesis. It describes a sequence of two bifurcations, and it is the first uniform approximation introduced in the literature which relies on a configuration space with non-trivial topology. Section 7.5 concludes by presenting both low- and high-resolution semiclassical spectra. They prove that uniform approximations

can indeed be included into a high-resolution semiclassical quantization. The results solve the long-standing problem of a closed-orbit theory quantization of the Stark effect and serve as a prototype example for the application of the novel method to other systems.

7.1 Separation of the equation of motion

In this section it is shown that the spinor equation of motion (4.19) can easily be separated and solved by elementary means. I then proceed to discuss the closed orbits present in this situation. The KS transformation leads to a remarkably compact representation of the closed orbits. It will further be shown that the sequence of closed orbit bifurcations found by Gao and Delos [116] from numerically calculated Poincaré surface of section plots can be derived by simple analytic arguments.

Sections 7.1–7.3 present purely classical calculations. Scaling with the electric field strength F according to the prescriptions of section 2.1 is used throughout. For the sake of simplicity, I refrain from marking the scaled quantities with a tilde. From section 7.4 on, the distinction between scaled and unscaled quantities will be taken up again.

The electronic motion for a hydrogen atom in an electric field \mathbf{F} can be described by the Hamiltonian

$$\mathcal{H} = \frac{1}{2}P^\dagger P - E U^\dagger U + \frac{1}{2}U^\dagger U \langle \mathbf{F} U \boldsymbol{\sigma}_3 U^\dagger \rangle = 2 \quad (7.1)$$

or the equation of motion

$$U'' = 2 \left(E - \frac{1}{2} \langle \mathbf{F} U \boldsymbol{\sigma}_3 U^\dagger \rangle - \frac{1}{2} \mathbf{F} U \boldsymbol{\sigma}_3 U^\dagger \right) U . \quad (7.2)$$

If the electric field, whose field strength is unity due to scaling, is assumed to point along the $\boldsymbol{\sigma}_3$ -axis, $\mathbf{F} = \boldsymbol{\sigma}_3$, a separation of (7.2) can be achieved by decomposing the spinor U according to

$$U = U_1 I_1 + U_2 , \quad (7.3)$$

where

$$U_j = \alpha_j + I_3 \beta_j \in \mathbb{C}(I_3) , \quad \alpha_j, \beta_j \in \mathbb{R}, \quad (7.4)$$

are “complex numbers”, with the role of the imaginary unit played by the bivector I_3 . (remember $I_3^2 = -1$.) Inserting this bicomplex decomposition of the position spinor into (7.2), I find

$$U_1'' I_1 + U_2'' = 2E (U_1 I_1 + U_2) + 2 \left(U_1 U_1^\dagger U_1 I_1 - U_2 U_2^\dagger U_2 \right) , \quad (7.5)$$

which can immediately be separated into

$$\begin{aligned} U_1'' &= 2E U_1 + 2 U_1 U_1^\dagger U_1 , \\ U_2'' &= 2E U_2 - 2 U_2 U_2^\dagger U_2 . \end{aligned} \quad (7.6)$$

Thus, the equation of motion (7.2) for the four-dimensional spinor U has been reduced to two independent complex differential equations. Further reduction can be achieved by introducing polar coordinates

$$U_j = \rho_j e^{I_3 \varphi_j}, \quad j = 1, 2. \quad (7.7)$$

Separating the real and imaginary parts of (7.6), I obtain

$$\rho_j'' - \rho_j \varphi_j'^2 - 2E\rho_j \mp 2\rho_j^3 = 0, \quad (7.8)$$

$$2\rho_j' \varphi_j' + \rho_j \varphi_j'' = 0. \quad (7.9)$$

Equation (7.9) yields

$$\frac{d}{d\tau} (\rho_j^2 \varphi_j') = 0, \quad (7.10)$$

so that

$$\Lambda_j = \rho_j^2 \varphi_j' \quad (7.11)$$

is a constant of motion. It characterizes the ‘‘angular momentum’’ in the abstract complex plane $\mathbb{C}I_3$. In terms of U_j , it can be written as

$$\Lambda_j = -I_3 \left\langle U_j' U_j^\dagger \right\rangle_2 = -I \left\langle U_j' \boldsymbol{\sigma}_3 U_j^\dagger \right\rangle_3. \quad (7.12)$$

With the decomposition (7.3), the constraint equation (4.9) reads

$$\left\langle U_1' \boldsymbol{\sigma}_3 U_1^\dagger \right\rangle_3 = \left\langle U_2' \boldsymbol{\sigma}_3 U_2^\dagger \right\rangle_3, \quad (7.13)$$

so that $\Lambda_1 = \Lambda_2$, and with the help of (4.67) I can identify

$$\Lambda_1 = \Lambda_2 = -\langle I_3 l \rangle = L_3 \quad (7.14)$$

as the physical angular momentum component along the electric field axis, which is a constant of motion.

The radial equation (7.8) simplifies to

$$\rho_j'' = \frac{L_3^2}{\rho_j^3} + 2E\rho_j \pm 2\rho_j^3. \quad (7.15)$$

It can be integrated to yield

$$\rho_j'^2 = \pm \rho_j^4 + 2E\rho_j^2 - \frac{L_3^2}{\rho_j^2} + c_j \quad (7.16)$$

with integration constants c_1 and c_2 related by the pseudo-energy conservation condition (7.1). Integrating a second time, I finally obtain

$$\begin{aligned} \tau &= \int \frac{d\rho_1}{\sqrt{\rho_1^4 + 2E\rho_1^2 - \frac{L_3^2}{\rho_1^2} + c_1}} = \frac{1}{2} \int \frac{d\eta}{\sqrt{\eta^3 + 2E\eta^2 + c_1\eta - L_3^2}}, \\ \tau &= \int \frac{d\rho_2}{\sqrt{-\rho_2^4 + 2E\rho_2^2 - \frac{L_3^2}{\rho_2^2} + c_2}} = \frac{1}{2} \int \frac{d\xi}{\sqrt{-\xi^3 + 2E\xi^2 + c_2\xi - L_3^2}}, \end{aligned} \quad (7.17)$$

which gives the orbital parameter τ as an elliptic integral in the coordinates ρ_1 and ρ_2 . Equivalently, the coordinates turn out to be elliptic functions of τ . The coordinates $\xi = \rho_2^2$ and $\eta = \rho_1^2$ correspond to the conventional parabolic coordinates [113] $\xi = r + z$ and $\eta = r - z$.

In the case of closed orbits, $L_3 = 0$, so that φ_1 and φ_2 are constants. By (7.16), $\rho_j'^2 = c_j$ at the nucleus. The initial conditions for an orbit starting at the nucleus at time $\tau = 0$ thus read

$$\begin{aligned} \rho_1(0) &= 0, & \rho_2(0) &= 0, \\ \rho_1'(0) &= \sqrt{c_1}, & \rho_2'(0) &= \sqrt{c_2}. \end{aligned} \quad (7.18)$$

The pseudo-energy condition (7.1) yields

$$c_1 + c_2 = 4. \quad (7.19)$$

The separation constants describe the distribution of energy between the uphill and the downhill motion. For the initial velocities (7.18) to be real, they must satisfy

$$0 \leq c_j \leq 4, \quad j = 1, 2. \quad (7.20)$$

According to the radial equations of motion (7.16), for real orbits ρ_j can only assume values which make

$$f_j(\rho_j) = \pm \rho_j^4 + 2E\rho_j^2 + c_j > 0. \quad (7.21)$$

For the motion in the ρ_j -direction to be bounded there must be a real turning point, where $f_j(\rho_j) = 0$, because otherwise ρ_j will keep increasing forever. From the factorized form

$$f_1(\rho_1) = (\rho_1^2 - \rho_{1+}^2)(\rho_1^2 - \rho_{1-}^2), \quad (7.22)$$

with

$$\rho_{1\pm}^2 = -E \pm \sqrt{E^2 - c_1}, \quad (7.23)$$

it is obvious that for $E < 0$ the zeros of $f_1(\rho_1)$ are real if

$$c_1 < E^2 \quad (7.24)$$

and complex otherwise. Therefore, a closed orbit can only exist if (7.24) holds. For energies E below the Stark saddle energy $E_S = -2$, this does not impose any restrictions beyond (7.20). For $E > E_S$, there must be a sufficiently strong component of the motion in the uphill direction so that the energy of the downhill motion does not suffice to cross the saddle.

For the ρ_2 motion I obtain similarly

$$f_2(\rho_2) = -(\rho_2^2 - \rho_{2+}^2)(\rho_2^2 - \rho_{2-}^2), \quad (7.25)$$

with

$$\rho_{2\pm}^2 = E \pm \sqrt{E^2 + c_2}. \quad (7.26)$$

The coordinate ρ_{2+} is real for any $c_2 > 0$. Therefore, the ρ_2 -motion is always bounded for real orbits.

With the help of the factorizations (7.22) and (7.25), the elliptic integrals (7.17) can easily be reduced to Legendre's standard integral of the first kind [44]

$$\begin{aligned}\tau &= \frac{1}{\rho_+} \mathcal{F} \left(\arcsin \left(\frac{\rho_+}{\sqrt{c_1}} \rho_1 \right) \middle| m_1 \right) \\ &= \frac{1}{\rho_-} \mathcal{F} \left(\arcsin \left(\frac{\rho_-}{\sqrt{c_2}} \rho_2 \right) \middle| m_2 \right) .\end{aligned}\tag{7.27}$$

The parameters are

$$\begin{aligned}m_1 &= \frac{\rho_{1-}^2}{\rho_{1+}^2} = \frac{c_1}{\rho_+^4} , \\ m_2 &= \frac{\rho_{2+}^2}{\rho_{2-}^2} = -\frac{c_2}{\rho_-^4} ,\end{aligned}\tag{7.28}$$

and the abbreviations

$$\rho_+ = \rho_{1+} , \quad \rho_- = \sqrt{-\rho_{2-}^2}\tag{7.29}$$

were introduced.

Equation (7.27) can be solved for ρ_1 and ρ_2 in terms of Jacobi's elliptic functions [44] to yield

$$\begin{aligned}\rho_1(\tau) &= \frac{\sqrt{c_1}}{\rho_+} \operatorname{sn}(\rho_+ \tau | m_1) , \\ \rho_2(\tau) &= \frac{\sqrt{c_2}}{\rho_-} \operatorname{sn}(\rho_- \tau | m_2) .\end{aligned}\tag{7.30}$$

These results incorporate the initial conditions (7.18).

Together with $\Lambda_j = L_3 = 0$, (7.11) and (7.3), equation (7.30) yields the KS spinor

$$\begin{aligned}U(\tau) &= \rho_1(\tau) e^{I_3 \varphi_1} I_1 + \rho_2(\tau) e^{I_3 \varphi_2} \\ &= e^{I_3 \varphi/2} (\rho_1(\tau) I_1 + \rho_2(\tau)) e^{I_3 \alpha/2} .\end{aligned}\tag{7.31}$$

The angle $\varphi = \varphi_1 + \varphi_2$ describes a rotation around the electric field axis, and $\alpha = \varphi_2 - \varphi_1$ is a gauge parameter. This equation neatly unifies the position information concerning an orbit into a single position spinor. It can serve as a convenient starting point for further investigations of the crossed-field regime. It is also apparent from (7.31) that, apart from the freedom of gauge inherent in the KS transformation, Stark orbits occur, as expected, in one-parameter families generated by a rotation around the electric field axis.

7.2 Closed orbits

Closed orbits are characterized by the condition that at a pseudotime $\tau_0 > 0$ the electron returns to the nucleus, so that

$$\rho_1(\tau_0) = \rho_2(\tau_0) = 0. \quad (7.32)$$

In the simplest cases, either ρ_1 or ρ_2 vanishes identically. The electron then moves along the electric field axis.

If $c_1 = 0$, the downhill coordinate ρ_1 is zero. The electron leaves the nucleus in the uphill direction, i.e. in the direction of the electric field, until it is turned around by the joint action of the Coulomb and external fields and returns to the nucleus at a pseudotime

$$\tau_2 = 2 \frac{\mathcal{K}(m_2)}{\rho_-}, \quad (7.33)$$

where $\mathcal{K}(m)$ denotes the complete elliptic integral of the first kind [44]. Thus, τ_2 corresponds to a half period of ρ_2 and, due to the freedom of gauge in KS coordinates, to a full period of the uphill orbit in position space. The uphill orbit is repeated periodically and closes again at $\tau_0 = l\tau_1$ with integer l .

The second case of axial motion is obtained if $c_1 = 4$, which corresponds to a downhill motion opposite to the direction of the electric field. The ρ_1 motion closes at pseudotimes $\tau = k\tau_1$ with

$$\tau_1 = 2 \frac{\mathcal{K}(m_1)}{\rho_+}, \quad (7.34)$$

if the energy E is less than the saddle point energy $E_S = -2$. If $E > E_S$, the electron crosses the Stark saddle and the orbit does not close.

In the case of a non-axial orbit, the uphill and downhill motions must close at the same time

$$\tau_0 = k\tau_1 = l\tau_2. \quad (7.35)$$

If (7.35) is satisfied for any given integer values of k and l , the orbit returns to the nucleus after k half periods of ρ_1 and l half periods of ρ_2 , corresponding, in Cartesian coordinates, to k full periods in the downhill and l full periods in the uphill direction. I therefore refer to k and l as the downhill and uphill repetition numbers, respectively, and identify a non-axial closed orbit by its repetition numbers (k, l) .

By (7.23), (7.26) and (7.28), the half-periods τ_1 and τ_2 depend on the separation constant c_1 . For given k and l , (7.35) can therefore be read as an equation for c_1 , thus determining the initial conditions of a closed orbit. I am now going to investigate the solution of this equation to determine the conditions for a (k, l) orbit to exist.

Figure 7.1 shows the dependence of τ_1 and τ_2 on c_1 for a fixed energy E . For all c_1 , the uphill period τ_2 is smaller than the downhill period τ_1 . Furthermore, as $c_1 \rightarrow -\infty$ I obtain from (7.33) and (7.34), to leading order,

$$\tau_1 - \tau_2 \approx \frac{2\mathcal{K}(-1)}{(-c_1)^{5/4}}, \quad (7.36)$$

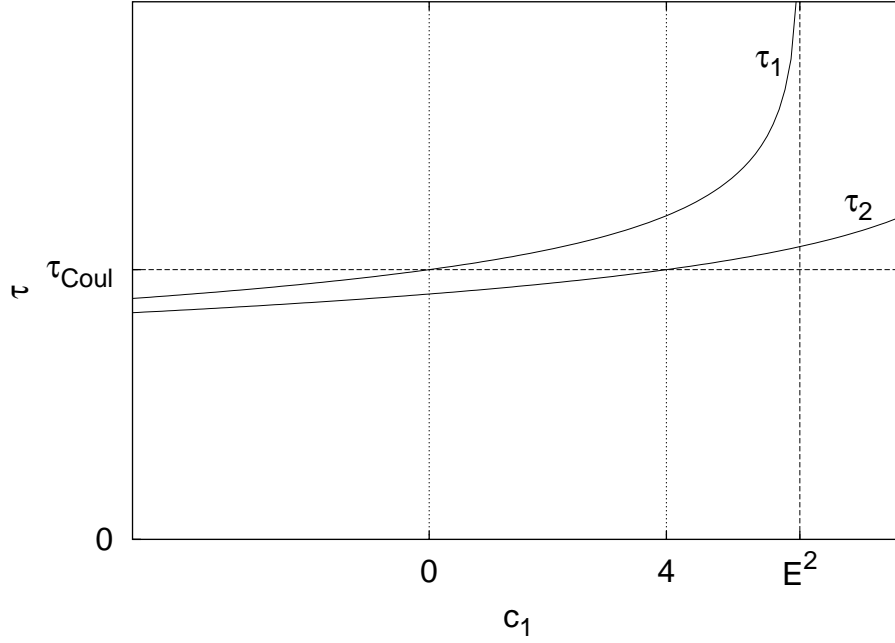


Figure 7.1: Downhill period τ_1 and uphill period τ_2 as a function of the separation constant c_1 .

whereas

$$\tau_1 \approx \frac{2\mathcal{K}(-1)}{(-c_1)^{1/4}}, \quad (7.37)$$

so that the ratio τ_1/τ_2 approaches 1 from above. On the other hand, τ_1 diverges at $c_1 = E^2$, so that $\tau_1/\tau_2 \rightarrow \infty$ as $c_1 \rightarrow E^2$. Thus, for any energy $E < 0$ and positive integers k, l with $l > k$, there is a unique solution c_1 to (7.35). It is in the range $-\infty < c_1 < E^2$. There is no solution for $l \leq k$, since τ_1 is complex for $c_1 > E^2$ whereas τ_2 remains real. Therefore, orbits (k, l) with $l \leq k$ do not exist.

A real closed orbit must satisfy $0 \leq c_1 \leq 4$ due to (7.18) and (7.19). If $c_1 > 4$, the initial velocity $\rho_2'(0)$ is imaginary, hence $\rho_2(\tau)$ will be imaginary at all times. Similarly, $\rho_1(\tau)$ will be imaginary if $c_1 < 0$. In both cases, if the complex conjugate of the ghost orbit is taken, one of the KS coordinates changes sign. This change of sign does not alter the Cartesian coordinates, and consequently all ghost orbits are invariant with respect to complex conjugation. By the same token, the starting angle of a ghost orbit is defined up to complex conjugation only. I will always choose the imaginary part of starting angles to be positive. The properties of real and ghost orbits are summarized in table 7.1.

To investigate the bifurcations a closed orbit undergoes, I will now discuss the dependence of c_1 on E for fixed repetition numbers k, l . For any energy E and $c_1 = 0$, the downhill period τ_1 is equal to the period

$$\tau_{\text{Coul}} = \frac{\pi}{\sqrt{-2E}} \quad (7.38)$$

of the pure Coulomb dynamics. For $c_1 = 4$, the uphill period τ_2 equals τ_{Coul} . For

	c_1	c_2	ρ_1	ρ_2	m_1	m_2
pre-bifurcation ghost	$c_1 > 4$	$c_2 < 0$	$\in \mathbb{R}$	$\in i\mathbb{R}$	> 0	> 0
real orbit	$0 \leq c_1 \leq 4$	$0 \leq c_2 \leq 4$	$\in \mathbb{R}$	$\in \mathbb{R}$	> 0	< 0
post-bifurcation ghost	$c_1 < 0$	$c_2 > 4$	$\in i\mathbb{R}$	$\in \mathbb{R}$	< 0	< 0

Table 7.1: Comparison of real and ghost orbits

any other value of c_1 , both τ_1 and τ_2 converge to τ_{Coul} as $E \rightarrow -\infty$, whence in this limit $\tau_1/\tau_2 \rightarrow 1$. Thus, $\tau_1/\tau_2 < l/k$ at $c_1 = 4$ if E is sufficiently low. The solution to (7.35) must then lie in the interval $c_1 \in [4, E^2]$, so that the (k, l) -orbit is a ghost. As E increases, c_1 decreases. At the critical energy E_{gen} where $c_1 = 4$, a real (k, l) orbit is generated. It bifurcates off the downhill orbit that is located at $c_1 = 4$. For $E > E_{\text{gen}}$, c_1 decreases further. When the energy E_{dest} where $c_1 = 0$ is reached, the (k, l) orbit collides with the uphill orbit and becomes a ghost again. As the singularity of τ_1 approaches zero as $E \nearrow 0$, there is an $E_{\text{dest}} < 0$ for any (k, l) .

The bifurcation energies E_{gen} and E_{dest} can be determined from (7.35) if $c_1 = 4$ is prescribed for the generation of an orbit, or $c_1 = 0$ for its destruction. For these cases, equation (7.35) simplifies to

$$\frac{l}{k} = \frac{2^{3/2}}{\pi \sqrt{1 + \sqrt{1 - \epsilon}}} \mathcal{K} \left(\frac{\epsilon}{(1 + \sqrt{1 - \epsilon})^2} \right) \quad (7.39)$$

in terms of the dimensionless variable $\epsilon = 4/E^2 = (E_S/E)^2$ for the generation of the (k, l) orbit and

$$\frac{k}{l} = \frac{2^{3/2}}{\pi \sqrt{1 + \sqrt{1 + \epsilon}}} \mathcal{K} \left(\frac{-\epsilon}{(1 + \sqrt{1 + \epsilon})^2} \right) \quad (7.40)$$

for its destruction. These equations provide a simple and stable method to determine the bifurcation energies. They can be expected to yield more accurate results than the numerically computed monodromy matrix elements used by Gao and Delos [116].

The sequence of bifurcations described above is illustrated in figure 7.2, where characteristic data of the orbit $(4, 5)$, and the downhill and uphill orbits it bifurcates from, is shown. The bifurcation energies $E_{\text{gen}} = -2.3597$ and $E_{\text{dest}} = -1.3790$ are characterized by the conditions $c_1 = 4$ and $c_1 = 0$, respectively. The transition between real and ghost orbits can most clearly be seen from the energy dependence of the starting angle ϑ_i , which is real between the bifurcation energies and acquires a non-zero imaginary part outside this interval. In addition, at the bifurcation energies the actions and orbital periods of the non-axial orbit coincide with those of the appropriate axial orbits. Note that the action of the non-axial orbit is always smaller than that of the axial orbits.

It is also apparent from figure 7.2 that the monodromy matrix element m_{12} vanishes at the bifurcations. For the axial orbits, further zeros of m_{12} appear in

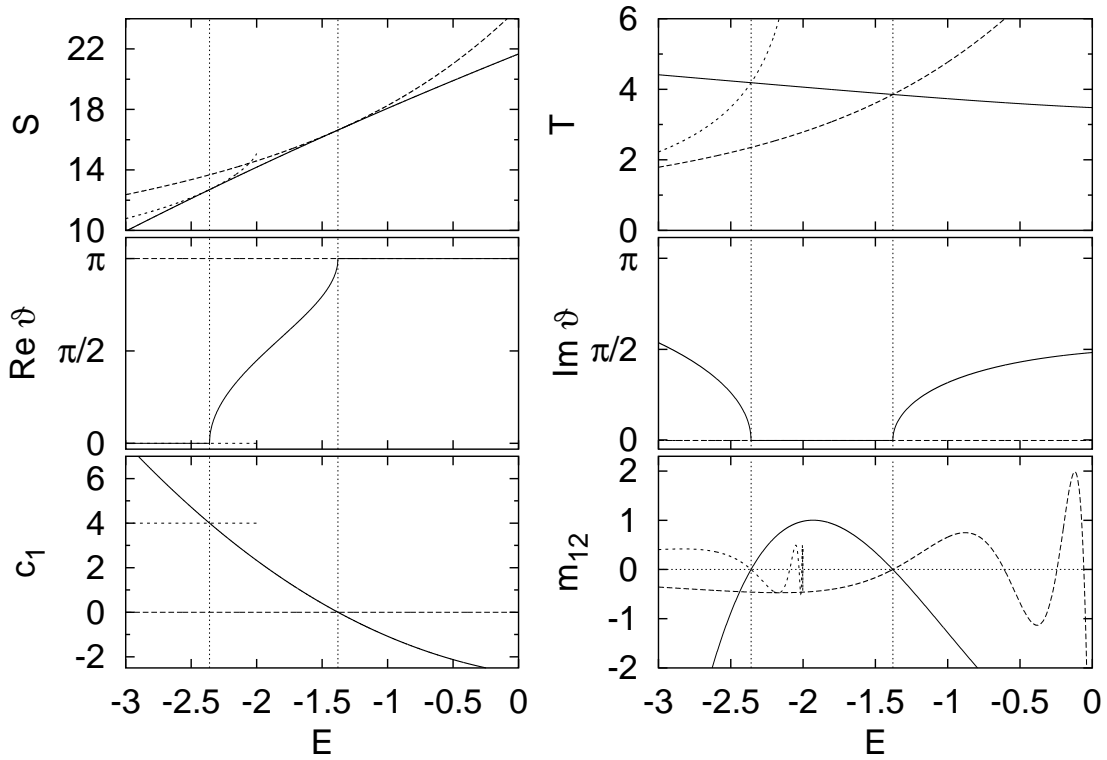


Figure 7.2: Orbital parameters close to the bifurcations of the orbit (4, 5). Solid line: non-axial orbit (4, 5), long-dashed line: fifth uphill orbit, short-dashed line: fourth downhill orbit. Vertical lines indicate the bifurcation energies $E_{\text{gen}} = -2.3597$ and $E_{\text{dest}} = -1.3790$, respectively

figure 7.2. They correspond to additional bifurcations these orbits undergo. As $k < l$ for a non-axial orbit, the l th repetition of the uphill orbit undergoes $l - 1$ bifurcations, where the orbits (k, l) with $k = 1, \dots, l - 1$ are destroyed. All four bifurcation energies of the fifth uphill orbit are visible in figure 7.2. A downhill orbit, on the contrary, undergoes infinitely many bifurcations before it ceases to exist at $E = -2$. Only the first members of this infinite cascade are resolved in figure 7.2.

The separation parameter c_1 for a closed orbit must be calculated numerically from (7.35). Once it is known, all orbital parameters can be found analytically. The pertinent formulae will now be derived.

First of all, comparing the closed-orbit initial conditions (7.18) to (4.80), I obtain the following relations for the initial and final angle $\vartheta = \vartheta_i = \vartheta_f$

$$2 \cos \frac{\vartheta}{2} = \sqrt{c_1}, \quad 2 \sin \frac{\vartheta}{2} = \sqrt{c_2}, \quad (7.41)$$

so that

$$\vartheta = 2 \arccos \frac{\sqrt{c_1}}{2}. \quad (7.42)$$

The angle ϑ determined from (7.42) is obviously real and confined to the interval $0 \leq \vartheta \leq \pi$ if $0 \leq c_1 \leq 4$, as was to be expected for a real orbit. For a pre-

bifurcation ghost orbit, i.e. $c_1 > 4$, the equations (7.41) can be satisfied if $\vartheta = i\alpha$ is chosen purely imaginary with

$$2 \cosh \frac{\alpha}{2} = \sqrt{c_1}, \quad 2i \sinh \frac{\alpha}{2} = \sqrt{c_2}. \quad (7.43)$$

This choice of ϑ , which is unique up to the addition of multiples of 4π , makes ϑ continuous at the bifurcation. Similarly, for $c_1 < 0$, i.e. for a post-bifurcation ghost orbit, I set $\vartheta = \pi + i\alpha$ with

$$2i \sinh \frac{\alpha}{2} = \sqrt{c_1}, \quad 2 \cosh \frac{\alpha}{2} = \sqrt{c_2}. \quad (7.44)$$

Again, the real part makes ϑ continuous at the bifurcation. In both cases I assume $\alpha > 0$, which is possible because the orbit is invariant under complex conjugation.

Using the KS spinor (7.31) and $P = U^\dagger$, I obtain the action integral

$$\begin{aligned} S &= \int_0^{\tau_0} \rho_1^2 d\tau + \int_0^{\tau_0} \rho_2^2 d\tau \\ &= 2k \int_0^{\sqrt{c_1}/\rho_+} \rho_1' d\rho_1 + 2l \int_0^{\sqrt{c_2}/\rho_-} \rho_2' d\rho_2. \end{aligned} \quad (7.45)$$

The equations of motion (7.16) then yield

$$\begin{aligned} S &= 2k \int_0^{\sqrt{c_1}/\rho_+} \sqrt{f_1(\rho_1)} d\rho_1 + 2l \int_0^{\sqrt{c_2}/\rho_-} \sqrt{f_2(\rho_2)} d\rho_2 \\ &= \frac{2kc_1}{3m_1\rho_+} I(m_1) + \frac{2lc_2}{3m_2\rho_-} I(m_2) \end{aligned} \quad (7.46)$$

with

$$I(m) = (m-1)\mathcal{K}(m) + (m+1)\mathcal{E}(m) \quad (7.47)$$

and the complete elliptic integrals of the first and second kinds $\mathcal{K}(m)$ and $\mathcal{E}(m)$ [44]. As can be seen from (7.45), S is real for both real and ghost orbits.

Similarly, the physical-time period of a closed orbit is given by

$$\begin{aligned} T &= \int_0^{\tau_0} \rho_1^2 d\rho_1 + \int_0^{\tau_0} \rho_2^2 d\rho_2 \\ &= \frac{2kc_1}{m_1\rho_+^3} (\mathcal{K}(m_1) - \mathcal{E}(m_1)) + \frac{2lc_2}{m_2\rho_-^3} (\mathcal{K}(m_2) - \mathcal{E}(m_2)). \end{aligned} \quad (7.48)$$

As is the action, the period T is always real.

The calculation of the monodromy matrix element m_{12} is more difficult. It proceeds from the 2×2 Jacobian matrix

$$J = \frac{\partial \boldsymbol{\rho}(\tau_0)}{\partial \boldsymbol{p}(0)} \quad (7.49)$$

that describes the change of the final position upon a variation of the initial momentum. The initial and final momenta are given by

$$\boldsymbol{p}(0) = \begin{pmatrix} \sqrt{c_1} \\ \sqrt{c_2} \end{pmatrix}, \quad \boldsymbol{p}(\tau_0) = \begin{pmatrix} (-1)^k \sqrt{c_1} \\ (-1)^l \sqrt{c_2} \end{pmatrix}, \quad (7.50)$$

They have norm 2 by (7.19). As the monodromy matrix characterizes variations perpendicular to the orbit, m_{12} is obtained from J by projecting onto unit vectors perpendicular to the momenta (7.50). Thus,

$$m_{12} = \frac{1}{2} \left((-1)^l \sqrt{c_2}, -(-1)^k \sqrt{c_1} \right) \cdot J \cdot \frac{1}{2} \begin{pmatrix} \sqrt{c_2} \\ -\sqrt{c_1} \end{pmatrix}. \quad (7.51)$$

Since the dynamics is separable, the matrix J is diagonal, whence

$$m_{12} = (-1)^l \frac{c_2}{4} \left. \frac{\partial \rho_1(\tau)}{\partial p_1(0)} \right|_{\tau=\tau_0} + (-1)^k \frac{c_1}{4} \left. \frac{\partial \rho_2(\tau)}{\partial p_2(0)} \right|_{\tau=\tau_0}. \quad (7.52)$$

For the remaining derivatives I find from (7.30)

$$\left. \frac{\partial \rho_1(\tau)}{\partial p_1(0)} \right|_{\tau=\tau_0} = \left(\frac{\partial}{\partial p_1(0)} \frac{\sqrt{c_1}}{\rho_+} \right) \text{sn}(\rho_+ \tau | m_1) + \frac{\sqrt{c_1}}{\rho_+} \frac{\partial}{\partial p_1(0)} \text{sn}(\rho_+ \tau | m_1). \quad (7.53)$$

A similar expression holds for ρ_2 . If a non-axial orbit (k, l) is considered, the first term in (7.53) vanishes at $\tau = \tau_0$ by virtue of the resonance condition (7.35). The second term can be evaluated in a elementary, but lengthy calculation to yield

$$\begin{aligned} m_{12} = & (-1)^{k+l} \frac{km_1 c_2}{4\rho_+ \sqrt{E^2 - c_1}} (2Ed(m_1) - \rho_+^2 \mathcal{K}(m_1)) \\ & + (-1)^{k+l} \frac{lm_2 c_1}{4\rho_- \sqrt{E^2 + c_2}} (2Ed(m_2) - \rho_-^2 \mathcal{K}(m_2)) \end{aligned} \quad (7.54)$$

with

$$d(m) = \frac{\mathcal{E}(m)}{m(1-m)} - \frac{\mathcal{K}(m)}{m}. \quad (7.55)$$

From (7.54) it can be verified that, up to a choice of sign, the matrix element m_{12} for the orbit (nk, nl) , which is the n th repetition of (k, l) , equals n times the matrix element for the orbit (k, l) , as has been shown previously by Gao and Delos [116] by an abstract argument using the neutral stability of the orbits. It is also clear from (7.54) that m_{12} vanishes when the orbit undergoes a bifurcation, because $m_1 \rightarrow 0$ as $c_1 \rightarrow 0$, and $\mathcal{K}(m_1)$ and $d(m_1)$ both approach finite limits.

For an uphill orbit the second term in (7.53) vanishes because $c_1 = 0$, whereas the first term is nonzero in general because the axial orbits do not obey a resonance condition akin to (7.35). The derivative reads

$$\left. \frac{\partial \rho_1(\tau)}{\partial p_1(0)} \right|_{c_1=0} = \frac{\sin(\sqrt{-2E} \tau)}{\sqrt{-2E}}, \quad (7.56)$$

so that

$$m_{12} = (-1)^l \frac{\sin(\sqrt{-2E} \tau_0)}{\sqrt{-2E}}. \quad (7.57)$$

Similarly, the matrix element for a downhill orbit is

$$m_{12} = (-1)^k \frac{\sin(\sqrt{-2E} \tau_0)}{\sqrt{-2E}}. \quad (7.58)$$

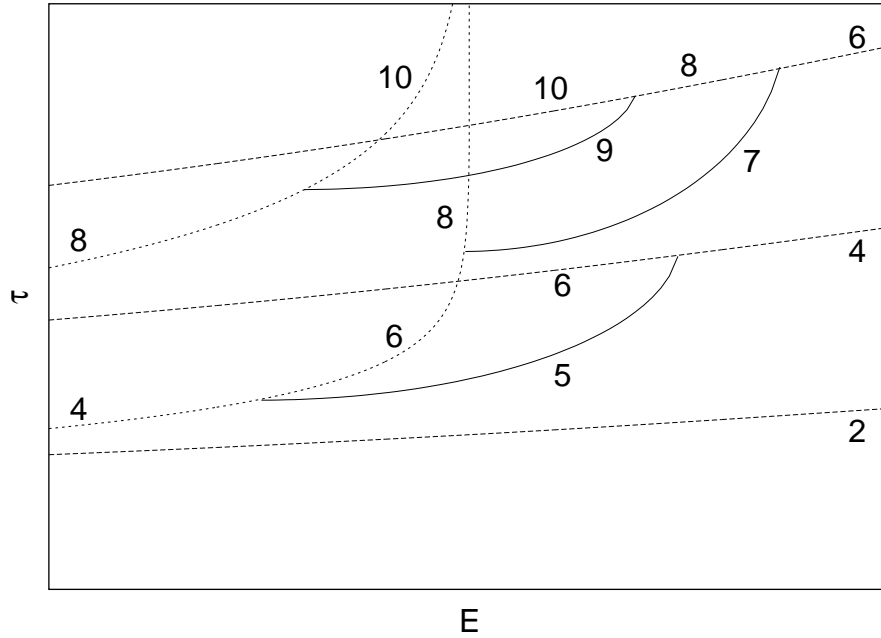


Figure 7.3: Periods of the shortest closed orbits, labelled by their Maslov indices, as a function of energy (schematic). Solid lines: non-axial orbits, short-dashed lines: downhill orbits, long-dashed lines: uphill orbits.

Finally, the Maslov indices of the closed orbits need to be determined. For the uphill orbits, I proceed as follows: First, there is a caustic whenever the orbit reaches either the nucleus or the turning point, totalling to $2l-1$ caustics. Second, the Maslov index increases by two (corresponding to two independent directions transverse to the orbit) whenever the orbit is intersected by neighbouring trajectories, i.e. when (7.56) vanishes. This occurs, by (7.56), after a pseudotime τ_{Coul} , so that the intersections contribute $2[\tau_0/\tau_{\text{Coul}}]$ to the Maslov index. $[x]$ denotes the integer part of x . Third, according to the derivation in section 2.4 the Maslov index must be increased by one, so that for an uphill orbit it finally reads

$$\mu = 2 \left(l + \left[\frac{l\tau_2}{\tau_{\text{Coul}}} \right] \right). \quad (7.59)$$

Using the same reasoning, I find

$$\mu = 2 \left(k + \left[\frac{k\tau_1}{\tau_{\text{Coul}}} \right] \right), \quad (7.60)$$

for a downhill orbit. As the downhill period τ_1 is always larger than τ_{Coul} , the downhill Maslov index (7.60) is equal to $4k$ for sufficiently low E .

The Maslov index of a non-axial orbit involves the number of zeros of m_{12} encountered along the orbit, which is hard to find from (7.31). Instead, I exploit the observation made in section 6.5.1 that the change of Maslov indices in a bifurcation can be determined from the normal form describing the bifurcation.

A normal form suitable for the bifurcations in the Stark effect will be given in section 7.4. It predicts that in a bifurcation the Maslov index of the axial orbit increases by two, which is consistent with (7.59) and (7.60), and the Maslov index of the non-axial orbit takes the intermediate value. A schematic drawing of the shortest orbits and their bifurcations is shown in figure 7.3. It implies that the Maslov index of a non-axial orbit is

$$\mu = 2(k + l) - 1. \quad (7.61)$$

Since along the orbit there are $k - 1$ zeros of ρ_1 and $l - 1$ zeros of ρ_2 , each corresponding to an intersection with the electric field axis and thus contributing 1 to the Maslov index, there must be $k + l - 1$ zeros of m_{12} . This result can be confirmed numerically.

For ghost orbits, Maslov indices cannot be determined by counting caustics. The uniform approximation to be developed requires the semiclassical amplitude of the non-axial orbit to be continuous across the bifurcation. This can be achieved if the Maslov index (7.61) is assigned to the ghost orbit and the factor $\sin \vartheta$ in (2.66), which was derived for real orbits, is replaced with $|\sin \vartheta|$, which is real and invariant under the exchange of the starting angle with its complex conjugate.

7.3 Bifurcations at low energies

From the discussion of the closed orbits in the preceding section it has become clear that, although the Stark system is integrable, bifurcations of closed orbits abound. For a semiclassical treatment to be successful, therefore, suitable uniform approximations must be constructed. I will turn to this problem in section 7.4. Without any detailed knowledge of the uniformization procedure, however, it is evident that there are two regions where the construction of uniform approximations poses a particular challenge:

First, as the Stark saddle energy $E_S = -2$ is approached from below, the downhill orbit undergoes infinitely many bifurcations in a finite energy interval before it is destroyed. The periods of the closed orbits thus created, as the period of the downhill orbit itself, grow arbitrarily large. The actions, however, remain finite, so that the action differences between the orbits stemming from two successive bifurcations become arbitrarily small. Similar cascades of isochronous bifurcations have been found, e.g., in the diamagnetic Kepler problem [117] and in Hénon-Heiles type potentials [118]. Their uniformization remains an open problem. A detailed discussion of this cascade in the Stark system must be referred to future work.

Second, non-axial orbits with winding ratios $z = l/k$ close to one are created and destroyed at low energies, and their generation and destruction are closely spaced (see figure 7.9 on page 152). Therefore, at low energies a uniform approximation describing both the creation of a non-axial orbit from the downhill

orbit and its destruction at the uphill orbit is required. It will be derived in section 7.4.2. As a prerequisite, to quantitatively assess its necessity, the asymptotic behaviour of closed-orbit bifurcations at low energies will be investigated in detail in this section.

Bifurcation energies can be determined from equations (7.39) and (7.40). As a winding ratio $z = l/k$ close to one corresponds to low bifurcation energies and small values of the parameter $\epsilon = (E_S/E)^2$, approximate bifurcation energies can be obtained by expanding the right hand sides of (7.39) and (7.40) in a Taylor series around $\epsilon = 0$. I then find the generation and destruction energies

$$E_{\text{gen}} = -\frac{\sqrt{3}}{2\sqrt{z-1}} - \frac{35}{16\sqrt{3}}\sqrt{z-1} + \mathcal{O}(z-1)^{3/2}, \quad (7.62)$$

$$E_{\text{dest}} = -\frac{\sqrt{3}}{2\sqrt{z-1}} + \frac{23}{16\sqrt{3}}\sqrt{z-1} + \mathcal{O}(z-1)^{3/2}, \quad (7.63)$$

for an orbit with a given rational z , so that the energy difference

$$\Delta E = E_{\text{dest}} - E_{\text{gen}} = \frac{29}{8\sqrt{3}}\sqrt{z-1} + \mathcal{O}(z-1)^{3/2} \quad (7.64)$$

indeed vanishes as $z \rightarrow 1$.

However, the crucial parameter determining whether or not the bifurcations can be regarded as isolated is not the difference of the bifurcation energies, but rather the action differences between the non-axial orbit and the two axial orbits. For the simple uniform approximation to be applicable, at any energy at least one of the two action differences must be large. In other words (see figure 7.2), at the critical energy where the actions of the downhill and the uphill orbits are equal, the difference between their action and the action of the non-axial orbit must be large.

To begin with, the actions of the downhill and uphill orbits are given by

$$\begin{aligned} S_{\text{down}} = \sqrt{2}\pi(-E)^{-1/2} \pm \frac{3\pi}{4\sqrt{2}}(-E)^{-5/2} + \frac{35\pi}{32\sqrt{2}}(-E)^{-9/2} \\ \pm \frac{1155\pi}{512\sqrt{2}}(-E)^{-13/2} + \frac{45045\pi}{8192\sqrt{2}}(-E)^{-17/2} + \mathcal{O}(-E)^{-19/2}. \end{aligned} \quad (7.65)$$

The critical energy for the orbit (k, l) is characterized by the condition $kS_{\text{down}} = lS_{\text{up}}$, so that $S_{\text{down}}/S_{\text{up}} = z$. I solve this equation for the critical energy

$$\begin{aligned} E_{\text{crit}} = -\frac{\sqrt{3}}{2\sqrt{z-1}} - \frac{\sqrt{3}}{8}\sqrt{z-1} - \frac{69\sqrt{3}}{64}(z-1)^{3/2} \\ + \frac{209\sqrt{3}}{256}(z-1)^{5/2} + \mathcal{O}(z-1)^{7/2}. \end{aligned} \quad (7.66)$$

As expected, the critical energy lies between the two bifurcation energies. If it is

substituted into (7.65), the critical action of the axial orbits

$$S_{\text{ax}} = kS_{\text{down}} = \frac{2\pi k}{3^{1/4}} (z-1)^{1/4} + \frac{3\pi k}{4 \cdot 3^{1/4}} (z-1)^{5/4} - \frac{455\pi k}{576 \cdot 3^{1/4}} (z-1)^{9/4} + \mathcal{O}(z-1)^{13/4} \quad (7.67)$$

is obtained

To determine the critical action of the non-axial orbit, the separation parameter c_1 for this orbit at the critical energy must be calculated from equation (7.35), which can be rewritten as

$$\frac{\tau_2}{\tau_1} - z = 0. \quad (7.68)$$

Substituting the critical energy (7.66) into (7.68), I find

$$\begin{aligned} \frac{\tau_2}{\tau_1} - z = & \frac{29(c_1 - 2)}{24} (z-1)^2 + \frac{219c_1^2 - 876c_1 + 526}{144} (z-1)^3 \\ & + \frac{17951c_1^3 - 107986c_1^2 + 188112c_1 - 76688}{9216} (z-1)^4 + \mathcal{O}(z-1)^5. \end{aligned} \quad (7.69)$$

I now make a power series ansatz for c_1 , insert it into (7.69) and solve for the coefficients to find

$$c_1 = 2 + \frac{175}{87} (z-1) - \frac{175}{174} (z-1)^2 + \mathcal{O}(z-1)^3. \quad (7.70)$$

From the knowledge of the critical energy and the separation parameter, the critical action of the non-axial orbit is found to be

$$S_{\text{non}} = \frac{2\pi k}{3^{1/4}} (z-1)^{1/4} + \frac{3\pi k}{4 \cdot 3^{1/4}} (z-1)^{5/4} - \frac{1151\pi k}{576 \cdot 3^{1/4}} (z-1)^{9/4} + \mathcal{O}(z-1)^{13/4}. \quad (7.71)$$

This result agrees with (7.67) in leading and next-to-leading order. The critical action difference is

$$\Delta S_{\text{crit}} = \frac{29\pi q}{24 \cdot 3^{1/4}} (z-1)^{5/4} + \mathcal{O}(z-1)^{9/4} \quad (7.72)$$

with $q = l - k$. If the critical action difference is written as a function of the critical energy by (7.66), it reads

$$\Delta S_{\text{crit}} = \frac{29\pi q}{32\sqrt{2}} (-E_{\text{crit}})^{-5/2} + \mathcal{O}(-E_{\text{crit}})^{-7/2}. \quad (7.73)$$

Note that due to delicate cancellations occurring during the calculation, all terms of the series expansions given above are needed to obtain the leading-order result (7.73). Due to these cancellations, the critical action difference is proportional to a high power of the energy, so that it vanishes fast at low energies.

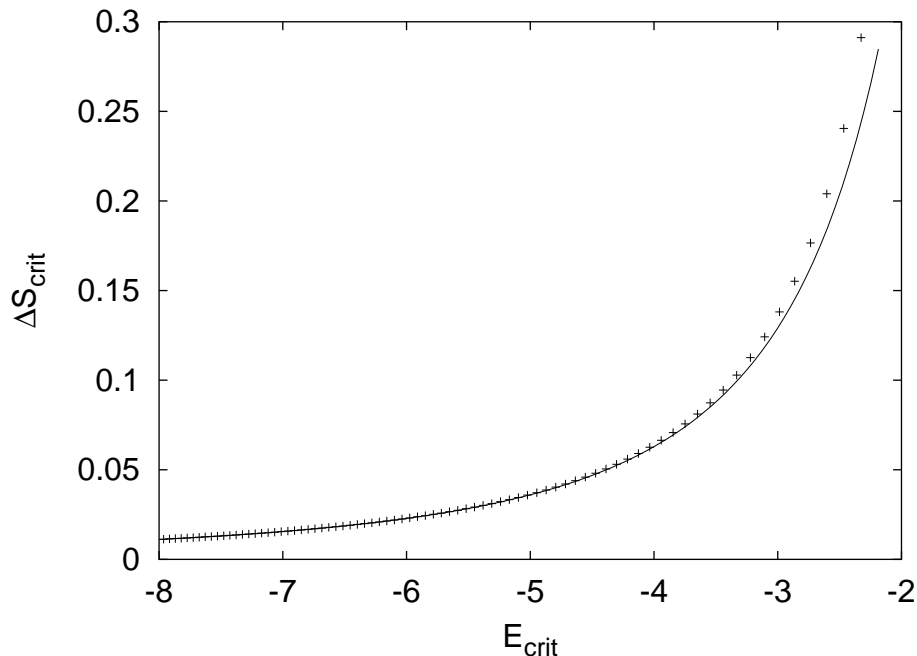


Figure 7.4: Numerically calculated critical action differences (crosses) for $q = l - k = 1$ as a function of the critical energies. The solid line gives the leading-order result (7.73).

Figure 7.4 shows numerically computed critical action differences as a function of the pertinent critical energies for $q = 1$. The leading-order result (7.73) is indicated by the solid line. It is accurate even at fairly high energies.

The results of this section confirm that at low energies a uniform approximation describing both the generation and the destruction of a non-axial orbit is required. It will be derived in section 7.4.2.

7.4 Uniform approximations

In the following sections I present the semiclassical treatment of the Stark effect. From now on, scaled quantities will again be marked with a tilde.

7.4.1 Isolated bifurcations

It has become clear in section 7.2 that the apparently simple dynamics of the hydrogen atom in an electric field contains numerous bifurcations of closed orbits. They will turn out to spoil the semiclassical spectrum (see section 7.5) unless a suitable uniform approximation is derived. For an isolated single bifurcation where a non-axial orbit is born out of a downhill orbit or destroyed in a collision with an uphill orbit, a suitable uniform approximation was given by Gao and Delos [30]. These authors constructed a semiclassical wave function

near a bifurcation and essentially redid the derivation of closed-orbit theory using that wave function. Their uniform approximation was extended by Shaw and Robicheaux [31] to include ghost orbits. In this section I will demonstrate that their result can be obtained within the general framework presented in section 6.5.1. It will be shown that with the help of the known recurrence strengths of the isolated orbits only the semiclassical divergences can be uniformized. The necessity to construct a semiclassical wave function does not arise. In particular, in contrast to previous work [30, 119], the present derivation does not depend on any knowledge about the ionic core.

According to section 6.5.1, the crucial step in the construction of a uniform approximation is the choice of a suitable ansatz function whose stationary points describe the classical closed orbits. In the Stark system, the structure of the bifurcations is determined by the rotational symmetry of the system. Non-axial orbits occur in one-parameter families generated by the rotation of any particular member around the electric field axis, whereas the axial orbit is isolated at all energies except at a bifurcation. The normal form must share these symmetry properties.

I choose the normal form Φ to be defined on a plane with Cartesian coordinates (x, y) or polar coordinates

$$x = r \cos \varphi, \quad y = r \sin \varphi. \quad (7.74)$$

Due to the rotational symmetry, Φ must be a function of the radial coordinate r only, independent of the angle φ . To be a smooth function of x and y , it must be a function of r^2 . Any such function has a stationary point at the origin $x = y = 0$ that corresponds to the axial orbit because it is rotation invariant. Any stationary point at a non-zero radial coordinate r_c occurs on a ring $r = r_c$ and describes a family of non-axial orbits. A normal form suitable to describe the bifurcations occurring in the Stark system must therefore have stationary points on a ring with radius r_c that shrinks to zero as the bifurcation is approached.

These requirements are fulfilled by the normal form

$$\Phi_a(x, y) = \frac{1}{4} r^4 - \frac{1}{2} a r^2 \quad (7.75)$$

with a real parameter a . Note that this is the symmetric cusp normal form already used in section 5.2, but with the variable r now interpreted as a radial rather than a Cartesian coordinate.

Apart from the trivial stationary point at the origin, (7.75) has a ring of stationary points at $r = \sqrt{a}$, which is real if $a > 0$ and imaginary if $a < 0$. Thus, (7.75) describes a family of non-axial real orbits present for $a > 0$ which then contracts onto an axial orbit and becomes a family of ghost orbits.

The uniform approximation using the normal form (7.75) reads

$$\Psi(E) = I(a) e^{iS_{\text{ax}}(E)}, \quad (7.76)$$

where $S_{\text{ax}}(E)$ denotes the action of the axial orbit and

$$I(a) = \int dx dy p(x^2 + y^2) e^{i\Phi_a(x, y)}, \quad (7.77)$$

with an arbitrary smooth rotationally symmetric function $p(r^2)$ used to adjust the amplitudes. A stationary-phase approximation to (7.77) must treat the stationary points at the origin and away from the origin differently. The contribution of the origin can easily be evaluated in Cartesian coordinates. It yields

$$I(a)|_{r=0} = \frac{2\pi i}{|a|} p(0) e^{-i\frac{\pi}{2}\nu_0} = -\frac{2\pi i}{a} p(0), \quad (7.78)$$

where

$$\nu_0 = \begin{cases} 0 & : a < 0 \\ 2 & : a > 0 \end{cases} \quad (7.79)$$

is the number of negative eigenvalues of the Hessian matrix. From this number it is apparent that the Maslov index of the axial orbit increases by 2 in the bifurcation.

The contribution of the non-axial orbits is present if $a > 0$. Due to the rotational symmetry, a straightforward stationary-phase approximation to this contribution fails because the stationary points are not isolated. For this reason, the amplitude condition (6.18) cannot be applied literally. In polar coordinates, the integration over the angle φ yields the constant 2π , and the stationary-phase approximation can be applied to the remaining integral over r . This yields

$$I(a)|_{\text{ring}} = 2\pi\sqrt{\pi i} p(a) e^{-ia^2/4}. \quad (7.80)$$

Note that the contribution of the non-axial orbit remains finite as $a \rightarrow 0$.

The conditions analogous to (6.17) and (6.18) read

$$S_{\text{non}} = S_{\text{ax}} - a^2/4, \quad (7.81)$$

$$\mathcal{A}_{\text{ax}} = -\frac{2\pi i}{a} p(0), \quad \mathcal{A}_{\text{non}} = 2\pi\sqrt{\pi i} p(a) \quad (7.82)$$

in terms of the actions and recurrence amplitudes of the axial and non-axial orbits. According to (7.81), the action of the non-axial orbits must always be smaller than that of the axial orbit out of which it bifurcates. This is the case for all bifurcations in the Stark system. The opposite case could be treated by changing the normal form Φ_a into $-\Phi_a$. The normal form parameter

$$a = \pm 2\sqrt{S_{\text{ax}} - S_{\text{non}}} \quad (7.83)$$

can be determined from (7.81). The sign of a has to be chosen according to whether the non-axial orbits are real or complex.

Equation (7.82) gives conditions the function $p(r^2)$ must satisfy. As usual, a simple form of the uniform approximation is obtained by setting $p(r^2)$ equal to a constant. This choice imposes the constraint

$$\frac{1+i}{\sqrt{2\pi}} \mathcal{A}_{\text{non}} = -a\mathcal{A}_{\text{ax}} \quad (7.84)$$

on the semiclassical amplitudes. Note that both sides of this equation are finite as $a \rightarrow 0$. In particular, \mathcal{A}_{non} is continuous at $a = 0$. This condition was used in section 7.2 to fix the Maslov indices for the ghost orbits. The actual semiclassical amplitudes satisfy (7.84) close to the bifurcation, but the agreement is satisfactory in the immediate neighbourhood of the bifurcation only.

To improve the uniform approximation, I choose a first-order polynomial

$$p(r^2) = p_0 + p_1(r^2 - a) \quad (7.85)$$

for the amplitude function. The coefficients p_0 and p_1 are chosen to satisfy (7.82) for arbitrary amplitudes:

$$p_0 = \frac{\mathcal{A}_{\text{non}}}{\sqrt{2\pi} \pi(1+i)}, \quad p_1 = \frac{1}{2\pi i a} \left(a\mathcal{A}_{\text{ax}} + \frac{1+i}{\sqrt{2\pi}} \mathcal{A}_{\text{non}} \right). \quad (7.86)$$

By (7.84), p_1 remains finite at the bifurcation. Thus, the uniform approximation (7.76) assumes the form

$$\Psi(E) = \left[\frac{\mathcal{A}_{\text{non}}}{(1+i)} I_0 + \frac{1}{a} \left(a\mathcal{A}_{\text{ax}} + \frac{1+i}{\sqrt{2\pi}} \mathcal{A}_{\text{non}} \right) I_1 \right] e^{iS_{\text{ax}}} \quad (7.87)$$

with the integrals

$$I_0 = \frac{1}{2^{1/2} \pi^{3/2}} \int dx dy e^{i\Phi_a(x,y)}, \quad I_1 = \frac{1}{2\pi i} \int dx dy (r^2 - a) e^{i\Phi_a(x,y)}. \quad (7.88)$$

I_0 can be evaluated in terms of the Fresnel integrals [44]

$$C(x) = \int_0^x \cos\left(\frac{\pi}{2} t^2\right) dt, \quad S(x) = \int_0^x \sin\left(\frac{\pi}{2} t^2\right) dt \quad (7.89)$$

to yield

$$I_0 = e^{-ia^2/4} \left[\frac{1+i}{2} - C\left(-\frac{a}{\sqrt{2\pi}}\right) - iS\left(-\frac{a}{\sqrt{2\pi}}\right) \right]. \quad (7.90)$$

I_1 can be reduced to

$$I_1 = \frac{1}{2i} e^{-ia^2/4} \int_{-a}^{\infty} dv v e^{iv^2/4} \quad (7.91)$$

with $v = r^2 - a$. The integral in (7.91) diverges at $v = \infty$. It can be regularized by adding a small exponential damping factor $e^{-\varepsilon v^2}$ and letting $\varepsilon \rightarrow 0$ at the end. This procedure yields

$$I_1 = 1. \quad (7.92)$$

The regularization can be justified by noting that the stationary phase approximation to (7.88) also yields $I_1 = 1$, so that (7.92) has the required asymptotic behaviour.

The calculation of the uniform approximation (7.76) is thus finished. As an example, the uniform approximation for the bifurcation of the (4,5) non-axial orbit off the downhill orbit is compared to the simple closed-orbit formula in figure 7.5. Obviously, the uniform approximation (7.87) smooths the divergence of the isolated-orbits approximation and, as desired, asymptotically reproduces the simple approximation perfectly.

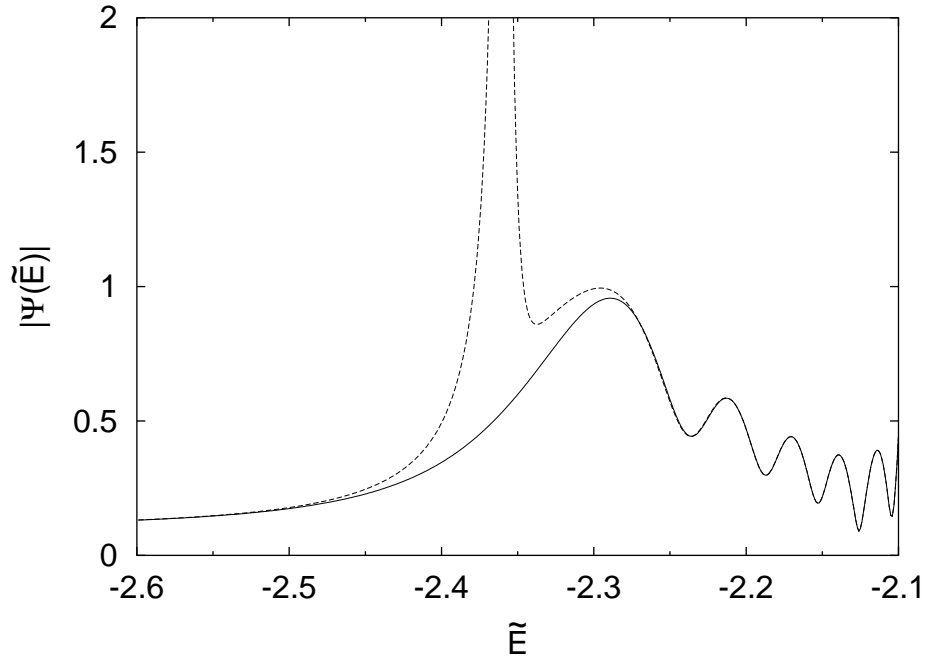


Figure 7.5: Uniform approximation for the generation of the (4,5) non-axial orbit from the downhill orbit for the electric field strength $F = 10^{-8}$. Solid line: Uniform approximation (7.87), dashed line: isolated-orbits approximation.

7.4.2 Non-isolated bifurcations

The uniform approximation for single bifurcations derived in section 7.4.1 cannot be applied if a closed orbit undergoes several bifurcations in a small energy range. As was discussed in detail in section 7.3, it is essential at low energies to construct a uniform approximation capable of simultaneously describing both bifurcations of a non-axial orbit.

A normal form describing the sequence of bifurcations must possess two isolated stationary points corresponding to the uphill and downhill orbits and a ring of stationary points related to the family of non-axial orbits. As the normal form parameters are varied, the ring must branch off the first isolated stationary point and later contract onto the second. This is impossible if the normal form is to be defined in a plane, but it is easily achieved if the normal form is based on a sphere. It can then be chosen such as to have isolated stationary points at the poles and a ring of stationary points moving from one pole to the other. A normal form satisfying these requirements is

$$\Phi_{a,b}(\vartheta) = b(\cos \vartheta - a)^2. \quad (7.93)$$

It is given in terms of the polar angle ϑ on the sphere. Due to the rotational symmetry, it is independent of the azimuth angle φ , and it contains two real parameters a and b needed to match the two action differences between the three closed orbits.

If, in the vicinity of the poles, $\Phi_{a,b}$ is expanded in terms of the distance $\rho = \sin \vartheta$ from the polar axis, it reads

$$\Phi_{a,b} = b(a-1)^2 + ba \left(\frac{1}{4}\rho^4 + \frac{a-1}{a}\rho^2 \right) + \mathcal{O}(\rho^6) \quad (7.94)$$

around $\vartheta = 0$ and

$$\Phi_{a,b} = b(a+1)^2 - ba \left(\frac{1}{4}\rho^4 + \frac{a+1}{a}\rho^2 \right) + \mathcal{O}(\rho^6) \quad (7.95)$$

around $\vartheta = \pi$, so that in both cases (7.93) reproduces the simpler normal form (7.75) up to re-scaling. From the coefficients of the quadratic terms in (7.94) and (7.95) it is apparent that a ring of stationary points bifurcates off $\vartheta = 0$ at $a = 1$, and off $\vartheta = \pi$ at $a = -1$.

These conclusions are confirmed by a discussion of the full normal form (7.93). The ring of stationary points is located at the polar angle ϑ_{non} satisfying

$$\cos \vartheta_{\text{non}} = a. \quad (7.96)$$

This angle qualitatively corresponds to the starting and returning angle of the non-axial orbit in that it describes its motion from the downhill orbit at $\vartheta = 0$ to the uphill orbit at $\vartheta = \pi$. Quantitatively, ϑ_{non} can not directly be identified with the classical angle ϑ because the energy-dependence of the normal form parameters a and b is fixed by matching the action differences rather than the angles. If $-1 \leq a \leq 1$, the angle ϑ_{non} defined by (7.96) is real. If $a > 1$, ϑ_{non} is purely imaginary, corresponding, by table 7.1, to a pre-bifurcation ghost orbit. For $a < -1$, ϑ_{non} is of the form $\vartheta_{\text{non}} = \pi + i\alpha$, as is characteristic of a post-bifurcation ghost.

The bifurcation scenario described by the normal form (7.93) is summarized in figure 7.6. For $b = 1$, the stationary values of (7.93), the complex polar angles ϑ where stationary points occur and the second derivative of $\Phi_{a,b}$ with respect to ϑ are shown as a function of a . Due to the rotational symmetry, the latter is well defined even at the poles.

Figure 7.6 should be compared to figure 7.7, which displays the orbital data pertinent to an actual bifurcation scenario. The qualitative agreement between figure 7.6 and figure 7.7 is obvious, so that (7.93) can be seen to describe the bifurcations correctly. (Note that a is a decreasing function of E .)

As the normal form (7.93) has been chosen such as to vanish at the non-axial stationary point ϑ_{non} , the pertinent uniform approximation reads

$$\Psi(E) = I(a, b) e^{iS_{\text{non}}(E)}, \quad (7.97)$$

where $S_{\text{non}}(E)$ denotes the action of the non-axial orbit and

$$I(a, b) = \int_0^\pi d\vartheta \int_0^{2\pi} d\varphi p(\vartheta) e^{i\Phi_{a,b}(\vartheta)} \quad (7.98)$$

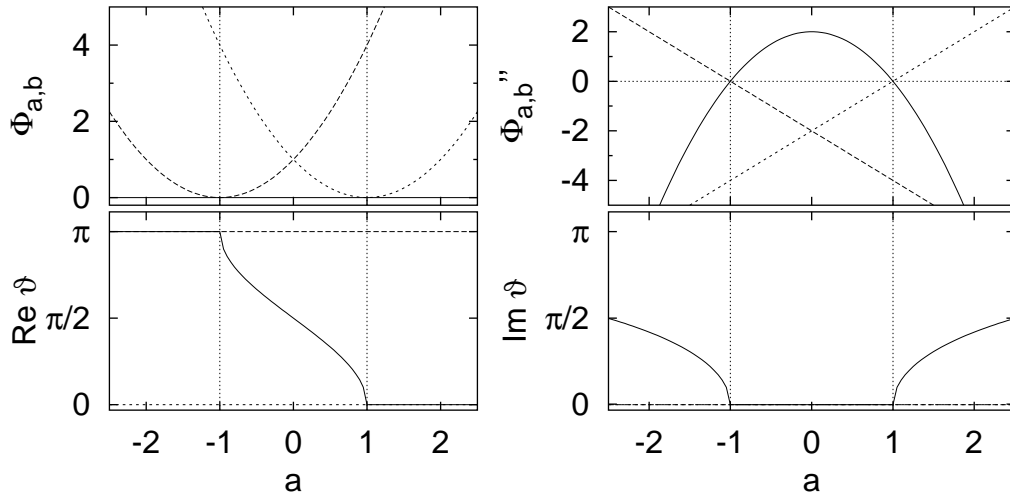


Figure 7.6: Bifurcation scenario described by the normal form (7.93) for $b = 1$. Location ϑ of the stationary points, stationary values of the normal form $\Phi_{a,b}$ and stationary values of its second derivative. Solid line: stationary point at ϑ_{non} , long-dashed line: stationary point at $\vartheta = \pi$, short-dashed line: stationary point at $\vartheta = 0$.

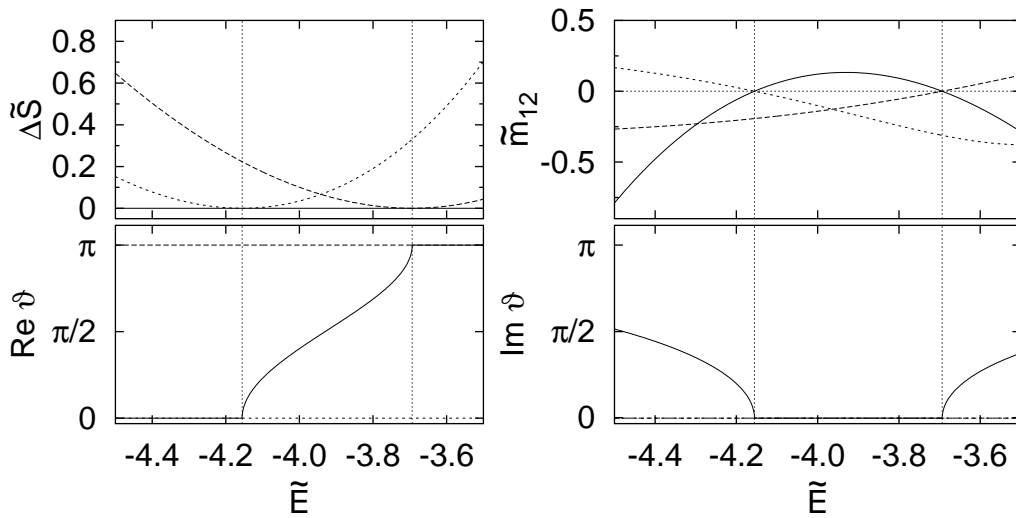


Figure 7.7: Orbital parameters for the bifurcations of the (20,21) non-axial orbit. Solid line: non-axial orbit (20,21), long-dashed line: 21st uphill orbit, short-dashed line: 20th downhill orbit. The vertical lines indicate the bifurcation energies $\tilde{E}_{\text{gen}} = -4.155542$ and $\tilde{E}_{\text{dest}} = -3.693431$, respectively.

with an amplitude function $p(\vartheta)$ to be determined below.

The connection with closed-orbit theory is again established with the help of a stationary-phase approximation. If $|a| > 1$, the only real stationary points of $\Phi_{a,b}$ are located at the poles, and the asymptotic approximation to (7.98) reads

$$I(a, b) \approx -\frac{\pi i}{b(1-a)} p(0) e^{ib(1-a)^2} - \frac{\pi i}{b(1+a)} p(\pi) e^{ib(1+a)^2}. \quad (7.99)$$

If $|a| < 1$, the contribution

$$I(a, b)|_{\vartheta_{\text{non}}} = 2\pi \sqrt{\frac{\pi i}{b}} p(\vartheta_{\text{non}}) \quad (7.100)$$

has to be added to (7.99). Together with the desired closed-orbit theory asymptotics, these expressions lead to the conditions

$$\begin{aligned} \Delta S_{\text{down}} &= S_{\text{down}} - S_{\text{non}} = b(1-a)^2, \\ \Delta S_{\text{up}} &= S_{\text{up}} - S_{\text{non}} = b(1+a)^2, \end{aligned} \quad (7.101)$$

and

$$\begin{aligned} \mathcal{A}_{\text{down}} &= -\frac{\pi i}{b(1-a)} p(0), & \mathcal{A}_{\text{up}} &= -\frac{\pi i}{b(1+a)} p(\pi), \\ \mathcal{A}_{\text{non}} &= 2\pi \sqrt{\frac{\pi i}{b}} p(\vartheta_{\text{non}}) \end{aligned} \quad (7.102)$$

connecting the actions and amplitudes of the downhill, uphill and non-axial orbits to the normal form parameters a and b and to the values of the amplitude function $p(\vartheta)$.

Equation (7.101) can be solved for the normal form parameters to yield

$$a = \frac{\sqrt{\Delta S_{\text{up}}} \mp \sqrt{\Delta S_{\text{down}}}}{\sqrt{\Delta S_{\text{up}}} \pm \sqrt{\Delta S_{\text{down}}}} \quad (7.103)$$

and

$$b = \frac{\Delta S_{\text{down}}}{(1-a)^2} = \frac{\Delta S_{\text{up}}}{(1+a)^2}, \quad (7.104)$$

where the upper or lower sign has to be chosen if the non-axial orbit is real or complex, respectively.

As usual, setting $p(\vartheta)$ equal to a constant in (7.102) yields the constraints

$$\begin{aligned} \frac{1+i}{2} \sqrt{\frac{b}{2\pi}} \mathcal{A}_{\text{non}} &= -b(1-a) \mathcal{A}_{\text{down}} \\ \frac{1+i}{2} \sqrt{\frac{b}{2\pi}} \mathcal{A}_{\text{non}} &= -b(1+a) \mathcal{A}_{\text{up}} \end{aligned} \quad (7.105)$$

the amplitudes must satisfy close to the individual bifurcations. These constraints, although different in form, must agree with (7.84), because the extended normal form (7.93) reduces to (7.75) as the bifurcations are approached.

To obtain a complete uniform approximation, I take the ansatz

$$p(\vartheta) = p_0 + p_1(\cos \vartheta - a) + p_2(\cos \vartheta - a)^2 \quad (7.106)$$

for the amplitude function. The coefficients are given by

$$\begin{aligned} p_0 &= p(\vartheta_{\text{non}}) , \\ p_1 &= \frac{(1+a)^2 p(0) - 4a p(\vartheta_{\text{non}}) - (1-a)^2 p(\pi)}{2(1-a^2)} , \\ p_2 &= \frac{(1+a)p(0) - 2p(\vartheta_{\text{non}}) + (1-a)p(\pi)}{2(1-a^2)} \end{aligned} \quad (7.107)$$

with the values $p(0)$, $p(\pi)$ and $p(\vartheta_{\text{non}})$ determined from (7.102). Due to (7.105), all coefficients are finite everywhere.

With this choice, the uniform approximation (7.97) reads

$$\Psi(E) = p_0 I_0 + p_1 I_1 + p_2 I_2 \quad (7.108)$$

with the integrals

$$\begin{aligned} I_0 &= \int_0^{2\pi} d\varphi \int_0^\pi d\vartheta \sin \vartheta e^{ib(\cos \vartheta - a)^2} \\ &= 2\pi \sqrt{\frac{\pi}{2b}} \left(C \left(\sqrt{\frac{2b}{\pi}}(1-a) \right) + iS \left(\sqrt{\frac{2b}{\pi}}(1-a) \right) \right. \\ &\quad \left. + C \left(\sqrt{\frac{2b}{\pi}}(1+a) \right) + iS \left(\sqrt{\frac{2b}{\pi}}(1+a) \right) \right) \end{aligned} \quad (7.109)$$

in terms of the Fresnel integrals (7.89),

$$\begin{aligned} I_1 &= \int_0^{2\pi} d\varphi \int_0^\pi d\vartheta \sin \vartheta (\cos \vartheta - a) e^{ib(\cos \vartheta - a)^2} \\ &= \frac{\pi i}{b} \left(e^{ib(1+a)^2} - e^{ib(1-a)^2} \right) \end{aligned} \quad (7.110)$$

and

$$\begin{aligned} I_2 &= \int_0^{2\pi} d\varphi \int_0^\pi d\vartheta \sin \vartheta (\cos \vartheta - a)^2 e^{ib(\cos \vartheta - a)^2} \\ &= -i \frac{d}{db} I_0 \\ &= -\frac{\pi i}{b} \left((1-a) e^{ib(1-a)^2} + (1+a) e^{ib(1+a)^2} \right) + \frac{i}{2b} I_0 . \end{aligned} \quad (7.111)$$

All integrals are finite without requiring any regularization. This somewhat atypical behaviour can be traced back to the fact that the domain of integration in this case is compact.

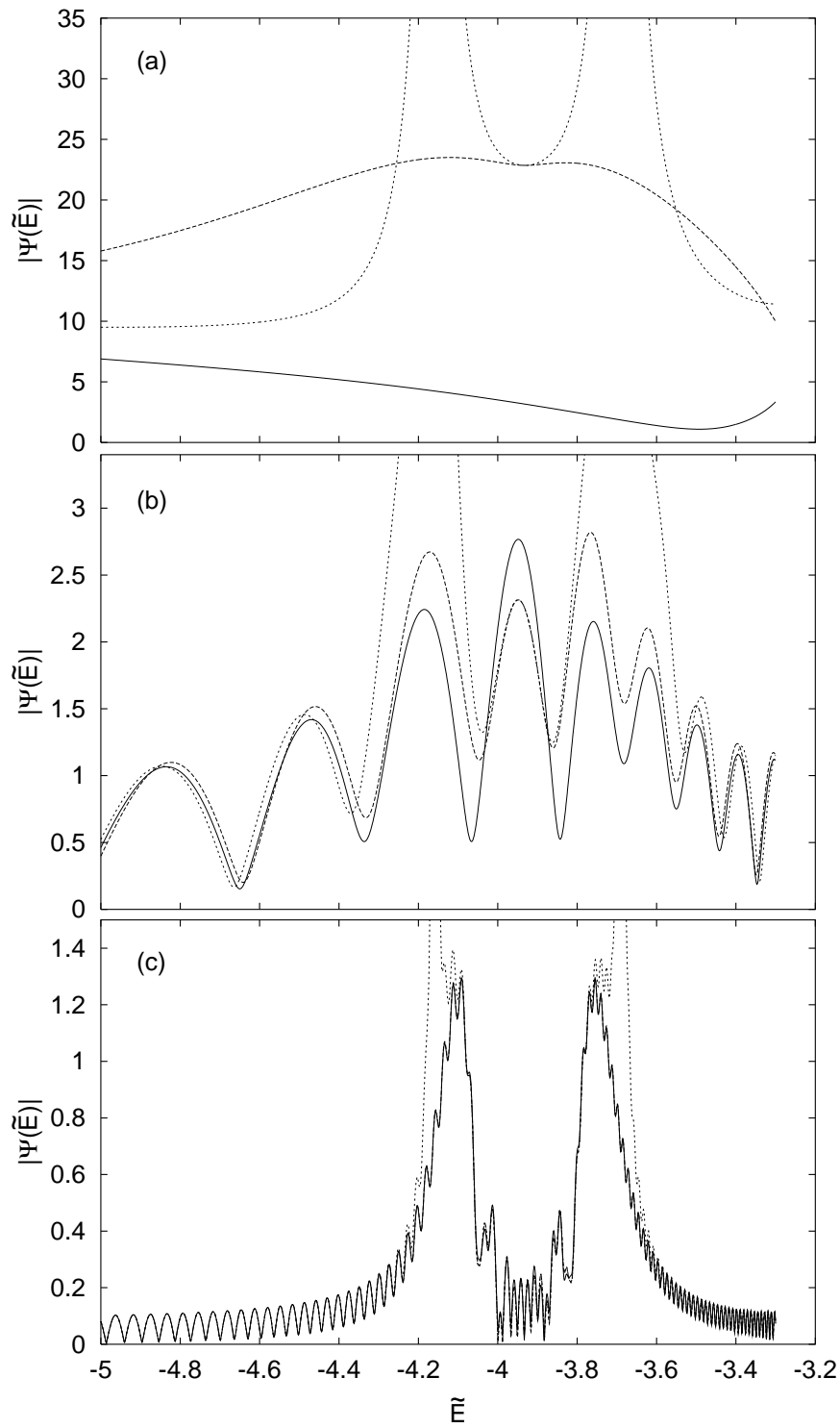


Figure 7.8: Uniform approximation for the generation and destruction of the (20,21) non-axial orbit for the electric field strengths (a) $F = 10^{-2}$, (b) $F = 10^{-6}$, (c) $F = 10^{-10}$. Solid lines: Uniform approximation (7.108), long-dashed lines: uniform approximation (7.87) for isolated bifurcations, short-dashed lines: isolated-orbits approximation.

As an example, figure 7.8 compares the uniform approximation (7.108) for the orbit (20,21) and three different electric field strengths to the isolated-orbits approximation and to the uniform approximation (7.87) for isolated bifurcations. For the latter, the non-axial orbit and the axial orbit for which the action difference is smaller are combined into the uniform approximation, whereas the second axial orbit is treated as isolated.

For the high electric field strength $F = 10^{-2}$ in figure 7.8(a), in the energy range shown none of the uniform approximations reaches the asymptotic region where they agree with the isolated-orbits approximation on either side of the bifurcations. Between the two bifurcations, the isolated-bifurcations approximation appears just to arrive at its asymptotic behaviour before the second bifurcation is felt. The behaviour of the complete uniform approximation is completely different here.

If the field strength is decreased, both uniform approximations reach their asymptotic regions faster. For $F = 10^{-6}$, they approach the isolated-orbits approximation at roughly equal pace on both sides of the bifurcations. Between the bifurcations, the isolated-bifurcations approximation now clearly attains its asymptotic behaviour, whereas the complete uniform approximation exhibits qualitatively similar behaviour, but differs significantly from the other two in quantitative terms. It requires the even lower field strength of $F = 10^{-10}$ used in figure 7.8(c) until both uniform approximations agree with the isolated-orbits result in the region between the bifurcations.

The complete uniform approximation was constructed because in the energy region between the bifurcations the isolated-bifurcations approximation must fail for low energies and high field strengths. However, the complete uniform approximation turns out to reach its asymptotic agreement with the isolated-orbits results considerably more slowly than the isolated-bifurcations approximation. In cases where the latter reproduces the isolated-orbits results between the bifurcations, of course, no further uniformization is required. The observation that the complete uniform approximation yields less precise results than the isolated-bifurcations approximation sheds some doubt on its reliability in cases where the latter fails. In practice, it might be found to do more harm than good.

In this case one is facing the problem discussed in section 6.5.1 that a uniform approximation is not specified uniquely if it is required to asymptotically reproduce the isolated-orbits approximation. The uniform approximation constructed here satisfies the asymptotic requirements, but must be assumed, from the numerical results, to deviate considerably from the correct semiclassical contribution. The problem is probably connected to the non-trivial spherical topology of the configuration space of the uniform approximation: The construction of uniform approximations as described in section 6.5.1 relies on the observation that the unknown phase function in the diffraction integral can be mapped to a certain standard form by a suitable coordinate transformation. The fundamental theorems of catastrophe theory guarantee that this is possible locally. In a Cartesian configuration space and close to a bifurcation, all stationary points of the normal form are close to the origin, so that coordinate regions away from the origin can,

in the spirit of the stationary-phase approximation, be assumed not to contribute to the diffraction integral, whence a local mapping of the exponent function to the normal form and a local approximation to the amplitude function by means of a Taylor series suffice to obtain good results. On the spherical configuration space, a global approximation to the unknown functions must be sought because the stationary points are distributed across the sphere: There is a stationary point at each pole. In the case at hand, I tried replacing the $(\cos \vartheta - a)^2$ -term in the amplitude function (7.106) with $\sin \vartheta$, which also gives only a rough approximation to the actual amplitude function and has no significant effect on the result. The construction of a quantitatively more reliable uniform approximation will presumably require a deeper global understanding of the bifurcation scenarios.

7.5 Semiclassical spectra

A low-resolution semiclassical photo-absorption spectrum can be obtained from the closed-orbit sum (2.47) by including orbits with an orbital period up to a maximum T_{\max} only. In order to resolve individual energy levels, T_{\max} must be larger than the Heisenberg time T_{H} . A rough estimate for T_{H} can be obtained from perturbation theory. To first order in the electric field strength, the energy splitting between two adjacent spectral lines with principal quantum number n is [98] $\Delta E_{\text{p}} = 3nF$, so that the scaled perturbative Heisenberg time is

$$\tilde{T}_{\text{H,p}} = \frac{2\pi F^{3/4}}{\Delta E_{\text{p}}} = \frac{2\pi}{3} \sqrt{-2\tilde{E}}. \quad (7.112)$$

This estimate is reasonable (although it may not be quantitatively precise) as long as different n -manifolds do not overlap. If they do, the mean level spacing is much smaller and the Heisenberg time therefore much larger than given by (7.112).

Multiples of the scaled perturbative Heisenberg time (7.112) are plotted in figure 7.9 together with the scaled energies and scaled periods of bifurcating orbits. For low scaled energies, the periods of bifurcating orbits are well approximated by $\tilde{T}_{\text{H,p}}$. Therefore, there is no parameter range where the closed-orbit sum can be extended up to the Heisenberg time without involving bifurcations, so that the uniformization of bifurcations must be an essential ingredient to any closed-orbit theory quantization of the Stark effect.

These findings can be confirmed numerically. Figure 7.10 displays the oscillatory part of the photo-absorption cross section as calculated from the closed-orbit sum. All spectra presented in this section are non-scaled spectra calculated for the hydrogen atom in an electric field $F = 10^{-8}$, corresponding to $w = 100$ and $\tilde{E} = 10^4 E$, with the initial state $|1s\rangle$ and light linearly polarized along the electric field axis. Small discontinuities are introduced in the low-resolution spectra because a closed orbit abruptly disappears from the truncated sum when its period increases beyond the chosen cut-off time \tilde{T}_{\max} . The discontinuities can be avoided by choosing a smooth cut-off function to gradually switch off the contribution of

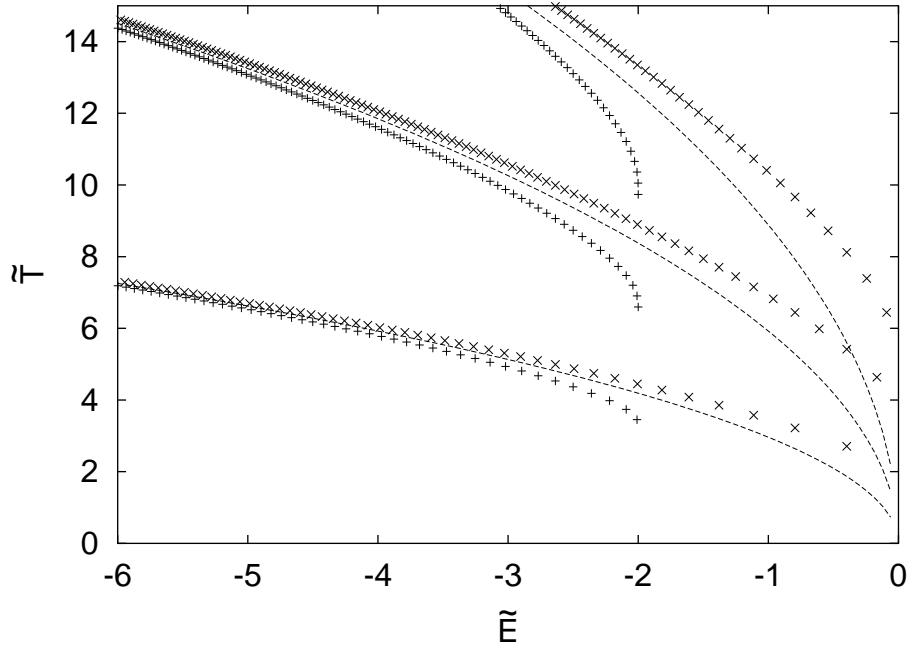


Figure 7.9: Bifurcations of non-axial orbits off the downhill (+) and uphill (\times) orbits in a scaled period vs. scaled energy plot. Bifurcation energies and scaled periods of the bifurcating orbits are indicated. Dashed lines: single, double and triple scaled perturbative Heisenberg time (7.112).

an orbit when its period approaches the cut-off time. The changes in the spectra are hardly visible, and as excellent results can be obtained with the simple hard cut-off, no smoothing will be used henceforth.

For the spectrum in figure 7.10(a), a scaled cut-off time of $\tilde{T}_{\max} = 5$, well below the perturbative Heisenberg time, was chosen. Consequently, one can distinguish groups of levels characterized by a fixed principal quantum number n , but no individual spectral lines can be resolved in the plot. The small oscillations are an artefact of the closed-orbit sum and cannot be identified with spectral lines. This is clear from the observations that the frequency of the oscillation increases with increasing cut-off time and that virtually the same oscillations are visible within an n -manifold and between manifolds.

At low energies, different n -manifolds do not overlap, so that spectral regions with high oscillator strength density alternate with regions where no spectral lines are present. (As the smooth part of the semiclassical spectrum has been omitted, the bottom line of the semiclassical spectrum is shifted to negative values of the oscillator strength density.) At $E \approx -4.7 \times 10^{-4}$, neighbouring n -manifolds start to overlap. In the overlap regions the spectral density is considerably higher than in regions of isolated n -manifolds.

To improve the resolution, the cut-off time must be increased. Figure 7.10(b) displays the results for a scaled cut-off time of $\tilde{T}_{\max} = 6.5$. At low energies, this is still below the perturbative Heisenberg time, and no significant improvement of

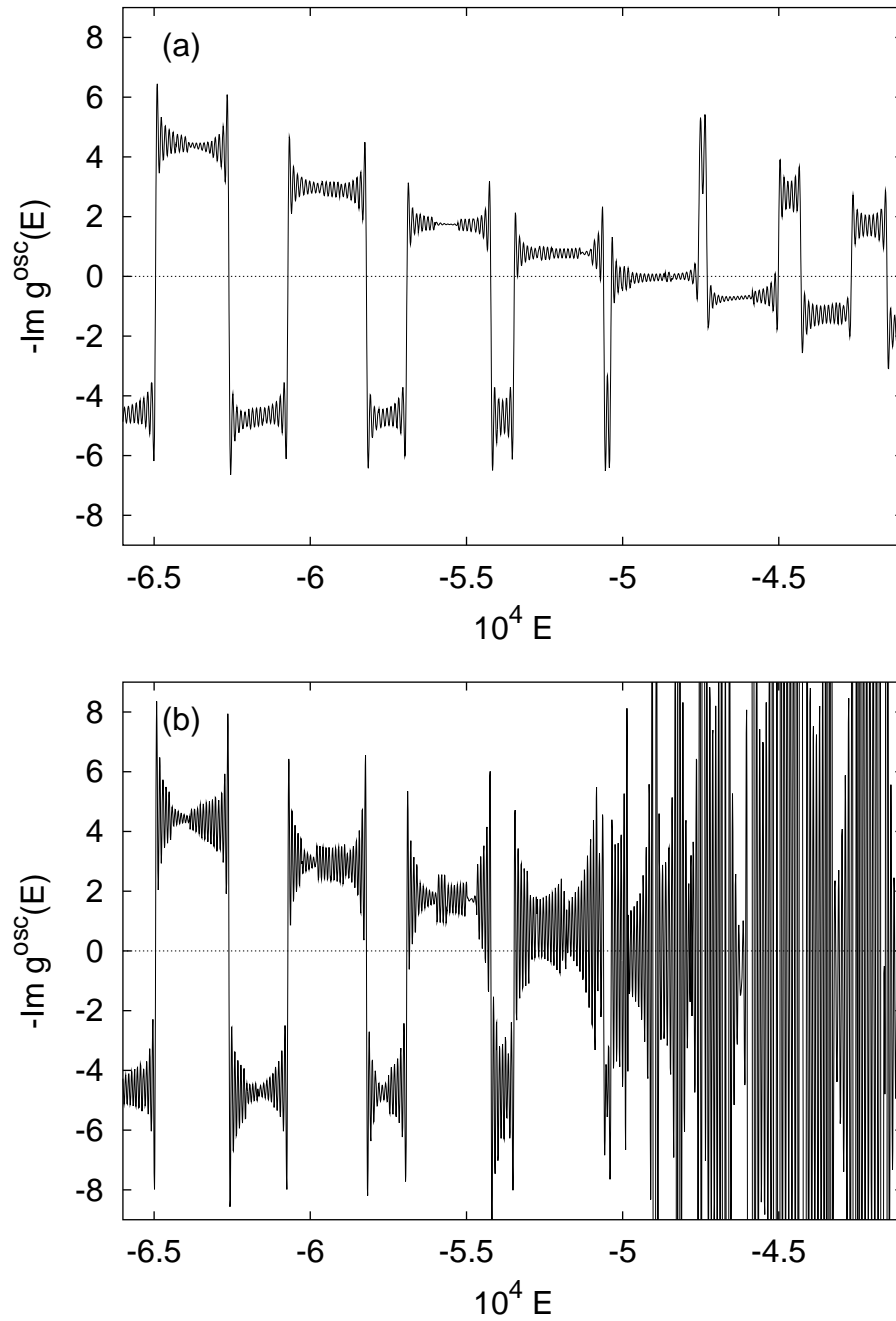


Figure 7.10: Closed-orbit sum without uniform approximations as a function of energy at the electric field strength of $F = 10^{-8}$ with scaled cut-off time (a) $\tilde{T}_{\text{max}} = 5$, (b) $\tilde{T}_{\text{max}} = 6.5$. At $E > -5 \times 10^{-4}$, the latter is dominated by bifurcation-induced divergences.

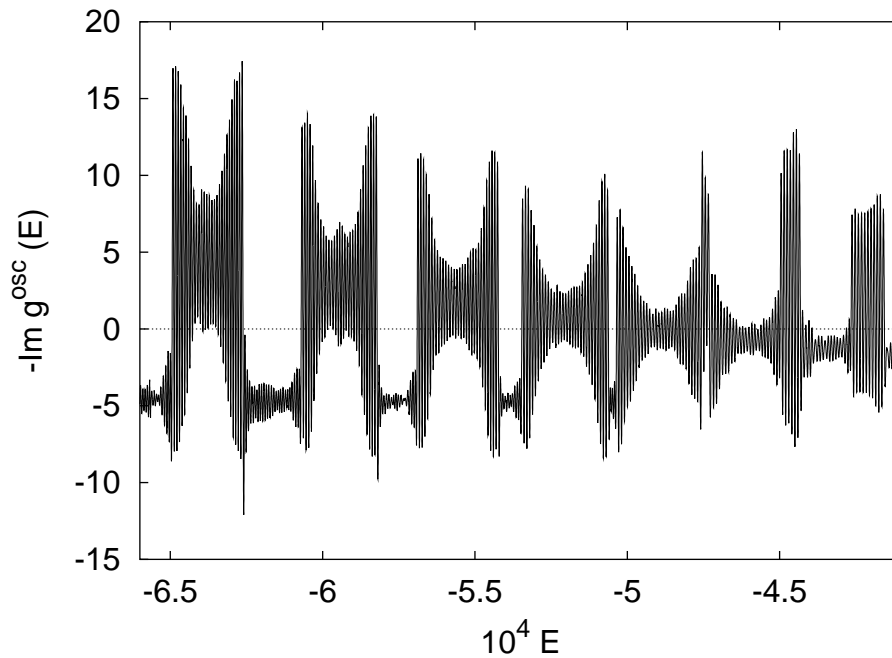


Figure 7.11: Low-resolution semiclassical spectrum using the uniform approximation for isolated bifurcations with scaled cut-off time $\tilde{T}_{\max} = 8$.

the resolution can be found. At high energies, bifurcations start to occur, and a dense sequence of bifurcation-induced divergences covers the semiclassical signal. As the cut-off time is further increased, bifurcations occur at ever lower energies and destroy ever larger parts of the semiclassical spectrum. It is thus obvious that in its simple form the closed-orbit sum is useless for a complete quantization.

If, on the contrary, the uniform approximations are included, the closed-orbit sum can be extended to longer orbits. Figure 7.11 shows the uniformized closed-orbit sum with the simple uniform approximation of section 7.4.1 for a scaled cut-off time $\tilde{T}_{\max} = 8$, which is slightly larger than the perturbative Heisenberg time. As will also be done in all subsequent semiclassical spectra, the uniform approximation was applied for bifurcating orbits whose action difference is less than 2π . If for a given orbit several other orbits satisfy this requirement, a more complicated uniform approximation describing several bifurcations should be used. For the time being, I resolve this conflict by calculating the simple uniform approximation for the two orbits with the smallest action difference and treating all other orbits as isolated.

Although individual spectral lines can be discerned in figure 7.11, it would be hard to obtain precise values of the energy levels and, in particular, of the associated dipole matrix elements from this figure. A more reliable method of extracting the spectral information from the semiclassical data is clearly desirable. To this end, I will use the generalized version of the harmonic inversion method introduced in section 3.4, thus proving it is indeed suitable for a semiclassical quantization including uniform approximations. As discussed in section 3.1, the

cut-off time of the closed orbit sum must be chosen larger than twice the Heisenberg time for this purpose.

The perturbative Heisenberg time thus suggests choosing a scaled cut-off time of $\tilde{T}_{\max} = 15$, which can be expected to be sufficient as long as different n -manifolds do not overlap. Figure 7.12 shows the low-resolution spectrum for this cut-off time. Figure 7.13 presents the energy levels and transition matrix elements obtained from it by the harmonic inversion procedure and compares them to the exact quantum results.

In the region of isolated n -manifolds the quantum and semiclassical spectra can indeed be compared line by line to reveal good agreement in both the position and the intensity of spectral lines. Note, in particular, that the low-resolution semiclassical spectrum apparently ascribes considerable amplitudes to spectral lines in the middle of an n -manifold, whereas the quantum amplitudes nearly vanish. The high-resolution semiclassical spectrum correctly identifies these amplitudes as being very small. Furthermore, it can be seen from the magnified low-resolution spectrum of the manifold $n = 31$ in figure 7.14(a) that the spectral lines, in particular the weak lines close to the centre of the manifold, appear asymmetric in the semiclassical spectrum: They extend farther to the right than to the left. Nevertheless, the high-resolution analysis identifies the lines correctly.

Figure 7.14(b) shows the low-resolution spectrum for the manifold $n = 31$ with a signal length of $\tilde{T}_{\max} = 40$. It can be seen that the spectral lines close to the centre of the manifold become smaller in comparison to the outer lines, thus approaching the true semiclassical spectrum, but that the asymmetry of the lines is exacerbated: They are clearly saw-tooth shaped, rising steeply on the left and falling off gently to the right.

At $E \approx -4.7 \times 10^{-4}$, neighbouring n -manifolds overlap for the first time, thus doubling the density of spectral lines. It can be seen in figure 7.13 that at this energy the harmonic inversion of the given semiclassical signal abruptly breaks down. It recovers at slightly higher energies, where again only levels of a single n -manifold are present. At $E \approx -4.5 \times 10^{-4}$ and $E \approx -4.2 \times 10^{-4}$, pairs of levels belonging to different n -manifolds are so close to being degenerate that they cannot be resolved by the harmonic inversion. In the semiclassical spectrum they appear as single lines with amplitudes equal to the sum of the two quantum amplitudes.

Similar effects can also be observed at higher energies. However, as the energy and the density of spectral lines are further increased, the harmonic inversion gradually ceases to yield meaningful results. In the high-energy region at $E \approx -3.2 \times 10^{-4}$, a few lines can, somewhat arbitrarily, be identified, whereas most of the lines from the quantum spectrum are absent. In this region the cut-off time of the semiclassical signal is evidently, and expectedly, too small.

As discussed in sections 3.1 and 3.2, the harmonic inversion always yields some spurious spectral lines together with an error parameter ϵ that can be used to distinguish between true and spurious lines. In figure 7.13, only lines with an error parameter $\epsilon < 6 \times 10^{-8}$ have been included. This threshold value will also be used for all other semiclassical spectra presented in this section. The selection

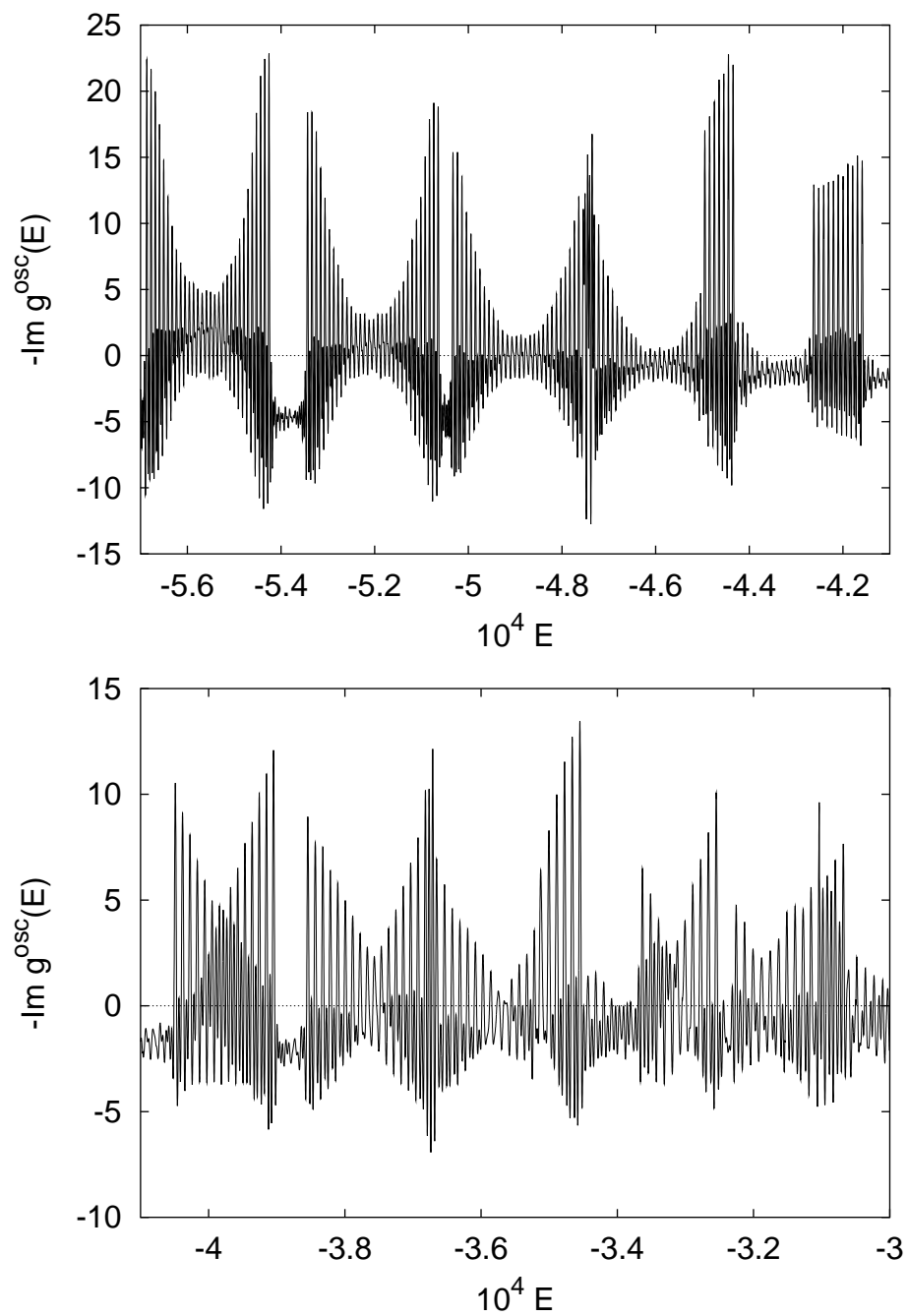


Figure 7.12: Low-resolution semiclassical spectrum with scaled cut-off time $\tilde{T}_{\max} = 15$.

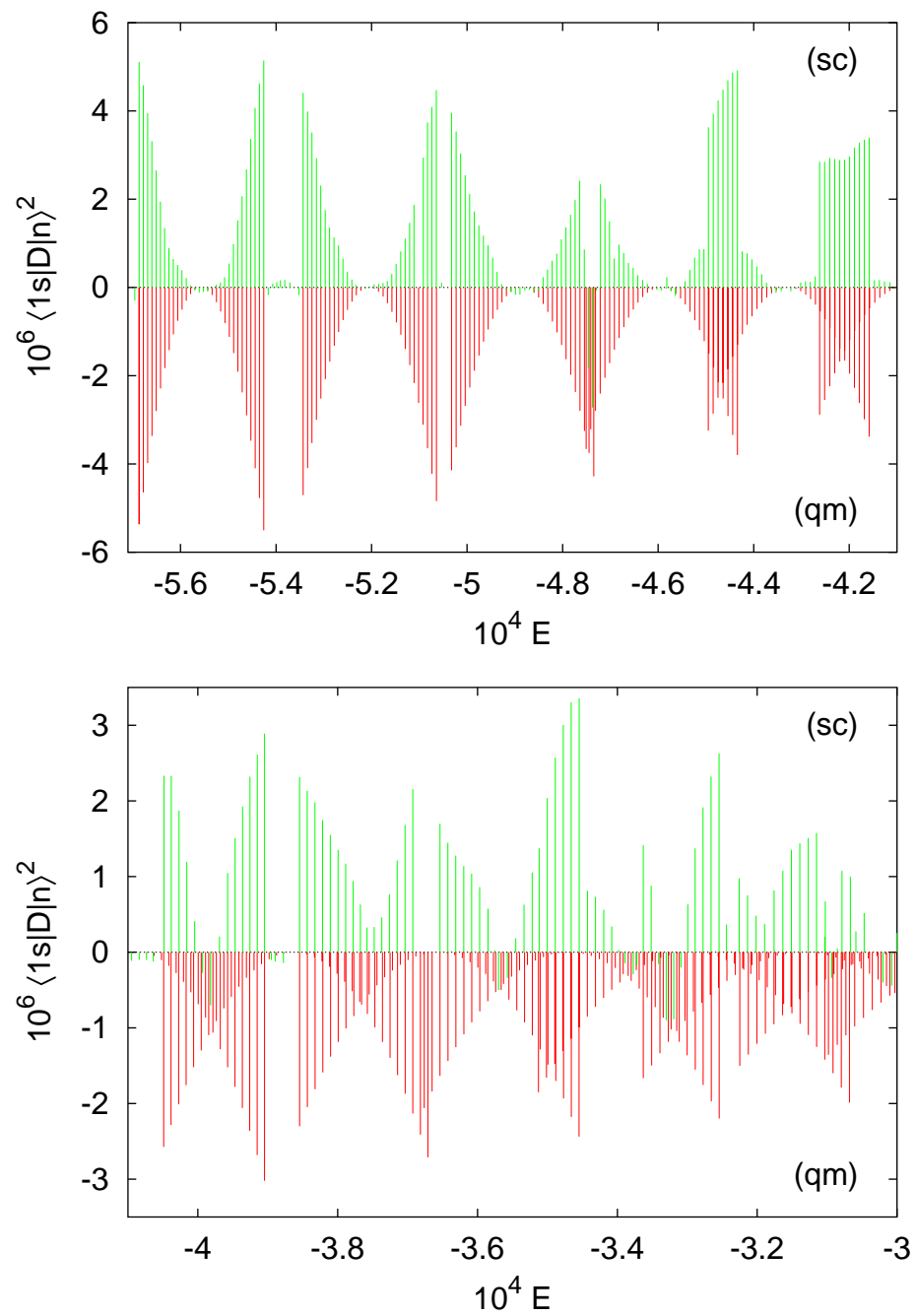


Figure 7.13: High-resolution semiclassical (sc) and quantum (qm, inverted) photo-absorption spectrum. The scaled cut-off time for the semiclassical spectrum is $\hat{T}_{\max} = 15$.

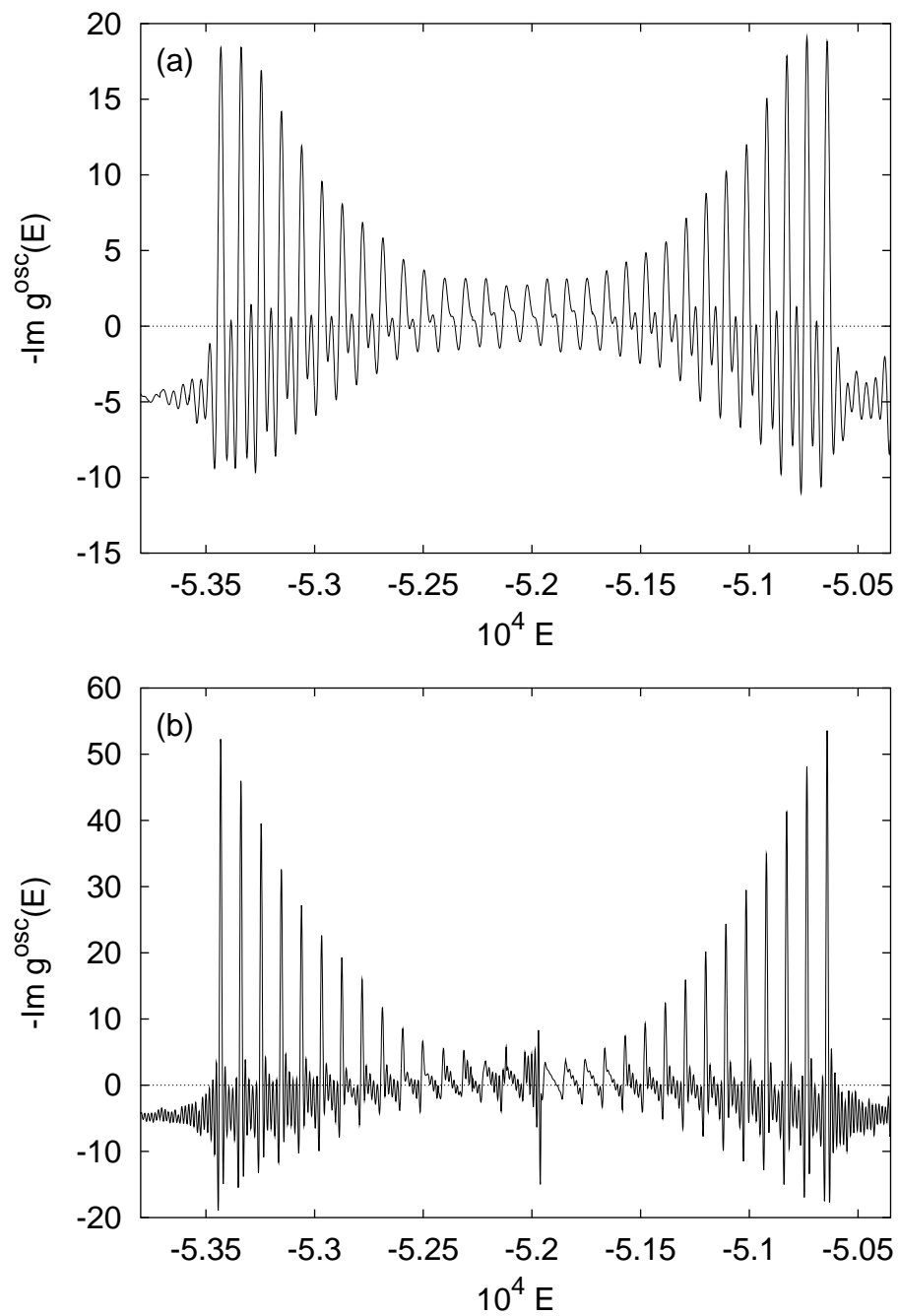


Figure 7.14: The manifold $n = 31$ in the low-resolution semiclassical spectrum with scaled cut-off time (a) $\tilde{T}_{\max} = 15$ and (b) $\tilde{T}_{\max} = 40$.

of “good” semiclassical eigenvalues is therefore solely based on criteria inherent in the semiclassical quantization procedure, no lines are selected according to how well they fit the quantum results. As can be seen from figure 7.13, some spurious lines pass the selection. They are all characterized by having small amplitudes, so that they exert little influence on the semiclassical signal. Only rarely does it occur that a true spectral line of considerable amplitude is removed. If the region of overlapping n -manifolds, where the signal is too short to resolve the spectral lines, is ignored, the only instance of this error present in the above spectrum can be found at $E \approx -5.1 \times 10^{-4}$.

To improve the resolution, the cut-off time needs to be increased. As in the spectral region around $E \approx -3.2 \times 10^{-4}$ three (or even four) different n -manifolds overlap, the true Heisenberg time can be expected to be close to three times its perturbative value. Figure 7.9 suggests choosing a scaled cut-off time of $\tilde{T}_{\max} = 40$. Results obtained with this semiclassical signal are shown in figure 7.15. In the low-energy spectral range, the amplitudes of the spurious lines have diminished. Thus, even in this range the longer signal yields a better semiclassical spectrum. In the region of overlapping n -manifolds around $E \approx -3.8 \times 10^{-4}$, all spectral lines are well resolved. At $E \approx -3.2 \times 10^{-4}$, groups of three closely spaced lines can be identified in the quantum spectrum. In many cases, all three of them are resolved in the semiclassical spectrum. In a few cases, nearly degenerate lines appear in the semiclassical spectrum as a single line whose amplitude is the sum of the two quantum amplitudes.

The most difficult spectral region appears at $E \approx -4.2 \times 10^{-4}$. In this region, spectral lines belonging to neighbouring n -manifold are so close to being degenerate that they are hard to distinguish even in the quantum spectrum. This degeneracy is somewhat accidental, as it will be lifted as the electric field strength is varied, but it nevertheless poses a particular challenge to the harmonic inversion. Even with the signal length of $\tilde{T}_{\max} = 40$, the degenerate levels cannot be resolved semiclassically. Their resolution would presumably require a significantly longer semiclassical signal. As an alternative, the harmonic inversion of cross-correlated signals has proven powerful in resolving nearly degenerate levels [99, 120]. It can be combined with the novel quantization procedure for non-scaling systems in an obvious way and can be expected to considerably reduce the signal length required to identify the unresolved spectral lines.

Results obtained with $\tilde{T}_{\max} = 30$ for lower energies are shown in figure 7.16. In this region all n -manifolds are well isolated. As the splitting of levels within a manifold is smaller than at higher energies, the perturbative Heisenberg time is $\tilde{T}_{\text{H,p}} = 9.4$ at $E = -10^{-4}$. Therefore, the chosen signal length should easily suffice to resolve the spectral lines. This is indeed achieved, the quantum and semiclassical spectra can be compared line by line.¹ However, the agreement between the spectra is not as perfect as was found at higher energies. In particular, considerable contributions to the semiclassical spectrum arise at the centres of the

¹Most of the small spurious lines between the manifolds can be removed if a stricter quality criterion for the semiclassical lines is applied. In figure 7.16, the same threshold $\epsilon < 6 \times 10^{-8}$ as in previous figures is used.

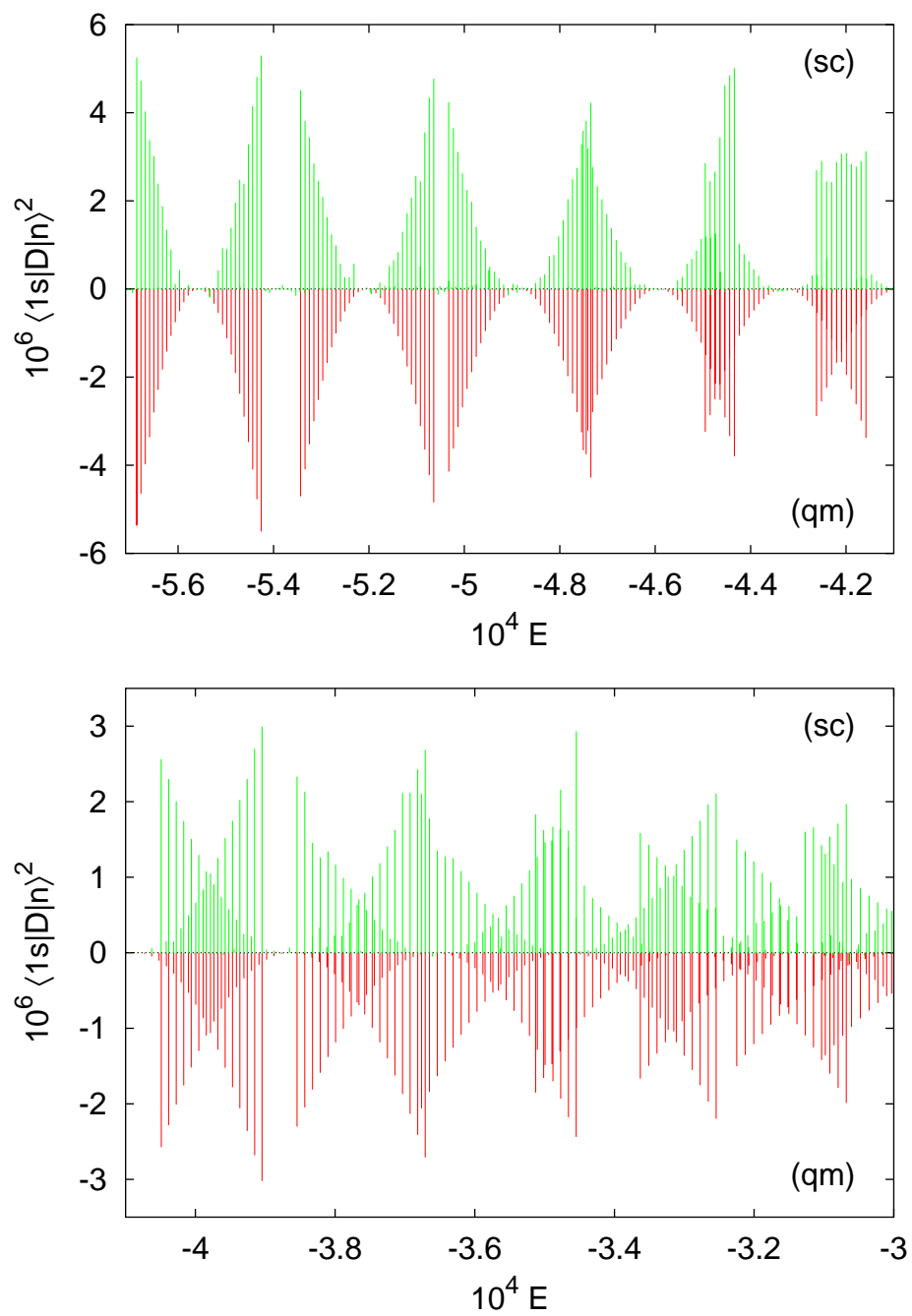


Figure 7.15: High-resolution semiclassical (sc) and quantum (qm, inverted) photo-absorption spectrum. The scaled cut-off time for the semiclassical spectrum is $\hat{T}_{\max} = 40$.

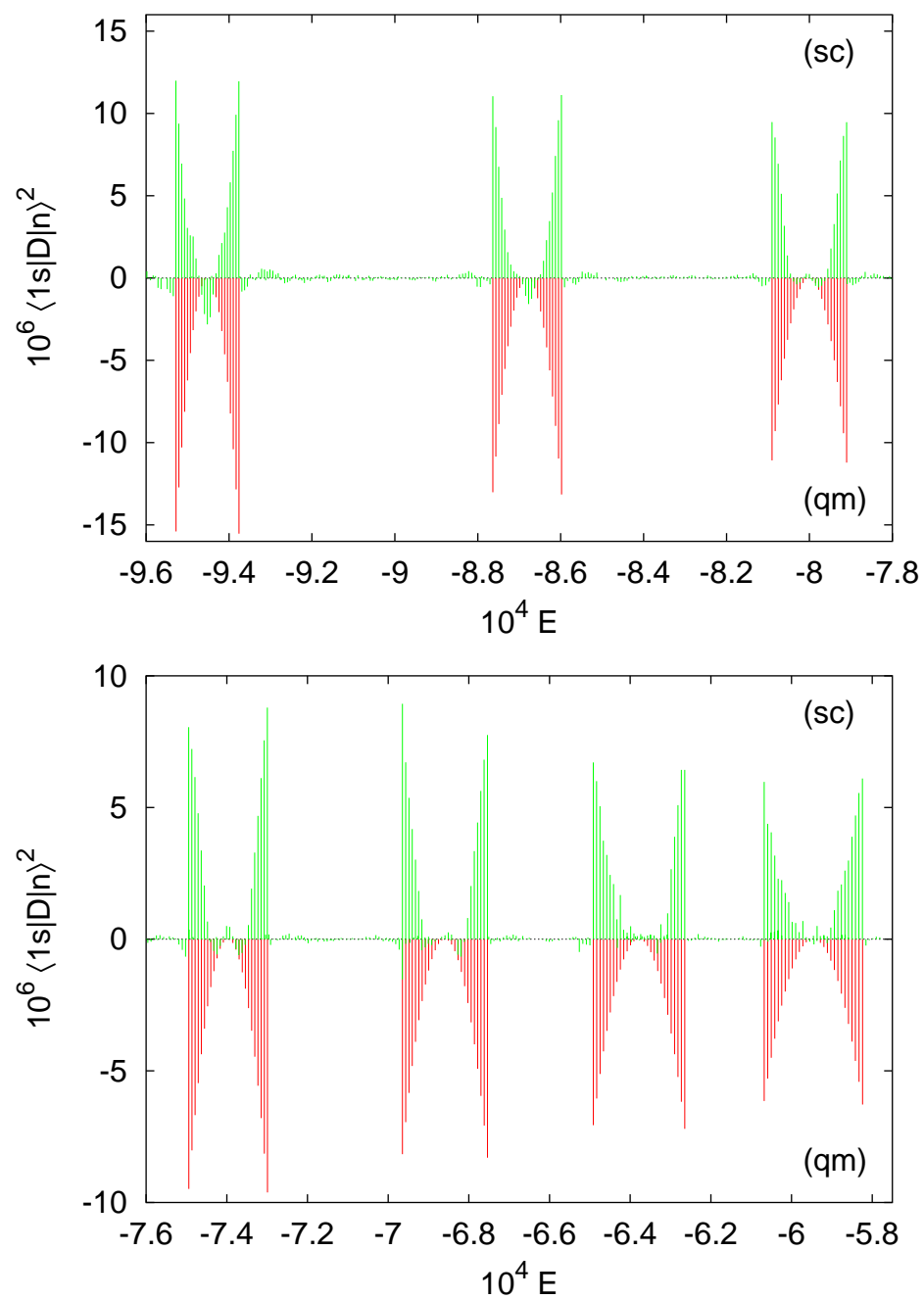


Figure 7.16: High-resolution semiclassical (sc) and quantum (qm, inverted) photo-absorption spectrum. The scaled cut-off time for the semiclassical spectrum is $\tilde{T}_{\max} = 30$.

n -manifolds at low energies. This decrease in quality should be expected when the semiclassical approximation is applied to low-lying states. This is a fundamental limitation of semiclassical methods. In this case, however, a technical problem may also be the source of the decreasing quality. As described in detail in section 7.3, at low energies the generation and destruction of a non-axial orbit occur in ever smaller energy intervals and with ever smaller action differences.

To overcome the difficulties introduced by the proximity of bifurcations, a uniform approximation describing both bifurcations of a non-axial orbit was constructed in section 7.4.2. I can now use this uniform approximation in the calculation of semiclassical spectra. It will be applied if the action differences between a non-axial orbit and both the downhill and uphill orbits it bifurcates out of are smaller than 2π . In the other cases, I revert to the simple uniform approximation or the isolated-orbits approximation, as appropriate. Results calculated with the same signal length $\tilde{T}_{\max} = 30$ as above are shown in figure 7.17. They differ only slightly from the results obtained with the simple uniform approximation in figure 7.16. In particular, the spurious lines at the centres of the low n -manifolds are still there. It is obvious from these results that the decrease in quality of the semiclassical spectrum observed at low energies cannot be overcome by means of the novel uniform approximation.

A difference between the two semiclassical spectra can be seen in the low-resolution spectra in figure 7.18: It has already been noted above for low-resolution spectra using the simple uniform approximation only that the spectral lines close to the centres of the n -manifolds tend to have considerable strengths. If the uniform approximation for non-isolated bifurcations is used, on the one hand the line strengths develop a second maximum at the centre of a manifold. On the other hand, however, the absolute intensity of the central lines is considerably reduced, so that the overall intensity distribution within an n -manifold is reproduced much better than with the isolated-bifurcations approximation.

Figure 7.19 compares the low-resolution spectra of the manifold $n = 23$, which is the lowest n -manifold included in the calculation, computed with both kinds of uniformization. The spectrum shown in figure 7.19(a), which uses the isolated-bifurcations approximation only, exhibits the asymmetric line shape already discussed above, although the asymmetry is weaker here than at higher energies. In the spectrum using the uniform approximation for non-isolated bifurcations, the strong outer lines of the manifold are virtually identical to those in the previous spectrum, but the central lines are completely distorted, some to the point of being hard to identify. On the other hand, again, as the central lines are weaker in the spectrum of figure 7.19(b) than in figure 7.19(a), the distribution of intensities within the manifold is described more accurately if the uniform approximation for non-isolated bifurcations is used. However, this increase in quality seems to be restricted to the low-resolution spectrum because, as noted above, the inclusion of the second uniform approximation does not help to remove the spurious spectral lines from the centres of the manifolds.

It is thus difficult to assess the merits of the uniform approximation for non-isolated bifurcations derived here. It should be added, however, that the spectral

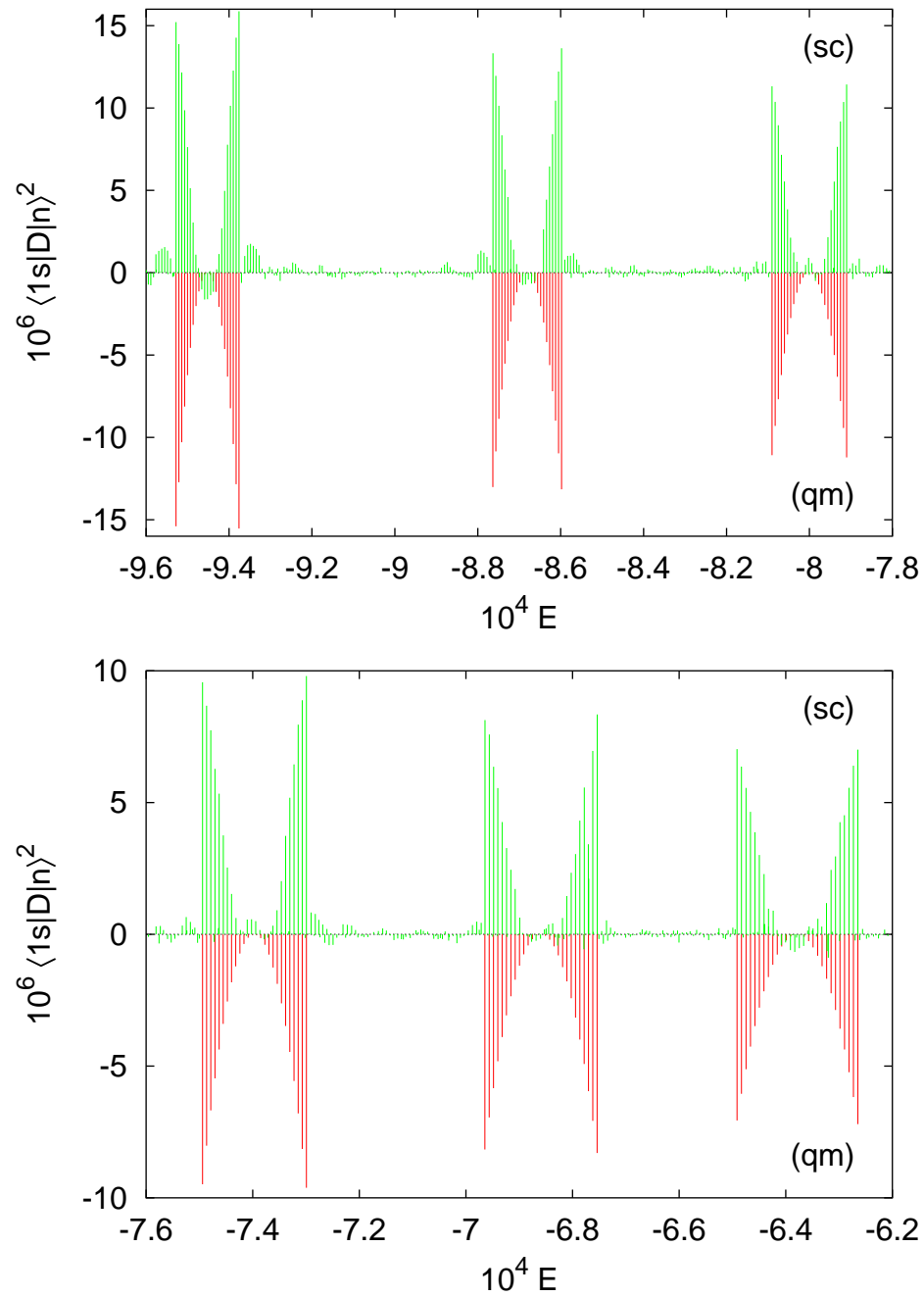


Figure 7.17: High-resolution semiclassical photo-absorption spectrum using the uniform approximation for non-isolated bifurcations. The scaled cut-off time for the semiclassical spectrum is $\tilde{T}_{\max} = 30$.

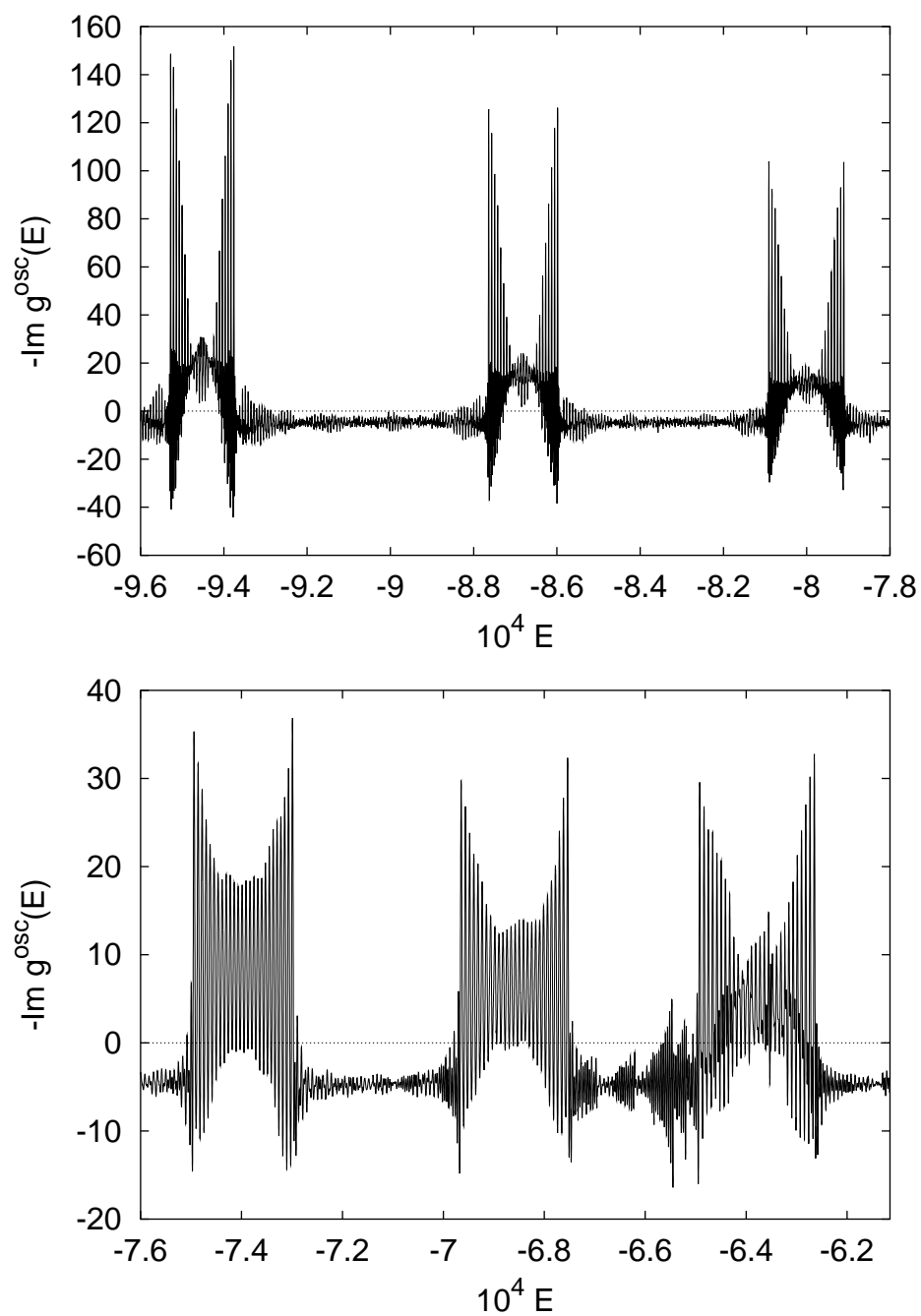


Figure 7.18: Low-resolution semiclassical photo-absorption spectrum using the uniform approximation for non-isolated bifurcations. The scaled cut-off time is $\tilde{T}_{\max} = 30$.

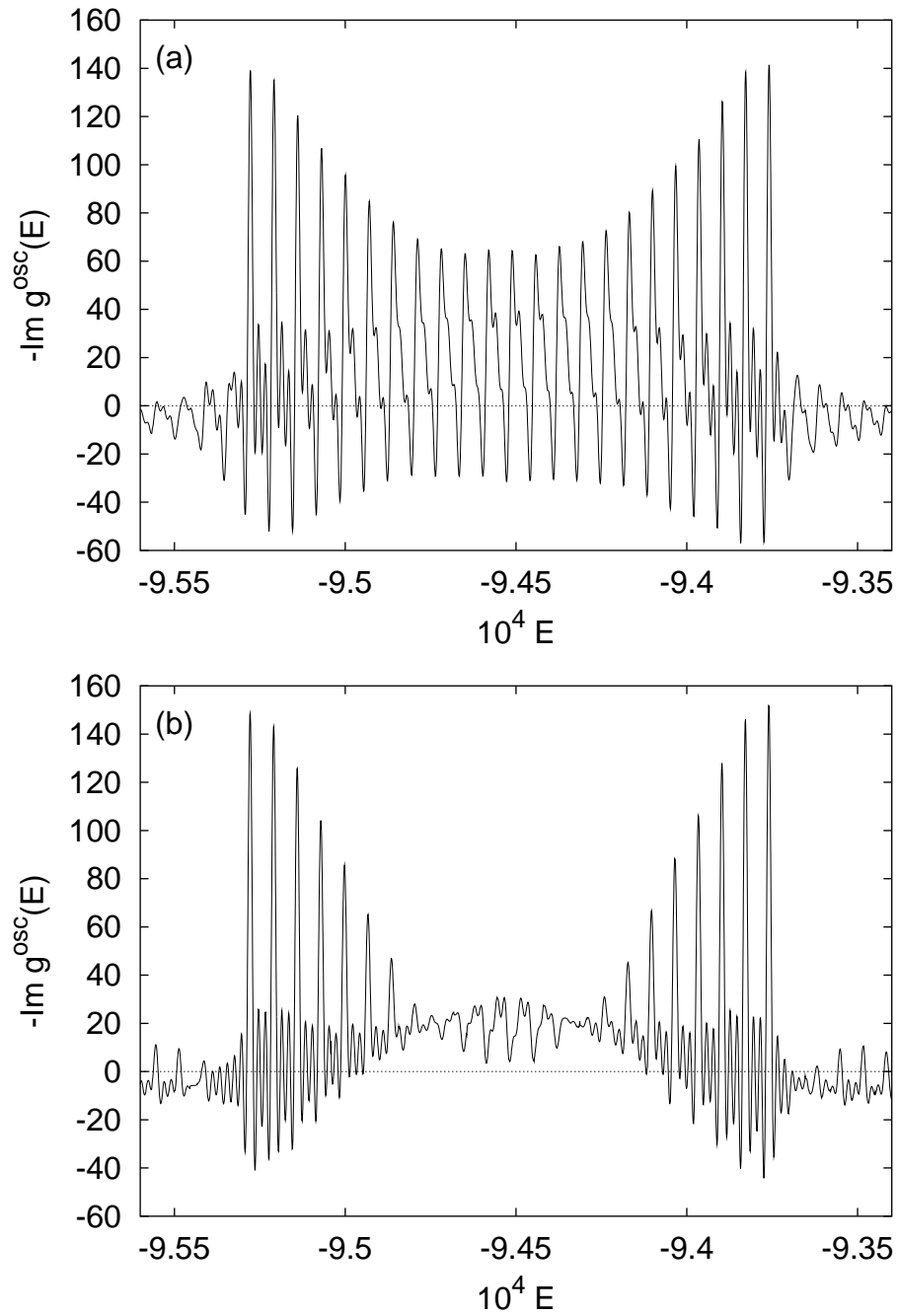


Figure 7.19: The manifold $n = 23$ in the low-resolution semiclassical spectrum with scaled cut-off time $\tilde{T}_{\max} = 30$, (a) not using and (b) using the uniform approximation for non-isolated bifurcations.

region considered here is at the very edge of where the isolated-bifurcations approximation can be expected to fail. The possibility remains, therefore, that at even lower energies or for stronger fields there may be a spectral region where the uniform approximation for non-isolated orbits, although not ideally suited for the bifurcation scenario it was intended for, still gives better results than the isolated-bifurcations approximation. These spectral regions must, however, lie well within the realm of perturbation theory, so that it does not seem worth while pursuing this possibility further.

It remains to conclude that the general semiclassical quantization scheme introduced in section 3.4 has been applied to the Stark system with great success. It has been shown to yield excellent results in spectral regions where the semiclassical signal is dominated by the contributions of bifurcating orbits. At low energies, a gradual decrease of the quality of the semiclassical spectra is observed. It probably indicates the spectral region where the semiclassical approximation is beginning to fail.

For the low energy region, a uniform approximation simultaneously describing both bifurcations of a non-axial orbit was constructed. This uniform approximation is of interest for reasons of principle, because it is the first uniform approximation introduced in the literature that relies on a topologically non-trivial configuration space. It could be demonstrated that uniform approximations with a non-Cartesian configuration space can indeed be constructed. At the same time, it has become clear that the basic requirements for uniform approximations, that they smooth the divergences of the simple semiclassical formulae and exhibit the correct asymptotic behaviour, are insufficient to guarantee quantitatively good results if non-local aspects of a bifurcation scenario, which necessitate the non-trivial topology of the configuration space, must be taken into account.

The description of the spectral region close to the Stark saddle energy remains an fundamental open problem. At this energy, the downhill orbits undergo an infinite cascade of bifurcations in a finite energy interval. The uniformization of this kind of cascade is far beyond present-day techniques for the construction of uniform approximations. It presents a worthwhile challenge for future research, both in itself and in view of its potential applications: The bifurcation cascade occurs at the continuum threshold, where the transition from bound states to a continuum with embedded resonances takes place [115]. The semiclassical description of this transition region is a task of special interest and importance. Presumably, it will require the uniformization of the bifurcation cascades.

Chapter 8

Conclusion

In this chapter I summarize the main results obtained in this thesis.

Closed-orbit theory provides a powerful framework both for the interpretation of atomic photo-absorption spectra and for their semiclassical calculation. In the latter case, it requires all closed orbits up to a certain maximal length to be given. For this reason, a complete classification of closed orbits present for given values of the energy and the field strengths is requisite.

As a decisive step in that direction, in this thesis a local bifurcation theory for closed orbits was developed. The study of closed-orbit bifurcations thus gains the firm theoretical underpinning which has been available in the case of periodic orbit bifurcations for a long time. Catastrophe theory was shown to provide a suitable framework for the discussion of closed orbit bifurcations. In codimension one, the tangent bifurcation and, due to the presence of discrete symmetries, the pitchfork bifurcation were found to be generic.

Apart from a bifurcation theory, the systematic classification of closed orbits requires the identification of fundamental closed orbits at low external field strengths, which serve as the roots of family trees from which further orbits bifurcate. Although fundamental orbits have not yet been identified, a coordinate-free reformulation of the KS transformation was described which can be expected to offer a convenient basis for analytic calculations in classical perturbation theory. Further work in this direction is in progress.

A systematic study of the closed orbits in the hydrogen atom in crossed electric and magnetic fields at low scaled energies was carried out. It revealed a surprisingly rich variety of bifurcation scenarios composed of the two elementary types of bifurcations. A classification scheme for the orbits based on the fundamental distinction between vibrator and rotator orbits in the diamagnetic Kepler problem was proposed, and algorithms for the automatic classification of orbits were described. The classification was shown to be applicable at least up to electric field strengths half as high, in atomic units, as the magnetic field strength.

For the first time, a high-resolution semiclassical quantization of the hydrogen atom in crossed electric and magnetic fields was presented. It achieved the identification of the strong spectral lines in different n -manifolds. By means of a detailed semiclassical analysis of the pertinent quantum spectrum, it was shown

that bifurcations of closed orbits play a crucial role in the semiclassical spectrum. They pose a particular challenge to the semiclassical quantization because they require a special treatment by uniform approximations.

A simple heuristic scheme for the construction of uniform approximations has been proposed. Its simplicity and efficacy was demonstrated by a derivation of the uniform approximations for the codimension-one generic bifurcations and the bifurcations occurring in the hydrogen atom in an electric field. It was also applied to a more complicated bifurcation scenario in the Stark system which required the introduction of a spherical configuration space. Although a quantitatively accurate result was not achieved, it could be shown that the general framework for the construction of uniform approximations is capable of handling topologically non-trivial configuration spaces. The notion of a uniform approximation with non-Cartesian configuration space presents a major extension of the previous uniform approximations on Cartesian spaces.

The derivation of a uniform approximation depends on the availability of a suitable normal form. Several complicated bifurcation scenarios were found where a normal form could not be given. They involve a rotational symmetry-breaking bifurcation as well as one or several codimension-one generic bifurcations. As the construction of normal forms for these two cases relies on completely different principles, they are not easy to combine. Thus, even the apparently well-understood subject of uniform approximations contains open problems as soon as a complicated system such as the crossed-fields hydrogen atom is studied.

The method of semiclassical quantization by harmonic inversion was generalized to permit the inclusion of uniform approximations in high-resolution semiclassical spectra. It is the first quantization scheme presented in the literature which is capable of dealing with uniform approximations. By way of example of the hydrogenic Stark effect, it was demonstrated that the novel method yields excellent semiclassical spectra even in a spectral region where bifurcations of closed orbits abound, so that a semiclassical spectrum without uniform approximations would be useless.

The technique of semiclassical quantization by harmonic inversion can be used in connection with semiclassical trace formulae as well as with closed-orbit theory. With the modifications developed in this work, it is no longer restricted to systems possessing a classical scaling property. Therefore, it is the only semiclassical quantization scheme available which has reached a stage where it does not impose any conditions on the classical dynamics of the system under study except that a semiclassical approximation to the quantum recurrence function can be given. Besides uniform approximations, any other non-standard semiclassical contribution such as diffractive corrections can be included in an obvious way. Thus, the harmonic inversion can now be regarded as a truly universal tool for the semiclassical quantization of arbitrary systems. It can therefore be expected to find widespread applications in all areas of semiclassical physics.

Appendix A

Atomic units

Throughout this work, atomic units are used. The values of the physical constants given here are 1998 CODATA recommendations. They were taken from <http://physics.nist.gov/cuu/Constants>.

- The unit of mass is the electron mass $m_e = 9.109\,381\,88(72) \times 10^{-31}$ kg.
- The unit of charge is the elementary charge $e = 1.602\,176\,462(63) \times 10^{-19}$ C. Its sign is chosen so that the electron charge in atomic units is -1 .
- The unit of action is Planck's constant $\hbar = 1.054\,571\,596(82) \times 10^{-34}$ Js.
- The unit of length is the Bohr radius $a_0 = 4\pi\epsilon_0\hbar^2/(m_e e^2) = 0.529\,177\,2083(19) \times 10^{-10}$ m.
- The unit of energy is the Hartree unit $E_0 = m_e c^2 \alpha^2 = e^2/(4\pi\epsilon_0 a_0) = 4.359\,743\,81(34) \times 10^{-18}$ J = 27.211 3834(11) eV. This is twice the ground state ionization energy of the hydrogen atom.
- The unit of time is $t_0 = \hbar/E_0 = 2.418\,884\,326\,500(18) \times 10^{-17}$ s.
- The unit of magnetic field strength is $B_0 = \hbar/(ea_0^2) = 2.350\,517\,349(94) \times 10^5$ T. In a magnetic field of strength B_0 a classical electron on the first Bohr orbit experiences a Lorentz force equal to the Coulomb force.
- The unit of electric field strength is $F_0 = e/(4\pi\epsilon_0 a_0^2) = 5.142\,206\,24(20) \times 10^{11}$ V/m. This is the field strength caused by a proton in a distance of a Bohr radius.

Appendix B

The angular functions $\mathcal{Y}(\vartheta, \varphi)$

In the semiclassical closed-orbit theory formulae derived in chapter 2, the properties of the initial state and the exciting laser field are summarized in the angular functions $\mathcal{Y}_{lm}(\vartheta, \varphi)$. For hydrogen atoms, these functions can easily be calculated because the hydrogenic core wave functions are known. The calculation first requires the determination of the coefficients (2.14)

$$d_k(E) = \langle \Psi_k^{\text{core}}(E) | D | i \rangle . \quad (\text{B.1})$$

Let the initial state be a state with fixed principal and angular momentum quantum numbers n, l, m :

$$|i\rangle = |nlm\rangle = R_{nl}(r)Y_{lm}(\vartheta, \varphi) \quad (\text{B.2})$$

with a known radial function R_{nl} . The application of the dipole operator D then yields

$$D|i\rangle = rR_{nl}(r) \sum_{l'm'} b_{l'm'} Y_{l'm'}(\vartheta, \varphi) , \quad (\text{B.3})$$

where the expansion coefficients $b_{l'm'}$ can be calculated once the polarization of the laser field is fixed. They can only be non-zero if $l' = l \pm 1$ and $m' = m$ or $m' = m \pm 1$ depending on the polarization.

As the hydrogenic core scattering matrix is the identity matrix, the core radial wave functions (2.4) read

$$F_{l'm',lm}^{\text{core}}(r) = \sqrt{2}f_l(r) \delta_{l'l} \delta_{m'm} \quad (\text{B.4})$$

with the regular Coulomb function $f_l(r) = -i(f_l^+(r) - f_l^-(r))/\sqrt{2}$. In accordance with the discussion of chapter 2, I pick the zero-energy wave function

$$f_l(r) = \sqrt{2r} J_{2l+1}(\sqrt{8r}) , \quad (\text{B.5})$$

so that the complete core wave functions (2.3) are

$$\Psi_{l'm'}^{\text{core}} = \sqrt{\frac{2}{r}} J_{2l'+1}(\sqrt{8r}) Y_{l'm'}(\vartheta, \varphi) . \quad (\text{B.6})$$

The coefficients d_k are given by

$$d_{l'm'} = b_{l'm'} R'_{nl} \quad (\text{B.7})$$

with the radial matrix elements

$$R'_{nl} = \sqrt{2} \int_0^\infty dr r^{5/2} R_{nl}(r) J_{2l'+1}(\sqrt{8r}). \quad (\text{B.8})$$

Since the radial functions are of the form

$$R_{nl}(r) = \sum_{k=l-l'+1}^{n-l'} c_k r^{l'+k-1} e^{-r/n}, \quad (\text{B.9})$$

the matrix elements can be evaluated [44, 11.4.28] in terms of Kummer's confluent hypergeometric function:

$$\begin{aligned} R'_{nl} &= \sum_k c_k 2^{l'+1} n^{2l'+k+3} \frac{\Gamma(2l' + k + 3)}{\Gamma(2l' + 2)} M(2l' + k + 3, 2l' + 2; -2n) \\ &= \sum_k c_k 2^{l'+1} n^{2l'+k+3} \frac{\Gamma(2l' + k + 3)}{\Gamma(2l' + 2)} e^{-2n} M(-k - 1, 2l' + 2; 2n) \\ &= 2^{l'+1} e^{-2n} \sum_{k=l-l'+1}^{n-l'} c_k n^{2l'+k+3} (2l' + 2)_{k+1} \sum_{p=0}^{k+1} \frac{(-k-1)_p (2n)^p}{(2l' + 2)_p p!} \end{aligned} \quad (\text{B.10})$$

with Pochhammer's symbol

$$(a)_n = \Gamma(a + n)/\Gamma(a) = a \cdot (a + 1) \cdot \dots \cdot (a + n - 1). \quad (\text{B.11})$$

Explicitly, the lowest radial matrix elements read

$$\begin{aligned} R_{10}^1 &= 2^4 e^{-2}, & R_{20}^1 &= 2^{17/2} e^{-4}, \\ R_{21}^2 &= \frac{2^{19/2}}{\sqrt{3}} e^{-4}, & R_{21}^0 &= \frac{2^{15/2}}{\sqrt{3}} e^{-4}. \end{aligned} \quad (\text{B.12})$$

Throughout this work, I assume π -polarized light, so that $D = r \cos \vartheta$. For the initial state $|i\rangle = |1s0\rangle$, then

$$D |1s0\rangle = r R_{10}(r) \cdot \frac{1}{\sqrt{3}} Y_{10}(\vartheta, \varphi), \quad (\text{B.13})$$

so that $b_{10} = 1/\sqrt{3}$, $d_{10} = 16e^{-2}/\sqrt{3}$ and

$$\mathcal{Y}(\vartheta, \varphi) = -d_{10} Y_{10}(\vartheta, \varphi) = -\frac{8}{\sqrt{\pi}} e^{-2} \cos \vartheta. \quad (\text{B.14})$$

Similarly, for the initial state $|i\rangle = |2p0\rangle$,

$$D |2p0\rangle = r R_{21}(r) \left(\frac{2}{\sqrt{15}} Y_{20}(\vartheta, \varphi) + \frac{1}{\sqrt{3}} Y_{00}(\vartheta, \varphi) \right) \quad (\text{B.15})$$

so that

$$d_{20} = \frac{2^{21/2}}{3\sqrt{5}} e^{-4}, \quad d_{00} = \frac{2^{15/2}}{3} e^{-4}, \quad (\text{B.16})$$

and

$$\mathcal{Y}(\vartheta, \varphi) = \frac{2^{13/2} e^{-4}}{\sqrt{\pi}} (4 \cos^2 \vartheta - 1). \quad (\text{B.17})$$

Appendix C

Introduction to geometric algebra

Geometric algebra is an algebraic system designed to represent the geometric properties of Euclidean space in the most comprehensive and systematic way possible. It was pioneered by Hermann Grassmann and William Kingdon Clifford during the nineteenth century. From the 1960's on, David Hestenes, with the aim of providing a universal mathematical framework for theoretical physics, extended the algebraic techniques of Grassmann and Clifford by a differential and integral calculus within the geometric algebra, which he called geometric calculus [121].

There are many algebraic systems used to describe geometric properties, most notably vector and tensor calculus. Hence, the reader will recognize many of the formulae presented in this chapter because they have close analogues in other formalisms. The power of geometric algebra lies largely in the fact that it unites the strengths of different formalisms into a single coherent framework.

The present chapter gives only a sketch of geometric algebra in so far as it is needed in the present work. A more extensive introduction, with an extension to Minkowski spacetime, is contained in [74, 122]. A thorough introduction to the geometric algebra of Euclidean 3-space, with a detailed discussion of applications to classical mechanics, can be found in [29]. A detailed presentation of the mathematical properties of the geometric algebra is given in [121].

C.1 The geometric algebra of Euclidean 3-space

The orientation of two vectors \mathbf{a} and \mathbf{b} in space can be characterized by the projection of one vector onto the other, which is described by the scalar product $\mathbf{a} \cdot \mathbf{b}$, and the plane spanned by \mathbf{a} and \mathbf{b} , which is characterized by the vector product $\mathbf{a} \times \mathbf{b}$. In the geometric algebra these complementary products $\mathbf{a} \cdot \mathbf{b}$ and $\mathbf{a} \times \mathbf{b}$ are unified into a single “geometric” product¹ \mathbf{ab} . I start the construction of the geometric product by picking a right-handed frame of orthonormal unit vectors $\boldsymbol{\sigma}_1$, $\boldsymbol{\sigma}_2$ and $\boldsymbol{\sigma}_3$. For them, I postulate the existence of an associative, but

¹Note that the geometric product is indicated by juxtaposition of the vector symbols, whereas the scalar product is written with a dot.

non-commutative geometric product satisfying

$$\boldsymbol{\sigma}_i \boldsymbol{\sigma}_j + \boldsymbol{\sigma}_j \boldsymbol{\sigma}_i = 2\delta_{ij} . \quad (\text{C.1})$$

In addition, the geometric product is required to obey the distributive law with respect to the usual addition of vectors. It follows from (C.1) that $\boldsymbol{\sigma}_i^2 = 1$ is a scalar. The reader may notice that the defining relation (C.1) is the same as obeyed by the Pauli spin matrices. Indeed, these matrices generate a matrix representation of the Clifford algebra of Euclidean 3-space. In the present context, however, it is important to retain the interpretation of the $\boldsymbol{\sigma}_i$ as ordinary vectors instead of regarding them as matrices. The elements of the Clifford algebra are thus given a geometric interpretation, as is indicated by the name “geometric algebra” introduced by Clifford himself. It turns out that all calculations within geometric algebra can be done without recourse to a matrix representation.

By virtue of the defining relation (C.1), the geometric product of two arbitrary vectors $\mathbf{a} = \sum_{i=1}^3 a_i \boldsymbol{\sigma}_i$ and $\mathbf{b} = \sum_{i=1}^3 b_i \boldsymbol{\sigma}_i$ is

$$\begin{aligned} \mathbf{a}\mathbf{b} = & a_1 b_1 + a_2 b_2 + a_3 b_3 \\ & (a_2 b_3 - a_3 b_2) \boldsymbol{\sigma}_2 \boldsymbol{\sigma}_3 + (a_3 b_1 - a_1 b_3) \boldsymbol{\sigma}_3 \boldsymbol{\sigma}_1 + (a_1 b_2 - a_2 b_1) \boldsymbol{\sigma}_1 \boldsymbol{\sigma}_2 . \end{aligned} \quad (\text{C.2})$$

The scalar terms of this equation comprise the scalar product $\mathbf{a} \cdot \mathbf{b}$. In addition, there are terms containing the product of two orthogonal vectors. These terms are neither scalars nor vectors. They are referred to as bivectors. As their coefficients are the components of the vector cross product $\mathbf{a} \times \mathbf{b}$, bivectors should be interpreted as describing an oriented area in the same way as a vector describes an oriented line segment. Accordingly, a product of three orthonormal vectors is called a trivector and interpreted as representing an oriented volume element. The unit trivector

$$I = \boldsymbol{\sigma}_1 \boldsymbol{\sigma}_2 \boldsymbol{\sigma}_3 , \quad (\text{C.3})$$

satisfies

$$I \boldsymbol{\sigma}_1 = \boldsymbol{\sigma}_1 \boldsymbol{\sigma}_2 \boldsymbol{\sigma}_3 \boldsymbol{\sigma}_1 = -\boldsymbol{\sigma}_1 \boldsymbol{\sigma}_2 \boldsymbol{\sigma}_1 \boldsymbol{\sigma}_3 = \boldsymbol{\sigma}_1 \boldsymbol{\sigma}_1 \boldsymbol{\sigma}_2 \boldsymbol{\sigma}_3 = \boldsymbol{\sigma}_2 \boldsymbol{\sigma}_3 .$$

Similarly, $I \boldsymbol{\sigma}_2 = \boldsymbol{\sigma}_3 \boldsymbol{\sigma}_1$ and $I \boldsymbol{\sigma}_3 = \boldsymbol{\sigma}_1 \boldsymbol{\sigma}_2$. Equation (C.2) can thus be rewritten as

$$\mathbf{a}\mathbf{b} = \mathbf{a} \cdot \mathbf{b} + I \mathbf{a} \times \mathbf{b} , \quad (\text{C.4})$$

which achieves the desired unification of the scalar and vector products. Notice that (C.4) contains a sum of quantities of different types, a scalar and a bivector. This should be regarded as a formal sum combining quantities of different types into a single object with a scalar and a bivector part, in analogy to how a real and an imaginary number are added to yield a complex number.

As the scalar product is symmetric in its factors whereas the vector product is anti-symmetric, these products can be recovered from the geometric product via

$$\mathbf{a} \cdot \mathbf{b} = \frac{1}{2}(\mathbf{a}\mathbf{b} + \mathbf{b}\mathbf{a}) , \quad (\text{C.5})$$

$$\mathbf{a} \times \mathbf{b} = \frac{1}{2I}(\mathbf{a}\mathbf{b} - \mathbf{b}\mathbf{a}) . \quad (\text{C.6})$$

In particular, parallel vectors commute under the geometric product, whereas perpendicular vectors anti-commute, and any vector \mathbf{a} satisfies $\mathbf{a}\mathbf{a} = \mathbf{a} \cdot \mathbf{a}$.

It is a crucial feature of the geometric algebra that it contains elements of different grades, viz. scalars, vectors, bivectors, and trivectors. A general element can be written as a sum of these pure-grade components and is called a multivector. The pure-grade parts of any multivector can be extracted by means of a grade projector. Let $\langle A \rangle_k$ be the grade- k part of the multivector A . For example, by (C.4) two vectors \mathbf{a} and \mathbf{b} satisfy

$$\begin{aligned}\langle \mathbf{a}\mathbf{b} \rangle_0 &= \mathbf{a} \cdot \mathbf{b} , \\ \langle \mathbf{a}\mathbf{b} \rangle_2 &= I\mathbf{a} \times \mathbf{b} , \\ \langle \mathbf{a}\mathbf{b} \rangle_1 &= \langle \mathbf{a}\mathbf{b} \rangle_3 = 0 .\end{aligned}$$

Due to its particular importance, the scalar projector can be abbreviated as $\langle A \rangle = \langle A \rangle_0$, and the scalar product of two multivectors A and B is defined by

$$A * B = \langle AB \rangle . \quad (\text{C.7})$$

For vectors, this agrees with the scalar dot product. Any two multivectors commute under the scalar product:

$$A * B = B * A . \quad (\text{C.8})$$

In a term containing different kinds of products, the scalar product as well as the vector cross product are understood to take precedence over the geometric product. This has already been used in (C.4).

A multivector which contains only parts of even grades, i.e., scalars and bivectors, is referred to as an even multivector. The even multivectors form a subalgebra of the full geometric algebra. This subalgebra is spanned by $1, I_1, I_2, I_3$, where $I_k = I\sigma_k$. It is isomorphic to the algebra of quaternions.

The basis $\sigma_1, \sigma_2, \sigma_3$ introduced above defines a basis for all pure-grade subspaces of the geometric algebra. This is summarized in table C.1. Notice that there are elements that square to -1 . When the geometric algebra is used, it is usually unnecessary, even in quantum mechanics [123, 124], to introduce scalar complex numbers. It is also worth noting that the unit trivector I commutes with all basis vectors, and hence with all elements of the algebra.

In three dimensions, the trivector subspace is one-dimensional. It therefore suffices to characterize a trivector αI by a single scalar α . Trivectors are therefore also referred to as pseudoscalars. Similarly, a bivector $I\mathbf{a}$ can be characterized by its normal vector \mathbf{a} , so that it can also be called a pseudovector. This terminology agrees with the more usual definitions of scalars, vectors, pseudovectors and pseudoscalars by means of their transformation properties under rotations and reflections.

Finally, the reversion A^\dagger of a multivector A is obtained by interchanging the order of vectors in any geometric product. Thus, bivectors and trivectors change

grade	name	basis	reversion	properties
0	scalar	1	$1^\dagger = 1$	
1	vector	$\boldsymbol{\sigma}_1, \boldsymbol{\sigma}_2, \boldsymbol{\sigma}_3$	$\boldsymbol{\sigma}_k^\dagger = \boldsymbol{\sigma}_k$	$\boldsymbol{\sigma}_k^2 = 1$
2	bivector pseudovector	I_1, I_2, I_3	$I_k^\dagger = -I_k$	$I_k^2 = -1$
3	trivector pseudoscalar	$I = \boldsymbol{\sigma}_1 \boldsymbol{\sigma}_2 \boldsymbol{\sigma}_3$	$I^\dagger = -I$	$I^2 = -1$ $I \boldsymbol{\sigma}_k = \boldsymbol{\sigma}_k I$

Table C.1: Basis elements of the geometric algebra of Euclidean 3-space. On the whole, the algebra is 8-dimensional.

sign under reversion, whereas scalars and vectors remain unchanged. Formally, the reversion can be defined by the properties $\mathbf{a}^\dagger = \mathbf{a}$ for any vector \mathbf{a} and

$$\begin{aligned} (AB)^\dagger &= B^\dagger A^\dagger, \\ (A+B)^\dagger &= A^\dagger + B^\dagger \end{aligned} \quad (\text{C.9})$$

for multivectors A and B .

C.2 The exponential function

With the help of the associative geometric product of multivectors, polynomials and even power series of multivectors can be constructed. The most important example is the exponential function of a multivector, defined by the usual power series

$$e^A = \sum_{n=0}^{\infty} \frac{A^n}{n!}, \quad (\text{C.10})$$

which is convergent for any multivector A . The multivector exponential satisfies the “power law” relation

$$e^{A+B} = e^A e^B \quad (\text{C.11})$$

if $AB = BA$. Furthermore, from the power series (C.10) it follows that

$$(e^A)^\dagger = e^{A^\dagger} \quad (\text{C.12})$$

for any A and

$$e^A B = B e^A \quad \text{if } AB = BA, \quad (\text{C.13})$$

$$e^A B = B e^{-A} \quad \text{if } AB = -BA. \quad (\text{C.14})$$

If the multivector i satisfies $i^2 = -1$ and φ is a scalar, Euler’s formula

$$e^{i\varphi} = \cos \varphi + i \sin \varphi \quad (\text{C.15})$$

holds. Similarly, if $j^2 = +1$,

$$e^{j\varphi} = \cosh \varphi + j \sinh \varphi. \quad (\text{C.16})$$

C.3 Rotations in the geometric algebra

The geometric algebra allows for a convenient representation of rotations, which is similar to that used in the formalism of Hamilton's quaternions. It plays a crucial role in the reformulation of the KS transformation presented in chapter 4.

A rotation of Euclidean 3-space is characterized by its rotation axis, given by a unit vector \mathbf{n} , and a rotation angle φ . In the geometric algebra, it can be represented by the linear map

$$\mathbf{a} \mapsto R(\mathbf{a}) = e^{-I\mathbf{n}\varphi/2} \mathbf{a} e^{I\mathbf{n}\varphi/2} . \quad (\text{C.17})$$

To verify (C.17), assume $\mathbf{n} = \boldsymbol{\sigma}_3$. By (C.13)-(C.15), the basis vectors $\boldsymbol{\sigma}_k$ then transform under (C.17) according to

$$\begin{aligned} R(\boldsymbol{\sigma}_3) &= e^{-I\boldsymbol{\sigma}_3\varphi/2} e^{I\boldsymbol{\sigma}_3\varphi/2} \boldsymbol{\sigma}_3 = \boldsymbol{\sigma}_3 , \\ R(\boldsymbol{\sigma}_1) &= e^{-I\boldsymbol{\sigma}_3\varphi} \boldsymbol{\sigma}_1 = (\cos \varphi + I\boldsymbol{\sigma}_3 \sin \varphi) \boldsymbol{\sigma}_1 = \boldsymbol{\sigma}_1 \cos \varphi + \boldsymbol{\sigma}_2 \sin \varphi , \\ R(\boldsymbol{\sigma}_2) &= e^{-I\boldsymbol{\sigma}_3\varphi} \boldsymbol{\sigma}_2 = (\cos \varphi + I\boldsymbol{\sigma}_3 \sin \varphi) \boldsymbol{\sigma}_2 = \boldsymbol{\sigma}_2 \cos \varphi - \boldsymbol{\sigma}_1 \sin \varphi , \end{aligned}$$

which is precisely the desired result. Notice that (C.17) contains the bivector $I\mathbf{n}$ rather than the vector \mathbf{n} , thus specifying a plane of rotation rather than an axis. The concept of representing rotations by exponentials of bivectors can be generalized to arbitrary dimensions, whereas the notion of a rotation axis is restricted to the three-dimensional space.

Equation (C.17) is of the form

$$\mathbf{a} \mapsto R(\mathbf{a}) = R\mathbf{a}R^\dagger \quad (\text{C.18})$$

with an even multivector R satisfying the normalization condition

$$RR^\dagger = 1 . \quad (\text{C.19})$$

Conversely, any even multivector can be represented as $R = r_0 + I\mathbf{r}$ with a scalar r_0 and a vector $\mathbf{r} = r\hat{\mathbf{r}}$. If $RR^\dagger = r_0^2 + \mathbf{r}^2 = 1$, there is an angle φ such that

$$r_0 = \cos \varphi \quad \text{and} \quad \mathbf{r} = \hat{\mathbf{r}} \sin \varphi$$

with $|\hat{\mathbf{r}}| = 1$. Thus, R can be written as

$$R = \cos \varphi + I\hat{\mathbf{r}} \sin \varphi = e^{I\hat{\mathbf{r}}\varphi} . \quad (\text{C.20})$$

By virtue of (C.20), any normalized even multivector represents a rotation. It is therefore called a rotor.

An arbitrary even multivector satisfies $\alpha = UU^\dagger \geq 0$, so that $U = \sqrt{\alpha}R$ is a multiple of a rotor R . Therefore,

$$U\mathbf{a}U^\dagger = \alpha R\mathbf{a}R^\dagger , \quad (\text{C.21})$$

and U describes a rotation-dilatation of 3-space. In particular,

$$U\mathbf{a}U^\dagger = \langle U\mathbf{a}U^\dagger \rangle_1 \quad (\text{C.22})$$

is a vector for any even multivector U and any vector \mathbf{a} .

Instead of giving an axis and an angle, a rotation can be characterized by specifying two vectors \mathbf{a} and \mathbf{b} so that \mathbf{a} is mapped to \mathbf{b} by a rotation in the plane $\langle \mathbf{a}\mathbf{b} \rangle_2$ spanned by \mathbf{a} and \mathbf{b} . The rotor R describing this rotation is

$$R = \frac{1 + \mathbf{b}\mathbf{a}}{|\mathbf{a} + \mathbf{b}|} = \frac{1 + \mathbf{b}\mathbf{a}}{\sqrt{2(1 + \mathbf{a} \cdot \mathbf{b})}}. \quad (\text{C.23})$$

C.4 The multivector derivative

The formalism of the multivector derivative provides a differential calculus for arbitrary multivector functions. Let $F(X)$ be a smooth multivector-valued function of the multivector argument X . Neither the grades contained in X nor in F are specified. The directional derivative in the direction of a fixed multivector A by

$$A * \partial_X F(X) = \left. \frac{dF(X + \tau P_X(A))}{d\tau} \right|_{\tau=0}, \quad (\text{C.24})$$

where $P_X(A)$ projects A onto the grades contained in X . It is needed because in many cases $F(X)$ is defined for X containing certain grades only. E.g., a field $\Phi(\mathbf{x})$ defined in space is a function of a vectorial argument \mathbf{x} . The directional derivative $A * \partial_{\mathbf{x}} \Phi(\mathbf{x})$ then depends on the vector part of A only. Apart from this subtlety, (C.24) agrees with the familiar definition of a directional derivative.

Let e_J , $J = 1, \dots, 8$ be a basis of the geometric algebra and e^J its dual basis, i.e., $e_J * e^K = \delta_J^K$. For example, if $e_J = 1, \boldsymbol{\sigma}_k, I_k, I$ is the basis given in table C.1, its dual basis is $e^J = 1, \boldsymbol{\sigma}_k, -I_k, -I$. The multivector derivative is then defined to be

$$\partial_X = \sum_J e^J e_J * \partial_X. \quad (\text{C.25})$$

It inherits the algebraic properties of its argument X . In particular, ∂_X contains the same grades as X . Notice that the scalar product $A * \partial_X$ is indeed the directional derivative in the direction A , justifying the notation introduced in (C.24).

For a vector argument \mathbf{x} , the multivector derivative $\partial_{\mathbf{x}}$ reduces to the vector derivative, which is analogous to the familiar nabla operator. In particular, the vector derivative of a scalar function $\Phi(\mathbf{x})$ yields the gradient $\partial_{\mathbf{x}} \Phi(\mathbf{x})$, whereas for a vector field $\mathbf{a}(\mathbf{x})$ the vector derivative

$$\partial_{\mathbf{x}} \mathbf{a}(\mathbf{x}) = \partial_{\mathbf{x}} \cdot \mathbf{a}(\mathbf{x}) + I \partial_{\mathbf{x}} \times \mathbf{a}(\mathbf{x}) \quad (\text{C.26})$$

decomposes into the divergence and curl of $\mathbf{a}(\mathbf{x})$ in a manner analogous to (C.4).

Both the directional derivative and the multivector derivative are linear operators and satisfy Leibniz' rule

$$A * \partial_X (F(X)G(X)) = (A * \partial_X F(X))G(X) + F(X)(A * \partial_X G(X)), \quad (\text{C.27})$$

$$\partial_X (F(X)G(X)) = \overset{*}{\partial}_X \overset{*}{F}(X)G(X) + \overset{*}{\partial}_X F(X)\overset{*}{G}(X). \quad (\text{C.28})$$

In (C.28), the overstars indicate the functions to be differentiated. Notice that the second term in (C.28) is in general different from $F(X)(\partial_X G(X))$, because due to its multivector properties the multivector derivative does not commute with F even if $F(X)$ is not differentiated. The directional derivative, on the contrary, is a scalar differential operator that commutes with any multivector that is not to be differentiated. For this reason it is often convenient to write the multivector derivative as

$$\partial_X = \partial_A A * \partial_X . \quad (\text{C.29})$$

This form decomposes ∂_X into a multivector ∂_A and a scalar differential operator $A * \partial_X$, which can be moved freely among multivectors.

In addition, the directional derivative satisfies the chain rule

$$A * \partial_X F(G(X)) = (A * \partial_X G(X)) * \partial_G F(G) , \quad (\text{C.30})$$

which is useful in many calculations.

A fundamental result concerning the multivector derivative is

$$\partial_X \langle XA \rangle = \partial_X \langle AX \rangle = P_X(A) \quad (\text{C.31})$$

for any multivector A . As a consequence,

$$\partial_X \langle X^\dagger A \rangle = \partial_X \langle AX^\dagger \rangle = P_X(A^\dagger) . \quad (\text{C.32})$$

With Leibniz' rule (C.28), equation (C.31) yields

$$\partial_X X X^\dagger = \partial_X \langle X X^\dagger \rangle = 2X^\dagger . \quad (\text{C.33})$$

Bibliography

- [1] A. Einstein, Zum Quantensatz von Sommerfeld und Epstein, Verh. Dtsch. Phys. Ges. **19**, 82–92 (1917).
- [2] M. C. Gutzwiller, *Chaos in Classical and Quantum Mechanics*, Springer-Verlag, New York, 1990.
- [3] M. L. Du and J. B. Delos, Effect of closed classical orbits on quantum spectra: Ionization of atoms in a magnetic field, Phys. Rev. A **38**, 1896–1912 and 1913–1930 (1988).
- [4] E. B. Bogomolny, Photoabsorption by atoms in external fields near the ionization threshold, Sov. Phys. JETP **69**, 275–283 (1989).
- [5] J. Main and G. Wunner, Semiclassical calculation of transition matrix elements for atoms in external fields, Phys. Rev. A **59**, R2548–R2551 (1999).
- [6] T. Ellerbrock, Der Zusammenhang zwischen den klassischen Trajektorien und dem Photoabsorptionsspektrum des hochangeregten Wasserstoffatoms in gekreuzten elektrischen und magnetischen Feldern, Master’s thesis, Universität Bielefeld, Germany, 1991.
- [7] J. Main, *Das hochangeregte Wasserstoffatom im Magnetfeld und in gekreuzten magnetischen und elektrischen Feldern*, PhD thesis, Universität Bielefeld, Germany, 1991.
- [8] G. Raithel, M. Fauth, and H. Walther, Quasi-Landau resonances in the spectra of rubidium Rydberg atoms in crossed electric and magnetic fields, Phys. Rev. A **44**, 1898–1909 (1991).
- [9] G. Raithel, H. Held, L. Marmet, and H. Walther, Rubidium Rydberg atoms in strong static fields, J. Phys. B **27**, 2849–2866 (1994).
- [10] J. Rao, D. Delande, and K. T. Taylor, Quantum manifestations of closed orbits in the photoexcitation scaled spectrum of the hydrogen atom in crossed fields, J. Phys. B **34**, L391–L399 (2001).
- [11] S. Freund, R. Ubert, E. Flöthmann, K. Welge, D. M. Wang, and J. B. Delos, Absorption and recurrence spectra of hydrogen in crossed electric and magnetic fields, Phys. Rev. A **65**, 053408 (2002).

- [12] K. R. Mayer, Generic Bifurcations of Periodic Points, *Trans. AMS* **149**, 95–107 (1970).
- [13] P. Cvitanović and B. Eckhard, Periodic-orbit quantization of chaotic systems, *Phys. Rev. Lett.* **63**, 823–826 (1989).
- [14] R. Artuso, E. Aurell, and P. Cvitanović, Recycling of strange sets, *Nonlinearity* **3**, 325–359 and 361–386 (1990).
- [15] M. V. Berry and J. P. Keating, A rule for quantizing chaos?, *J. Phys. A* **23**, 4839–4849 (1990).
- [16] J. Keating, The semiclassical functional equation, *Chaos* **2**, 15–17 (1992).
- [17] R. Aurich and F. Steiner, Staircase function, spectral rigidity, and a rule for quantizing chaos, *Phys. Rev. A* **45**, 583–592 (1992).
- [18] R. Aurich, C. Matthies, M. Sieber, and F. Steiner, Novel Rule for Quantizing Chaos, *Phys. Rev. Lett.* **68**, 1629–1632 (1992).
- [19] J. Main, V. A. Mandelshtam, G. Wunner, and H. S. Taylor, Harmonic inversion as a general method for periodic orbit quantization, *Nonlinearity* **11**, 1015–1035 (1998).
- [20] H. Primack and U. Smilansky, Quantization of the Three-Dimensional Sinai Billiard, *Phys. Rev. Lett.* **74**, 4831–4834 (1995).
- [21] H. Primack and U. Smilansky, The quantum three-dimensional Sinai billiard – a semiclassical analysis, *Phys. Rep.* **327**, 1–107 (2000).
- [22] T. Prosen, Quantization of generic chaotic 3D billiard with smooth boundary, *Phys. Lett. A* **233**, 323–331 and 332–342 (1997).
- [23] M. Henseler, A. Wirzba, and T. Guhr, Quantization of Hyperbolic N -Sphere Scattering Systems in Three Dimensions, *Ann. Phys.* **258**, 286–319 (1997).
- [24] M. Sieber, Billiard systems in three dimensions: the boundary integral equation and the trace formula, *Nonlinearity* **11**, 1607–1623 (1998).
- [25] T. Papenbrock, Numerical study of a three-dimensional generalized stadium billiard, *Phys. Rev. E* **61**, 4626–4628 (2000).
- [26] B. E. Granger and C. H. Greene, Extending closed-orbit theory using quantum-defect ideas: Basic concepts and derivations, *Phys. Rev. A* **62**, 012511 (2000).
- [27] J. Main, V. A. Mandelshtam, and H. S. Taylor, High Resolution Quantum Recurrence Spectra: Beyond the Uncertainty Principle, *Phys. Rev. Lett.* **78**, 4351–4354 (1997).

- [28] E. Stiefel and G. Scheifele, *Linear and Regular Celestial Mechanics*, Springer, 1971.
- [29] D. Hestenes, *New Foundations for Classical Mechanics*, Kluwer Academic Publishers, 1990.
- [30] J. Gao and J. B. Delos, Quantum manifestations of bifurcations of closed orbits in the photoabsorption spectra of atoms in electric fields, *Phys. Rev. A* **56**, 356–364 (1997).
- [31] J. A. Shaw and F. Robicheaux, Recurrence spectroscopy of atoms in electric fields: Failure of classical scaling laws near bifurcations, *Phys. Rev. A* **58**, 1910–1917 (1998).
- [32] T. Bartsch, J. Main, and G. Wunner, Semiclassical quantization by harmonic inversion: Comparison of algorithms, *Phys. Rev. E* **64**, 056705 (2001).
- [33] B. Hüpper, J. Main, and G. Wunner, Nonhydrogenic Rydberg atoms in a magnetic field: A rigorous semiclassical approach, *Phys. Rev. A* **53**, 744–759 (1996).
- [34] K. Weibert, J. Main, and G. Wunner, General Rydberg Atoms in Crossed Electric and Magnetic Fields: Calculation of Semiclassical Recurrence Spectra with Special Emphasis on Core Effects, *Ann. Phys. (NY)* **268**, 172–204 (1998).
- [35] J. Gao, J. B. Delos, and M. Baruch, Closed-orbit theory of oscillations in atomic photoabsorption cross sections in a strong electric field, *Phys. Rev. A* **46**, 1449–1454 and 1455–1467 (1992).
- [36] J.-M. Mao, K. A. Rapelje, S. J. Blodgett-Ford, and J. B. Delos, Photoabsorption spectra of atoms in parallel electric and magnetic fields, *Phys. Rev. A* **48**, 2117–2126 (1993).
- [37] M. Courtney, Scaled-energy spectra and closed classical orbits of the hydrogen atom in parallel electric and magnetic fields, *Phys. Rev. A* **51**, 4558–4562 (1995).
- [38] A. D. Peters and J. B. Delos, Photodetachment cross section of H^- in crossed electric and magnetic fields., *Phys. Rev. A* **47**, 3020–3035 and 3036–3043 (1993).
- [39] P. A. Dando, T. S. Monteiro, D. Delande, and K. T. Taylor, Beyond Periodic Orbits: An Example in Nonhydrogenic Atoms, *Phys. Rev. Lett.* **74**, 1099–1102 (1995).
- [40] P. A. Dando, T. S. Monteiro, D. Delande, and K. T. Taylor, Role of core-scattered closed orbits in nonhydrogenic atoms, *Phys. Rev. A* **54**, 127–138 (1996).

- [41] A. Matzkin and T. S. Monteiro, Rydberg Molecules in External Fields: A Semiclassical Analysis, *Phys. Rev. Lett.* **87**, 143002 (2001).
- [42] M. Aymar, C. H. Greene, and E. Luc-Koenig, Multichannel Rydberg spectroscopy of complex atoms, *Rev. Mod. Phys.* **68**, 1015–1123 (1996).
- [43] F. Robicheaux, Preconvolving theoretical photoabsorption cross sections using multichannel quantum-defect theory, *Phys. Rev. A* **48**, 4162–4169 (1993).
- [44] M. Abramowitz and I. A. Stegun, *Pocketbook of Mathematical Functions*, Verlag Harri Deutsch, Frankfurt/Main, 1984.
- [45] S. C. Creagh and R. G. Littlejohn, Semiclassical trace formulas in the presence of continuous symmetries, *Phys. Rev. A* **44**, 836–850 (1991).
- [46] S. C. Creagh and R. G. Littlejohn, Semiclassical trace formulae for systems with non-Abelian symmetry, *J. Phys. A* **25**, 1643–1669 (1992).
- [47] J. Main, V. A. Mandelshtam, and H. S. Taylor, Periodic Orbit Quantization by Harmonic Inversion of Gutzwiller’s Recurrence Function, *Phys. Rev. Lett.* **79**, 825–828 (1997).
- [48] J. Main, Use of harmonic inversion techniques in semiclassical quantization and analysis of quantum spectra, *Physics Reports* **316**, 233–338 (1999).
- [49] M. Brack and R. K. Bhaduri, *Semiclassical Physics*, Addison-Wesley Publishing Company, Reading, Mass., 1997.
- [50] J. M. Robbins, Discrete symmetries in periodic-orbit theory, *Phys. Rev. A* **40**, 2128–2136 (1989).
- [51] M. C. Gutzwiller, Periodic Orbits and Classical Quantization Conditions, *J. Math. Phys.* **12**, 343–358 (1971).
- [52] M. V. Berry and M. Tabor, Closed orbits and the regular bound spectrum, *Proc. R. Soc. Lond. A* **349**, 101–123 (1976).
- [53] M. V. Berry and M. Tabor, Calculating the bound spectrum by path summation in action-angle variables, *J. Phys. A* **10**, 371–379 (1977).
- [54] A. Holle, J. Main, G. Wiebusch, H. Rottke, and K. H. Welge, Quasi-Landau Spectrum of the Chaotic Diamagnetic Hydrogen Atom, *Phys. Rev. Lett.* **61**, 161–164 (1988).
- [55] J. Main, G. Wiebusch, K. Welge, J. Shaw, and J. B. Delos, Recurrence spectroscopy: Observation and interpretation of large-scale structure in the absorption spectra of atoms in magnetic fields, *Phys. Rev. A* **49**, 847–868 (1994).

- [56] V. A. Mandelshtam and H. S. Taylor, Harmonic inversion of time signals and its applications, *J. Chem. Phys.* **107**, 6756–6769 (1997).
- [57] J. Main, Private communication, 2001.
- [58] S. Marple, Jr., *Digital Spectral Analysis with Applications*, Prentice-Hall, Englewood Cliffs, NJ, 1987.
- [59] W. H. Press, S. A. Teukolsky, W. T. Vetterling, and B. P. Flannery, *Numerical Recipes*, Cambridge University Press, Cambridge, UK, 1992.
- [60] M. R. Wall and D. Neuhauser, Extraction, through filter-diagonalization, of general quantum eigenvalues or classical normal mode frequencies from a small number of residues or a short-time segment of a signal. I. Theory and application to a quantum-dynamics model, *J. Chem. Phys.* **102**, 8011–8022 (1995).
- [61] B. Grémaud and D. Delande, Ghost orbits in the diamagnetic hydrogen spectrum using harmonic inversion, *Phys. Rev. A* **61**, 032504 (2000).
- [62] Dž. Belkić, P. A. Dando, J. Main, and H. S. Taylor, Three novel high-resolution nonlinear methods for fast signal processing, *J. Chem. Phys.* **113**, 6542–6556 (2000).
- [63] J. Main, P. A. Dando, Dž. Belkić, and H. S. Taylor, Decimation and harmonic inversion of periodic orbit signals, *J. Phys. A* **33**, 1247–1263 (2000).
- [64] M. V. Berry, Riemann’s zeta function: A model for quantum chaos?, in *Quantum Chaos and Statistical Nuclear Physics*, edited by T. H. Seligman and H. Nishioka, pages 1–17, Springer, Berlin, 1986.
- [65] V. A. Mandelshtam and H. S. Taylor, Multidimensional harmonic inversion by filter-diagonalization, *J. Chem. Phys.* **108**, 9970–9977 (1998).
- [66] V. A. Mandelshtam, The multidimensional filter diagonalization method. I. Theory and numerical implementation, *J. Magn. Reson.* **144**, 343–356 (2000).
- [67] H. Hu, A. A. De Angelis, V. A. Mandelshtam, and A. J. Shaka, The multidimensional filter diagonalization method. II. Applications to 2D, 3D and 4D NMR experiments, *J. Magn. Reson.* **144**, 357–366 (2000).
- [68] L. Euler, De motu rectilineo trium corporum se mutuo attrahentium, *Novi Comm. Acad. Sci. Petrop.* **11**, 144–151 (1765).
- [69] T. Levi-Civita, Sur la résolution qualitative du problème restreint des trois corps, *Opere matematiche* **2** (1956).

- [70] P. Kustaanheimo, Spinor regularization of the Kepler motion, *Annales Universitatis Turkuensis. Ser. AI.* **73** (1964).
- [71] P. Kustaanheimo and E. Stiefel, Perturbation theory of Kepler motion based of spinor regularization, *J. Reine Angew. Mathematik* **218**, 204–219 (1965).
- [72] P. A. M. Dirac, Homogeneous variables in classical dynamics, *Proc. Camb. Phil. Soc.* **29**, 389–400 (1933).
- [73] P. A. M. Dirac, Generalized Hamiltonian Dynamics, *Canad. J. Math.* **2**, 129–148 (1950).
- [74] A. N. Lasenby, C. J. L. Doran, and S. F. Gull, A Multivector Derivative Approach to Lagrangian Field Theory, *Found. Phys.* **23**, 1295–1327 (1993).
- [75] J. Main, G. Wiebusch, A. Holle, and K. H. Welge, New Quasi-Landau Structure of Highly Excited Atoms: The Hydrogen Atom, *Phys. Rev. Lett.* **57**, 2789–2792 (1986).
- [76] M. A. Al-Laithy, P. F. O’Mahony, and K. T. Taylor, Quantisation of new periodic orbits for the hydrogen atom in a magnetic field, *J. Phys. B* **19**, L773–L777 (1986).
- [77] M. A. Al-Laithy and C. M. Farmer, Stability of periodic orbits in atomic hydrogen in a magnetic field, *J. Phys. B* **20**, L747–L752 (1987).
- [78] J. Main, A. Holle, G. Wiebusch, and K. H. Welge, Semiclassical quantization of three-dimensional quasi-Landau resonances under strong-field mixing, *Z. Phys. D* **6**, 295–302 (1987).
- [79] J.-M. Mao and J. B. Delos, Hamiltonian bifurcation theory of closed orbits in the diamagnetic Kepler problem, *Phys. Rev. A* **45**, 1746–1761 (1992).
- [80] M. J. Gourlay, T. Uzer, and D. Farrelly, Asymmetric-top description of Rydberg-electron dynamics in crossed external fields, *Phys. Rev. A* **47**, 3113–3117 (1993), erratum 48,2508.
- [81] E. Flöthmann, J. Main, and K. H. Welge, The Kepler ellipses of the hydrogen atom in crossed electric and magnetic fields, *J. Phys. B* **27**, 2821–2833 (1994).
- [82] E. Flöthmann and K. H. Welge, Crossed-field hydrogen and the three-body Sun-Earth-Moon problem, *Phys. Rev. A* **54**, 1884–1888 (1996).
- [83] J. von Milczewski, G. H. F. Diercksen, and T. Uzer, Intramanifold Chaos in Rydberg Atoms in External Fields, *Phys. Rev. Lett.* **73**, 2428–2431 (1994).
- [84] J. von Milczewski, D. Farrelly, and T. Uzer, $1/r$ dynamics in External Fields: 2D or 3D?, *Phys. Rev. Lett.* **78**, 2349–2352 (1997).

- [85] J. von Milczewski and T. Uzer, Chaos and order in crossed fields, *Phys. Rev. E* **55**, 6540–6551 (1997).
- [86] D. A. Sadovskii and B. I. Zhilinskii, Tuning the hydrogen atom in crossed fields between the Zeeman and Stark limits, *Phys. Rev. A* **57**, 2867–2884 (1998).
- [87] N. Berglund and T. Uzer, The Averaged Dynamics of the Hydrogen Atom in Crossed Electric and Magnetic Fields as a Perturbed Kepler Problem, *Found. Phys.* **31**, 283–326 (2001).
- [88] D. M. Wang and J. B. Delos, Organization and bifurcation of planar closed orbits of an atomic electron in crossed fields, *Phys. Rev. A* **63**, 043409 (2001).
- [89] H. Goldstein, *Classical Mechanics*, Addison-Wesley Publishing Company, Reading, MA, 1965.
- [90] D. McDuff and D. Salamon, *Introduction to symplectic topology*, Clarendon Press, Oxford, 1995.
- [91] T. Poston and I. Stewart, *Catastrophe Theory and its Applications*, Pitman, Boston, 1978.
- [92] P. T. Saunders, *An introduction to catastrophe theory*, Cambridge University Press, Cambridge, UK, 1980.
- [93] D. P. L. Castrigiano and S. A. Hayes, *Catastrophe Theory*, Addison-Wesley Publishing Company, Reading, MA, 1993.
- [94] R. Balian, G. Parisi, and A. Voros, Discrepancies from Asymptotic Series and Their Relation to Complex Classical Trajectories, *Phys. Rev. Lett.* **41**, 1141–1144 (1978).
- [95] M. Kuś, F. Haake, and D. Delande, Prebifurcation Periodic Ghost Orbits in Semiclassical Quantization, *Phys. Rev. Lett.* **71**, 2167–2171 (1993).
- [96] J. Main and G. Wunner, Hydrogen atom in a magnetic field: Ghost orbits, catastrophes, and uniform semiclassical approximations, *Phys. Rev. A* **55**, 1743–1759 (1997).
- [97] C. Neumann, R. Ubert, S. Freund, E. Flöthmann, B. Sheehy, K. H. Welge, M. R. Haggerty, and J. B. Delos, Symmetry Breaking in Crossed Magnetic and Electric Fields, *Phys. Rev. Lett.* **78**, 4705–4708 (1997).
- [98] M. Born, *Vorlesungen über Atommechanik*, Springer, Berlin, 1925.
- [99] J. Main, K. Weibert, V. A. Mandelshtam, and G. Wunner, Semiclassical spectra and diagonal matrix elements by harmonic inversion of cross-correlated periodic orbit sums, *Phys. Rev. E* **60**, 1639–1642 (1999).

- [100] A. M. Ozorio de Almeida and J. H. Hannay, Resonant periodic orbits and the semiclassical energy spectrum, *J. Phys. A* **20**, 5873–5883 (1987).
- [101] M. Sieber, Uniform approximation for bifurcations of periodic orbits with high repetition numbers, *J. Phys. A* **29**, 4715–4732 (1996).
- [102] H. Schomerus and M. Sieber, Bifurcations of periodic orbits and uniform approximations, *J. Phys. A* **30**, 4537–4562 (1997).
- [103] M. Sieber and H. Schomerus, Uniform approximation for period-quadrupling bifurcations, *J. Phys. A* **31**, 165–183 (1998).
- [104] H. Schomerus, Semiclassical interference of bifurcations, *Europhys. Lett.* **38**, 423–428 (1997).
- [105] J. Main and G. Wunner, Uniform semiclassical approximations for umbilic bifurcation catastrophes, *Phys. Rev. E* **57**, 7325–7328 (1998).
- [106] H. Schomerus, Periodic orbits near bifurcations of codimension two: Classical mechanics, semiclassics and Stokes transitions, *J. Phys. A* **31**, 4167–4196 (1998).
- [107] T. Bartsch, J. Main, and G. Wunner, Significance of ghost orbit bifurcations in semiclassical spectra, *J. Phys. A* **32**, 3013–3027 (1999).
- [108] T. Bartsch, J. Main, and G. Wunner, Uniform Approximations for Non-generic Bifurcation Scenarios Including Bifurcations of Ghost Orbits, *Ann. Phys. (NY)* **277**, 19–73 (1999).
- [109] I. S. Gradshteyn and I. M. Ryzhik, *Table of Integrals, Series, and Products*, Academic Press, New York, 1965.
- [110] S. Tomsovic, M. Grinberg, and D. Ullmo, Semiclassical Trace Formulas of Near-Integrable Systems: Resonances, *Phys. Rev. Lett.* **75**, 4346–4349 (1995).
- [111] D. Ullmo, M. Grinberg, and S. Tomsovic, Near-integrable systems: Resonances and semiclassical trace formulas, *Phys. Rev. E* **54**, 136–152 (1996).
- [112] M. Sieber, Semiclassical transition from an elliptical to an oval billiard, *J. Phys. A* **30**, 4563–4596 (1997).
- [113] L. D. Landau and E. M. Lifshitz, *Mechanics*, Pergamon Press, Oxford, 1960.
- [114] V. Kondratovich and J. B. Delos, Semiclassical formula for oscillator strengths in atomic spectra, *Phys. Rev. A* **56**, R5–R8 (1997).
- [115] V. Kondratovich and J. B. Delos, Semiclassical formula for oscillator strengths of atomic spectra in external fields, *Phys. Rev. A* **57**, 4654–4661 (1998).

- [116] J. Gao and J. B. Delos, Resonances and recurrences in the absorption spectrum of an atom in an electric field, *Phys. Rev. A* **49**, 869–880 (1994).
- [117] D. Wintgen, Calculation of the Liapunov exponent for periodic orbits of the magnetised hydrogen atom, *J. Phys. B* **20**, L511–L515 (1987).
- [118] M. Brack, Bifurcation Cascades and Self-Similarity of Periodic Orbits with Analytical Scaling Constants in Hénon-Heiles Type Potentials, *Found. Phys.* **31**, 209–232 (2001).
- [119] A. D. Peters, C. Jaffé, J. Gao, and J. B. Delos, Quantum manifestations of bifurcations of closed orbits in the photodetachment cross section of H^- in parallel fields, *Phys. Rev. A* **56**, 345–355 (1997).
- [120] K. Weibert, J. Main, and G. Wunner, Use of harmonic inversion techniques in the periodic orbit quantization of integrable systems, *Eur. Phys. J. D* **12**, 381–401 (2000).
- [121] D. Hestenes and G. Sobczyk, *Clifford Algebra to Geometric Calculus*, D. Reidel Publishing Company, 1984.
- [122] S. F. Gull, A. N. Lasenby, and C. J. L. Doran, Imaginary Numbers are not Real. – The Geometric Algebra of Spacetime, *Found. Phys.* **23**, 1175–1201 (1993).
- [123] D. Hestenes and R. Gurtler, Local Observables in Quantum Theory, *Am. J. Phys.* **39**, 1028–1038 (1971).
- [124] C. J. L. Doran, A. N. Lasenby, and S. F. Gull, States and Operators in the Spacetime Algebra, *Found. Phys.* **23**, 1239–1264 (1993).

Zusammenfassung

Die Frage nach dem Zusammenhang zwischen klassischen Trajektorien und atomaren Spektren beschäftigt Physiker seit der Entdeckung der atomaren Linienspektren im 19. Jahrhundert. Die von Bohr und Sommerfeld angegebenen Quantisierungsvorschriften der „älteren“ Quantentheorie wählen aus dem Kontinuum klassisch möglicher Trajektorien diskrete Bahnen aus, die mit Quantenzuständen identifiziert werden. Diese Quantisierungsbedingungen wurden von Einstein [1] in größtmöglicher Allgemeinheit angegeben. Einstein erkannte auch bereits, dass sie eine Blätterung des klassischen Phasenraums in invariante Tori voraussetzen und dass diese Voraussetzung nur in Ausnahmefällen erfüllt ist. Damit war das Problem, eine Quantisierungsvorschrift für klassisch nichtintegrale Systeme anzugeben, bereits 1917 in aller Schärfe gestellt. Es trat in den Hintergrund, als die „exakte“ Quantenmechanik die Durchführung von Berechnungen ohne Bezug auf klassische Bahnen gestattete, obwohl das Korrespondenzprinzip, das für hoch angeregte Zustände ein Übergehen von der Quantenmechanik zur klassischen Mechanik fordert, ein entscheidender Wegweiser in der Entwicklung der Quantenmechanik gewesen war. Konzepte und Verfahren, die diesen Übergang näher zu untersuchen gestatteten, standen erst nach der Entwicklung der periodic-orbit-Theorie durch Gutzwiller [2] und der closed-orbit-Theorie durch Du und Delos [3] und Bogomolny [4] zur Verfügung. In der Folge dieser Entwicklungen rückte das schon von Einstein formulierte und noch immer ungelöste Problem, eine semiklassische, d.h. auf Grundlage der klassischen Mechanik arbeitende Quantisierungsvorschrift für nichtintegrale Systeme anzugeben, wieder in den Mittelpunkt des Interesses.

Als besonders dankbares Objekt semiklassischer Untersuchungen erweist sich das Wasserstoffatom in elektrischen und magnetischen Feldern. Während das Wasserstoffatom in einem elektrischen Feld ein klassisch integrables System ist, zeigt es in einem Magnetfeld einen Übergang von regulärer zu chaotischer Dynamik. Es kann daher als Musterbeispiel dienen, an dem sich der Einfluss von Integrabilität oder Chaos auf Quantenspektren experimentell und theoretisch studieren lässt.

Die closed-orbit-Theorie ermöglicht die semiklassische Berechnung atomarer Photoabsorptionsspektren. Sie stellt die Dichte der Oszillatorstärken als Summe zweier Ausdrücke dar: Der erste ist eine glatte Funktion der Energie und der zweite eine Überlagerung oszillierender Beiträge. Jede dieser Oszillationen wird auf den Einfluss einer „geschlossenen“ klassischen Bahn, die am Ort des Kerns beginnt und dorthin zurückkehrt, zurückgeführt [3, 4]. Für das Wasserstoffatom im

Magnetfeld liegt eine vollständige Klassifikation der geschlossenen Bahnen vor [7], und auf dieser Grundlage konnten die großräumigen Strukturen des Spektrums semiklassisch interpretiert werden. Umgekehrt ist es ebenfalls gelungen, atomare Energieniveaus und die zugehörigen Oszillatorstärken aus der Kenntnis der geschlossenen Bahnen zu bestimmen [5].

Da das Wasserstoffatom im Magnetfeld Rotationssymmetrie um die Feldachse aufweist, ist der Drehimpuls um diese Achse eine Konstante der Bewegung. Er erlaubt, die Zahl der Freiheitsgrade auf zwei zu reduzieren. Im Gegensatz dazu besitzt das Wasserstoffatom in gekreuzten elektrischen und magnetischen Feldern keine kontinuierliche Symmetrie mehr, so dass drei nicht separierbare Freiheitsgrade betrachtet werden müssen. Hinzu kommt, dass die Dynamik von zwei statt von einer einzigen äußeren Feldstärke abhängt. Daher sind sowohl die klassische als auch die quantenmechanische Dynamik des Wasserstoffatoms in gekreuzten Feldern wesentlich komplizierter als im reinen Magnetfeld. Auch nach zehn Jahren intensiver Forschung ist sie bei weitem nicht vollständig verstanden.

Für Atome in gekreuzten Feldern existiert eine closed-orbit-Theorie [6, 7], die derjenigen für ein reines Magnetfeld analog ist. In ihrem Rahmen konnten großräumige Strukturen in Photoabsorptionsspektren durch den Einfluss geschlossener Bahnen erklärt werden [7–11]. Bisher sind jedoch nur vergleichsweise kurze Bahnen identifiziert worden, und eine vollständige Übersicht über die geschlossenen Bahnen in gekreuzten Feldern steht nicht zur Verfügung. Es ist bekannt, dass die geschlossenen Bahnen mit wachsenden äußeren Feldstärken eine Reihe von Bifurkationen durchlaufen und dass so immer mehr geschlossene Bahnen erzeugt werden. Eine wichtige Vorbedingung für eine Klassifikation der geschlossenen Bahnen wäre deshalb einerseits die Beschreibung fundamentaler geschlossener Bahnen, die bei kleinen äußeren Feldstärken vorliegen, und andererseits eine Klassifikation der generischen Bifurkationen. Beides liegt für das Wasserstoffatom in gekreuzten Feldern bislang nicht vor.

Seit der Entwicklung der modernen semiklassischen Theorien haben verschiedene Autoren intensiv an allgemeinen semiklassischen Quantisierungsvorschriften für nichtintegrale Systeme gearbeitet, Beispiele sind [13–19]. Die closed-orbit-Theorie stellt ein mächtiges Hilfsmittel zur Verfügung, um über kleine Energieintervalle gemittelte Spektren zu berechnen, sie ist jedoch nicht ohne weiteres zur Berechnung einzelner Spektrallinien geeignet, da die Summe über alle geschlossenen Bahnen divergiert. Die periodic-orbit-Theorie stellt eine semiklassische Näherung für die Zustandsdichte eines Quantensystems zur Verfügung. Sie ist der closed-orbit-Theorie in formaler Hinsicht analog und führt daher auf dieselben Schwierigkeiten. Verschiedene Verfahren sind vorgeschlagen worden, um die Konvergenzprobleme der semiklassischen Theorien zu umgehen. Alle sind dadurch eingeschränkt, dass sie gewisse Voraussetzungen über die zu Grunde liegende klassische Dynamik machen. Insbesondere ist keine der bisher entwickelten Techniken anwendbar, wenn Bifurkationen klassischer Bahnen berücksichtigt werden müssen.

Die meisten Arbeiten zur semiklassischen Quantisierung betreffen Systeme mit zwei Freiheitsgraden. Wegen der zusätzlichen Schwierigkeiten, die die Be-

handlung eines dritten Freiheitsgrades mit sich bringt, mussten sich Arbeiten an Systemen mit drei Freiheitsgraden bisher auf dreidimensionale Billardsysteme beschränken [20–25], obwohl es von grundlegender Bedeutung wäre zu klären, in wie weit semiklassische Verfahren auf höherdimensionale Systeme anwendbar sind. Eine semiklassische Quantisierung, d.h. die Bestimmung von Energieeigenwerten, ist bislang nur für das dreidimensionale Sinai-Billard [20] und für N -Kugel-Streusysteme [23] gelungen. Das Wasserstoffatom in gekreuzten Feldern ist wegen des Übergangs von regulärer zu chaotischer Dynamik wesentlich komplizierter als die genannten Billardsysteme. Zu seiner semiklassischen Quantisierung gibt es nicht einmal Ansätze. Damit sie gelingen kann, müssen unterschiedliche Probleme gelöst werden. Zum ersten müssen die geschlossenen Bahnen des Systems gefunden und ihre Systematik verstanden werden. Zum zweiten stellt sich dabei heraus, dass Bifurkationen geschlossener Bahnen in gekreuzten Feldern häufig auftreten und daher eine wichtige Rolle bei der Quantisierung spielen. Sie verursachen Divergenzen des semiklassischen Spektrums, zu deren Regularisierung geeignete uniforme Näherungen konstruiert werden müssen. Drittens muss ein semiklassisches Quantisierungsverfahren entwickelt werden, das die uniformen Näherungen verarbeiten kann. All diesen Problemen werde ich mich im Verlauf der Arbeit zuwenden.

Das **2. Kapitel** beginnt mit einer Diskussion der Hamiltonfunktion für das Wasserstoffatom in äußeren Feldern und beschreibt ihre Skalierungseigenschaften und ihre Symmetrien. Danach wendet es sich der closed-orbit-Theorie zu. Granger und Greene [26] haben eine neue Formulierung der Theorie vorgestellt, die auf der Verwendung semiklassischer S -Matrizen an Stelle semiklassischer Wellenfunktionen basiert. In dieser Formulierung werden die Eigenschaften des Atomrumpfes und der äußeren Felder durch separate S -Matrizen beschrieben, so dass die Trennung der physikalisch verschiedenen Raumbereiche, die die Grundlage der closed-orbit-Theorie ist, im Formalismus klar zum Ausdruck kommt. Dadurch verspricht der Ansatz von Granger und Greene eine größere Flexibilität als frühere Darstellungen. Ich stelle ihn in **Abschnitt 2.2** kurz vor und verallgemeinere ihn in **Abschnitt 2.3** auf Atome in gekreuzten Feldern.

Für den Fall eines Atoms im reinen Magnetfeld leiten Granger und Greene [26] eine semiklassische S -Matrix her und stellen bei niedrigen Energien eine Diskrepanz zwischen ihren Resultaten und der von Du und Delos [3] eingeführten Form der closed-orbit-Theorie fest. Sie führen diese Diskrepanz darauf zurück, dass Du und Delos an entscheidender Stelle Wellenfunktionen für die Energie $E = 0$ benutzen, während sich diese Näherung in der S -Matrix-Formulierung vermeiden lässt. Diese Behauptung diskutiere ich in **Abschnitt 2.4**. Ich zeige dort, dass die von Du und Delos angegebene Form der semiklassischen Amplitude empfindlich davon abhängt, in welchem Abstand r vom Kern Innenraum- und Außenraumlösungen aneinander angepasst werden, während die von Granger und Greene verwendete Amplitude von r unabhängig ist. Obwohl daher die Amplitude von Granger und Greene als geeigneter erscheint, ist sie nicht an die S -Matrix-Formulierung der Theorie gebunden, sondern wurde schon früher von Bogomolny gefunden [4]. Im Grenzfall $r \rightarrow 0$ stimmt sie mit dem Ergebnis von Du und Delos überein. Die

beobachtete Diskrepanz geht daher auf die Verwendung eines endlichen r zurück und nicht auf die $E = 0$ -Näherung. Da letztere sich bisher immer gut bewährt hat, besteht nach wie vor kein Anlass, an ihrer Gültigkeit zu zweifeln.

Für die semiklassischen Untersuchungen in dieser Arbeit verwende ich die Methode der harmonischen Inversion. Sie wurde in [19, 27] als allgemeines Verfahren zur semiklassischen Quantisierung und zur semiklassischen Analyse von Quantenspektren, d.h. zur Bestimmung der Beiträge klassischer Bahnen zum Spektrum, eingeführt. Diese Methode wird in **Kapitel 3** dargestellt. In **Abschnitt 3.1** beschreibe ich den Ansatz, der die harmonische Inversion in der Semiklassik flexibel einsetzbar macht. Ich stelle dann in **Abschnitt 3.2** vier verschiedene Algorithmen zur harmonischen Inversion vor, die in der Literatur vorgeschlagen worden sind.

In der Semiklassik ist das zu analysierende Signal gegeben durch ein Quantenspektrum oder durch eine Liste geschlossener Bahnen. Oft ist es gar nicht oder nur mit großem Aufwand möglich, ein gegebenes Signal zu verlängern, um mehr Information für die Analyse zur Verfügung zu haben. Es ist dann wichtig, dasjenige Verfahren zur Analyse zu verwenden, das bei gegebenem Signal die besten Ergebnisse liefert. Um die Stärken und Schwächen der verschiedenen Algorithmen beurteilen zu können, vergleiche ich Ergebnisse, die sie für zwei einfache Modellsysteme liefern. Diese Resultate werden in **Abschnitt 3.3** dargestellt.

Bisherige Anwendungen der harmonischen Inversion in der Semiklassik waren eingeschränkt auf Systeme mit einer klassischen Skalierungseigenschaft. Obwohl dies eine schwache Voraussetzung ist, die viele physikalisch interessante Systeme, darunter auch Atome in äußeren Feldern, zulässt, ist die Berechnung skaliertener Spektren oft nicht die natürliche Herangehensweise an ein System. So liegt es z.B. im Fall von Atomen in äußeren Feldern näher, nach Spektren bei konstanten Feldstärken zu fragen als nach Spektren bei konstanter skaliertener Energie. Daher ist es wünschenswert, die Einschränkung auf skalierende Systeme zu überwinden. In **Abschnitt 3.4** führe ich ein semiklassisches Quantisierungsverfahren auf Grundlage der harmonischen Inversion ein, das keine klassischen Skalierungseigenschaften mehr voraussetzt. Es basiert auf der Beobachtung, dass ein für die harmonische Inversion geeignetes Signal, das die spektrale Information über Energieniveaus in einem endlichen Energieintervall enthält, konstruiert werden kann, wenn die klassischen Bahnen in diesem Intervall bekannt sind. Über den Geltungsbereich der closed-orbit-Theorie hinaus ist das Verfahren auch zusammen mit semiklassischen Spurformeln anwendbar. Da schon früher [19, 120] gezeigt worden ist, dass die semiklassische Quantisierung durch harmonische Inversion für Systeme mit regulärer oder chaotischer Dynamik gleichermaßen gute Ergebnisse liefert, ist ihre Verallgemeinerung auf nichtskalierende Systeme das erste wirklich allgemein anwendbare Quantisierungsverfahren, das keinerlei Bedingungen an die zu Grunde liegende klassische Dynamik stellt.

Da die klassische Dynamik des Wasserstoffatoms in äußeren Feldern im allgemeinen nichtintegrabel ist, müssen die Bewegungsgleichungen numerisch gelöst werden. Dies wird erschwert durch die Singularität des Coulomb-Potenzials bei $r = 0$. Die Kustaanheimo-Stiefel-Transformation [28] bietet eine Möglichkeit,

diese Singularität zu regularisieren. Sie wird in **Kapitel 4** beschrieben. Die KS-Transformation bildet den dreidimensionalen Ortsraum in einen vierdimensionalen Raum regularisierender Koordinaten ab. Das reine Keplerproblem wird dabei abgebildet auf einen isotropen vierdimensionalen harmonischen Oszillator. Hestenes [29] hat eine neue Formulierung der KS-Transformation in der Sprache der geometrischen Algebra vorgeschlagen. Dabei erscheinen die vier KS-Koordinaten als die Komponenten eines Spinors, d.h. sie beschreiben eine Drehstreckung des Ortsraumes, die einen festen Referenzvektor auf den augenblicklichen Ortsvektor abbildet. Diese geometrische Interpretation der KS-Koordinaten ist in der bekannteren matrizenbasierten Formulierung der KS-Transformation nicht erkennbar. Damit verhilft der neue Formalismus zu einer klareren Darstellung, bei der etwa der Ursprung des zusätzlichen vierten Freiheitsgrades anschaulich wird. Gleichzeitig vereinfacht er analytische Berechnungen, wie sie etwa zur klassischen Störungstheorie notwendig sind.

Ich stelle die Herleitung der Spinor-Bewegungsgleichung in **Abschnitt 4.1** dar. In **Abschnitt 4.2** zeige ich mit Hilfe des Spinor-Formalismus, wie die KS-Transformation in den Rahmen der Lagrange- und Hamilton-Formulierungen der Mechanik eingefügt werden kann. Dabei verallgemeinere ich vorherige Herleitungen, die sich auf den Fall homogener äußerer Felder beschränken, auf beliebige zeitunabhängige elektromagnetische Felder. **Abschnitt 4.3** beschreibt das reine Kepler-Problem. Dessen Erhaltungsgrößen, der Drehimpuls und der Lenz-Vektor, werden durch den KS-Spinor ausgedrückt. **Abschnitt 4.4** geht auf die speziellen Probleme ein, die bei der Beschreibung von Bahnen, die am Ort des Atomkerns beginnen, auch nach der Regularisierung noch auftreten. Die Sprache der geometrischen Algebra erlaubt eine einfache Beschreibung dieser Bahnen und ihrer Stabilität.

Das **5. Kapitel** ist der Beschreibung der klassischen geschlossenen Bahnen beim Wasserstoffatom in gekreuzten Feldern gewidmet und wendet sich zunächst den Bifurkationen geschlossener Bahnen zu. Für periodische Bahnen in beliebigen Hamiltonschen Systemen existiert eine Klassifikation generischer Bifurkationen der Kodimension eins, die von Mayer [12] entwickelt wurde. Das Wasserstoffatom im reinen Magnetfeld weist für Bahnen mit verschwindendem Drehimpuls Zeitumkehrinvarianz auf, so dass geschlossene Bahnen nach ihrer Rückkehr zum Kern in umgekehrter Richtung durchlaufen werden und nach der zweiten Rückkehr periodisch werden. Daher ist Mayers Bifurkationstheorie auf Bifurkationen geschlossener Bahnen in diesem System anwendbar. In gekreuzten Feldern ist die Zeitumkehrinvarianz gebrochen, so dass keine allgemeine Beziehung zwischen geschlossenen und periodischen Bahnen besteht. Daher muss für geschlossene Bahnen eine eigene Bifurkationstheorie entwickelt werden.

Ich zeige in **Abschnitt 5.1**, wie eine Poincaré-Abbildung für geschlossene Bahnen sinnvoll definiert werden kann. Wenn eine erzeugende Funktion der Poincaré-Abbildung geeignet gewählt wird, entsprechen ihre stationären Punkte den geschlossenen Bahnen. Die Bifurkationstheorie für geschlossene Bahnen ist damit zurückgeführt auf die Katastrophentheorie. Mit Hilfe dieser Beobachtung identifiziere ich in **Abschnitt 5.2** die beiden Typen generischer Bifurkationen

der Kodimension eins. Die erste Form ist die Tangentenbifurkation, in der zwei geschlossene Bahnen erzeugt oder zerstört werden und die im Rahmen der Katastrophentheorie durch die Falte beschrieben wird. Ein zweiter Bifurkationstyp existiert in Kodimension eins nur, weil das Wasserstoffatom in gekreuzten Feldern Reflexionssymmetrien aufweist. Diese Symmetrien ermöglichen Heugabelbifurkationen, in denen ein Paar von asymmetrischen Bahnen von einer reflexionssymmetrischen Bahn abspaltet. Sie werden beschrieben durch die symmetrische Form der Spitze.

Ausgehend von der Bifurkationstheorie und von den geschlossenen Bahnen beim Wasserstoffatom im Magnetfeld, deren Klassifikation ich in **Abschnitt 5.3** kurz darstelle, beschreibe ich in **Abschnitt 5.4** eine Reihe von Bifurkationsszenarien, die in gekreuzten Feldern tatsächlich stattfinden. Dabei zeigt sich, dass sich aus den beiden elementaren Bifurkationstypen eine große Vielfalt unterschiedlicher komplizierter Szenarien bildet und dass bereits bei kleinen elektrischen Feldstärken viele eng benachbarte Bifurkationen stattfinden. In **Abschnitt 5.5** schlage ich eine heuristische Klassifikation der geschlossenen Bahnen in gekreuzten Feldern vor, die auf der Klassifikation der Bahnen im reinen Magnetfeld basiert. Ich zeige, dass die Klassifikation auch bei vergleichsweise starken elektrischen Feldern noch anwendbar ist und beschreibe Algorithmen, mit deren Hilfe sich Bahnen automatisch klassifizieren lassen.

In **Kapitel 6** wird die semiklassische Beschreibung des Wasserstoffatoms in gekreuzten Feldern behandelt. **Abschnitt 6.1** beschreibt ein Quantenspektrum, das als Ausgangspunkt für weitere Untersuchungen dient. Ich verwende hier ein skaliertes Spektrum bei der skalierten Energie $\tilde{E} = -1.4$ und elektrischen Feldstärke $\tilde{F} = 0.1$, das eine genauere semiklassische Analyse erlaubt als ein Spektrum bei festen Feldstärken. In **Abschnitt 6.2** stelle ich semiklassische Spektren in niedriger Auflösung vor, die durch glattes Abschneiden der closed-orbit-Summe gewonnen wurden, und vergleiche sie mit entsprechend geglätteten Quantenspektren. Es zeigt sich, dass die großräumige Struktur des Spektrums, die durch näherungsweise erhaltene Hauptquantenzahlen bestimmt ist, semiklassisch gut wiedergegeben wird. Teilweise lässt sich auch eine Unterstruktur der einzelnen n -Mannigfaltigkeiten semiklassisch auflösen, bei geringer Glättung treten allerdings im semiklassischen Spektrum Strukturen auf, die das Quantenspektrum nicht aufweist.

In **Abschnitt 6.3** führe ich eine hochauflösende Quantisierung des Wasserstoffatoms in gekreuzten Feldern mit Hilfe der harmonischen Inversion durch. Dabei gelingt es, in den Mannigfaltigkeiten $n = 6$ bis 11 die jeweils stärksten Linien zu identifizieren. Die Konvergenz des Verfahrens ist mit dem gegebenen semiklassischen Signal allerdings schlecht, so dass es weder gelingt, schwächere Linien aufzulösen noch den gefundenen Linien semiklassisch Übergangsstärken zuzuordnen. Eine Verlängerung des semiklassischen Signals führt wider Erwarten zu einer Verschlechterung statt einer Verbesserung der Ergebnisse. Dies spricht dafür, dass ein fundamentales Problem beim Signalaufbau vorliegt. Eine offensichtliche Schwierigkeit liegt darin, dass die Liste der geschlossenen Bahnen unvollständig ist. Die Bahnen häufen sich in der Nähe einer Separatrix im Phasenraum, und es

gelingt in diesem Bereich nicht, alle geschlossenen Bahnen numerisch zu bestimmen. Obwohl der Bereich um die Separatrix instabil ist, ist zu vermuten, dass die Beiträge der fehlenden Bahnen nicht vernachlässigbar klein sind.

Um das vorliegende Problem klar diagnostizieren zu können, führe ich eine semiklassische Analyse des vorliegenden Quantenspektrums sowohl mit hochauflösenden Verfahren als auch mit Hilfe der Fourier-Transformation des Quantenspektrums durch. Die so bestimmten Wiederkehrspektren werden in **Abschnitt 6.4** mit semiklassischen Ergebnissen verglichen. Sie bestätigen zum einen, dass die fehlenden geschlossenen Bahnen das semiklassische Spektrum beeinträchtigen. Zum anderen zeigt sich aber auch, dass viele Linien im semiklassischen Wiederkehrspektrum stärker sind als im Quantenspektrum. Dies ist auf Bifurkationen geschlossener Bahnen zurückzuführen. Wenn eine geschlossene Bahn eine Bifurkation durchläuft, divergiert ihr Beitrag zum semiklassischen Spektrum. Dieses Problem ist in der closed-orbit-Theorie wie in der periodic-orbit-Theorie gleichermaßen bekannt. Es wird dadurch verursacht, dass die Bahnen sich in der Nähe der Bifurkation sehr nahe kommen und die in der Semiklassik zentrale Näherung der stationären Phase für diese Bahnen versagt. Es lässt sich lösen, indem man die Beiträge der bifurkierenden Bahnen zur closed-orbit-Summe durch einen kollektiven Beitrag, der uniforme Näherung genannt wird, ersetzt.

In **Abschnitt 6.5** beschreibe ich ein allgemeines Verfahren zur Konstruktion uniformer Näherungen. Das Verfahren setzt voraus, dass eine Normalform bekannt ist, die das Bifurkationsszenario beschreibt. Im Falle der beiden generischen Bifurkationstypen kann hier die in Abschnitt 5.2 eingeführte katastrophentheoretische Normalform verwendet werden. Die uniforme Näherung wird ausgedrückt durch die klassischen Wirkungen und semiklassischen Amplituden der beteiligten Bahnen, sie verlangt also keine weiteren Daten als die, die zur Anwendung der semiklassischen Theorie ohnehin bestimmt werden müssen. Ich leite uniforme Näherungen für die beiden generischen Typen von Bifurkationen geschlossener Bahnen her. Ich zeige dann, dass die uniformen Näherungen nicht nur verwendet werden können, um semiklassische Photoabsorptionsspektren zu regularisieren, sondern dass sie sich ebenso einsetzen lassen, um die zu großen Beiträge der bifurkierenden Bahnen zum Wiederkehrspektrum zu reduzieren.

Das Verfahren der semiklassischen Quantisierung durch harmonische Inversion beruht auf der harmonischen Analyse von Wiederkehrspektren. Mit dem Nachweis, dass uniforme Näherungen in Wiederkehrspektren verwendet werden können, ist deshalb der Weg geebnet, sie auch in der hochauflösenden Quantisierung einzusetzen. Dabei ist es die in Abschnitt 3.4 eingeführte Verallgemeinerung der harmonischen Inversion auf nichtskalierende Systeme, die das Verfahren von der funktionalen Form des semiklassischen Spektrums unabhängig macht und damit auch die Einbeziehung uniformer Näherungen gestattet. Im Fall des Wasserstoffatoms in gekreuzten Feldern treten jedoch technische Probleme auf. Zum einen müssen Bahnen, die durch Bifurkationen auseinander hervorgehen, in der Liste der geschlossenen Bahnen identifiziert werden, damit sie in einer uniformen Näherung zusammengefasst werden können. Wegen der großen Zahl geschlossener Bahnen ist das nur möglich, wenn diese Zuordnung durch einen geeigneten Algo-

rithmus automatisiert werden kann. Zum anderen treten Folgen eng benachbarter Bifurkationen auf. Für diese Fälle müssten uniforme Lösungen konstruiert werden, die mehrere Bifurkationen gleichzeitig beschreiben. Dies ist zwar im Prinzip möglich, verlangt aber die gesonderte Behandlung jedes einzelnen Bifurkations-szenarios. Eine besondere Herausforderung stellen hierbei Szenarien dar, die die mit der Brechung der Rotationssymmetrie bei infinitesimal kleiner elektrische Feldstärke verbundene Bifurkation mit weiteren Bifurkationen verknüpfen. Da die Normalform für die Symmetriebrechung sich nicht leicht mit den Normalformen für die generischen Bifurkationen verbinden lässt, bleibt die Uniformisierung dieser Szenarien ein ungelöstes Problem.

Da die klassische Dynamik des Wasserstoffatoms in gekreuzten Feldern sich als zu kompliziert erweist, um die beschriebene Uniformisierung des Wiederkehrspektrums konsequent durchführen zu können, wende ich mich in **Kapitel 7** einem einfacheren System zu: dem Wasserstoffatom in einem elektrischen Feld. Dieses System ist klassisch integrabel, so dass es nach den Regeln der Torusquantisierung semiklassisch quantisiert werden kann. Andererseits beansprucht die closed-orbit-Theorie, auf integrable wie chaotische Systeme gleichermaßen anwendbar zu sein, so dass eine Quantisierung dieses einfach erscheinenden Systems ein fundamentales Problem der closed-orbit-Theorie darstellt. Dass sie bisher nicht gelungen ist, ist darauf zurückzuführen, dass das System trotz seiner Integrabilität eine große Zahl von Bifurkationen geschlossener Bahnen aufweist. Erst mit dem in dieser Arbeit entwickelten Quantisierungsverfahren für nichtskalierende Systeme steht ein Hilfsmittel zur Verfügung, mit dem sich die Bifurkationen im Rahmen einer semiklassischen Quantisierung erfolgreich behandeln lassen.

In **Abschnitt 7.1** stelle ich die Bewegungsgleichung auf, die das Elektron im Wasserstoffatom im elektrischen Feld beschreibt, und löse sie für im Ursprung startende Bahnen explizit. Die KS-Transformation ermöglicht es, die Bewegungsgleichung ohne Rückgriff auf die Hamilton-Jacobi-Theorie elementar zu separieren, und die Formulierung der Theorie im Rahmen der geometrischen Algebra erlaubt es, einen einfachen Ausdruck für den Positionsspinor als Funktion der Zeit anzugeben, der die Bewegung vollständig beschreibt.

In **Abschnitt 7.2** beschreibe ich die geschlossenen Bahnen. Sie erfüllen die Resonanzbedingung, dass sie nach k Perioden der „downhill“-Bewegung (entgegen dem elektrischen Feld) und l Perioden der „uphill“-Bewegung (mit dem elektrischen Feld) zum Kern zurückkehren. Außerdem existieren die uphill- und downhill-Bahnen, bei denen sich das Elektron entlang der elektrischen Feldachse bewegt, und ihre Wiederholungen. Aus der expliziten Form der Resonanzbedingung lässt sich das Bifurkationsszenario qualitativ ablesen: Eine geschlossene Bahn ist charakterisiert durch die Umlaufzahlen k und $l > k$. Sie existiert als reelle Bahn in einem Energieintervall $E_{\text{gen}} \leq E \leq E_{\text{dest}}$, außerhalb dieses Intervalls als Geisterbahn. Bei der ersten Bifurkationsenergie $E_{\text{gen}} < -2\sqrt{F}$ spaltet die Bahn von der downhill-Bahn ab, bei E_{dest} kollidiert sie mit der uphill-Bahn und wird zerstört. Dieses Bifurkationsszenario ist bereits von Gao und Delos [116] aufgrund numerischer Befunde beschrieben worden. Es wird hier erstmals analytisch abgeleitet.

Die Resonanzbedingung legt bei gegebener Energie die Starttrichtung einer geschlossenen Bahn oder, äquivalent, einen Separationsparameter fest. Im allgemeinen muss er numerisch bestimmt werden. Ist dies geschehen, sind alle weiteren Kenngrößen der Bahn analytisch gegeben. Die hierzu nötigen Formeln sind in der Literatur noch nicht angegeben worden. Ich leite sie ebenfalls in Abschnitt 7.2 her.

Das beschriebene Bifurkationsszenario wirft bei niedrigen Energien ein besonderes Problem für die semiklassische Quantisierung auf. Hier wird der Energieabstand zwischen der Erzeugung und der Zerstörung einer nichtaxialen Bahn ebenso wie die Wirkungsdifferenzen zur uphill- und downhill-Bahn sehr klein, so dass beide Bifurkationen in einer gemeinsamen uniformen Lösung behandelt werden müssen. In **Abschnitt 7.3** leite ich Näherungen für diese Differenzen her, um die Notwendigkeit einer solchen uniformen Näherung quantitativ zu fassen.

In **Abschnitt 7.4** werden uniforme Näherungen für das Wasserstoffatom im elektrischen Feld hergeleitet. Die Erzeugung einer nichtaxialen Bahn aus der downhill-Bahn und ihre Zerstörung an der uphill-Bahn lassen sich mit der gleichen Normalform und daher auch mit der gleichen uniformen Näherung beschreiben. Geeignete uniforme Näherungen sind bereits in der Literatur angegeben worden [30, 31]. Ich leite sie im Rahmen des allgemeinen Verfahrens von Abschnitt 6.5 neu her und gewinne sie dadurch in einer Form, die allein aus den klassischen Wirkungen und semiklassischen Amplituden der beteiligten Bahnen berechnet werden kann und deshalb einfacher anzuwenden ist als frühere Darstellungen. Danach konstruiere ich eine uniforme Näherung für die Abfolge von Erzeugung und Vernichtung einer nichtaxialen Bahn. Sie ist von besonderem Interesse, da sie als erste bekannte uniforme Näherung als Konfigurationsraum keinen euklidischen Raum, sondern einen Raum mit nichttrivialer Topologie verwendet, in diesem Fall eine Kugeloberfläche. Es ist damit bewiesen, dass solche Konstruktionen auf topologisch nichttrivialen Räumen möglich sind. Es zeigt sich jedoch, dass die uniforme Näherung auf der Kugel die einfache closed-orbit-Theorie erst in wesentlich größerem Abstand von den Bifurkationen reproduziert als eine uniforme Näherung, die nur eine der beiden Bifurkationen berücksichtigt. Diese Beobachtung macht es fraglich, ob die kompliziertere uniforme Näherung ein semiklassisches Spektrum tatsächlich verbessern kann. Gründe für diese Schwierigkeit werden diskutiert.

Abschnitt 7.5 wendet sich schließlich der eigentlichen semiklassischen Quantisierung des Wasserstoffatoms im elektrischen Feld zu. Eine störungstheoretische Abschätzung der Heisenbergzeit und damit der benötigten semiklassischen Signallänge zeigt, dass es aussichtslos ist, eine Quantisierung ohne Verwendung uniformer Näherungen zu versuchen. Die Berechnung niedrig aufgelöster semiklassischer Spektren bestätigt dies: Durch Bifurkationen verursachte Divergenzen zerstören die Spektren vollständig lange bevor die Auflösung hoch genug ist, um einzelne Linien erkennen zu können. Unter Verwendung von uniformen Näherungen lassen sich längere Bahnen in die Spektren einbeziehen, so dass einzelne Spektrallinien erkennbar werden. Damit sind die Voraussetzungen für eine Anwendung der harmonischen Inversion zur hochauflösenden Quantisierung geschaf-

fen. Tatsächlich lassen sich mit dem Verfahren Spektrallinien mit hoher Genauigkeit bestimmen, auch in Bereichen, wo drei oder vier n -Mannigfaltigkeiten sich überlagern. Damit ist einerseits gezeigt, dass das in Abschnitt 3.4 eingeführte Verfahren zur Quantisierung nichtskalierender Systeme geeignet ist. Andererseits ist es erstmals gelungen, uniforme Näherungen zur semiklassischen Bestimmung einzelner Energieeigenwerte heranzuziehen.

Insgesamt konnten in dieser Arbeit sowohl bei der Beschreibung der klassischen geschlossenen Bahnen des Wasserstoffatoms in gekreuzten elektrischen und magnetischen Feldern als auch bei seiner semiklassischen Behandlung wesentliche Fortschritte erzielt werden. Auf der Seite der klassischen Mechanik wurde eine Bifurkationstheorie für geschlossene Bahnen entwickelt, und es wurden die generischen Bifurkationen der Kodimension eins identifiziert. Es wurden dann eine Reihe unterschiedlicher Bifurkationsszenarien beschrieben, die sich aus den elementaren Bifurkationen zusammensetzen, und es wurde ein Klassifikationsschema für geschlossene Bahnen vorgeschlagen, das für nicht zu starke elektrische Felder anwendbar ist.

Erstmals gelang, wenn auch mit geringer Genauigkeit, eine semiklassische Quantisierung des Wasserstoffatoms in gekreuzten Feldern. Als Gründe, die eine Steigerung der Genauigkeit verhinderten, wurden einerseits die Schwierigkeit identifiziert, eine vollständige Liste geschlossener Bahnen zu erhalten, andererseits, und wichtiger, die Allgegenwart von Bifurkationen, die das semiklassische Spektrum entstellen. Sie erzwingen die Einbeziehung uniformer Näherungen in das Quantisierungsverfahren.

Das Verfahren der semiklassischen Quantisierung durch harmonische Inversion wurde so verallgemeinert, dass es sowohl die Quantisierung nichtskalierender Systeme als auch die Berücksichtigung uniformer Näherungen gestattet. Das Verfahren wurde am Beispiel des Wasserstoffatoms im elektrischen Feld demonstriert. Hier gelang die Berechnung eines semiklassischen Spektrums bei konstanter äußerer Feldstärke in einem Spektralbereich, in dem die closed-orbit-Theorie ohne uniforme Näherungen wegen der Vielzahl von Bifurkationen keine brauchbaren Ergebnisse mehr liefern könnte. Damit ist gezeigt, dass die Technik der harmonischen Inversion nunmehr ein wirklich universelles Quantisierungsverfahren darstellt, das im Rahmen der closed-orbit- oder der periodic-orbit-Theorie zur semiklassischen Quantisierung beliebiger Systeme eingesetzt werden kann, da es keine speziellen Voraussetzungen an die zu Grunde liegende klassische Dynamik mehr enthält.

Wegen der hohen Aktualität des Themas wurde ein Teil der Ergebnisse dieser Arbeit vorveröffentlicht [32].

Danksagung

An dieser Stelle möchte ich mich bei allen Mitgliedern des Instituts für Theoretische Physik I bedanken, die in der einen oder anderen Weise zum Gelingen dieser Arbeit beigetragen haben.

Insbesondere danke ich

- Prof. Dr. Günter Wunner dafür, dass er mir die Bearbeitung dieses interessanten Themas ermöglichte und mich in jeder Weise unterstützte,
- Prof. Dr. Manfred Fähnle für die Übernahme des Mitberichts,
- PD Dr. Jörg Main für die hervorragende Betreuung und dafür, dass er immer für Diskussionen zur Verfügung stand und manchen wichtigen Hinweis gegeben hat,
- den Systemadministratoren Dirk Engel, Steffen Bücheler, Georg Wöste und Markus Stollsteimer dafür, dass immer ein gut funktionierendes Rechner-system zur Verfügung stand,
- Rosi Bund dafür, dass sie bei organisatorischen Problemen immer hilfsbereit war.